Photoinduced Electron, Proton and Proton-Coupled Electron Transfer in H-Bonded Complexes

A Thesis Submitted in Partial Fulfillment of the
Requirements for the degree of
Doctor of Philosophy
in
Chemistry

by

Tousif Hossen
156122043

Department of Chemistry
Indian Institute of Technology Guwahati
Assam, India

INDIAN INSTITUTE OF TECHNOLOGY GUWAHATI

Department of Chemistry

Declaration

I do hereby declare that the work contained in this thesis entitled **“Photoinduced Electron, Proton and Proton-Coupled Electron Transfer in H-Bonded Complexes”** is the outcome of the research work carried out by me under the supervision of Dr. Kalyanasis Sahu, Associate Professor, Department of Chemistry, Indian Institute of Technology Guwahati, India.

In keeping with the general practice of reporting scientific observations, due acknowledgements have been made whenever work described here has been based on the findings of other investigators. This work has not been submitted elsewhere for the award of any degree.

Dated:

Department of Chemistry
Indian Institute of Technology Guwhati, (Tousif Hossen)
Guwahti-781039, India

INDIAN INSTITUTE OF TECHNOLOGY GUWAHATI

Department of Chemistry

Certificate

It is certified that the work included in this thesis entitled **"Photoinduced Electron, Proton and Proton-Coupled Electron Transfer in H-Bonded Complexes"** is the results obtained from the research work carried out by **Tousif Hossen** (Roll No. 156122043) under my supervision in the Department of Chemistry, Indian Institute of Technology Guwahati, Assam, India. I am forwarding his thesis to submit for the award of degree of Doctor of Philosophy, from this institute. I hereby certify that he has fulfilled all the requirements, according to the rules of this institute regarding the investigations embodied in his thesis and this work has not been submitted elsewhere for a degree.

Dr. Kalyanasis Sahu
(Thesis Supervisor)
Associate Professor
Department of Chemistry
IIT Guwahati
Assam - 781039, India

Dedicated to my Mom and Dad

“You have to dream before your dreams can come true.”

Dr. A.P.J. Abdul Kalam

Acknowledgement

First and foremost, with due humble submissions, I would like to thank my Almighty, most Gracious, and most Compassionate for blessing me with the attire of a researcher and being always benevolent in guiding my life.

At this stage of ending my PhD programme, I would like to appreciate the people around me throughout my academic journey without whom this thesis would not have been a reality. First of all, I take this opportunity to convey my heartfelt and overwhelming gratitude and respect to my thesis supervisor, Dr. Kalyanasis Sahu, who has been an excellent supervisor and taught me how to carry out research supervision. I have been lucky to have a supervisor who took so much care of my work and responded so promptly to my questions and queries.With his enthusiasm, inspiration, and efforts to explain things lucidly, he helped me in making this thesis a reality. His integral vision on research, meticulous eye for details, and a scientific yet straightforward approach towards any problem will always leave a deep impression in my mind. Besides this, he has provided me scientific knowledge, computational, and experimental skills and also made me to understand a broader perspective of life as well. I find myself privileged to have worked under his guidance.

I would like to acknowledge my sincere gratitude to the doctoral committee members Prof. Aditya N. Panda (Chairman), Prof. Sandip Paul, Dr. Shyam Prosad Biswas, and Dr. Manabendra Sarma who have constantly been guiding me with their valuable suggestions, encouragements and constructive criticism which helped to improve my thesis. I take this opportunity to thank Prof. Gopal Das (HOD) and Prof. Tharmalingam Punniyamurthy (former HOD).

I take this opportunity to thank IIT Guwahati for providing me Fellowship for my PhD programme. I thank the Department of Chemistry for providing instrumental and computational facilities, PARAM-ISHAN HPC, for the computational facilities and CIF for instrumental facilities. I am grateful to all the faculties and scientific staff of the department of chemistry for their kind help at different stages of my doctoral work.

Further, I would like to thank all my past and present group members for their support, helpful discussions, and creating an enjoyable environment in the lab. A big thanks to Dr. Nabajeet Barman, Dr. Debabrata Singha, Dr. Aparajita Phukon, Dr. Dillip kumar sahu, Tapas, Nilanjana, Priyanka, and Sanchari for their help, suggestions and sharing their many experiences during my work.

At this stage, I offer my sincere thanks to Prof. Abu Taleb Khan for his valuable suggestions. I also offer my sincere thanks to Prof. J. N. Moorthy for collaboration with us. I would like to thank Prof. Aditya N. Panda and his student Mohd Shavez for generous help in Gaussian installation. I am thankful to Krishna Gopal Chattaraj for discussing many aspects of MD simulations.

I extend my sincere thanks to my friends namely Subrata, Kalicharan, Bappa, Abbas, Soutick, Aniruddha, Maimur, Gopal, Adil, dillip da, Bapan da, Mostakim da, Arghni, and the other research scholars of Chemistry department who have shared their thoughts and views with me and all the joyful moments we shared in this campus.

Finally, I would like to thank my parents for their unreserved endurance, encouragement, and support throughout my life.

Sincerely

Tousif Hossen

Contents

Chapter 1: Introduction

Chapter 2: Theoretical and Experimental Methods

Chapter 3: H-Bonding around C102 in a Phenol−Cyclohexane Mixture for Implications in H-Bond-Guided Photoinduced Electron Transfer

Chapter 4: Proton Coupled Electron Transfer as a potential Fluorescence Quenching Mechanism in H-bonded C102-Phenol Complex

Chapter 5: Proton-Coupled Electron Transfer Vs. Photoinduced Electron Transfer in Methylbipyridine/Phenol Complexes

Chapter 6: Effect of Photoacid Strength on Fluorescence Modulation of 2-Naphthol Derivatives inside β-Cyclodextrin

Chapter 7: Contrasting pK_a Shift and Fluorescence Modulation of 6-Cyano-2-Naphthol inside α- and β-Cyclodextrins

SYNOPSIS OF THE THESIS

Abstract

Photo-excited hydrogen-bonded donor-acceptor systems often show unusual fluorescence behaviour and sometimes, it is difficult to assign a particular excited-state process to them. The thesis includes investigations on some simple but interesting hydrogen-bonded complexes and their photophysical processes like photoinduced electron transfer (PET), excited-state proton transfer (ESPT), and proton-coupled electron transfer (PECT). The thesis utilized seven chapters to distribute its contents.

Chapter 1 presents a brief account of recent experimental and theoretical advancements of the primary excited-state processes in H-bonded systems. Chapter 2 summarizes theoretical methods and experimental strategies adopted throughout the thesis. In chapter 3, molecular dynamics (MD) simulation was employed to unveil the exact H-bonding configuration of an experimental system comprising of a coumarin 102 (C102) as acceptor with varying number of phenol and cyclohexane molecules as a donor and a non-interacting partner, respectively. The main aim of this chapter was to get molecular insights of the molecular arrangement around the acceptor (C102) at different mole fractions of the phenol-cyclohexane mixture. The results assist to understand the unusual fluorescence modulation of C102 observed in the mixture in a previous experimental study.[1-2] In chapter 4, time-dependent density functional theory (TD-DFT) reveals the possibility of PCET as an alternative mechanism for the experimentally observed fluorescence quenching of the H-bonded C102-phenol complex. Chapter 5 deals with another H-bonded system methylbipyridine/methoxyphenol complex, which shows quite controversial spectroscopic signatures, which may be due to conventional PET or PCET. TD-DFT calculations presented in this chapter indicates that conventional PET is a more favorable excited-state pathway than PCET in the system. Finally, in chapter 6, the fluorescence modulation of three photoacids (2-naphthol, 6-sulfonate-2-naphthol, and 6-cyano-2-naphthol) was investigated inside the nanocavity of β-cyclodextrin (β-CD). The differential fluorescence modulation of the photoacid was found to be not due to very different hydration environment around the deprotonation site (hydroxyl group), but is linked to the intrinsic chemical nature ($\mathrm{p}K_a^*$) of the photoacids. Chapter 7 reports very different $\mathrm{p}K_a$ shift and fluorescence modulation of the strong photoacid 6-cyano-2-naphthol inside α- cyclodextrin (α-CD) vs β-CD.

Chapter 1: Introduction

Hydrogen bonding (H-bonding) is ubiquitous in molecular and supramolecular systems including self-assembly of lipids and surfactants, secondary and tertiary structures of proteins, DNA and RNA helices and so on.[3-4] Absorption of a photon by a chromophore in a H-bonded complex may induce a strong charge distribution within H-bonded donor or acceptor, and thus, the H-bond geometry (HB length, strength or angle) may alter significantly.[5] Modulation of H-bonding in the excited-state may be considered as a vital factor for governing photophysical and photochemical response in a H-bonding environment. [6-9] However, this aspect remains relatively unexplored in literature. Here, I am going to discuss excited-state H-bond guided three principal photophysical processes: - photoinduced electron transfer (PET), excited-state proton transfer (ESPT), and proton-coupled electron transfer (PCET).

In photoinduced electron transfer (PET), an electronically excited molecule can either take up an electron from another molecule (reductive PET) or release an electron to another molecule (oxidative PET).[10] Excited-state intermolecular proton transfer (ESPT) is commonly initiated by photo-excitation of an aromatic fluorophore, which is generally weak acid in the ground state but becomes much stronger acid in the excited electronic state. Such molecules are termed as photoacid, which can eject a proton to neighbouring solvent (water) or other bases (proton acceptor).[11-13] In a chemical reaction, an electron and a proton can transfer in a stepwise pathway involving initial electron transfer (ET) or initial proton transfer (PT), or by a concerted pathway without an intermediate. The concerted mechanism is termed proton-coupled electron transfer (PCET).[14-15]

Chapter 2: Theoretical and Experimental Methods

In the present chapter, we have discussed theoretical methodologies such as density functional theory (DFT), time-dependent density functional theory (TD-DFT) and molecular dynamics (MD) simulation that have been used in our studies. We have presented a brief description of several instrumentations, including absorption spectrophotometer, steady-state fluorometer, time-correlated single photon counting (TCSPC), and isothermal titration calorimetry (ITC), which have been used for completing the works described in the thesis. Chemicals used, sample preparation procedures, MD simulation procedure, and pK_a, pK_a^* calculations have also been included.

Chapter 3: H-Bonding around C102 in a Phenol−Cyclohexane Mixture for Implications in H-Bond-Guided Photoinduced Electron Transfer[16]

In a recent experiment, it was observed that the fluorescence intensity of C102 was quenched drastically and quite anomalously in the presence of phenol in a non-interacting solvent cyclohexane.[1] The fluorescence intensity is first quenched gradually up to a particular mole fraction ($X_{PH} \approx 0.013$) of phenol, but after that increases with further increase in the mole fraction.[2] The details of donor-acceptor H-bonding environment may be affected by the presence of the non-interacting solvent, which may lead to the anomalous variation of fluorescence intensity. In this chapter, molecular dynamics simulation was performed to elucidate the exact H-bonding environment around the acceptor C102 at different mole fractions of phenol in the phenol-cyclohexane solvent mixture. From the MD simulation, we observed mainly 1:1 H-bonded C102−phenol complex and some 1:2 H-bonded C102−(phenol)$_2$ complexes with two different types of geometries in addition. It was found that the total number of C102−phenol hydrogen bonding continuously increases with the increase in the phenol mole fraction and saturates at a significantly higher mole fraction. However, if we only consider the single H-bonding between one C102 with one phenol, then we obtain an excellent correlation with the experimentally observed critical mole fraction for maximum fluorescence quenching. Furthermore, DFT and TD-DFT calculations were applied on these H-bonded complexes to understand their excited state behavior and contribution to the fluorescence quenching. Thus, the study shows that single H-bonding is very important in inducing fluorescence quenching. The overall concept of this chapter has been schematically presented in **Figure 3.1**.

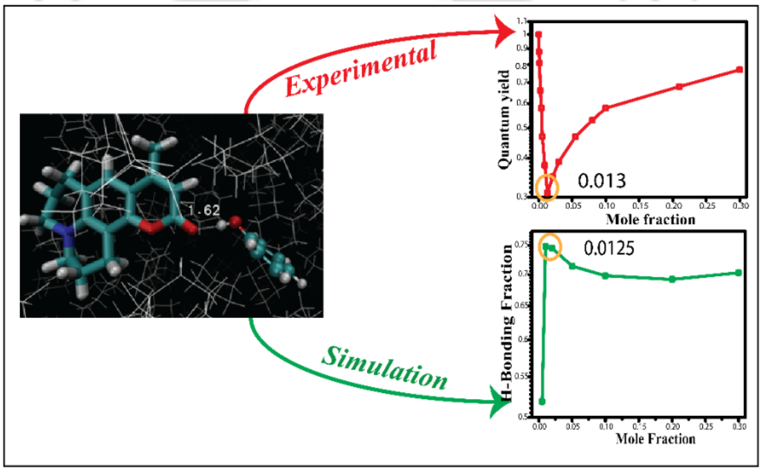

Figure 3.1: A scheme summarising the concept of Chapter 3.

Chapter 4: Proton Coupled Electron Transfer as a potential Fluorescence Quenching Mechanism in H-bonded C102-Phenol Complex[17]

Zhao and Han first reported a significant strengthening of the H-bond in the electronic excited state for the C102−phenol complex and proposed the possibility of fluorescence quenching in the complex via internal conversion from locally excited (LE) state to a low-lying charge transfer (CT) state.[5] However, in the previous work (Chapter 3), when TD-DFT calculations were applied on the C102−phenol complex, it was found that the energy ordering of the LE and CT states depends critically on the choice of the functional and solvent model.[16] In this chapter, the C102−phenol system was reinvestigated, applying more acceptable functionals. The excited-state potential energy surface was computed considering complete H-atom transfer from phenol to C102 along the H-bonding coordinate. Interestingly, two distinct minima were noticed, which are separated by a low-energy barrier. One minimum corresponds to the complex with the shortening of the H-bond distance, which is consistent with that of the Zhao and Han proposal. On the other hand, the second minimum, which has even lower energy than the first minimum, is likely to be arising from the proton-coupled electron transfer (PCET) process from phenol to C102. Furthermore, the nature of the lowest excited state alters from LE to CT type at the second lower energy minimum, which may account for the fluorescence quenching phenomena in the system. Thus, a new H-bond assisted fluorescence quenching pathway was reported for the H-bonded C102−phenol complex via PCET. The concept of this chapter has been schematically presented in **Figure 4.1**.

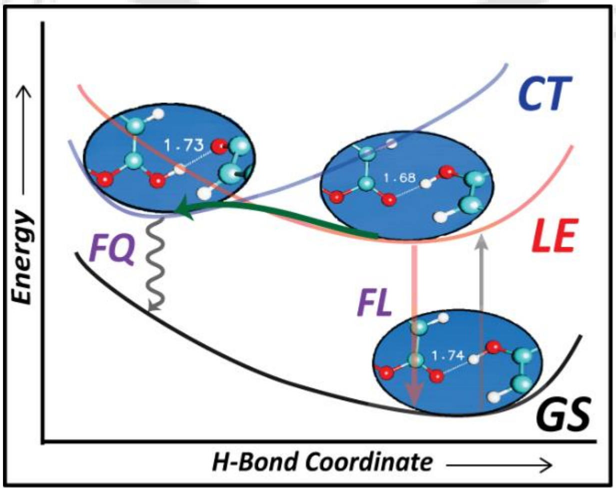

Figure 4.1: A scheme summarising the concept of Chapter 4.

Chapter 5: Proton-Coupled Electron Transfer Vs. Photoinduced Electron Transfer in Methylbipyridine/Phenol Complexes[18]

In the previous chapter 4, a new H-bond guided excited state PCET mechanism was proposed from the phenol donor to the C102 acceptor. The similarity of features between PCET and PET often creates confusion to track down the actual nature of the process in other H-bonded systems as well. The methylbipyridine/phenol complex is a classic example.[19-20] Gagliardi et al. proposed that an H-bond guided PCET process may occur from donor phenol to acceptor methylbipyridine (MQ$^+$).[19] However, Tyburski et al. argued that the process should be considered as a conventional charge transfer between the MQ$^+$/methoxyphenol system in the excited state.[20] In this chapter, TD-DFT calculations were implemented to elucidate the actual nature of the process occurring in the MQ$^+$/methoxyphenol complex. For the MQ$^+$/methoxyphenol complex, two types of configurations are possible in the ground state− H-bonded and π-stacked. Interestingly, it was found that the PCET reaction is only possible from the H-bonded complex. In contrast, a conventional PET was observed from donor methoxyphenol to the acceptor MQ$^+$ for the π-stacked complex. Furthermore, the calculated absorption band of the π-stacked complex matches well with the experimental absorption spectra. Hence, the π-stacked complex may be the main species in the ground state. Similarly, calculations of complexation energy also show that ground-state π-stacked complexes are energetically more favourable than the H-bonded complex. Hence, conventional PET is a more favourable excited-state process for the methylbipyridine/methoxyphenol complex than PCET (**Figure 5.1)**.

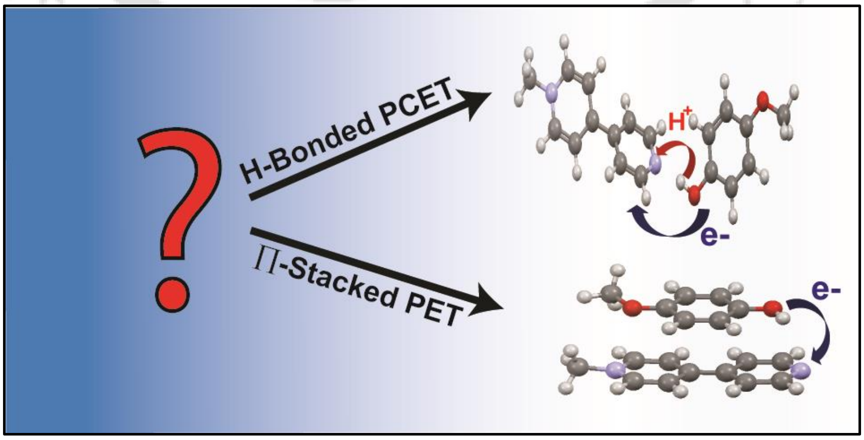

Figure 5.1: A scheme summarising the concept of Chapter 5. Schematic representation PCET and PET of the H-bond and π−π stacking configuration of the methylbipyridine/methoxyphenol complex, respectively.

Chapter 6: Effect of Photoacid Strength on Fluorescence Modulation of 2-Naphthol Derivatives inside β-Cyclodextrin[21]

In this chapter, three photoacids: 2-naphthol (2OH, pK_a^* = 3.3), 6-sulfonate-2-naphthol (6SO$_3$-2OH, pK_a^* = 3.06), and 6-cyano-2-naphthol (6CN-2OH, pK_a^* = 0.6) were chosen to investigate fluorescence modulation inside the nanocavity of β-cyclodextrin (β-CD). The photoacid derivatives differ by the substitution at the 6-position and have remarkably different excited-state acidities (pK_a^*). Significant fluorescence modulation was observed for 2OH and 6SO$_3$-2OH, but almost none was for 6CN-2OH upon the addition of β-CD. This is because the photoacids may bind differently to β-CD, 2OH, and 6SO$_3$-2OH may bind favourably, while 6CN-2OH may not bind at all. However, isothermal calorimetry measurements confirmed that all three photoacids form 1:1 inclusion complex with β-CD with comparable binding constants. Furthermore, MD simulation study revealed that binding modes are quite similar, and the distribution of water molecules around the proton-donating hydroxyl group of the photoacids are also comparable for all three inclusion complexes. Thus, the result shows that the difference in the fluorescence response of the photoacids should be accounted solely for the difference in the photoacidity strengths. The overall concept of this chapter has been schematically presented in **Figure 6.1**.

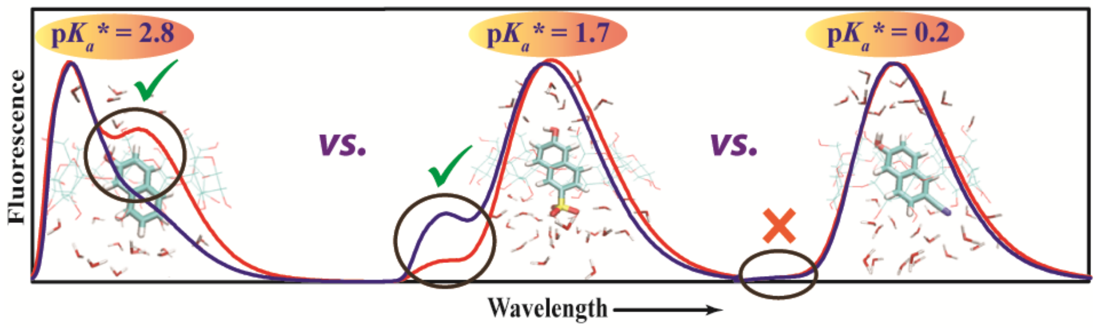

Figure 6.1: A scheme summarising the concept of Chapter 6. Emission spectra are shown for each photoacid in water and β-CD.

Chapter 7: Contrasting pK_a Shift and Fluorescence Modulation of 6-Cyano-2-Naphthol inside α- and β-Cyclodextrins

In this chapter, we have shown remarkably different pK_a shift and fluorescence modulation of a strong photoacid, 6-cyano-2-naphthol (6CN-2OH) upon inclusion complex formation with α-cyclodextrin (α-CD) and β-cyclodextrin (β-CD). In the previous chapter (chapter 6), it was observed that β-CD inclusion lowers pK_a and pK_a^* of 6CN-2OH compared to those in water. However, herein, the opposite trend is reported in the case of α-CD inclusion complex; the values of both pK_a and pK_a^* increase significantly than those of water. Moreover, the fluorescence modulation of the photoacid is also remarkably different in the two inclusion complexes; no noticeable change was observed in the fluorescence spectrum for the β-CD but a remarkable modulation was observed for the α-CD inclusion complex. Fluorescence transient measurements confirm significant suppression of excited-state proton transfer (ESPT) dynamics in the presence of α-CD but almost none for the β-CD complex. The rotational relaxation time of 6CN-2OH significantly increases in the α-CD complex than in the β-CD. Isothermal calorimetry measurements reveal that 6CN-2OH forms a 1:1 inclusion complex with β-CD with a moderate binding constant of 580 M^{-1}; whereas a 1:2 inclusion complex with α-CD with a high binding constant of 5.0×10^4 M^{-2}. Molecular dynamics simulation of the corresponding inclusion complexes reveal that the water molecules are severely depleted from the proton-donating hydroxyl group of the 6CN-2OH in the 6CN-2OH:(α-CD)$_2$ complex than in the 6CN-2OH:β-CD complex. Thus, the slow ESPT dynamics should be due to the lesser number of accessible 1st solvation shell water molecules in the 1:2 inclusion complex of α-CD. The overall concept of this chapter has been schematically presented in **Figure 7.1**.

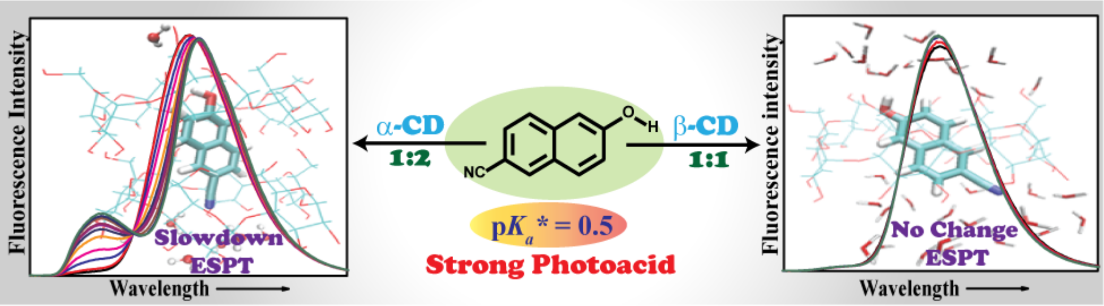

Figure 7.1: A scheme summarising the concept of Chapter 7.

References.

1. Barman, N.; Singha, D.; Sahu, K., Fluorescence Quenching of Hydrogen-Bonded Coumarin 102-Phenol Complex: Effect of Excited-State Hydrogen Bonding Strength. *J. Phys. Chem. A* **2013,** *117* (19), 3945-3953.
2. Barman, N.; Sahu, K., Reduced fluorescence quenching of coumarin 102 at higher phenol mole fractions in cyclohexane–phenol and anisole–phenol solvent mixtures: role of competitive hydrogen bonding. *RSC Adv.* **2014,** *4* (102), 58299-58306.
3. Wu, Y.-D.; Han, W.; Wang, D.-P.; Gao, Y.; Zhao, Y.-L., Theoretical Analysis of Secondary Structures of β-Peptides. *Acc. Chem. Res.* **2008,** *41* (10), 1418-1427.
4. Wu, Y. D.; Houk, K. N.; Valentine, J. S.; Nam, W., Is intramolecular hydrogen-bonding important for bleomycin reactivity? A molecular mechanics study. *Inorg. Chem.* **1992,** *31* (5), 718-720.
5. Zhao, G.-J.; Han, K.-L., Early Time Hydrogen-Bonding Dynamics of Photoexcited Coumarin 102 in Hydrogen-Donating Solvents: Theoretical Study. *J. Phys. Chem. A* **2007,** *111* (13), 2469-2474.
6. Chudoba, C.; Nibbering, E. T. J.; Elsaesser, T., Ultrafast Structural Response of Hydrogen Bonded Complexes to Electronic Excitation in the Liquid Phase. *J. Phys. Chem. A* **1999,** *103* (29), 5625-5628.
7. Zhao, G.-J.; Han, K.-L., Effects of Hydrogen Bonding on Tuning Photochemistry: Concerted Hydrogen-Bond Strengthening and Weakening. *ChemPhysChem* **2008,** *9* (13), 1842-1846.
8. Nibbering, E. T. J.; Elsaesser, T., Ultrafast Vibrational Dynamics of Hydrogen Bonds in the Condensed Phase. *Chem. Rev.* **2004,** *104* (4), 1887-1914.
9. Zhao, G.-J.; Han, K.-L., Hydrogen Bonding in the Electronic Excited State. *Acc. Chem. Res.* **2012,** *45* (3), 404-413.
10. Lakowicz, J., *Principles of Fluorescence Spectroscopy*. 2006; Vol. 1.
11. Pines, E.; Huppert, D., Geminate recombination proton-transfer reactions. *Chem. Phys. Lett.* **1986,** *126* (1), 88-91.
12. Leiderman, P.; Genosar, L.; Huppert, D., Excited-State Proton Transfer: Indication of Three Steps in the Dissociation and Recombination Process. *J. Phys. Chem. A* **2005,** *109* (27), 5965-5977.
13. Simkovitch, R.; Shomer, S.; Gepshtein, R.; Huppert, D., How Fast Can a Proton-Transfer Reaction Be beyond the Solvent-Control Limit? *J. Phys. Chem. B* **2015,** *119* (6), 2253-2262.
14. Hammes-Schiffer, S., Proton-Coupled Electron Transfer: Moving Together and Charging Forward. *J. Am. Chem. Soc.* **2015,** *137* (28), 8860-8871.
15. Lennox, J. C.; Kurtz, D. A.; Huang, T.; Dempsey, J. L., Excited-State Proton-Coupled Electron Transfer: Different Avenues for Promoting Proton/Electron Movement with Solar Photons. *ACS Energy Lett.* **2017,** *2* (5), 1246-1256.
16. Hossen, T.; Sahu, K., Elucidating the H-Bonding Environment of Coumarin 102 in a Phenol–Cyclohexane Mixture by Molecular Dynamics Simulation: Implications for H-Bond-Guided Photoinduced Electron Transfer. *J. Phys. Chem. A* **2017,** *121* (3), 616-622.
17. Hossen, T.; Sahu, K., New Insights on Hydrogen-Bond-Induced Fluorescence Quenching Mechanism of C102–Phenol Complex via Proton Coupled Electron Transfer. *J. Phys. Chem. A* **2018,** *122* (9), 2394-2400.

18. Hossen, T.; Sahu, K., Photo-induced Electron Transfer or Proton-Coupled Electron Transfer in Methylbipyridine/Phenol Complexes: A Time-Dependent Density Functional Theory Investigation. *J. Phys. Chem. A* **2019,** *123* (38), 8122-8129.

19. Gagliardi, C. J.; Wang, L.; Dongare, P.; Brennaman, M. K.; Papanikolas, J. M.; Meyer, T. J.; Thompson, D. W., Direct Observation of Light-Driven, Concerted Electron-ProtonTransfer. *Proc. Natl. Acad. Sci. U.S.A.* **2016,** *113* (40), 11106-11109.

20. Tyburski, R.; Fohlinger, J.; Hammarstrom, L., Light Driven Electron Transfer in Methylbipyridine/Phenol Complexes Is Not Proton Coupled. *J. Phys. Chem. A* **2018,** *122* (18), 4425-4429.

21. Hossen, T.; Sahu, K., Effect of Photoacid Strength on Fluorescence Modulation of 2-Naphthol Derivatives inside β-Cyclodextrin Cavity: Insights from Fluorescence, Isothermal Calorimetry, and Molecular Dynamics Simulations. *J. Phys. Chem. B* **2019,** *123* (44), 9291-9301.

LIST OF PUBLICATIONS

Publications included in the thesis:

1. Hossen, T.; Sahu, K., Elucidating the H-Bonding Environment of Coumarin 102 in a Phenol–Cyclohexane Mixture by Molecular Dynamics Simulation: Implications for H-Bond-Guided Photoinduced Electron Transfer. *J. Phys. Chem. A* **2017,** *121* (3), 616-622.

2. Hossen, T.; Sahu, K., New Insights on Hydrogen-Bond-Induced Fluorescence Quenching Mechanism of C102–Phenol Complex via Proton Coupled Electron Transfer. *J. Phys. Chem. A* **2018,** *122* (9), 2394-2400.

3. Hossen, T.; Sahu, K., Photo-induced Electron Transfer or Proton-Coupled Electron Transfer in Methylbipyridine/Phenol Complexes: A Time-Dependent Density Functional Theory Investigation. *J. Phys. Chem. A* **2019,** *123* (38), 8122-8129.

4. Hossen, T.; Sahu, K., Effect of Photoacid Strength on Fluorescence Modulation of 2-Naphthol Derivatives inside β-Cyclodextrin Cavity: Insights from Fluorescence, Isothermal Calorimetry, and Molecular Dynamics Simulations. *J. Phys. Chem. B* **2019,** *123* (44), 9291-9301.

5. Hossen, T.; Pramanik S.; Sahu, K., Contrasting pK_a Shift and Fluorescence Modulation of a Strong Photoacid 6-Cyano-2-Naphthol Inside α- and β-Cyclodextrin. (Communicated)

Publications not included in the thesis:

1. Barman, N.; Hossen, T.; Mondal, K.; Sahu, K., Modulation of ultrafast photoinduced electron transfer in H-bonding environment: PET from aniline to coumarin 153 in the presence of an inert co-solvent cyclohexane. *Phys. Chem. Chem. Phys.* **2015,** *17* (48), 32556-32563.

2. Mukhopadhyay, A.; Hossen, T.; Ghosh, I.; Koner, A. L.; Nau, W. M.; Sahu, K.; Moorthy, J. N., Helicity-Dependent Regiodifferentiation in the Excited-State Quenching and Chiroptical Properties of Inward/Outward Helical Coumarins. *Chem.: Eur. J.* **2017,** *23* (59), 14797-14805.

3. Mukhopadhyay, A.; Jana, K.; Hossen, T.; Sahu, K.; Moorthy, J. N., Coumarin-Annelated Regioisomeric Heptahelicenes: Influence of Helicity on Excited-State Properties and Chiroptical Properties. *J. Org. Chem.* **2019,** *84* (17), 10658-10668.

Conferences attended:

1. Poster presented in ***Research Conclave 2017,*** Indian Institute of Technology Guwahati, Guwahati, 2017.
2. Poster presented in ***Chemconvene 2017,*** Indian Institute of Technology Guwahati, Guwahati, 2017
3. Poster presented in ***ICANN 2017,*** Indian Institute of Technology Guwahati, Guwahati, 2017
4. Poster presented in ***FCS 2017,*** Indian Institute of Technology Guwahati, Guwahati, 2017
5. Poster presented in ***FICS 2018,*** Indian Institute of Technology Guwahati, Guwahati, 2018

List of Tables

Chapter 1

Chapter 2

Chapter 3

Chapter 4

Chapter 5

Chapter 6

Chapter 7

List of Figures

Chapter 1

fluorescence intensity monotonically decreases with an increase in the mole fraction of anisole.

Figure 1.7. Free-energy correlation found in the proton dissociation reaction of 2-naphthol derivatives (6X-2OH). Also shown in the correlation are the kinetic rate constants for the pyranol derivatives and 1-naphthol derivatives (5X-1OH). The solid line is the Marcus BEBO equation.

Figure 1.8. The free-energy correlation found in the proton dissociation reaction of 1a, 1b, DCN2, $NM6HQ^+$, HPTS, HPTA, and 5C1N in water. The dashed line is for the Marcus equation, and the solid line is for the Marcus BEBO equation.

Figure 1.9. Representative structures of β-CD: (a) side view and (b) front view (looking through the pore) and (c) a schematic representation as a truncated cone. Cavity dimensions of α-CD, β-CD and γ-CD are also tabulated for comparison.

Figure 1.10. The cavity dimensions of CB[5], CB[6], CB[7] and CB[8] macrocycles.

Figure 1.11. In the presence of various concentrations of β-CD (left side) and α-CD (right side) steady-state emission spectra of 2-naphthol (6CN-2OH) (a and b); (λ_{ex} = 310 nm).

Figure 1.12. Effect of inclusion complex of cucurbit[7]uril with β-naphthol and 4-methyl-7-hydroxyflavylium on ESPT dynamics.

Figure 1.13. Representation of the (a) four diabatic electronic states employed in the PCET theory; (b) free energy curves for the ground reactant (I, blue) and product (II, red) diabatic electron-proton vibronic states along with the collective solvent coordinate for an EPT reaction.

Figure 1.14. (a) Schematic representation of the net hydrogen atom transfer catalyzed by SLO with the linoleic acid substrate. (b) Change in SOMO along the N-H bond-forming reaction path for the oxidation of hydroquinone by cytochrome *bc₁* complex in complex III. R_{NH} corresponds to the N-H distance in Å.

Chapter 3

Figure 3.1. A representative MD simulation snapshot is showing C102-phenol H-bonding in the phenol-cyclohexane mixture at a phenol mole fraction of 0.005. C102, phenol, and cyclohexane molecules are denoted by LICORICE, CPK, and lines, respectively.

Figure 3.2. Structures of Coumarin 102 (C102) and phenol with the main atom labels used in the RDF calculations.

Figure 3.3. The radial distribution function, g(r) of the distance between the carbonyl oxygen (O1) of C102 and the hydroxyl hydrogen (H6) of phenol. The inset shows the 1st RDF peak strength against the mole fraction of phenol.

Figure 3.4. Integrated number n(r) is shown for above each mole fractions against distance.

Figure 3.5. Provide snapshots of mixtures forming 1:1:1 and 1:2 hydrogen bonds of phenol molecules with C102 at mole fraction of solvent phenol molecules (X_{ph}) - 0.3, where figure (a) shows MD snapshot for (1:2) complex and (b) shows MD snapshot for (1:1:1) complex. Cyclohexane molecules are omitted for clarity.

Figure 3.6. Optimized ground state (S_0) and excited state (S_3) structures of the hydrogen-bonded cumarin102-$(phenol)_2$ complexes are gas phase - (a) linear type structure (1:1:1) cumarin102-phenol-phenol complex, (b) bifurcated H-bonding of two phenols with one C102. It is evident that H-bond in (a) is shorter than in (b) complex in both states, and H-bond shortens in the excited state than in the ground state.

Chapter 4

Figure 4.1. The energy minimized ground state structure of the C102-phenol complex computed using CAM-B3LYP/6-311++G** and IEFPCM solvent (cyclohexane) model. The atoms involved in the H-bonding are labelled for representing the potential energy surface along the H-bond coordinate.

Figure 4.2. Potential energy surfaces of the C102-phenol complex in cyclohexane solution as a function of the H-atom transfer coordinate ((C102)O^1•••HO^2(phenol)) using CAM-B3LYP/6-311++G**(IEFPCM, cyclohexane). GS, ES1, ES2 and ES* respectively denote ground state minimum, two minima and barrier maximum in the first excited state.

Chapter 5

Chapter 6

Chapter 7

List of schemes

Chapter 1

ES H^+/e^- Acceptors, (C) ES e^- Acceptors, (D) ES e^- Donors, (E) ES H^+ Donors, and (F) ES H^+ Acceptors.

Scheme 1.14. (a) Chemical structures of the two hydrogen-bonded adducts (1) 4-hydroxy-4′-nitro biphenyl and t-butylamine and (2) 7-hydroxy-4-(trifluoromethyl)-coumarin and 1 methylimidazole. (b) The ICT and ICT-EPT energy-coordinate surfaces. Blue arrow represents excitation to the ICT state and red arrow excitation to the ICT-EPT state.

Scheme 1.15. (a) Proposed PCET scheme between *N*-methyl-4, 4′-bipyridinium cation (MQ^+), and para-substituted phenols through H-bonding. (b) Protonation equilibrium between the protonated (HMQ^{2+}) and deprotonated (MQ^+) forms of MQ^+.

Scheme 1.16. (a) Schematic depiction of the proposed mechanism for excited state MS-CPET in 1H. (b) Schematic depiction of the proposed excited state landscape along the H-atom transfer coordinate from phenol (PhOH) to TAHz.

Scheme 1.17. Sketch of the photoinduced electron transfer (ET) and proton transfer (PT) processes- (a) Ir(III) complex with dinitrobenzoate, (b) $[(bpy)_2Ru(phen(OH)_2]^{2+}$ with *N*-methylbipyridinium and (c) $[Ru(bpy)_2(bpz)]^{2+}$ with 1,4-hydroquinone.

Scheme 1.18. Schematic of the steps of the photocycle of the BLUF Slr1694 photoreceptor.

Chapter 5

Scheme 5.1. Schematic Representation of the grouping of the MQ^+/methoxyphenol Complex into Different Parts (A, H and D).

Chapter 6

Scheme 6.1. Molecular structure of the photoacids: 2-napththol (2OH), 6-sulfonate-2-napththol ($6SO_3$-2OH), 6-cyano-2-naphthol (6CN-2OH) and β-CD host (side and top views).

LIST OF ABBREVIATIONS

A	Acceptor
AN	Aniline
AN-*d*2	Amino Deuterated Aniline
AN-*d*7	per-Deuterated Aniline
APTS	8-aminopyrene-1,3,6-Trisulfonic Acid
BEBO	Bond-Energy-Bond-Order
CT	Charge Transfer
CB	Cucurbit-urils
CD	Cyclodextrin
C102	Coumarin 102
C151	Coumarin 151
C152	Coumarin 152
C153	Coumarin 153
C337	Coumarin 337
D	Donor
DFT	Density functional theory
DMA	*N*,*N*-Dimethylaniline
DMA-*d*6	Deuterated *N*,*N*-Dimethylaniline
DMSO	Dimethyl sulfoxide
DFT	Density Functional Theory
EDG	Electron Donating Group
EPT	Electron-Proton Transfer
ET	Electron Transfer
ESPT	Excited State Proton Transfer
ESIPT	Excited State Intramolecular Proton Transfer
ESHBD	Excited-State Hydrogen Bonding Dynamics
ES-PCET	Excited State Proton-Coupled Electron Transfer
EWG	Electron Withdrawing Group
HAT	Hydrogen Atom Transfer
HOMO	Highest Occupied Molecular Orbital
H-bonding	Hydrogen Bonding
HP-γ-CD	2-hydroxypropyl-γ-cyclodextrin

HPTS	8-hydroxypyrene-1, 3, 6-trisulfonate
IC	Internal Conversion
KIE	Kinetic Isotope Effect
LE	Locally Excited
LUMO	Lowest Unoccupied Molecular Orbital
MAN	*N*-Methyl aniline
MCP	Micro-Channel Plate
MD	Molecular Dynamics
MO	Molecular Orbital
MS-EPT	Multiple Site Electron−Proton Transfer
MQ^+	*N*-methyl-4, 4′-bipyridinium cation
Mβ-CD	Methyl-β-cyclodextrin
NADH	Nicotinamide Adenine Dinucleotide
NMR	Nuclear Magnetic Resonance Spectroscopy
OX750	Oxazine 750
QCy9	Quinone-cyanine 9 dye
PCET	Proton-Coupled Electron Transfer
PET	Photoinduced Electron Transfer
PES	Potential Energy Surfaces
PhOH	Phenol
PMT	Photomultiplier Tube
PT	Proton Transfer
QY	Quantum Yield
R800	Rhodamine 800
SLO	Soybean Lipoxygenase
TCSPC	Time Correlated Single Photon Counting
TDDFT	Time-Dependent Density Functional Theory
1OH	1-naphthol
2OH	2-naphthol
6CN-2OH	6-cyano-2-naphthol
$6SO_3$-2OH	6-sulfonate-2-naphthol
α-CD	Alpha-Cyclodextrin
β-CD	Beta-Cyclodextrin
γ-CD	Gamma-Cyclodextrin

Chapter-1

Introduction

Chapter 1: Introduction

Hydrogen bonding (H-bonding) is ubiquitous in many molecular and supramolecular systems including neat protic solvents, molecular crystals, self-assembly, biological macromolecules (protein secondary and tertiary structures, H-bonding within DNA and RNA bases, etc.), enzyme-substrate binding etc.[1-8] According to the International Union of Pure and Applied Chemistry (IUPAC) recommendation 2011, H-bond is an attractive interaction between a hydrogen atom within a molecule or a molecular fragment X–H, in which X is more electronegative than H, and an atom or a group of atoms within the same or a different molecule, in which there is evidence of bond formation.[9] H-bonding interaction is defined as X-H ...Y type, where X and Y (usually N, O and F) are more electronegative than H. The X-H and Y are donating and accepting sites of an H-bond, respectively. If these two sites belong to the same molecule, it is known as intramolecular H-bonding, but if the sites belong to different molecules, it is known as intermolecular H-bonding.

Photo-excitation of an H-bonded complex X-H…Y may be of three different types. Either of the H acceptor molecule (case I) or H donor molecule (case II) or both (case III) can be excited (**Scheme 1.1**).[10] Photo-excitation of an H-bonded complex may induce a strong charge redistribution within H-bond donor-acceptor complex, and thus, the H-bond geometry (e.g., H-bond length, strength or angle) and the electronic properties may alter significantly. The dynamics of this reorganization process is generally referred to as excited-state hydrogen bonding dynamics (ESHBD).[10]

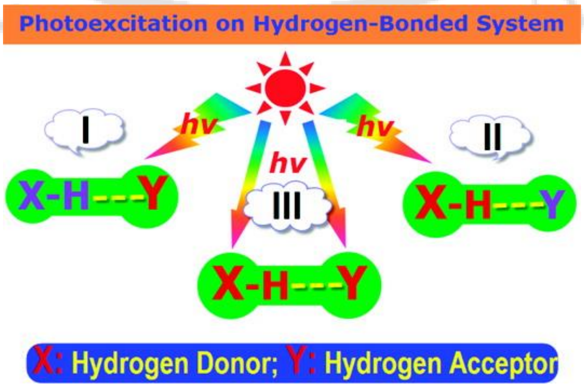

Scheme 1.1. Three cases of photo-excitation of the hydrogen-bonded systems. Unexcited and excited parts of the complex are denoted by blue and red color, respectively.[10] Reprinted with permission from ref 10. Copyright © 2012, American Chemical Society.

The intermolecular H-bond may have a crucial role in tuning the photochemistry and dynamics of photo-excited complex.[10-13] The energetics and dynamics of H-bonding in the ground state have been investigated extensively both experimentally and theoretically.[14-19] However, H-bonding in the higher electronic excited states remains relatively less explored. The excited-state H-bonding dynamics usually occur on hundreds of femtosecond timescale.[20-23] To monitor the ultrafast dynamical behaviour of H-bonding in the excited states, various ultrafast spectroscopic techniques such as femtosecond vibrational spectroscopy, femtosecond stimulated Raman spectroscopy, femtosecond absorption, and fluorescence spectroscopy have been applied.[23-24] Excited-state quantum chemistry calculations like time-dependent density functional theory, configuration interaction singles, multi-configurational self-consistent field, and coupled-cluster methods have also been applied to elucidate the nature of H-bonding in the electronic excited-states.[20, 25] Excited-state H-bonding is a vital factor for governing photophysical and photochemical responses in complex H-bonding environments. However, this aspect remains relatively less explored in literature. Here, I am going to discuss excited-state H-bond guided three principal photophysical processes (**Scheme 1.2**): i) photoinduced electron transfer (PET), ii) excited-state proton transfer (ESPT) and iii) proton-coupled electron transfer (PCET).

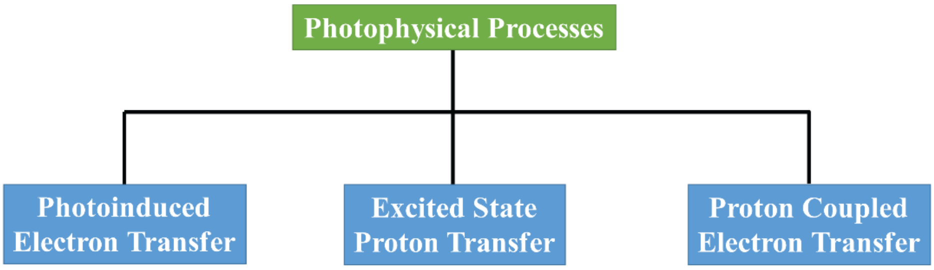

Scheme 1.2. Principal photophysical processes discussed in the thesis.

1.1. Photoinduced Electron Transfer

Photoinduced electron transfer (PET) is a process where a photoexcited donor molecule (upon absorption of light) can transfer an electron to another ground-state acceptor molecule (Oxidative PET), or a photoexcited acceptor molecule can take up an electron from another ground state donor molecule (Reductive PET).[26] Though photoinduced single electron transfer is more common, but the transfer of multiple electrons is also possible. Recently, Wenger and co-worker found the photoinduced multielectron transfer in a fully integrated molecular heptad composed of four donors, two photosensitizers, and one acceptor.[27] A molecule shows a thermodynamically greater tendency to accept or donate an electron in the higher electronic states upon photo-excitation. Thus, electronic excitation may activate a redox reaction (oxidation or reduction) between a pair of molecules which do not show electron transfer in the ground state.[26] The donor and acceptor molecules may be neutral or charged moiety. Photoinduced oxidative and reductive electron transfer processes between two neutral species can be expressed as follows-

$$D^* + A \rightarrow D^{\cdot+} + A^{\cdot-} \tag{1.1}$$

$$D + A^* \rightarrow D^{\cdot+} + A^{\cdot-} \tag{1.2}$$

where, D and A represent donor and acceptor molecules, respectively, in the ground state while asterisk denotes their electronically excited states.[26] $A^{\cdot-}$ and $D^{\cdot+}$ represent radical anion and radical cation, respectively, formed after the electron transfer reaction.

Furthermore, PET reactions can also be categorized based on the type of interaction between the D-A pair. If the D and A molecules are covalently linked or belong to the same molecule, it is often mentioned as intramolecular PET. Conversely, if D and A are separate molecules, it is referred to as intermolecular PET.[28-29]

Electron transfer (ET) is the most common ubiquitous elementary process in Chemistry and Biology.[30-46] PET plays a vital role in natural and artificial photosynthesis and allows conversion of solar light into chemical energy.[28-29] Besides, PET is important for designing a variety of optoelectronic devices, in photo-polymerization and photography.[47] Organic chemists are also showing great attention in PET as it involves in facile photochemical synthesis of many organic compounds after being oxidized or reduced by a photosensitizer.[48-50] Due to its huge importance, PET has been subject to numerous theoretical and experimental studies.[32, 34, 40-43, 46, 51-52]

1.1.1. Free Energy of Photoinduced Electron Transfer

The free energy ΔG_{ET}^0 of photoinduced electron transfer (PET) reaction can be determined from the Rehm-Weller thermodynamic relationship according to the equation.[35, 44, 53]

$$\Delta G^{0}_{ET} = E(D/D^{+}) - E(A/A^{-}) - E_{00} - E_{IPS} + \Delta E_{sol} \tag{1.3}$$

Where $E(D/D^{+})$ and $E(A/A^{-})$, denote the standard oxidation and reduction potentials of the electron donor (D) and an electron acceptor (A) in the medium, respectively. E_{00} represents the effective excitation energy, i.e., the difference in energy between the lowest vibrational level of ground electronic state and the lowest vibrational level of the first electronic excited state of the photoexcited species. E_{IPS} is the ion-pair stabilization energy of the medium. ΔE_{sol} is the correction term for the solvation energy of the A^{-} and D^{+} ions in solvents of different dielectric constants.

1.1.2. Rate Constant of Photoinduced Electron Transfer

The Marcus theory is widely used to calculate the rate of electron transfer (ET) reactions.[54] The rate constant of ET is given by

$$k_{ET} = \frac{2\pi}{\hbar} |V^{el}|^{2} \frac{1}{\sqrt{4\pi\lambda k_B T}} exp\left(-\frac{(\lambda+\Delta G^{0})^{2}}{4\lambda k_B T}\right) \tag{1.4}$$

Where ΔG^{0} is the total Gibbs free energy change for the electron transfer reaction, λ is solvent reorganization energy, and V^{el} is electronic donor-acceptor coupling, that is, the off-diagonal matrix element for the Hamiltonian of the initial and final states. k_B is the Boltzmann constant and T is temperature.

However, Marcus theory has some limitations – (i) Marcus equation doesn't consider modifications in electronic coupling that occur with increasing temperature, (ii) Marcus theory conflicts with the law of conservation of energy and has the error in principle.

1.1.3. Factors Affecting Photoinduced Electron Transfer

Several factors affect the rate of ET (or PET), including the free energy difference between reactant and product, solvent relaxation, intra-molecular vibrations, and electronic coupling between donor and acceptor. The D-A distance and their relative orientation play an essential role in determining the electronic coupling, which is controlled by the overlap of the electronic orbitals of D and A.[32, 55-56] Hydrogen bond may also exert a strong influence on the rate of ET (or PET) of the H-bonded donor-acceptor complex. H-bonding may control ET by changing the donor-acceptor distance and relative orientations compared to the non-hydrogen bonded analog.[55]

1.1.4. H-bond Guided Photoinduced Electron Transfer

H-bond guided electron transfer (ET) is an important phenomenon for chemical and biological systems (e.g., proteins and DNA).[30, 57-62] Numerous studies have tried to understand the role of H-bonding on photoinduced electron transfer (PET) process.[44, 63-64]

(i) Photoinduced Electron Transfer in a Neat Electron-Donating Solvent

Recently, Zhao and Han proposed a new PET mechanism for the H-bonded coumarin 102 (C102)-phenol complex (**Figure 1.1a**) in the excited-state using TD-DFT calculations.[20] From molecular orbital (MO) analysis of the H-bonded C102-phenol complex, they observed that the electron density of LUMO and HOMO-1 orbitals are entirely localized over the C102 fragment of the H-bonded complex. In contrast, electron densities of HOMO and HOMO-2 orbitals are entirely localized in phenol moiety (**Figure 1.1b**). Furthermore, they found that the S_2 state of the H-bonded complex with the highest oscillator strength is generated from the orbital transition HOMO-1 → LUMO. Thus, the S_2 state of the C102-phenol complex is locally excited (LE) in nature. Conversely, the S_1 is generated from the orbital transition HOMO → LUMO state of the C102-phenol complex, which corresponds to a charge-transfer (CT) state. Since H-bonding lowers the energy of the S_1 and S_2 state, hence, PET process in the H-bonded C102-phenol complex can be represented in the following way (**Scheme 1.3**)- (i) initially photo-excitation promotes the electrons of the C102-phenol complex in the S_2 (LE) state, (ii) then the excited H-bonded complex may relax directly through a radiative pathway to the ground state (S_0) or undergo internal conversion (IC) to the low lying CT (S_1) state depending upon the energy gap between the S_1 (CT) and S_2 (LE) states. H-bond strengthening in the excited state decreases this energy gap and hence facilitates the IC (or PET) from a LE state to a CT state within the H-bonded complex. Sahu et al. showed that internal conversion from the S_2 (LE) to S_1 (CT) state occurs on a much faster time scale (~600 ps) than the electronic relaxation of the unbound C102.[65]

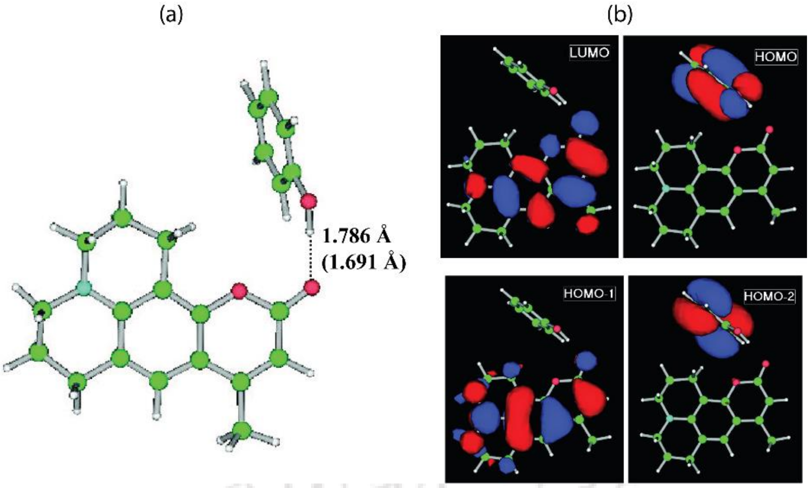

Figure 1.1. (a) 1:1 hydrogen-bonded complex of C102 and phenol in the ground state. The calculated H-bond lengths are displayed, and the excited state H-bond lengths are given in the bracket. (b) Frontier molecular orbitals (MOs) of hydrogen-bonded C102-phenol complex.[20] Reprinted with permission from ref 20. Copyright © 2007, American Chemical Society.

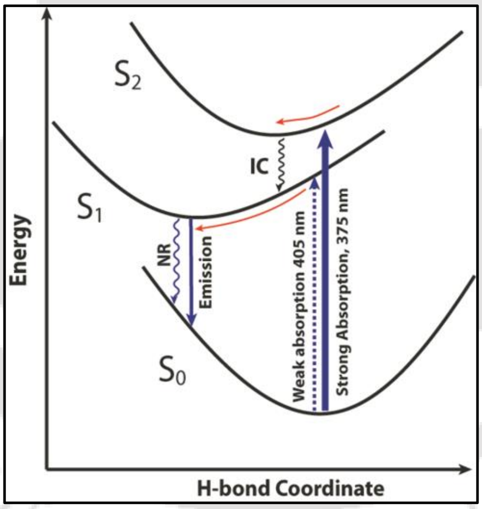

Scheme 1.3. Relaxation of the H-bonded complex. Absorption and emission are indicated by upward and downward, respectively, whereas internal conversion (IC) and non-radiative transitions are represented as wavy arrows; red curved arrows show the excited-state hydrogen-bonding dynamics.[65] Reprinted with permission from ref 65. Copyright © 2013, American Chemical Society.

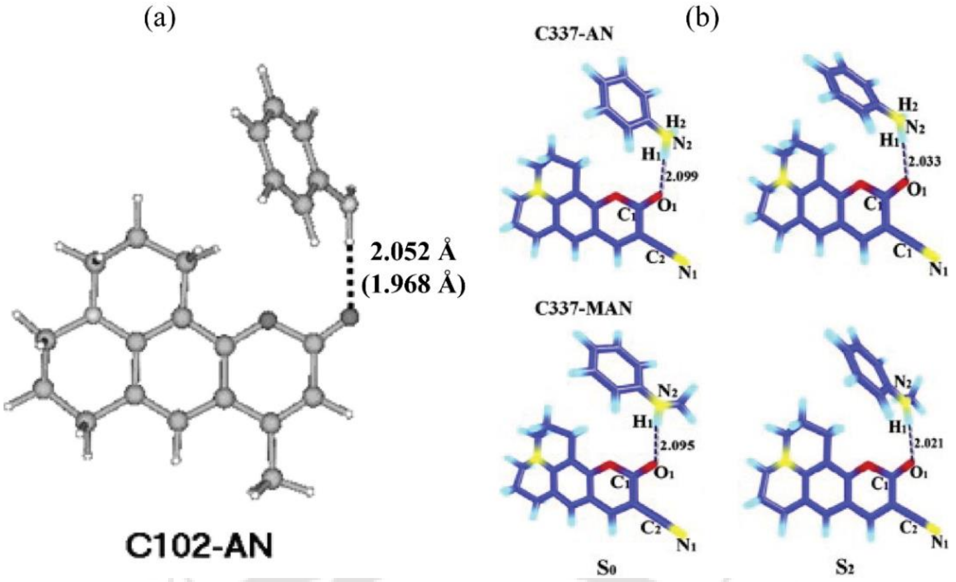

Figure 1.2. (a) Optimized structure of 1:1 complex of C102 and aniline in the ground state showing the hydrogen bond distance in angstrom and the excited state (in the bracket).[25] (b) Optimized structure of 1:1 complex of C337-aniline (top) and C337-N-methylaniline (bottom) in the ground (S_0) and excited state (S_2). The dashed lines represent hydrogen bonds between C337 and Aniline (or N-methylaniline). Corresponding H-bond distances in angstrom are also shown.[64] Reprinted with permission from ref 64. Copyright © 2012, Elsevier B.V.

Liu et al. showed a similar PET mechanism for the H-bonded C102-aniline system.[25] Using TD-DFT calculation for the 1:1 C102-aniline complex (**Figure 1.2a**), they observed that the H-bond, C=O···H-N between C102 and aniline (AN) becomes strengthened in the electronically excited state. They proposed that the H-bond strengthening in the excited state (LE) increases the electronic coupling between C102 and AN. This increased coupling facilitates electron transfer from the LE to CT state. Yang et al. also found similar H-bond strengthening between coumarin 337 (C337) and aniline (or N-methylaniline (DMA)) in the excited state (**Figure 1.2b**).[64] They also proposed that the H-bond strengthening in the electronically excited state should significantly assist PET within the H-bonded complex. In conclusion, a series of theoretical studies show that H-bond strengthening in the excited state favours PET in H-bond complex.[20, 25, 63]

However, experimental observations do not always support this proposal. To measure the dynamics of the photoinduced electron transfer process experimentally, the convenient way is to probe the fluorescence lifetime either of the donor or the acceptor. Using fluorescence up-conversion measurements, Yoshihara and co-workers have extensively investigated PET process for many fluorophores (Coumarins, Oxazines, Nile

Blue, etc.) in neat electron-donating solvents such as *N*,*N*-dimethylaniline (DMA) and Aniline.[41, 43-44, 46] In these PET reaction, the excited fluorophores act as an acceptor and receive an electron from the donor solvent. Many coumarins show energetically favourable PET in their excited state with AN/DMA donor and undergo PET even at a faster timescale than solvation dynamics[44, 46] and result in strong fluorescence quenching.[41, 43-44, 46]

Since H-bond dynamics occur in sub-picosecond time scales,[11, 13, 66-71] its influence would probably be more dominant in the ultrafast electron transfer process. Several studies tried to understand the role of H-bonding on the PET process using a series of coumarins fluorophore as acceptor and aromatic as well as aliphatic amines as donor solvent.[44, 63, 66] For example, C102 forms H-bond with aniline, which acts as an electron-donating solvent as well as an H-bond donor through its NH_2 group. Isotopic substitution technique is commonly used to unravel the mechanistic pathways of the intermolecular PET process. Effect of isotopic substitution on PET is usually observed due to the changes in the solvation time, vibrational frequencies, free energy change, etc.[44-46, 72-76] Several researchers applied the deuterium isotopic substitution effect to elucidate the role of H-bonding on PET.[44, 46]

Yoshihara and co-workers studied the deuterium isotopic substitution of both the donor solvents and acceptor dyes in the coumarin-aniline system (**Scheme 1.4**).[44, 46] Significant deuterium isotope effects have been observed in cases of per-deuterated aniline (AN-*d*7) and amino deuterated aniline (AN-*d*2) donors but were not observed with deuterated DMA (DMA-*d*6) and deuterated coumarins (**Scheme 1.4**).[44, 46] The extent of the isotope effect on PET was almost the same for both AN-*d*2 and AN-*d*7, which implies that the isotope effect is only linked with the NH_2 group of AN. They found that C153 shows faster PET in normal AN compared to the deuterated one. Similar isotope effect on PET was also observed for coumarin in deuterated ortho-methoxyaniline.[45]

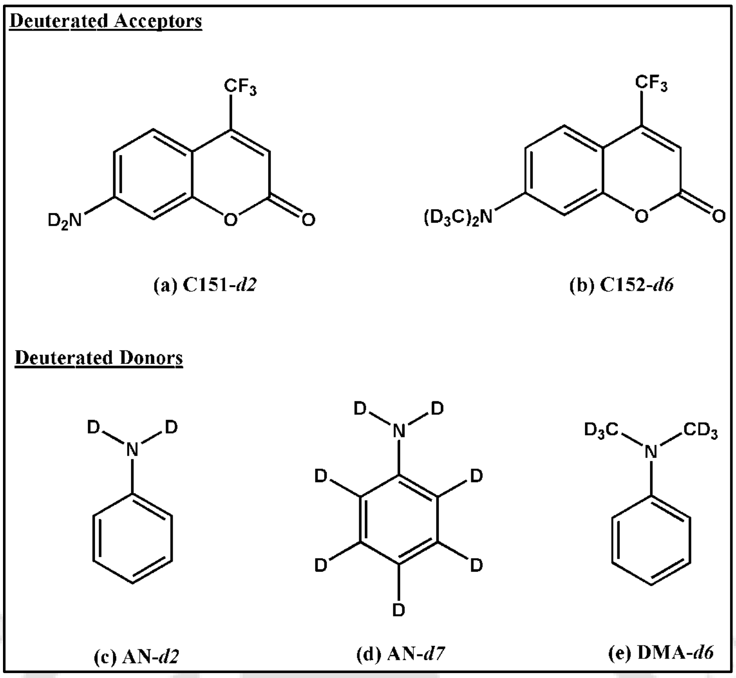

Scheme 1.4: Deuterated coumarin dyes (acceptor, a-b) and aromatic amines (donor, c-e).

However, Ghosh et al. did not find any evidence for the role of H-bonding on PET of C337 in AN (or MAN).[63] Using ultrafast IR spectroscopy, they studied PET of C337 in aromatic amine-AN, MAN, and DMA. H-bond formation between C337 and AN (or MAN) was confirmed by probing the red-shifted stretching modes of the C=O and C≡N of C337. C337 shows a fast PET of ~ 500 fs in all three solvents. Thus PET kinetics was the same in AN, MAN, and DMA, even though AN and MAN form H-bond with C337. The results indicated that H-bonding does not play any significant role in PET of C337. Moreover, they have not observed any H/D isotope effect. Nibbering and co-workers studied PET dynamics between FN and amine solvents such as diethylamine (DEA) and triethylamine (TEA).[77] DEA can form H-bond with the C=O group of FN, whereas no H-bond formation occurs with TEA. Fluorescence intensity of FN shows a drastic reduction in the emission intensity in both solvent TEA or DEA, and probably it is caused by the ET reaction with the amine solvents. They proposed that ultrafast fluorescence quenching is caused by forwarding PET from the amine solvent to the optically excited FN. Comparing the experimental rate constants with the driving force (i.e., free energy change) dependencies for forward and backward ET in amine solvents with and without H-bonding capabilities has provided key insights into the vital role of H-bonding in assisting ET processes.

(ii) Photoinduced Electron Transfer in a Solvent Mixture

PET in binary solvent mixtures is much less explored. Castner and co-workers first studied the change of PET rate of two different coumarin acceptors (C151 and C152) in a mixture of DMA and non-interacting solvent toluene using femtosecond up-conversion measurements and simulation.[78] They found that PET rate gradually decreases in addition to the non-interacting component. For instance, the rate of the electron transfer of C151 in neat DMA was 3.30 ps^{-1}, whereas, at an intermediate mole fraction of X_{DMA} (= 0.638), the ET rate decreases to 0.415 ps^{-1}. They also used chlorobenzene as a better co-solvent to minimize dielectric constants and dipole moment effects. They found a similar trend of PET reduction for chlorobenzene addition also. The retardation of PET was explained by the significant reduction in the electronic coupling between acceptor (coumarin) and the donor (DMA) due to the exchange of the inert solvent molecules with some of the DMA molecules from the first solvation layer of the acceptor (C151 or C152). On the contrary, Pshenichnikov and co-workers observed an unusual acceleration of electron transfer for rhodamine 800 (R800) upon addition of polar solvent acetonitrile to DMA.[79] Using frequency-resolved pump-probe transient spectroscopy they measured the backward ET rate for R800 at different mole fraction of acetonitrile. With an increase of the content of acetonitrile, the backward ET rate constant gradually decreased. Thus, the forward PET rate of the mixture was significantly higher than in neat DMA. It appears that the reduction of a number of donors results in more facile PET. They interpreted this anomalous behaviour to the change in dynamical properties of the medium.[79]

Nibbering and his group measured the response of an H-bonded complex formed between an organic fluorophore coumarin 102 (C102) and phenol in non-interacting solvent tetrachloroethylene upon electronic excitation by femtosecond visible pump-IR probe spectroscopy.[11] The complex may exist as 1:1 or 1:1:1 type. Electronic excitation of the coumarin chromophore initiates a rapid modification of the intermolecular hydrogen bond on two distinct time scales: $(phenol)_{1,2}$ is detached from coumarin within ~200 fs, followed by a reorganization of the $(phenol)_2$ moiety with 800 fs time constant. They monitored this structural response through strong changes in the vibrational frequencies of the C=O unit of C102 and –OH frequency of phenol moiety. In non-interacting solvent tetrachloroethylene, the C=O stretching band was observed at 1735 cm^{-1} (**Figure 1.3a**). The C=O stretching band of C102 exhibited significant downshift to 1695 cm^{-1} in the presence of phenol, which indicates the formation of strong H-bond between the C=O group of C102 and -O-H group of phenol in tetrachloroethylene. However, upon photo-excitation, the C=O stretching frequency of the H-bonded complex shifted back to 1740 cm^{-1} in the excited state within ~200 fs (**Figure 1.3b**). The C=O stretching frequency of the H-bonded complex in the excited state (1740 cm^{-1}) resembles the C=O stretching frequency of un-complexed C102. Thus, they concluded that the H-bond between C102 and phenol in both the C102-phenol and the C102-(phenol)$_{1,2}$ complexes break within 200 fs after excitation of C102.

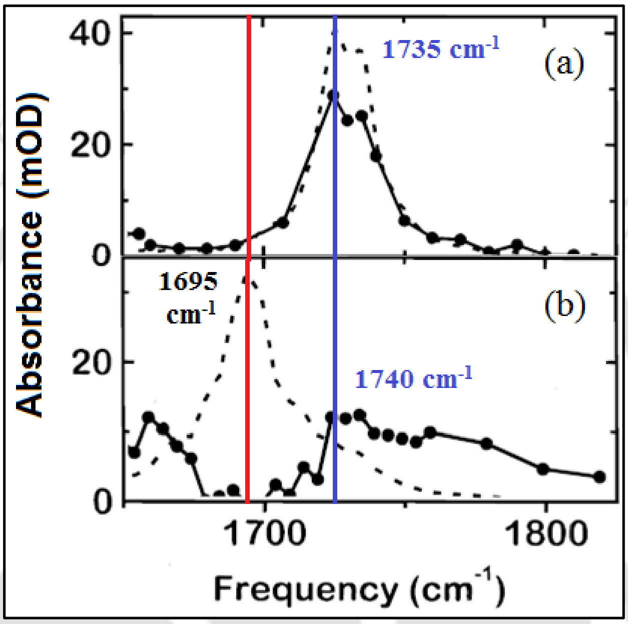

Figure 1.3. Ground state (dashed lines) and excited state (dotted lines) C=O stretching bands of (a) C102 and (b) C102-phenol complexes in C_2Cl_4.[11] Reprinted with permission from ref 11. Copyright © 1999, American Chemical Society.

On the contrary, Zhao and Han challenged the H-bond breaking formalism by computing the HB dynamics in the photoexcited state for the first time using time-dependent density functional theory (TDDFT) calculations. They computed the potential energy curves along the H-bonding coordinate in the different electronic states in the gas phase. The minimum of the potential energy curve in the excited state was found at 1.691 Å, which is considerably shorter than the minimum (at 1.785 Å) in the ground state (**Figure 1.4a**). They claimed the intermolecular HB between C102 and phenol becomes shorted rather than being not cleaved after photo-excitation. They also calculated the IR frequency of the C=O and the –OH groups of phenol by TDDFT method at BP-86/TZVP level.[20] Isolated C102 shows a C=O stretching frequency 1741 cm^{-1} in the ground state, which is blue-shifted to 1761 cm^{-1} in the excited state. However, in the ground state, the C=O stretching frequency of the H-bonded complex exhibited a strong red-shift by 55 cm^{-1} from 1741 cm^{-1} (isolated C102) to 1686 cm^{-1} (C102-Phenol) following the experimental result.[11, 68] In contrast to the experiment, in the excited state the C=O stretching frequency of H-bonded C102-phenol complex exhibited a red-shift from 1761 cm^{-1} (isolated C102) to 1686 cm^{-1} (C102-Phenol). Thus, the larger red-shift of the C=O stretching frequency in the excited state (75 cm^{-1}) compared to the ground state (55 cm^{-1}) suggested that H-bond between C102 and phenol strengthened in the excited state (**Figure 1.4b**).

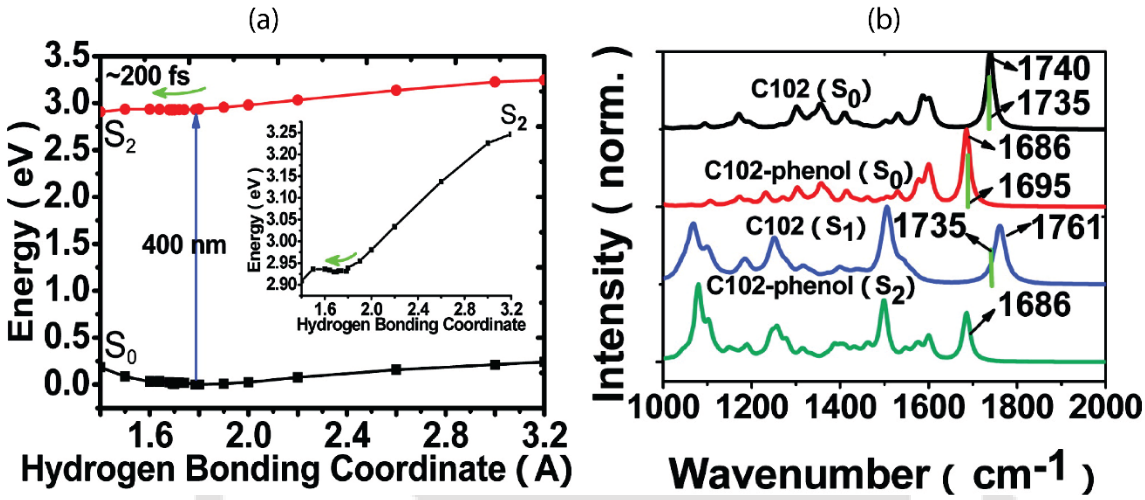

Figure 1.4. (a) Calculated Potential energy surfaces of the electronic states of hydrogen-bonded C102-phenol long with the hydrogen-bonding coordinate. (b). Calculated C=O stretching bands of isolated C102 and hydrogen-bonded C102-phenol dimer in different electronic states. The green lines show the experimental C=O stretching vibrational frequency in different states.[20] Reprinted with permission from ref 20. Copyright © 2007, American Chemical Society.

To resolve this discrepancy, our group recently revisited the C102-phenol system in non-interacting solvent cyclohexane both experimentally and theoretically.[65] A strong quenching of the C102 emission is observed in the H-bonded complex when phenol is added to C102 dissolved in non-interacting solvent cyclohexane (**Figure 1.5A**). They selectively excited the (λ_{ex} = 405 nm) H-bonded complex, and it relaxes on a fast time scale of 400−600 ps. They attributed this incident to the conversion of the locally excited (LE) state to a non-fluorescent charge transfer (CT) state assisted by the strong excited-state Hydrogen bond formation (**Figure 1.5B**). Their findings are following the new fluorescence quenching mechanism that the excited-state intermolecular hydrogen bond strengthening facilitates CT from phenol to coumarin in the excited state.[20] They also investigated with anisole and *p*-chlorophenol for comparison. No fluorescence quenching was observed for anisole where H-bond formation is not possible. On the contrary, more pronounced quenching was reported for p-Cl-phenol, where H-bonding is even stronger than phenol. [65]

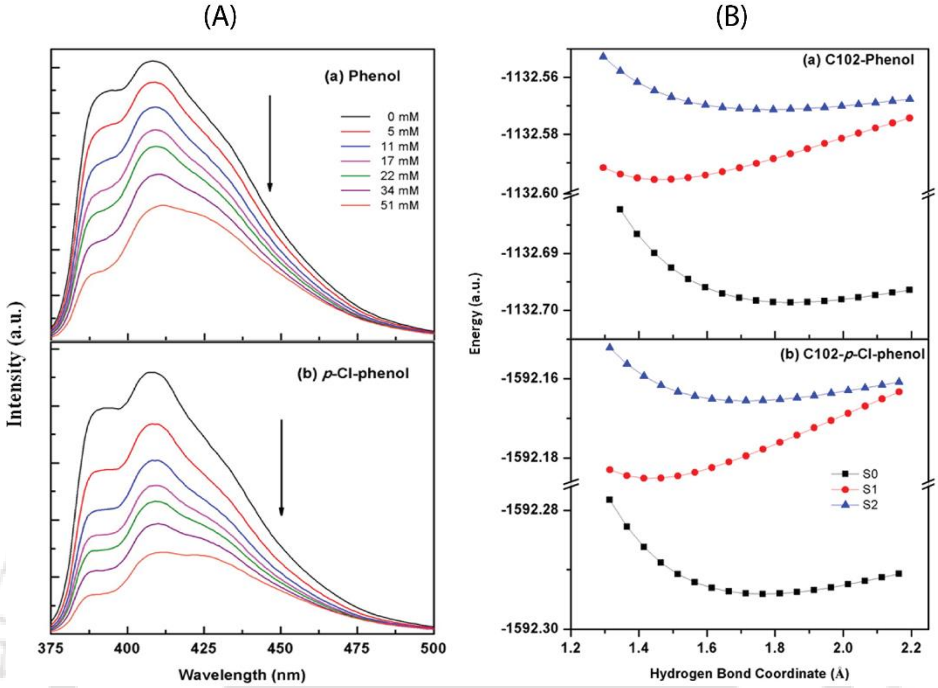

Figure 1.5. (A) Emission spectra of C102 in cyclohexane in the presence of different concentrations (0−51 mM) of (a) phenol and (b) p-Cl-phenol at an excitation wavelength (λ_{ex}) of 370 nm. (B) Potential energy variation along with the H-bond coordinates (i.e., the distance C=O······H−O in angstroms) for the C102-phenol (a) and C102-p-Cl-phenol (b) complexes in the three electronic states.[65] Reprinted with permission from ref 65. Copyright © 2013, American Chemical Society.

The above-mentioned work was limited to low concentrations of phenol, where 1:1 C102–phenol complexes predominately exist.[65] They also extended their work at higher concentration of phenol. Interestingly, an unusual fluorescence modulation of C102 was obtained when a large range of phenol concentrations were investigated. They found that the fluorescence quantum yield (φ_f) and fluorescence lifetime (τ_f) of C102 chromophore first diminish steadily with the increase of concentration of phenol but after a particular mole fraction (X_{PhOH} =0.013) both the quantities (φ_f and τ_f) increase upon further increase in the phenol content (**Figure 1.6a**).[80] They attributed this result due to the competitive nature of C102–phenol, and phenol–phenol H-bonding. Since PET quenching operates through the H-bond between the C=O group of C102 and the HO– group of phenol, the H-bond may fail to attain an optimum geometry when the phenol is linked with other phenols via the H-bond. They also studied phenol–anisole and anisole–cyclohexane binary mixtures, respectively. A similar unusual variation of the C102 fluorescence is observed in the phenol–anisole mixtures to a lesser extent (**Figure 1.6b**), but is completely absent in the anisole–cyclohexane mixtures, where H-bonding is practically impossible (**Figure 1.6c**).

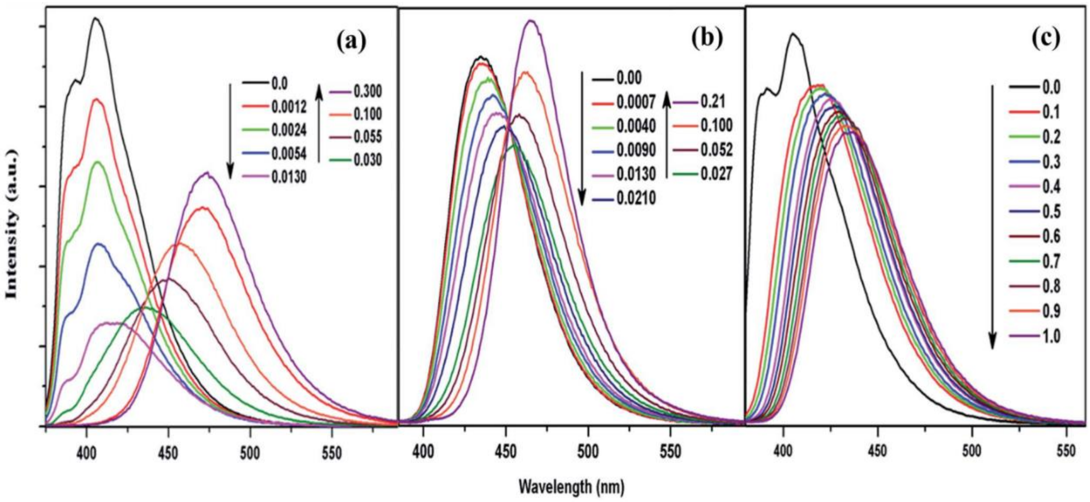

Figure 1.6. Emission spectra of C102 in (a) cyclohexane–phenol (λ_{ex} = 370 nm), (b) anisole–phenol (λ_{ex} = 375 nm) and (c) cyclohexane–anisole (λ_{ex} =375 nm). In (a) and (b) fluorescence intensity of C102 decreases with an increase in the mole fraction of phenol up to a certain mole fraction, after that increases with further enrichment of phenol. In (c), fluorescence intensity monotonically decreases with an increase in the mole fraction of anisole.[80] Reprinted with permission from ref 80.

Another important discrepancy between theory and experiment existed while considering the effect of H-bonding on PET between C102 and aniline. Experimentally, Palit et al. reported that the H-bond between excited C102 and aniline cleaves within 250 fs after photo-excitation but again reforms within 30 ps.[66] Similar to Zhao and Han's observation,[20] Liu et al. observed the strengthening of the excited-state H-bond between excited C102 and aniline for C102–aniline system using TD-DFT method.[25] To resolve this, our group studied the same system (C102-Aniline) in the presence of non-interacting solvent cyclohexane or toluene.[53] Similar to their previous work with C102-phenol,[65] they observed enhancement of PET in a binary mixture of aniline of mole fraction (X_{AN} = 0.075) compared to neat aniline. They found that both the fluorescence quantum yield and the lifetime of C102 first decreases up to a particular mole fraction (X_{AN} = 0.075) of aniline, and after that increases upon further addition of aniline. They proposed that, however, the non-interacting component cannot directly take part in the H-bond formation, but it may disrupt the aniline–aniline H-bond or change the polarity of the medium of C102–aniline system. To elucidate the exact reason for this anomalous PET process between C102–aniline in the presence of an inert solvent, they further continued their study. They used

AN–dimethylaniline (DMA) binary mixture instead of AN-cyclohexane to nullify the polarity effect variation.[81] Polarity of AN and DMA are almost the same. Interestingly, they found that the quantum yield and lifetime of C102 in AN–DMA follow the similar anomalous modulation, as observed previously in the AN–cyclohexane or AN–toluene mixtures. Therefore, in conclusion, 1:1 H-bonded C102–AN complex assist PET, which is favourable over H-bonded C102–$(AN)_{n\geq2}$ and AN-AN complex at an intermediate mole fraction of aniline rather than neat aniline. Recently they further worked with a well-known ultrafast PET acceptor coumarin 153 (C153) in both neat donor solvent (AN and DMA) and binary mixtures.[82] Experimentally they found that PET rate is maximum at some intermediate mole fraction of aniline ($X_{AN} = 0.74$) compared to neat aniline, whereas PET process gradually becomes retarded upon addition of cyclohexane to DMA. In this work, classical MD simulation was introduced to visualize molecular orientation around acceptor C153 for such a binary system. MD simulation reveals that the number of H-bond between C=O (C153) and H-N (AN) is higher at the intermediate mole fraction ($X_{AN} = 0.74$) of aniline in a mixture rather than in neat aniline. Therefore, they again established their previous hypothesis for an ultra-fast PET process, that H-bond assists PET process. Smitha and co-worker observed that for the hydrogen-bonded system in the normal region, the PET rate constant increases with increase in temperature.[83]

1.2. Excited State Proton Transfer

Proton transfer (PT) plays a crucial role in many ultrafast fundamental chemical processes, biological processes, and material properties.[84-86] Excited-state proton transfer (ESPT) is a variant of PT that occurs in the electronically excited state of a molecule. ESPT has been a subject of intensive research, both theoretically,[87-89] and experimentally.[86] In this process, the proton is transferred from one molecule to the neighbouring solvent molecule (intermolecular ESPT) or from one part of a molecule to another part of the same molecule (intramolecular ESPT or ESIPT) in the excited state. ESPT process is commonly initiated by photo-excitation of a suitable aromatic organic chromophore, known as photoacid. Experimentally, the ESPT process is usually investigated by steady-state and time-resolved absorption, fluorescence, and vibrational spectroscopy. An ESPT process usually occurs on an ultrafast time scale of sub-ps or ps.[90,91] To explore the mechanism of ESPT, theorists typically performed potential energy surface (PES) scan, transition state geometry optimization and calculation of transition energy barrier of ESPT reaction using ab initio excited-state calculations such TD-DFT method.[92-95]

1.2.1. Mechanism of Excited-State Proton Transfer

The kinetics of the excited-state proton transfer reactions of a photoacid and the potential energy surfaces in the ground and excited state along the proton transfer coordinate is represented in the **Scheme 1.5**.[96-97]

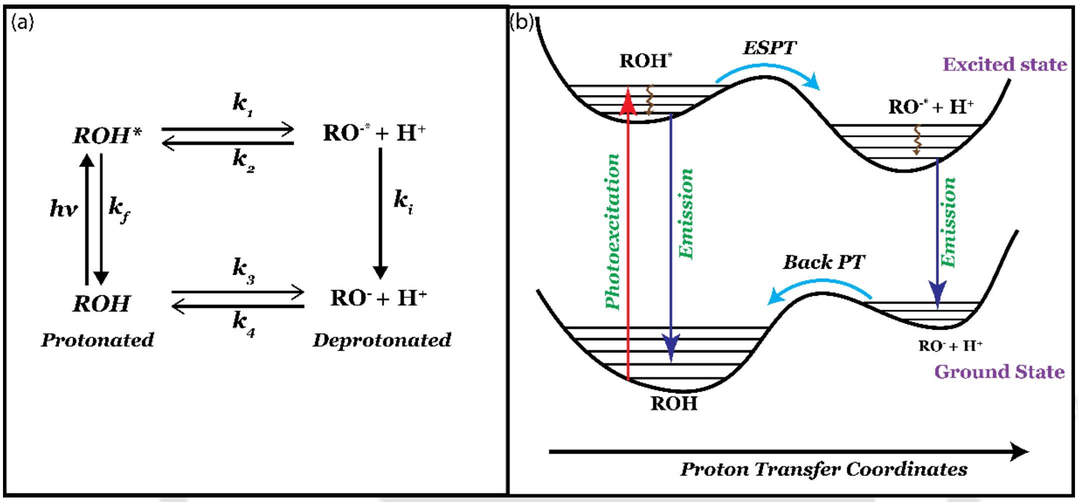

Scheme 1.5. (a) The photo-protolytic cycle of a photoacid. (b) Potential energy surfaces for excited-state proton transfer (ESPT) in the electronic ground and excited state of a photoacid along the proton transfer coordinate.

In **Scheme 1.5a**, ROH is the protonated form of a photoacid in the ground state. ROH* is a protonated form of the photoacid in the electronically excited state, which is obtained after photo-excitation. ROH* dissociates to form an excited anion with the proton. There are two fates to the dissociated proton– (i) it can do geminate recombination with the excited anion form of the photoacid (RO^{-}*) or (ii) it can diffuse away from the parent ion to ground state. Since the ground state dissociation is not an energetically favourable process, the ground state proton and anion quickly recombine to generate the ground state protonated form of the photoacid *ROH.* Here, k_1 and k_2 are the dissociation and recombination rate constants in the excited state. k_3 and k_4 are the dissociation and recombination rate constants in the ground state. k_f and k_i are the radiative rate constants of the excited protonated and deprotonated (anion) molecule, respectively. k_4 is the smallest kinetic constant among all. In the above **Scheme 1.5b**, we have graphically presented the proton transfer pathway both in the ground state and excited state. However, we have shown here favorable potential energy surface for excited-state proton transfer.

Furthermore, Huppert group proposed an "*Extended Reversible Diffusion-Influenced Two-Step Model*" to explain the ESPT process of photoacid in bulk water (**Scheme 1.6**).[98] This *Two-Step Model* involves the dissociation of excited protonated acid ROH^* into a contact ion pair, consisting of an anion and a hydrogen-bonded hydrated proton complex, designated as H_3O^+. The contact ion pair $RO^- \cdots H_3O^+$ shows almost similar spectroscopic signature as the RO^- emission band in the separated and solvated ion pair.

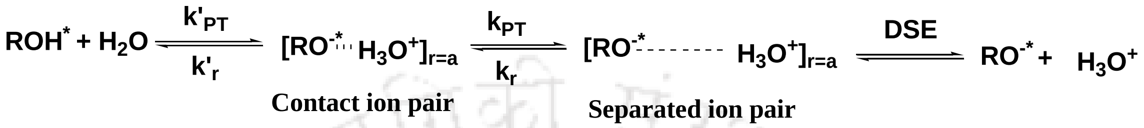

Scheme 1.6. The *Extended Reversible Diffusion-Influenced Two-Step Model*[98] for photo-protolytic dissociation of a photoacid.

It has been observed that temperature plays a pivotal role in determining the ESPT dynamics. Huppert and co-worker studied temperature dependence of the proton-transfer rate of wt-green fluorescent protein in H_2O and D_2O.[99] They observed that as the temperature decreases, the proton-transfer rate from the protonated form slows down. They also studied the temperature dependence of the photoprotolytic process of quinone-cyanine-7 (QCy7) in H_2O and D_2O ice, over a wide temperature range, 85–270 K.[100] They found that the ESPT rate to the solvent decreases as the temperature is lowered. Mitra and co-worker investigated the ESPT process of a photo-acid d-luciferin at different temperatures in reverse micelles.[101] They found that the rate of ESPT increases near-linearly with temperature.

1.2.2. Photoacids

Photoacids are aromatic organic compounds that are generally weak acids in the ground state but become much stronger acids in the excited electronic state. The excited-state equilibrium constant (K_a^*) of the photoacids (like 1-naphthol, 2-naphthol, etc.) is 5-10 order of magnitude greater than those at the ground state (K_a). Generally, this enhanced excited-state photoacidity is due to intramolecular charge transfer (ICT) from the hydroxyl oxygen to the aromatic ring in the excited-state (ES). It is considered that redistribution of the charge occurs almost immediately after photo-excitation, and the ultrafast dynamics can be observed through the spectral changes arising from excited-state proton transfer. Ground and excited-state photo-acidity are denoted by pK_a ($= -\log_{10}K_a$) and pK_a^*, respectively. At equilibrium, we get the pH change by **equation 1.5**. Excited-state photoacidity pK_a^* is commonly determined by using the Förster cycle.[102] Based on the ground state pK_a of the molecule and the absorption/emission spectra of the molecule, Förster proposed a method for estimating the pK_a^*. The enhancement of photoacidity is normally governed by the ΔpK_a, which is the difference between the pK_a and pK_a^* values. Hence, the higher the value of ΔpK_a indicates stronger the photoacid.

$$\mathrm{p}K_a^* = \mathrm{p}K_a - \frac{\mathrm{N_A}hc(\nu_{\mathrm{ArOH}} - \nu_{\mathrm{ArO-}})}{2.303\mathrm{RT}} \tag{1.5}$$

$$\Delta pK_a = pK_a - pK_a^* \tag{1.6}$$

Where c is the speed of light; *h* is the Planck's constant; N_A is Avogadro's constant; ν is the transition frequencies of ArOH and ArO− in wavenumbers (cm^{-1}); R is the ideal gas constant, and T is the temperature.

There are numerous examples of photo-acids, e.g., hydroxyl-aryls, aromatic amines, etc. Huppert and co-workers have grouped photo-acids into four categories according to the strength of photoacids.[103] The photoacids with p$K_a^* > 0$ (*regime I*) weak to intermediate-strength and can transfer a proton to only water.[104] Photoacids belonging to *regime II* ($-4 <$ p$K_a^* < 0$) can transfer a proton to many other protic solvents. For photoacids in *regime III* ($-7 <$ p$K_a^* <$ -4) ESPT dynamics is same order of solvation dynamics. The photoacids that belong to *regime IV* (p$K_a^* < -7$) are the strongest photo-acids and show exceptionally rapid ESPT rate ($\tau_{PT} \sim 100$ fs) in water, methanol, and ethanol. These photo-acids can undergo ESPT faster than solvation dynamics. Quinone-cyanine 9 dye (QCy9) and its derivatives,[105] belongs to *regime IV* and show an exceptionally rapid ESPT rate, $\tau_{PT} \sim 100$ fs was measured in water, methanol, and ethanol. In **Scheme 1.7**, a list representing an example for each class is described.

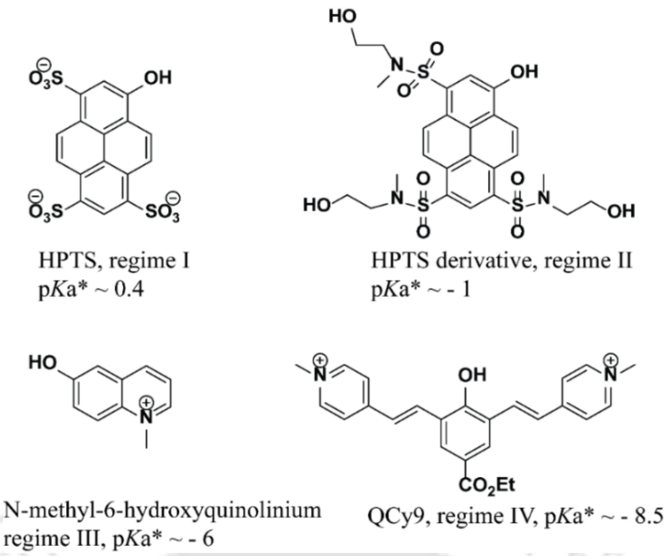
HPTS, regime I
pKa* ~ 0.4

HPTS derivative, regime II
pKa* ~ - 1

N-methyl-6-hydroxyquinolinium
regime III, pKa* ~ - 6

QCy9, regime IV, pKa* ~ - 8.5

Scheme 1.7. Different photo-acids representing the classified four regimes.[103]

The excited-state dynamics of strong photoacids with cationic and neutral acidic groups are quite different. Fayer and co-worker investigated a cationic photoacid 8-aminopyrene-1,3,6-trisulfonic acid trisodium salt (APTS, the total net charge of −2) and a neutral 8-hydroxypyrene-1,3,6-trisulfonic acid trisodium salt (HPTS) to compare the nature of intramolecular charge redistribution and ESPT rate between them (**Scheme 1.8**).[106] In the time-dependent pump-probe spectroscopy measurement, APTS shows single exponential dynamics in water, whereas HPTS shows bi-exponential dynamics. The redistribution of charges upon excitation explained this different modulation in dynamics. Unlike the neutral photoacid HPTS, cationic photoacid APTS do not have the available electron density in the protonated state to enable an intramolecular charge redistribution process upon photo-excitation.

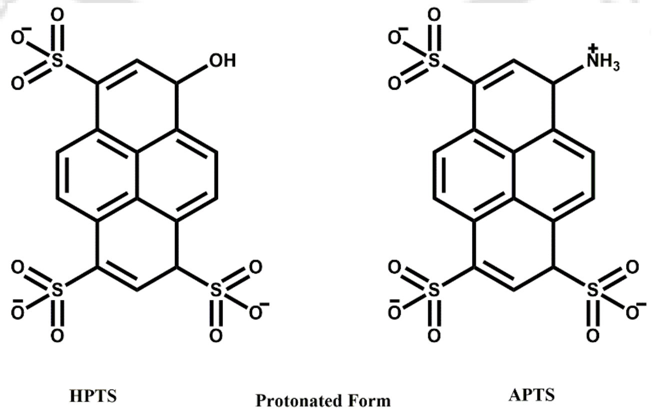

Scheme 1.8. HPTS is a neutral photoacid (left side), and APTS is a cationic photoacid (right side).

1.2.3. Substitution Effect on Photoacidity and ESPT

Enhancement of the acidities of aromatic alcohols upon photo-excitation has been discovered for several decades and has been utilized in several technological applications.[107] Most of these research has focused on the commercially available 1- and 2-naphthols, their sulfonated derivatives, and 8-hydroxypyrene-1,3,6-trisulfonic acid. Excited-state pK_a^* values of Naphthols is in the range 0-3. Thus, ESPT of Naphthols is limited to only aqueous solvents and does not transfer protons to alcohols or Me_2SO.[108-110] The photoacidity of 2-naphthol can be tuned by substitution on the naphthalene ring.

Tolbert and co-worker synthesized and calculated acidity for a series of cyano substituted 2-naphthol compounds- 5-cyano, 6-cyano, 7-cyano, and 8-cyano-2-naphthol (**Scheme 1.9 and Table 1.1**).[111] Because of the presence of a strong electron-withdrawing cyano group, they found that pK_a^* values were lower in comparison with simple 2-naphthol in the aqueous medium. Similarly, this decrease in the excited-state pK_a^* value was significantly higher than the reduction in ground-state pK_a values. This observation illustrates the more significant amount of the anion charge-transfer upon excitation. Furthermore, these compounds show efficient excited-state proton transfer to neutral non-aqueous solvents, like Me_2SO. They also proposed that ESPT without a Grotthuss chain-transfer pathway is possible to these kinds of highly acidic cyanonaphthol derivatives. By extending the range of excited-state acidities, cyanonaphthols can also be used to new photo-polymerization catalysts. Further, they continued the study of substitution effect on 1-naphthol. 1-naphthol has relatively higher photoacidity than 2-naphthol. This enhanced acidity is related to the relative energies of the L_a and L_b states (named after the short and long axes of symmetry in naphthalene).[112] The more polar L_a state is lower in energy for 1-naphthol, whereas for 2-naphthol, the more diffuse L_b state is lower. The mixing of L_a and L_b states increases the acidity of 1-naphthol, which is absent for 2-naphthol. They synthesized and compared the photoacidity of 5-cyano and 8-cyano-1-naphthol with simple 1-naphthol.[113] Similar to the 2-naphthol case, they found significantly enhanced photoacidity upon cyano substitution of 1-naphthol. Due to this enhanced photoacidity, the substituted cyanonaphthols undergo ESPT in a non-aqueous solvent such as alcohol and Me_2SO. They also proposed that solvent reorganization is less important for such strong cyanonaphthols photoacids compared to weak 2-naphthol photoacids.

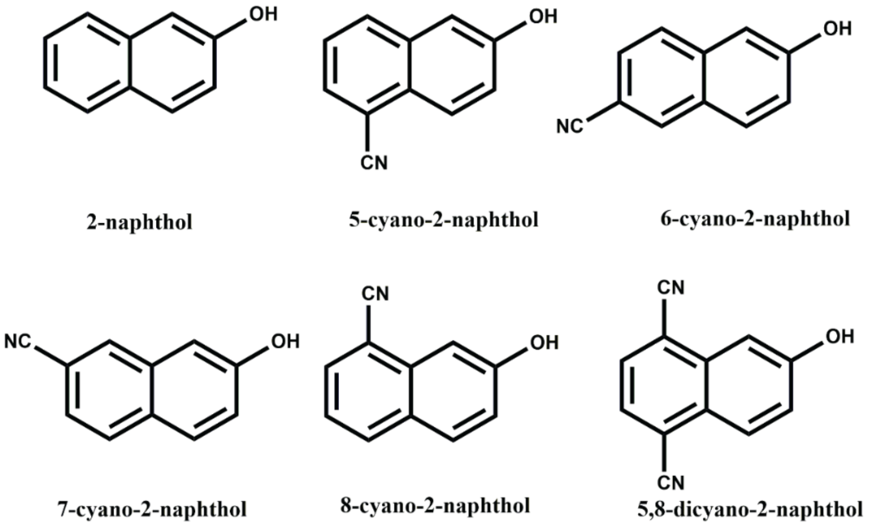

Scheme 1.9. Different cyano-substituted 2-naphthol photo-acids.

Agmon et al. systematically investigated 2-naphthol and some of its cyano derivatives in both ground and excited states using semi-empirical quantum calculations and considered both neutral and anionic forms.[114] For an investigation, the atomic Mulliken charge,[115] of the oxygen atom to monitor the intramolecular charge transfer from the oxygen atom, and the C=O bond length were measured. A systematic variation in charge density on the oxygen atom and C=O bond lengths are found within this cyanonaphthol family. Photoacids with a smaller negative charge on the oxygen atom and a shorter C=O bond length is more acidic nature, and substitution in the more electronegative ring sites also results in stronger acidity. It is also observed that the intramolecular charge transfer from the hydroxyl to the aromatic system is much more pronounced for the anion form than for the neutral photoacid upon excitation. Since Naphthalene possesses 10π-electrons (*n* = 2), hence it is an aromatic molecule. Thus, 2-naphthol derivatives are also aromatic. But in the anion form, conjugation of the negative oxygen charge with the aromatic ring results in a 12π-electrons system containing the anti-aromatic character. Therefore, they suggested that the drop of the aromaticity of the anion form of the photoacids decreases the S_0 - S_1 gap and increases the acidity.[114] However, recently, Chia-Hua et al. reported different aromatic nature of the bi-functional photoacids in the ground and excited-states.[116] They found that bi-functional aromatic compounds with [4n + 2]π- electron in the ground state become anti-aromatic in the first $^1\pi\pi^*$ states and compounds with [4n]π-electron become aromatic in the S_1 state.[116-117] They suggested that fast excited-state proton transfer (either inter- or intramolecular) occurs to get rid of the anti-aromaticity of the excited state.

Table 1.1. Experimental Values for Ground- and Excited-State pK_a Values of Cyano Substituted 2-Naphthols in Water.[111, 113]

Molecule	pK_a	pK_a^*
2-naphthol	9.5	2.8
5-cyano-2-naphthol	8.75	-0.75
6-cyano-2-naphthol	8.4	-0.4
7-cyano-2-naphthol	8.75	-0.2
8-cyano-2-naphthol	8.35	-0.75
5,8-dicyano-2-naphthol	7.8	-4.5

Takematsu and co-worker studied the photochemistry of 8-amino-2-naphthol (8N-2OH) and 5-amino-2-naphthol (5N-2OH) using a combination of time-resolved emission spectroscopy and time-dependent density functional theory calculations (**Scheme 1.10**).[118] Aminonaphthols have two protonation sites – oxygen atom of OH group and nitrogen-atom of NH_2 and can show ESPT at both OH and NH_2 protonation sites. Aminonaphthols forms zwitterion in the excited-state through the ESPT mechanism. Time-resolved studies showed that the zwitterion was formed only from excitation of the protonated form of 5N-2OH and 8N-2OH; as a result, ESPT occurs only at the single hydroxyl group. The protonation state of the amino group drastically changed the photoacidity of OH, and in the protonated state (NH_3^+), the pK_a^*(OH) values of both 5N-2OH and 8N-2OH become 1.1 ± 0.2. In contrast, in the deprotonated state (NH_2), pK_a^*(OH) values are much like the ground state proton acidity, pK_a(OH) = 9.5 ± 0.2. They also investigated ESPT reactions of the photoacids 1-amino-2-naphthol (1N-2OH) and 3-amino-2-naphthol (3N-2OH) in water and methanol, respectively.[119] Interestingly, they found that ESPT depends on the solvents at both protic sites of 1N-2OH and 3N-2OH. For 1N-2OH, ESPT was found at both the OH and NH_3^+ sites in water and in methanol just at the NH_3^+ site, but for 3N-2OH, ESPT was seen at the OH site in water, however at neither of the sites in methanol. They further studied the substitution effect of both electron-withdrawing group (EWG) and electron-donating group (EDG) on the photoacidity and excited-state proton transfer (PT) dynamics of 2-naphthol (2OH) through time-resolved emission spectroscopy and ab initio quantum calculations. To investigate, they chose the symmetric C7 position and took 7-amino-2-naphthol (7N-2OH) and 7-methoxy-2-naphthol (7OMe-2OH) (**Scheme 1.10**). The photochemical studies of 7N-2OH appeared that the photoacidity of the hydroxyl group behaves unexpectedly in the presence of an EWG (NH_3^+) vs. EDG (NH_2). For the excited protonated state (NH_3^+), the photoacidity pK_a^* becomes 1.1 and forms the zwitterion. Conversely, for the excited neutral state (NH_2), the photoacidity pK_a^* is reduced to 9.6. Surprisingly, investigations of 7OMe-2OH showed that the presence of EDG (OCH_3) has no impact on the photoacidity (pK_a^* = 2.7).

In the investigation of 6-carboxyl-2-naphthol (6C-2OH), Pines et al. found that the protonation state of the carboxylic acid raises the photoacidity of 2OH, pK_a^* = 1.2 vs. 2.5 for COOH and COO^- respectively.[120] They further constructed a Marcus (free-energy) diagram between excited-state proton dissociation rate constants (k_{PT}) vs. the excited-state equilibrium constants of the photoacids (K_a^*) like 6-substituted 2-naphthol derivatives and several 1-naphthol. It is already reported that the Marcus free-energy correlation,[121-122] and the Marcus Bond-Energy-Bond-Order (BEBO) expression,[123] provides good semi-empirical correlations between proton equilibria and proton transfer rates (**Figure 1.7**). Interestingly, from the curvature in the free-energy correlation between the proton transfer rate and equilibrium constant for strong acids, it is observed that proton transfer rate increases at protonation of the side group are predicted to be of a similar magnitude for ground and excited states cyanonaphthol. However, the predicted pK_a^* effect should be much greater than the corresponding pK_a effect.

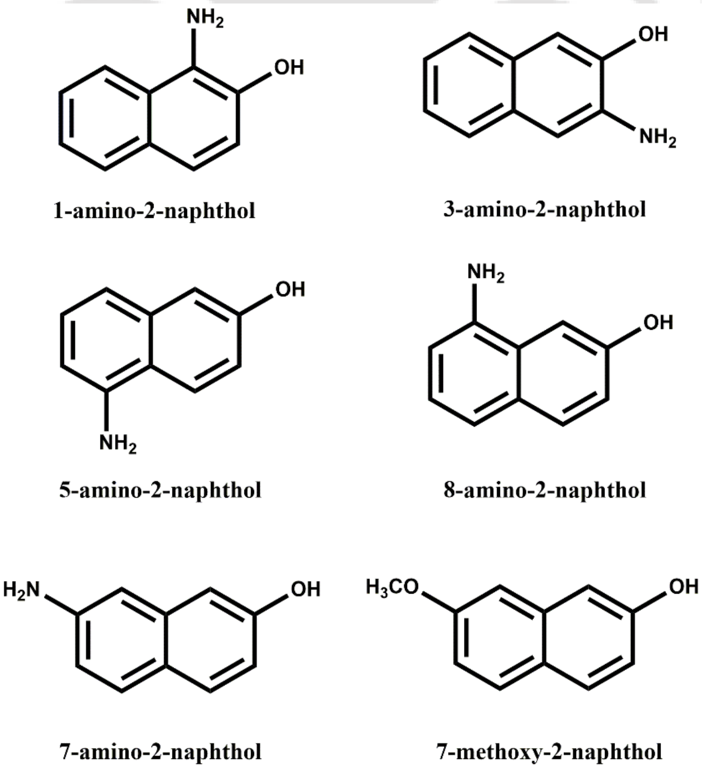
1-amino-2-naphthol
3-amino-2-naphthol
5-amino-2-naphthol
8-amino-2-naphthol
7-amino-2-naphthol
7-methoxy-2-naphthol

Scheme 1.10. Different amino-substituted 2-naphthol photo-acids and 7-methoxy-2-naphthol.

Similarly, Spies et al. studied the correlation between ESPT rate and photoacidity of two newly synthesized derivatives of 8-hydroxy-1,3,6-pyrenetrisulfonate (pyranine, HPTS) in water, methanol, and ethanol.[124] One is tris(1,1,1,3,3,3-hexafluoropropan-2-yl)-8-hydroxypyrene-1,3,6-trisulfonate (1a) with pK_a^* value -4, and another one is 8-Hydroxy-N1,N3,N6-tris(2-hydroxyethyl)-N1,N3,N6-trimethylpyrene-1,3,6-trisulfonamide (1b) with pK_a^* value -1. Unlike the weaker photoacid, HPTS, which only dissociates in water, both the (1a, 1b) photoacids can transfer a proton to alcohol.

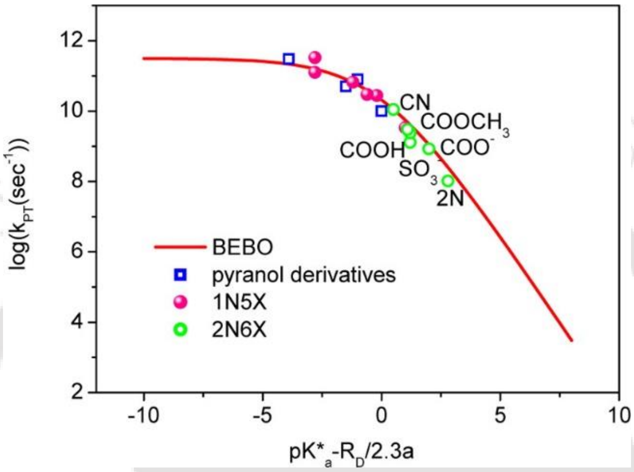

Figure 1.7. Free-energy correlation found in the proton dissociation reaction of 2-naphthol derivatives (6X-2OH). Also shown in the correlation are the kinetic rate constants for the pyranol derivatives,[124] and 1-naphthol derivatives (5X-1OH).[125] The solid line is the Marcus BEBO equation.[123] Reprinted with permission from ref 125. Copyright © 2013, American Chemical Society.

Thus, from the Marcus free-energy correlation plot (**Figure 1.8**), they stated that their newly synthesized photoacids would be the best group of structured photoacids studied to date to compare their respective reaction rates of proton transfer. A few previously studied strong photoacids are also included in **Figure 1.8**.[104, 126-128] The plot of the logarithm of ESPT rate constant as a function of pK_a^* shows that the slope of the free-energy correlation is dependent on the pK_a^* values of photoacids and the proton transfer rate of the strong photoacids weakly depends on the pK_a^*. However, it is important to note that the lifetime of the excited state must allow for proton transfer. Otherwise, the thermodynamic pK_a^* cannot yield a proton transfer.

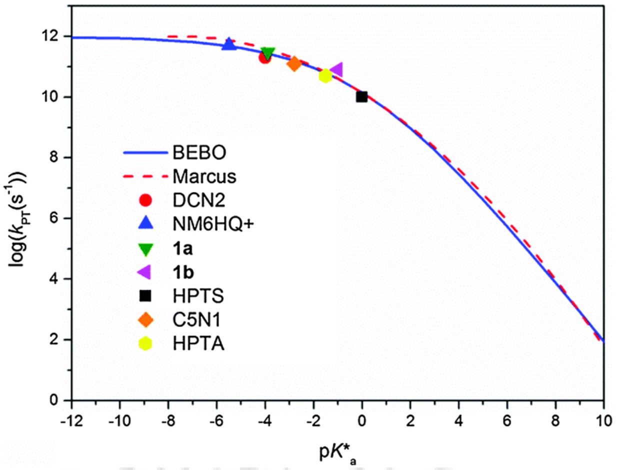

Figure 1.8. The free-energy correlation found in the proton dissociation reaction of 1a, 1b, DCN2, NM6HQ$^+$, HPTS, HPTA, and 5C1N in water. The dashed line is for the Marcus equation, and the solid line is for the Marcus BEBO equation.[124] Reprinted with permission from ref 124.

1.2.4. Macrocyclic Hosts: Cyclodextrin and Cucurbit uril

Among the different variety of bio-mimetic supramolecular macrocyclic hosts, cyclodextrins and cucurbit[n]urils are the most important and applied hosts.

The macrocyclic cyclodextrin molecules have a three-dimensional hydrophobic hollow cavity. Cyclodextrin molecules are known to form inclusion complexes with a variety of neutral molecules and ions of suitable size, shape, and charge/polarity. The well-defined host-guest inclusion complex mainly gets stability through non-covalent interaction mainly, van der Waals interaction, hydrogen bond, and dipole-dipole interaction.[129-133] Due to its hydrophobic nature of the cavity, cyclodextrin shows greater selectivity for hydrophobic and neutral molecules. The cyclodextrin (CD) molecules are made of D-glucopyranose monomer units and interconnected by α-1,4 linkages in a cyclic manner.[134-135] The natural α-, β- and γ-cyclodextrins contain 6, 7, and 8 glucopyranose units, respectively (**Figure 1.9**). The size of the cavity increases with increasing the number of monomer units. Hence the cavity size order is γ- > β- > α-CD. CDs are crucial in the field of supramolecular host-guest chemistry and pharmaceutical industry because of their non-toxic nature. The external surface of the CD molecules is hydrophilic in nature due to the presence of the hydroxyl groups at the portals, and this also makes them soluble in water.[136-137] Entropy factor associated with the expulsion of water molecules from the cavity is important for association of the guest. The solubility, stability, and bioavailability of drug molecules increases inside the CDs after encapsulation, and this quality of CD made them a potential candidate for carrying and drugs delivering in the pharmaceutical industry.[138-141]

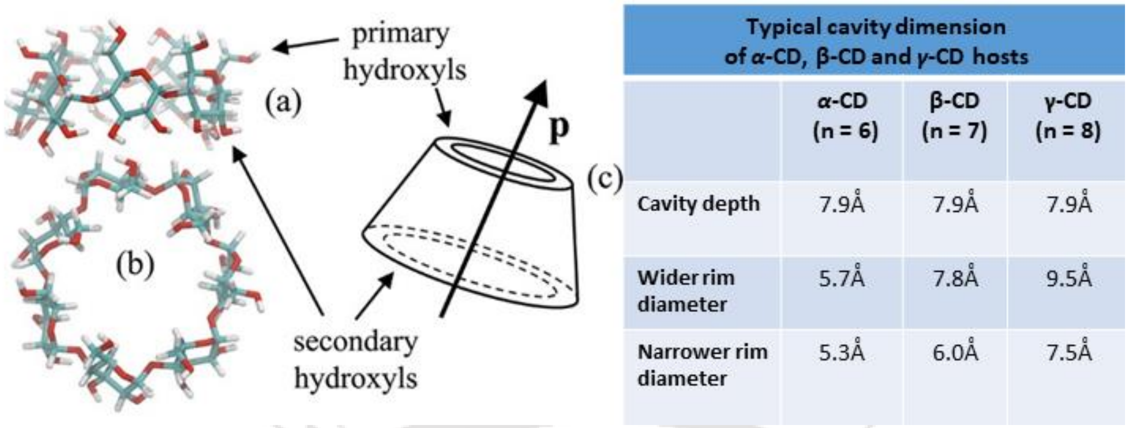

Typical cavity dimension of α-CD, β-CD and γ-CD hosts

	α-CD (n = 6)	β-CD (n = 7)	γ-CD (n = 8)
Cavity depth	7.9Å	7.9Å	7.9Å
Wider rim diameter	5.7Å	7.8Å	9.5Å
Narrower rim diameter	5.3Å	6.0Å	7.5Å

Figure 1.9. Representative structures of β-CD: (a) side view and (b) front view (looking through the pore) and (c) a schematic representation as a truncated cone.[142] Cavity dimensions of α-CD, β-CD and γ-CD are also tabulated for comparison.[135] Reprinted with permission from ref 142. Copyright © 2017, American Chemical Society.

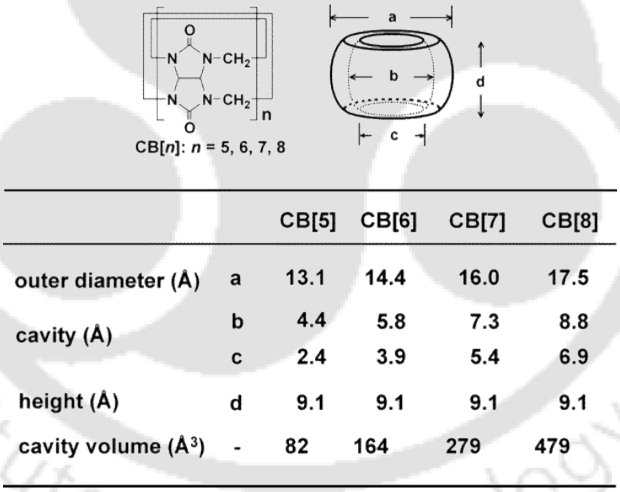

		CB[5]	CB[6]	CB[7]	CB[8]
outer diameter (Å)	a	13.1	14.4	16.0	17.5
cavity (Å)	b	4.4	5.8	7.3	8.8
	c	2.4	3.9	5.4	6.9
height (Å)	d	9.1	9.1	9.1	9.1
cavity volume (Å^3)	-	82	164	279	479

Figure 1.10. The cavity dimensions of CB[5], CB[6], CB[7] and CB[8] macrocycles.[143] Reprinted with permission from ref 143. Copyright © 2003, American Chemical Society.

Nowadays use of Cucurbit-uril CB[n] family increase over CD family in many areas of fundamental and applied science — chemistry, biology, material science, and nanotechnology. Macrocyclic CB[n] molecules are made of glycoluril monomers and interconnected by *2n* methylene bridges.[143-144] Pumpkin-shaped CB[n] molecules have a highly symmetrical hydrophobic cage of low polarity and polarizability with two identical dipolar portal ends composed of carbonyl functional groups (**Figure 1.10**). Four different sizes of cucurbit-urils are commercial availability in the market. CB[n] show high binding affinity and selectivity with guest molecules than other host molecules, and it is soluble in both organic and aqueous solution.[143]

1.2.5. Excited-State Proton Transfer inside Macrocyclic Host

2-Naphthol (2OH) is a well-known photoacid and well investigated with cyclodextrin host molecules. The photoacidity in the ground state (pK_a) of 2OH is 9.5, and excited-state photoacidity (pK_a^*) is 2.8.[113] Köhler and co-workers thoroughly studied the ground- and excited-state photophysical properties of 2-naphthol inclusion complexes with *α*-, β-, and some substituted β-cyclodextrins molecules.[145] From the measured steady-state absorption spectra, they found that the absorption peak (at 330 nm) of 2OH is red-shifted with increasing concentration of *α*- and β-cyclodextrins solution. Using absorption spectra data, they calculated the association constants for the photoacid:CD inclusion complexes. Interestingly, the interaction between 2OH and β-CD shows 1:1 type inclusion complex (2OH:β-CD) with an association constant of 590 M^{-1} at pH 6.5. In contrast, α-CD shows 1:2 type inclusion complex ($2OH:(\alpha\text{-}CD)_2$) with an association constant of 250 M^{-1} and 35 M^{-1}. An aqueous solution of 2OH exhibits two peak emission peaks – (i) protonated 2OH molecule (350 nm), and (ii) the deprotonated naphtholate ion (420 nm) (**Figure 1.11**). Upon the addition of CD molecules, the emission intensity of the protonated form increases at the expense of deprotonated emission. This observation indicates the decrease of the dissociation efficiency of 2OH, i.e., retardation of the ESPT process upon complexation with CD. Furthermore, their time-resolved measurements confirmed the slowdown of the ESPT process of 2OH inside CD cavities. They also determined the effect of hydrophobic inclusion on the pK_a and pK_a^* of 2OH. It was observed that the pK_a and pK_a^* values shifted to a higher value than aqueous solutions of 2OH in the presence of both CD solutions. The reduction of the photoacidity on the complexation is due to the decrease of the deprotonation rate of 2OH inside the CD cavities.

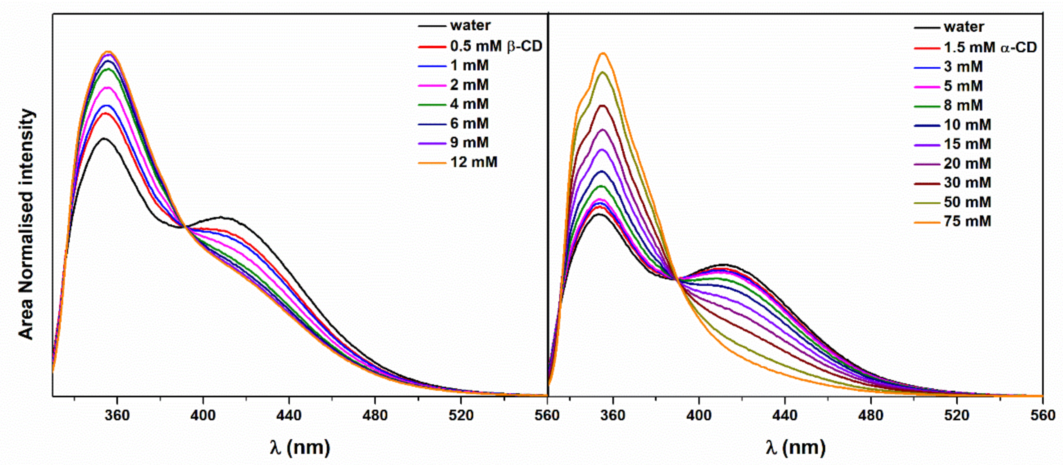

Figure 1.11. In the presence of various concentrations of β-CD (left side) and α-CD (right side) steady-state emission spectra of 2-naphthol (6CN-2OH) (a and b); (λ_{ex} = 310 nm).[145]

Stam et al. further studied the 1:1 2OH:β-CD complex in the absence and presence of linear alcohols.[146] From the steady-state fluorescence measurement data, the association constants (K_a) were determined. Interestingly, it was observed that K_a value decreases linearly as the number of carbon (n_C) atoms in the alcohol chain increases up to $n_C = 5$. They considered this observation because of competition between 2OH and alcohol molecules for the β-CD cavity. Fluorescence studies confirm the redistribution of 2OH from the CD environment to the aqueous phase in the presence of alcohol.

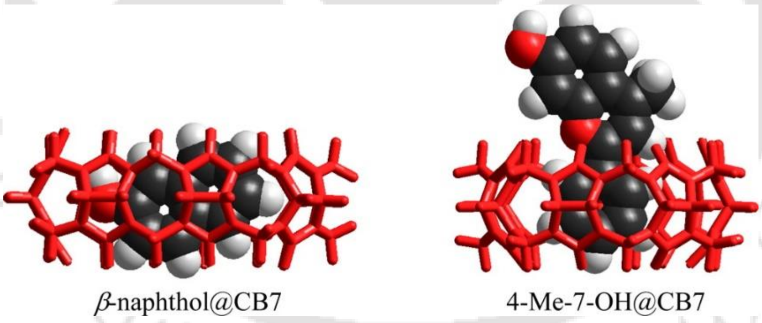

Figure 1.12. Effect of inclusion complex of cucurbit[7]uril with β-naphthol and 4-methyl-7-hydroxyflavylium on ESPT dynamics.[147] Reprinted with permission from ref 147. Copyright © 2015, American Chemical Society.

The ESPT dynamics of 2-naphthol and 4-methyl-7-hydroxyflavylium were investigated inside the CB7 cavity.[147] These two photoacids show contradictory results upon inclusion complex formation with CB7. For 2-naphthol:CB7 inclusion complex, no ESPT of 2OH was found. This was due to the complete inclusion of the 2-naphthol within CB7 cage and, as a result, no access to water molecules. However, 4-methyl-7-hydroxyflavylium still exhibits ESPT after the formation of the inclusion complex. It was assumed that the acidic hydroxyl proton remains exposed to the water environment permitting ESPT, and only a part of the fluorophore is inside the CB7 (**Figure 1.12**). Hence, the ESPT process is dependent on the binding pattern and the local solvent environment around the photoacid.

Hansen et al. investigated two photoacids with very different natures: 1-aminopyrene, a very strong cationic photoacid, and 1-naphthol, a moderately strong neutral photoacid in the presence of β-CD (**Scheme 1.11**).[148] These two photoacids show contradictory results upon inclusion complex formation with β-CD. The neutral photoacid 1-naphthol shows an expected up field shift of pK_a and pK_a^* values upon complexation compared to water along with retardation of ESPT rate inside the cavity. On the other hand, the pK_a and pK_a^* values of the cationic photoacid shift to lower values upon complexation, and the rate of ESPT is increased by a factor of 2-3 relative to bulk water. Thus, the electronic structure of the photoacid may illustrate the effect of complexation within the nonpolar cavity of β-cyclodextrin.

Abdel-Shafi studied the photophysical properties of 2-naphthol-6-sulfonate ($6SO_3$-2OH) within the β-CD cavity by steady-state fluorescence and NMR spectroscopy. Steady-state absorption and fluorescence measurements showed a 1:1 inclusion complex between $6SO_3$-2OH and β-CD with a binding constant of $330 \pm 30 M^{-1}$. Furthermore, they found significant retardation of the ESPT process inside the nanocavity.[149] Similarly, they also studied the photophysical properties of 1-naphthol-4-sulfonate photoacid within different cyclodextrin derivatives (α-cyclodextrin (α-CD), β-cyclodextrin (β-CD), γ-cyclodextrin (γ-CD), methyl-β-cyclodextrin (Mβ-CD), 2-hydroxypropyl-β-cyclodextrin (HPβ-CD)).[150] It was observed that 1-naphthol-4-sulfonate formed 1:1 inclusion complex with all cyclodextrin derivatives along with retardation of the ESPT process inside the nanocavity.

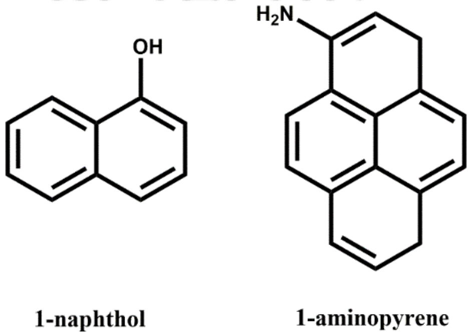

Scheme 1.11. Chemical structure of 1-naphthol and 1-aminopyrene.

Bhattacharyya and co-workers studied ESPT dynamics of HPTS in the presence of γ-CD.[151] They observed significant modulation of ESPT dynamics upon encapsulation within γ-CD. In the presence of γ-CD, the initial proton transfer and the dissociation of geminate ion pair of HPTS become retarded, whereas the recombination rate of the geminate ion pair increases.[152-153] The retardation of the proton-transfer rate was addressed by the rigidity of the water hydrogen bond network and slower solvent reorganization around photoacid inside the cavity.[152] Furthermore, ESPT from HPTS to acetate also become slower in the presence of γ-cyclodextrin (γ-CD) and 2-hydroxypropyl-γ-cyclodextrin (HP-γ-CD) cavities (90 and 200ps) than in the bulk water (0.15 and 6ps). This is due to the confinement effect of CD and rearrangement of the hydrogen bond network inside the cavity, where water bridges separate the acetate molecule from the OH group of HPTS.[153] It was observed that ESPT dynamics is even slower in substituted γ-CD than that in the unsubstituted one. This was due to the hydroxyl-propyl groups which prevent acetate from closely approaching HPTS.[153]

1.3. Proton-Coupled Electron Transfer

Ground and excited state electron transfer (ET) and proton transfer (PT) are two fundamental and widespread processes in chemistry and biology. Some chemical reactions involve the transfer of both protons and electrons, and these take place widely in organic, inorganic, biological environmental, electrochemistry, and other areas of chemistry. Such reactions are termed as proton-coupled electron transfer (PCET).[154-156] Proton-coupled electron transfer (PCET) is crucial for many energy conversion processes, like natural, artificial photosynthesis and solar fuel cell,[157-161] the catalytic oxidation and production of molecular hydrogen,[162-164] and various enzyme reactions.[165-166] According to a broad definition, PCET incorporates any process that involves the movement of both electrons and protons transfer in concerted or a stepwise manner.[154-156]

1.3.1. Concerted and Sequential Electron-Proton Transfer

Two types of mechanistic pathways are observed for PCET reactions- (i) a concerted mechanism, and (ii) a sequential mechanism. For concerted reactions, the electron and proton transfers occur simultaneously, whereas for sequential reactions, the electron and proton transfers take place in a stepwise manner (**Figure 1.13a**). Typically concerted and sequential PCET mechanisms are differentiated by the presence of a stable thermally equilibrated intermediate for the sequential mechanism. This stable intermediate may be generated via either electron or proton transfers. A minimum on the potential energy surface is also found for the sequential reaction, and the intermediate can also be isolated experimentally. However, such a definite distinction is not always possible. This distinction becomes very difficult for photoinduced PCET reactions as these photoinduced reactions are inherently non-equilibrium processes. Subsequently, these non-equilibrium processes involve high energy excited states and occur on a very fast timescale without sufficient time for thermal equilibration of intermediates.

1.3.2. Hydrogen Atom Transfer and Electron-Proton Transfer

Concerted reactions may be divided into two different classes- (i) hydrogen atom transfer (HAT) and (ii) electron-proton transfer (EPT).[167-168] HAT is defined by the transfer of both electron and proton between the same donors and acceptors (i.e., between the same orbitals or bonds). EPT is defined by the electron and proton transfer between different donors and acceptors (i.e., between different orbitals or bonds). However, this distinction between HAT and EPT is not meticulous because of the quantum mechanical nature of both the electron and the proton. It is often observed that HAT reactions do not show significant charge redistribution because the electron and proton transfer occur between the same donor and acceptor. In contrast, EPT reactions involve significant charge redistribution because the electron and proton transfer occur between different donors and acceptors.

1.3.3. Multiple Site Electron−Proton Transfer

There is another class of EPT reactions, called multiple site electron-proton transfer (MS-EPT). It involves concerted electron-proton transfer but to different acceptors, or electron-proton transfer occurs from different donors to a common acceptor. In a typical MS-EPT: (i) an electron-proton donor transfers electrons and protons to spatially separated acceptors or (ii) an electron-proton acceptor accepts electrons and protons from spatially separated donors. An example of MS-PCET is the oxidation of (TyrOH) by $Os^{III}(bpy)_3^{3+}$.[169-170] As shown in **Scheme 1.12**, tyrosine forms an H-bond adduct with HPO_4^{2-} as the base. The reaction between the adduct and $Os^{III}(bpy)_3^{3+}$ is a concerted electron-proton transfer. In this EPT step, electron transfer occurs to $Os^{III}(bpy)_3^{3+}$, and proton transfer occurs to the base, and the two acceptors are spatially separated.

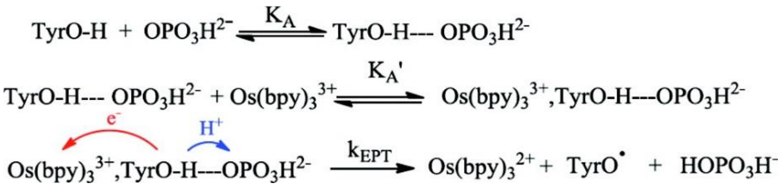

Scheme 1.12. Schematic representation of the MS-PCET reaction of (TyrOH) with $Os^{III}(bpy)_3{}^{3+}$.

1.3.4. Mechanism of Proton-Coupled Electron Transfer

For a PCET reaction, one electron and one proton transfer can be described by considering four diabatic electronic states represented in **Figure 1.13a**.[171-172] The electron and proton are located on their donors in the initial state, and on their acceptors in the final state. The remaining two states correspond to the transferred either only the proton or the only electron. Inside this framework, a concerted reaction corresponds to moving along the diagonal, while a sequential reaction corresponds to moving along the rectangle edges (**Figure 1.13a**). The mechanism is determined based on the relative energies and couplings among these four diabatic states. If the off-diagonal states are much higher in energy, there will be a concerted reaction, which is known as EPT for distinct donors and acceptors. The concerted PCET,[154, 173] theory, incorporates concepts from the Marcus theory for electron transfer,[54] and similar theories for proton transfer.[174] In the most simple way, the reaction is represented in terms of the two diagonal states shown in **Figure 1.13a**, where the electron is located on the donor for the reactant and the acceptor for the product. The free energy curves of the reactant (I) and product (II) are depicted in **Figure 1.13b**. The energy curves are approximately parabolic along a collective solvent coordinate for an EPT reaction. The collective solvent coordinate refers to the reorganization of the solvent environment associated with the charge transfer reaction. A quantum mechanical wave function represents the transferring hydrogen nucleus. Thus, the free energy curves correspond to electron−proton vibronic states instead of pure electronic states, as considered in the Marcus theory. Energies of the ground proton vibrational states change along the collective reaction coordinate, and the energies are identical at the crossing point, as shown by the proton potential energy curves and the associated ground proton vibrational states in **Figure 1.13b**. The general mechanism for a thermal PCET reaction is such that: (i) reorganization of the surrounding environment leads to the crossing point; (ii) a nonadiabatic transition takes place between the degenerate vibronic states of reactant and product, corresponding to the simultaneous tunneling of the electron and proton from their donors to their acceptors; (iii) further reorganization of the environment stabilizes the product.

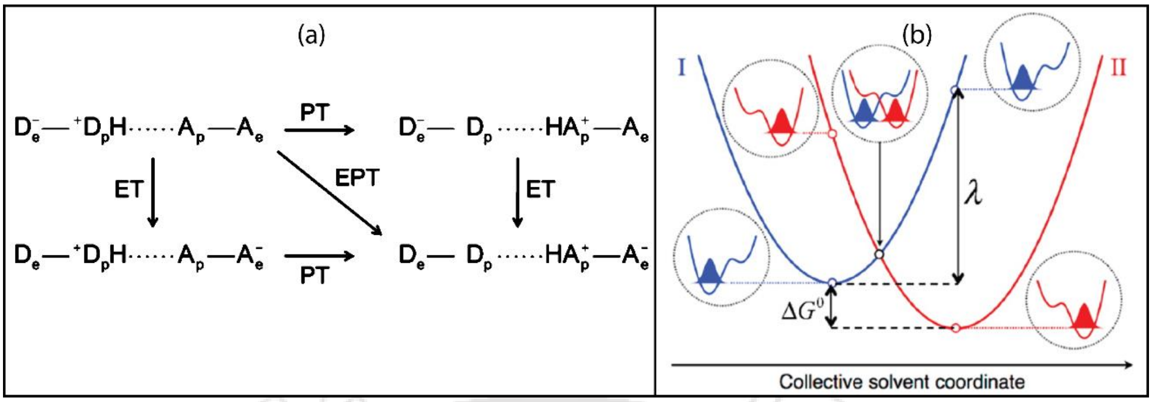

Figure 1.13. Representation of the (a) four diabatic electronic states employed in the PCET theory; (b) free energy curves for the ground reactant (I, blue) and product (II, red) diabatic electron-proton vibronic states along with the collective solvent coordinate for an EPT reaction.[172] Reprinted with permission from ref 172. Copyright © 2015, American Chemical Society.

1.3.5. Rate Constant Expression of Proton-Coupled Electron Transfer

A series of expressions for PCET rate constants have been derived in various well-defined limits.[173] The most straightforward nonadiabatic PCET rate constant expression is,[175]

$$k^{EPT} = \sum_\mu P_\mu \sum_\nu \frac{|V^{el} S_{\mu\nu}|^2}{\hbar} \sqrt{\frac{\pi}{\lambda k_B T}}\, exp\left[-\frac{\left(\Delta G^0_{\mu\nu} + \lambda\right)^2}{4\lambda k_B T}\right] \tag{1.7}$$

where the summations are on reactant and product vibronic states, P_μ is the Boltzmann probability for the reactant state μ, V^{el} is the electronic coupling, $S_{\mu\nu}$ is the overlap between the reactant and product proton vibrational wave functions for states μ and ν, λ is the reorganization energy, $\Delta G^0_{\mu\nu}$ is the reaction free energy for states μ and ν, and k_B is Boltzmann's constant. In **Figure 1.13b**, the reorganization energy and reaction free energy are shown, and the overlap is illustrated at the crossing point. This overlap strongly depends on the proton donor-acceptor distance. The overlap increases significantly for a shorter distance, and as a result, the rate constant increases.

1.3.6. Kinetic Isotope Effect of Proton-Coupled Electron Transfer

The kinetic isotope effect (KIE) is determined by the ratio of the hydrogen transfer rate constant, and the deuterium transfer rate constant. KIE is proportional to the square of the ratio of the hydrogen and deuterium overlap integrals for a given pair of vibronic states:

$$KIE \propto \frac{|S_H|^2}{|S_D|^2} \tag{1.8}$$

Where S_H and S_D are the overlaps of the hydrogen and deuterium wave functions, respectively. As the proton donor-acceptor distance increases, the overlaps (S) decrease for both hydrogen and deuterium. However, due to its larger mass, the deuterium overlap drops faster. Hence, the ratio of the hydrogen to deuterium overlap also increases as proton donor-acceptor distance increases for a given pair of vibronic states. The relation between the KIE and the proton donor-acceptor distance is not always straightforward due to contributions from different excited vibronic states.[176-177] According to the theory, the rate constant decreases, and the KIE often increases as the proton donor-acceptor distance increases.

1.3.7. Proton-Coupled Electron Transfer in Various Fields

(i) Proton-Coupled Electron Transfer in Biology

PCET reactions play a crucial role in many biological processes like photosynthesis, respiration, and enzyme reactions.[178-179] PCET reactions are often observed in many different types of proteins. The iron-containing enzyme soybean lipoxygenase (SLO) is experimentally found to catalyze the PCET reaction from the linoleic acid substrate to the iron cofactor.[180] Using quantum mechanical calculations, Hammes-Schiffer and co-coworker showed that SLO catalyzes the hydrogen abstraction step of linoleic acid, and this step occurs by a PCET mechanism (**Figure 1.14a**).[172, 181] In this PCET step, the electron transfers from the π-system of the linoleic acid substrate to the iron of the cofactor, and the proton transfers from the C11 carbon atom of the substrate to the hydroxyl ligand of the cofactor. A thermodynamic analysis based on the electrochemical experiment confirms the concerted pathway of PCET. Yoshioka and co-workers investigated the mechanism of two-electron oxidation of ubiquinol (UQH_2, but modeled as hydroquinone) by cytochrome *bc₁* complex.[182] A potential energy scan between the hydrogen•••nitrogen atom shows a favorable proton transfer to form the N-H bond from QH_2 to anionic Glu272, followed by ET. EPT mechanism is represented by the change of the position of SOMO along the scanning pathway (**Figure 1.14b**). Using DFT calculation, Kaila and co-workers proposed a mechanism of PCET reaction between nicotinamide adenine dinucleotide (NADH) and (flavin mononucleotide) FMN site of bacterial respiratory complex I.[183] Using large-scale DFT and QM/MM models with atomistic molecular dynamics simulations, they found that PCET from NADH to FMN involves a favourable exergonic concerted hydrogen atom ($H^{\bullet}$) transfer along with another ET between the aromatic ring systems of the cofactors. Liu and co-workers also observed that oxygenation of the reduced lumiflavin anion follows an electronically nonadiabatic PCET mechanism through H-bond.[184]

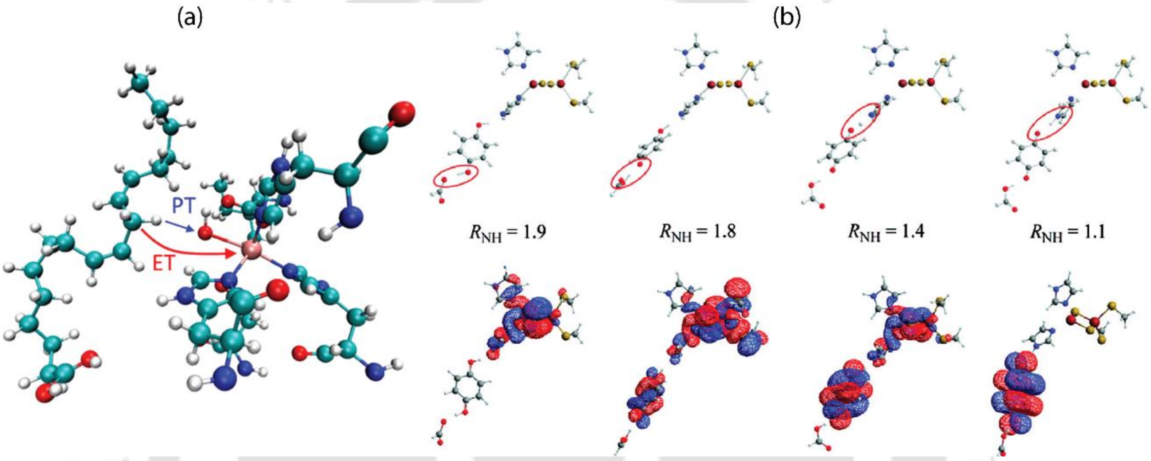

Figure 1.14. (a) Schematic representation of the net hydrogen atom transfer catalyzed by SLO with the linoleic acid substrate.[172] (b) Change in SOMO along the N-H bond-forming reaction path for the oxidation of hydroquinone by cytochrome *bc₁* complex in complex III. R_{NH} corresponds to the N-H distance in Å.[182] Reprinted with permission from ref 172. Copyright © 2015, American Chemical Society.

(ii) Proton-Coupled Electron Transfer in Organic Molecules

Phenol behaves as PCET reagents in biological systems like tyrosine and flavonoids. Hydrogen atom abstraction reactions from a variety of phenols,[185] and flavonoids,[186] by 2,2 diphenyl-1-picrylhydrazyl radical ($dpph^{\bullet}$) are reported. Quercetin shows HAT reaction with $dpph^{\bullet}$ in nonpolar solvents.[186] Oxidation of ascorbate occurs through EPT reaction by nitrosobenzene, phenoxyl, or nitroxyl radicals.[187] The mechanisms of debromination of 8-bromoguanosine (8BG) and 8-bromoxanthosine (8BA) were investigated by the reduction of the corresponding 8-bromopurine and by DFT calculations. The neutral compounds

8BG and the protonated form of 8BA shows favorable sequential ET-PT, whereas anionic 8BA undergoes a concerted EPT mechanism to avoid a high-energy di-anion form.[188]

(iii) Proton-Coupled Electron Transfer in Electrochemistry

Electrochemical measurements have been applied to the study kinetics, thermodynamics, and mechanism of PCET reactions. Cyclic voltammetry (CV), rotating disk electrodes (RDEs), electrochemical impedance spectroscopy (EIS) are frequently used to investigate PCET reactions electrochemically. Savéant, and co-workers investigated $[\mathrm{Os^{II}(bpy)_2py(OH_2)}]^{2+}$ in buffered water solutions under electrochemical conditions.[189-190] From the systematic kinetic analysis of the successive oxidative cyclic voltammetric measurement and determination of H/D isotope effect, they found that stepwise mechanisms (ET-PT and PT-ET) prevail for PCET reactions of oxidation of $[\mathrm{Os^{II}(bpy)_2(py)(OH_2)}]^{2+}$. PCET reaction converts the osmium(II)–aqua complex into the osmium(III)–hydroxo complex.

1.3.8. Excited State Proton-Coupled Electron Transfer

Excited-state proton-coupled electron transfer (ES-PCET) reactions are frequent in several chemical, biological, and solar cell systems.[154, 191-194] Due to photo-excitation, the electronic charges become redistributed in the excited states, which often create a significant difference in reactivity between the excited and ground states of the molecules. ES-PCET is different from conventional PET and ESPT. In the PET process, an electronically excited molecule (upon absorption of light), can either take up an electron from another molecule (Reductive PET) or release an electron to another molecule (Oxidative PET). In the ESPT process, the proton is transferred from one molecule to the solvent (intermolecular ESPT) or from one part of a molecule to another part of the same molecule (intramolecular ESPT or ESIPT) in the excited state. In contrast, ES-PCET involves an electron transfer reaction with a concerted proton transfer reaction. Several factors influence ES-PCET reactions, like local changes in molecular and solvent structure, and changes in the local hydrogen-bonding environment. Scientists observed both experimentally, and theoretically, the role of these factors on the kinetics and thermodynamics of the PCET reaction in-ground and excited-states.[191-192, 195-198] For a clear understanding between the thermal PCET and ES-PCET processes, Dempsey and co-workers recently represented these reactions in a schematic manner (**Scheme 1.13a**).[199]

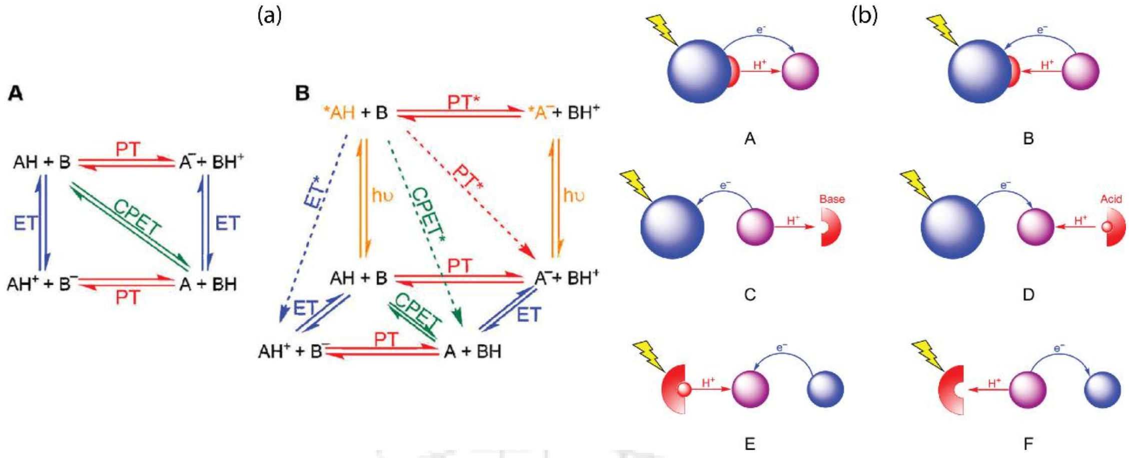

Scheme 1.13 (a) (I) Square and (II) Cube Schemes describing thermal and excited-state PCET Reactivity, Respectively. (b) Six Classes of ES-PCET: (A) ES H^+/e^- Donors, (B) ES H^+/e^- Acceptors, (C) ES e^- Acceptors, (D) ES e^- Donors, (E) ES H^+ Donors, and (F) ES H^+ Acceptors.[199] Reprinted with permission from ref 199. Copyright © 2017, American Chemical Society.

They also classified ES-PCET reactions into six categories. They differentiated them based on the nature of the photoexcited reactant: (A) excited-state proton/electron donors, (B) excited-state proton/electron acceptors, (C) excited-state electron acceptors, (D) excited-state electron donors, (E) excited-state proton donors and (F) excited-state proton acceptors (**Scheme 1.13b**). Here, the examples of ES-PCET reactions are presented in three categories – (i) ES-PCET of organic molecules, (ii) ES-PCET of metal complexes, and (iii) ES-PCET of biological systems.

1.3.9. Excited State Proton-Coupled Electron Transfer of Organic Molecules

In this section, first experimentally observed ES-PCET reactions of the organic molecules are described, followed by theoretical studies on the ES-PCET in recent times. Since I have worked on the ES-PCET of the organic molecules in my thesis, I am discussing this section in little bite details.

Using femtosecond pump-probe and coherent Raman spectroscopic techniques, Meyer and co-workers observed photochemically driven concerted electron-proton transfer process (photo-EPT) in two H-bonded adducts- (i) 4-hydroxy-4′-nitro-biphenyl (*p*-nitrophenyl-phenol) and t-butylamine base in solvent 1,2 dichloro-ethane, and (ii) 7-hydroxy-4-(trifluoromethyl) coumarin and 1-methylimidazole base in toluene solvent (**Scheme 1.14a**).[200] From the transient absorption spectra, two spectroscopic states having different dynamical signatures were found. One state is assigned for a conventional excited-state proton transfer process, and the other state corresponds to an ultrafast concerted electron-proton transfer process, i.e., ES-PCET (**Scheme 1.14b**). They proposed that charge transfer occurred in a concerted manner with a proton transfer to the nitrogen atom of the acceptor base with the newly formed H─N bond.

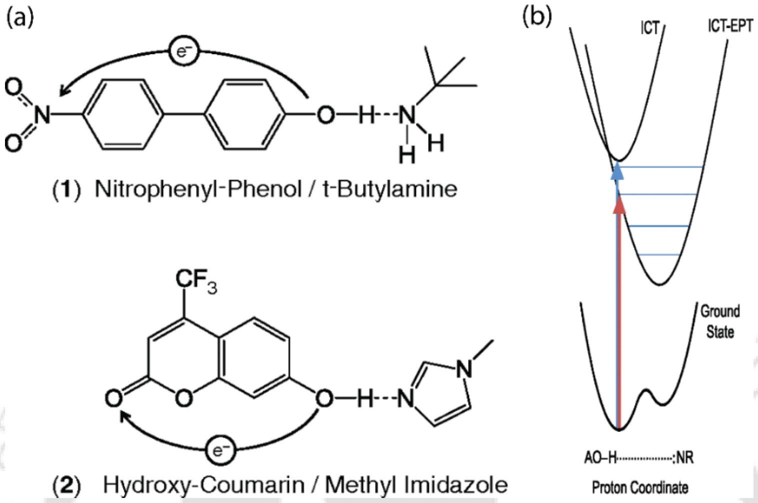

Scheme 1.14. (a) Chemical structures of the two hydrogen-bonded adducts (1) 4-hydroxy-4′-nitro biphenyl and t-butylamine and (2) 7-hydroxy-4-(trifluoromethyl)-coumarin and 1 methylimidazole. (b) The ICT and ICT-EPT energy-coordinate surfaces. Blue arrow represents excitation to the ICT state and red arrow excitation to the ICT-EPT state.[200] Reprinted with permission from ref 200.

N-methyl-4, 4′-bipyridinium cation (MQ^+) acts as an electron and proton acceptor. Meyer and co-workers performed steady-state and ultrafast transient absorption measurements on the complex of MQ^+ with different phenols- tyrosine, 4-methyl phenol, and 4-methoxy phenol. They observed a weak red-shifted absorption band at 375 nm, which was attributed to the H-bonded complex between MQ^+ and phenol. Upon excitation at this new band, they observed transient absorption bands at 360 nm, 440 nm, and 560 nm. The transient bands were designated to the absorption of radical ions, which were proposed to occur via hydrogen bond (H-bond) aided PCET. MQ^+ accepts both proton and an electron from the phenol moiety (**Scheme 1.15a**).[201]

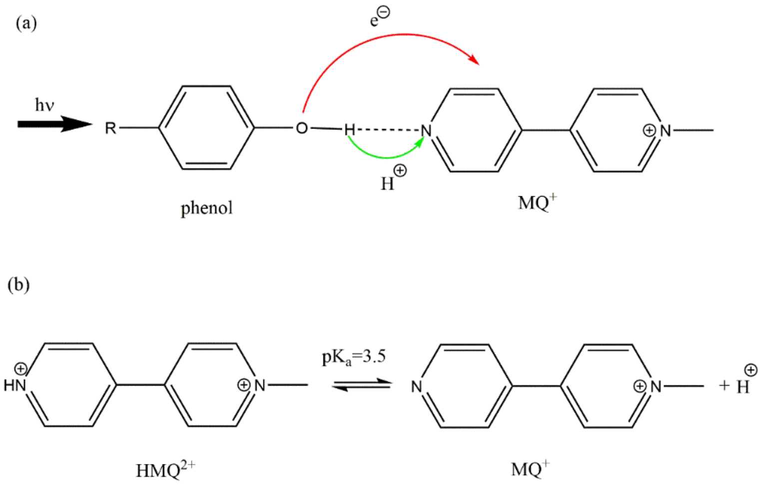

Scheme 1.15. (a) Proposed PCET scheme between *N*-methyl-4, 4′-bipyridinium cation (MQ^+), and para-substituted phenols through H-bonding. (b) Protonation equilibrium between the protonated (HMQ^{2+}) and deprotonated (MQ^+) forms of MQ^+.[202] Reprinted with permission from ref 202. Copyright © 2019, American Chemical Society.

However, Tyburski et al. also performed a similar set of experiments of *N*-methyl-4, 4′-bipyridinium cation (MQ^+) with phenols but at two different pHs (2 and 8.5).[203] They observed almost identical spectral features at both pHs. Since the pK_a of MQ^+ is 3.5 (**Scheme 1.15b**), it is expected that at low pH (pH = 2), the pyridinium nitrogen should be protonated, and hence, it can not accept a proton from the phenol unit omitting the possibility of PCET at this condition. Since the band positions are almost similar at both pHs, the same excited state process may occur at both pHs. They attributed the process as conventional charge transfer between the MQ^+/methoxyphenol system in the excited state. They also suggested that the charge transfer may be mediated by donor-acceptor interaction. Dempsey and co-worker reported a detailed mechanistic study of the ES-PCET reaction from the triplet excited state of acridine orange (^{3}AO*) to tri-tert-butylphenol (^{ttb}PhOH) in acetonitrile.[204] Biomimetic anthracene–phenol–pyridine (An−PhOH−py) molecular triads show Marcus inverted region behavior.[205] Recently, Mayer and co-workers reported a photoinduced activation less multiple-cite concerted proton−electron transfer (MS-CPET) of an anthracene−phenol−pyridine triad (1H).[206] They selectively excited the anthracene portion of the triad 1H for fluorescence measurement. Time-resolved photon-counting streak camera and uv-vis transient absorption (TA) spectroscopic results show a fast Photoinduced intramolecular electron and proton transfer of 1H in different directions in a single kinetic step. ET is observed from the phenol-pyridine to the locally excited state (S_1) of anthracene with simultaneous PT across the hydrogen bond (PhOH)OH···N(py) (**Scheme 1.16a**). This results in a charge-separated state (CSS), An$^{\bullet-}$−PhO$^{\bullet}$−pyH^{+}, which is characterized by transient absorption spectroscopy. Schiffer and her group further extended this work to understand the effect of substitutions on the pyridine and anthracene rings of the triad.[207]

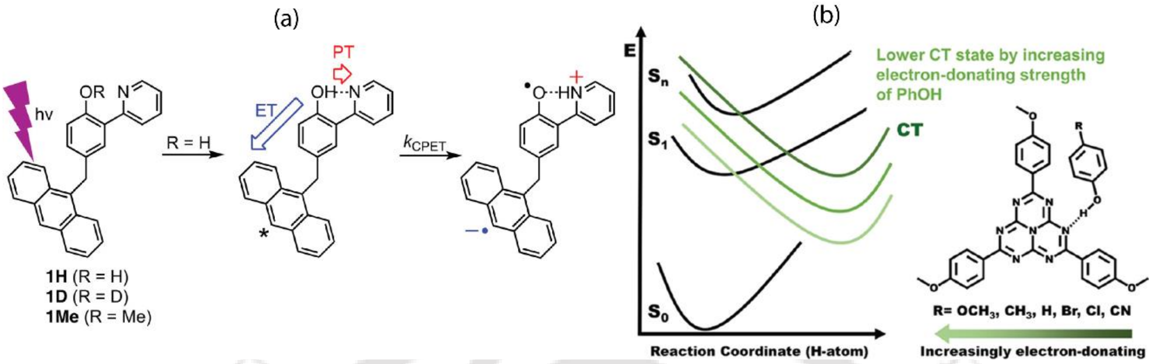

Scheme 1.16. (a) Schematic depiction of the proposed mechanism for excited state MS-CPET in 1H.[206] (b) Schematic depiction of the proposed excited state landscape along the H-atom transfer coordinate from phenol (PhOH) to TAHz.[208] Reprinted with permission from ref 208. Copyright © 2019, American Chemical Society.

Recently, Schlenker and co-workers investigated experimentally as well as theoretically the intermolecular ES-PCET of 2,5,8-tris(4-methoxyphenyl)-1,3,4,6,7,9,9b-heptaazaphenalene (TAHz) with a series of phenol (PhOH) derivatives as proton and electron donors (**Scheme 1.16b**).[208] From spectroscopic measurements, they observed that quenching rate constant increases with more electron-donating substituents on PhOH derivatives. To explain this experimental observation, they performed two dimensional (2D) relaxed potential energy surfaces for the lowest excited singlet state along with the H-bond coordinates of the TAHz with different PhOH derivatives. The height of the transition-state barrier decreases with increasing electron-donating substituents on PhOH, and it becomes completely barrier less for the most electron-donating derivative, OCH$_3$−PhOH. The height of the transition-state barrier ($\Delta E^{\ddagger}$) on the potential energy surface of the S$_1$ state simply governs the feasibility of ES-PCET. Hence, they concluded that the rate of ES-PCET between heptazine chromophores and hydroxylic compounds could be increased by adding electron-donating groups to the hydroxylic compound. They also synthesized and studied PCET of 2,5,8-tris(4-methoxyphenyl) 1,3,4,6,7,9,9b-heptaazaphenalene (TAHz, a model molecular photocatalyst) to hydrogen-bonded water molecule.[209]

Hammes-Schiffer and her group mostly contribute to the theoretical frameworks of PCET and ES-PCET. The H-bonded complex of p-nitrophenylphenol and t-butylamine system was revisited computationally by Hammes-Schiffer and co-workers to get insights into the nature of ES-PCET process.[210] Using time-dependent density functional theory (TD-DFT) with long-range corrected functionals in conjunction with the polarizable continuum model (PCM), they investigated excited state properties of the singlet excited states of the H-bonded *p*-nitrophenyl-phenol−methylamine complex in 1,2-dichloroethane. They computed the 2D relaxed potential energy surfaces of the same singlet excited states. They found that at the Franck−Condon geometry, the S_1 state is $\pi\pi^*$ state in nature, and the S_2 state is $n\pi^*$ type state. The $\pi\pi^*$ state has charge transfer character having a change in electronic density on the amine and the minimum-energy structure on the potential energy surfaces corresponding to the proton bonded to the nitrogen acceptor, i.e., consistent with proton transfer. Whereas the $n\pi^*$ state has little charge-transfer character, and no proton transfer occurred. Therefore, they denoted the $\pi\pi^*$ state as the ICT-EPT state, and the $n\pi^*$ is mentioned as ICT state as in the experimental analysis.[200] Furthermore, they studied the same system to investigate the role of solvent dynamics following photoexcitation to the EPT state using on-the-fly surface hopping nonadiabatic dynamics simulation.[211-212] They treated the hydrogen-bonded complex surrounded by explicit solvent molecules within a quantum mechanical/molecular mechanical approach (QM/MM) framework. Simulation studies show proton transfer (PT) upon photoexcitation to the EPT state. Subsequent analysis of these simulations reveals the role of the solvent dynamics in facilitating PT in the EPT state. It also shows the relaxation pathway from the EPT state to the ground state. Kaila and co-workers theoretically investigated ground state proton transfer (PT) and photoinduced proton-coupled electron transfer (ES-PCET) between the H-bonded complex *p*-nitrophenyl-phenol and *t*-butylamine in 1,2-dichloroethane, which was earlier studied experimentally.[200] Their investigating system was also close to the previously described work of Hammes-Schiffer.[210] Here, they used *t*-butylamine in place of methylamine to understand the substitution effect on the transition barriers of PT and PCET.[213] Using TD-DFT and algebraic diagrammatic-construction through second-order ADC(2), the obtained potential energy surfaces show a favourable ground state PT and excited state PCET processes in the studied complex. They also used a kinetic Brønsted analysis to distinguish between an excited state PCET and a ground state PT. Recently, Chu and co-workers studied ES-PCET reaction on the benzimidazole phenolic derivatives with proper electron/proton donating and withdrawing functional groups using DFT and TD-DFT methods.[214] Analysing the optimized geometries, charge distributions, and the potential energy surface of the proton transfer in the S_1 state, and they noticed that electron-driven two protons transfer in a stepwise manner is more favourable compared to the common electron-driven single-proton transfer process. It is due to the smaller transition energy barrier for the former one. This lower energy barrier and the longer proton-transfer distance are beneficial in producing solar fuels more efficiently.

1.3.10. Excited State Proton-Coupled Electron Transfer of Metal Complexes

Early studies of excited-state PCET employed amidinium-carboxylate salt bridges between $Ru(bpy)_3{}^{2+}$ (bpy = 2,2′-bipyridine) complexes and electron donors/acceptors.[62] There are numerous examples of ES-PCET in metal complexes.[193, 215] Wenger and co-workers studied ES-PCET reaction between cationic iridium complex with a 2,2′-biimidazole ligand and 3,5-dinitrobenzoate in CH_2Cl_2.[216] This Ir(III) metal complex forms 1:1 hydrogen-bonded between the imidazole N-H functions and the carboxylate group of dinitrobenzoate. From the analysis of the luminescence spectra, they found that upon photoexcitation, the proton density of the N atoms of biimidazole is shifted to the O atoms of carboxylate. Hence, they considered this process as ES-PCET (**Scheme 1.17a**). Similarly, $[(bpy)_2Ru(phen(OH)_2]^{2+}$ (where $phen(OH)_2$ is 1,10-phenanthroline-5,6-diol) complex has a deprotonatable OH groups. When the photoexcited metal complex reacts with *N*-methyl bipyridinium (MQ^+), it shows ES-PCET reaction (**Scheme 1.17b**).[193] Moreover, in this reaction, the products can be easily detected by the transient absorption spectra of MQ^+, which has a great advantage for ES-PCET case. Recently, Schmehl and co-workers also worked with *N*-methyl-4,4′-bipyridinium and observed sequential excited-state electron and proton transfer from $[(bpy)_2Ru(4,4'\text{-dhbpy})]^{2+}$ (where 4,4′-dhbpy = 4,4′-dihydroxy-2,2′-bipyridine, $[Ru(II)\text{-}OH]^{2+}$) complex to MQ^+ (*N*-methyl-4,4′-bipyridinium) in an aprotic solvent (CH_3CN) using transient absorption spectroscopy in the visible region.[217] 1,4-benzoquinone is also known as the electron and proton acceptor in ES-PCET reaction. Kumbhar and co-workers reported the existence of both ES-PCET and simple PET processes between donor ruthenium (II) imidazole phenanthroline (ipH) complex $[Ru(bpy)_2ipH]^{2+}$ and acceptor 1,4-benzoquinone in buffered 1:1 (v:v) $CH_3CN:H_2O$ solution.[218] From their transient absorption spectroscopy results, the band around 420-430 nm in the spectra suggests the presence of both 1,4-benzoquinone radical anion as well as the 1,4-benzosemiquinone radical in the studied donor-acceptor system.

In the above examples, the metal complexes act as both proton and electron donor. Meyer and co-workers studied metal complex $[Ru(bpy)_2(bpz)]^{2+}$ in the presence of both proton and electron donor 1,4-hydroquinone. Using transient absorption and EPR spectroscopy, they observed ES-PCET from 1,4-hydroquinone to metal complex after photoexcitation. This ES-PCET results reduced and protonated metal complex in addition to semiquinone (**Scheme 1.17c**).[219-220]

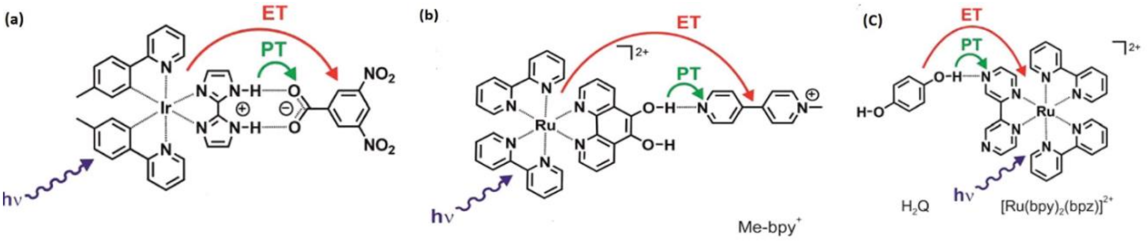

Scheme 1.17. Sketch of the photoinduced electron transfer (ET) and proton transfer (PT) processes- (a) Ir(III) complex with dinitrobenzoate, (b) $[(bpy)_2Ru(phen(OH)_2]^{2+}$ with *N*-methylbipyridinium and (c) $[Ru(bpy)_2(bpz)]^{2+}$ with 1,4-hydroquinone.[215] Reprinted with permission from ref 215. Copyright © 2019, American Chemical Society.

Hammarström and co-workers investigated ES-PCET of a fac-$[(CO)_3Re^I(bpy)(4,4'\text{-}bpy)]^+$ (bpy = 2,2′-bipyridine and 4,4′-bpy = 4,4′-bipyridine) with a series of substituted phenols with different pK_a and E° values.[221] Interestingly, they observed that metal to ligand charge transfer (MLCT) transition occurs at first, and Re^I becomes $*Re^{II}$ and an ET from a hydrogen-bonded phenol to $*Re^{II}$ occurs with a concerted PT from the phenol to the pyridine. In this work, they also determined and compared the ground and excited state association constants (K_A and K_A'), and PCET rate constant (k_{PCET}) of these metal complex− substituted phenol assemblies. Interestingly, they found that neither ground state K_A nor excited-state K_A' showed any significant variation within the series of phenols, and there was also no significant difference between experiments in H_2O and D_2O.

1.3.11. Excited State Proton-Coupled Electron Transfer of Biological Complexes

Very recently, Hammes-Schiffer and co-workers investigated the photocycle of the Slr1694 blue light using flavin (BLUF) photoreceptor.[222] It is a photoactive protein essential to various light-activated biological responses in some bacteria and algae. In their two-dimensional excited-state potential energy surface scan of double proton-transfer, they included the protein and solvent environment with electrostatic embedding.[223] They observed an energetically unfavourable double proton-transfer-reaction in the ground state and locally excited state. But, it interestingly becomes a favourable double proton-transfer in the charge-transfer (CT) state, which is generated due to electron transfer from Tyr8 to the flavin after photoexcitation of flavin. This observation indicates a favourable excited-state proton-transfer after an electron transfer process. Hence this reaction is sequentially ET-PT type. The double proton-transfer-reaction also follows a sequential pathway from Tyr8 via Gln50 to the Flavin (**Scheme 1.18**). Furthermore, they found that both the transition barriers significantly depend on the proton donor-acceptor distance as well as the protein environment.[223-224] Recently, using transient absorption spectroscopy measurement Essen and co-workers reported a very fast ES-PCET from tyrosine to tryptophan in animal-like cryptochrome of Chlamydomonas reinhardtii.[225]

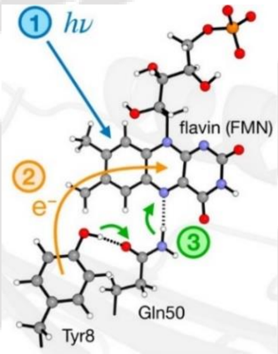

Scheme 1.18. Schematic of the steps of the photocycle of the BLUF Slr1694 photoreceptor.[224] Reprinted with permission from ref 224. Copyright © 2019, American Chemical Society.

1.4. Aim and Scope of the Present Work

The primary aim of the present work is to elucidate the role of the excited state H-bond in the photophysical processes like electron transfer (PET), excited-state proton transfer (ESPT), and proton-coupled electron transfer (PECT), etc. In this thesis, we have investigated some simple but interesting hydrogen-bonded complexes and their photophysical processes like PET, ESPT, and PCET.

H-bonded C102-phenol complex is a long-debated system between the experimental and theoretical groups. Our group experimentally observed that the fluorescence intensity of C102 was quenched drastically in the presence of phenol in a non-interacting solvent cyclohexane. The fluorescence intensity is first quenched gradually up to a particular mole fraction ($X_{PH} \approx 0.013$) of phenol, but after that increases with further increases in the mole fraction. Hence, here molecular dynamics (MD) simulation was employed to unveil the exact H-bonding configuration of C102 of an experimental system at different mole fractions of the phenol-cyclohexane mixture. Our results assist in understanding the unusual fluorescence modulation of C102 observed in the binary mixture in the previous experimental study. Furthermore, time-dependent density functional theory (TD-DFT) reveals the possibility of PCET as an alternative mechanism for the experimentally observed fluorescence quenching of the H-bonded C102-phenol complex.

Similarly, methylbipyridine/methoxyphenol complex is another interesting H-bonded system, which shows quite controversial spectroscopic signatures, which may be due to conventional PET or PCET. Hence, we were interested to understand the actual nature of the excited-state process.

In this work, we were interested in studying the modulation of the ESPT process of the photoacids due to inclusion inside the hydrophobic cavity. The fluorescence modulation of three photoacids (2-naphthol, 6-sulfonate-2-naphthol, and 6-cyano-2-naphthol) was investigated inside the nanocavity of β-cyclodextrin. The photoacid derivatives differ by the substitution at the 6-position and have remarkably different excited-state acidities (pK_a^*). Finally, we observed very different pK_a shift and fluorescence modulation of the strong photoacid 6-cyano-2-naphthol inside α-cyclodextrin vs. β-cyclodextrin.

Chapter-2

Theoretical and Experimental Methods

Chapter 2: Theoretical and Experimental Methods

In the present chapter, we have discussed theoretical methodologies such as density functional theory (DFT), time-dependent density functional theory (TD-DFT) and molecular dynamic (MD) simulation that have been used in our studies. We have presented a brief description of several instrumentations including absorption spectrophotometry, steady-state fluorescence spectrophotometry, time-correlated single photon counting (TCSPC), and isothermal titration calorimetry (ITC), which have been used for completing the works described in this thesis. Chemicals used, sample preparation procedures and pK_a, pK_a^* calculations have been also included.

Theoretical Methods

The calculation of the ground and excited electronic states of molecular systems are the most popular application of theoretical ab-initio quantum chemistry. Molecular properties such as molecular structures, vibrational frequencies, ionization energies, electronic and magnetic properties, potential energy surfaces of the electronic states, etc. are computationally calculated based on quantum mechanical theory.

2.1. Density Functional Theory (DFT)

Similar to ab-initio and semi-empirical methods, density functional theory (DFT) is another computational chemistry tool and also based on Schrödinger's equation. However, unlike both approaches, it does not derive conventional wave function; instead, it directly derives from electron density distribution to calculate physical properties. Density functional theory is based on the electron density, which is a function of three spatial parameters (X, Y, and Z), no matter how big the molecule is. In comparison, the wave function of a molecule containing n number of electrons is a function of 4n (three spatial and one spin coordinate) variables. Due to reasonable accuracy and less computational cost of DFT, considerable interest in modern computational chemistry has been gained in recent years. DFT presently the most successful and the most promising approach to compute the electronic structure of the molecule.[226]

2.1.1. Electron Density

Electron probability density function or simply electron density denoted as ρ(x, y, z), is extracted from the electronic wave function. It is a function of only three variables (x, y, z), while an N-electron wave function depends on 4N variables, i.e., three spacial and one spin coordinates of each electron. The single-particle probability density corresponding to a normalized ground-state N electron wave function is given by,

$$\rho(r) = N \int |\psi(r_1, r_2, \dots \dots \dots \dots .., r_N)|^2 d^3r_2 \dots \dots \dots d^3r_N \qquad (2.1)$$

Electron density ρ(r) have some specific properties mentioned below, which makes it a useful physical observable for the prediction of energy and other properties instead of complicated N-electron wave function.

Integrated overall space it gives the total number of electrons N, i.e.,

$$\int \rho(r)dr = N \qquad (2.2)$$

Earlier Fermi-Dirac statistics, the Thomas-Fermi model, were used to calculate molecular properties from electron density.[227] However, all produce inadequate results, as a consequence, presently Kohn-Sham method is used in modern computations.[228]

2.1.2. The Hohenberg-Kohn Theorems and The Kohn-Sham Approach

Two important theorems were published by Hohenberg and Kohn which formed the platform of the modern Kohn-Sham (KS) approach.[228-229]

(i) The Hohenberg-Kohn existence theorem says that the ground-state electron density function can determine all the properties of a molecule in a ground electronic state.

(ii) The Hohenberg-Kohn variational theorem states that any trial electron density function will give energy higher than or equal to the actual ground-state energy, which is only valid for the exact functional.

The Hohenberg-Kohn theory is valid for both interacting and non-interacting electrons. The realization by Kohn and Sham is that a system of non-interacting electrons can be taken as a reference that has their ground state density the same as that of the real system made the major breakthrough. The non-interacting part can be easily treated, which constitutes a significant portion of the electronic energy, and a relatively small portion is associated with the interacting part that can be determined by a density functional.

The ground-state energy of a real molecule is

$$E_0 = T_S[\rho_0] - \sum_A Z_A \int \frac{\rho_0 (r_1)}{r_{1A}} dr_1 + \frac{1}{2} \iint \frac{\rho_0 (r_1) \rho_0 (r_2)}{r_{12}} dr_1 dr_2 + E_{XC}[\rho_0] \tag{2.3}$$

Where the terms on the right hand side of equation 2.3, indicate the kinetic energy of the noninteracting electrons, the nuclear-electron interaction, the classical electron-electron repulsion, and the exchange-correlation energy, respectively.

2.1.3. Approximate Exchange-Correlation Functionals

The exact functionals for the exchange and correlation are unknown and, therefore, many approximations are employed to calculate the Exchange-Correlation Functionals (E_{XC}). In the local-density approximation (LDA), at each point r in space, the E_{XC}(r) is approximated as that of a homogeneous electron liquid of density ρ(r), and it is computed exclusively from the value of ρ(r). The LDA functional, which includes electron spin, is called the local spin-density approximation (LSDA) functional. As the electron density is far from the spatially uniform model in a molecular system, the functional is further improved by including the first derivative or the gradient in addition to the ρ(r), called generalized gradient approximations (GGA). In the meta-GGA functionals, in addition to the spin densities and their gradients, additional terms, such as Laplacians of the spin density, are also included to construct the functional. Nowadays, the most popular functionals are hybrid functionals, which are constructed by mixing a fraction of the exact exchange energy functional to the LDA/LSDA or GGA functional. A hybrid functional can be written as,

$$\mathrm{E_{XC}^{hybrid}} = \mathrm{aE_X^{exact}} + (1-\mathrm{a})\mathrm{E_X^{DFT}} + \mathrm{E_C^{DFT}} \tag{2.4}$$

Where $\mathrm{E_X^{exact}}$ is the nonlocal HF exchange energy, ‘a’ is the percentage of HF exchange in the hybrid functional, $\mathrm{E_X^{DFT}}$is the local DFT exchange energy, and $\mathrm{E_C^{DFT}}$ is the local DFT correlation energy.

The Becke’s three-parameter Lee–Yang–Parr (B3LYP) exchange-correlation functional,[230] is a well-known hybrid functional, and it can be expressed as

$$E_{XC}^{B3LYP} = 0.80E_X^{LSDA} + 0.20E_X^{exact} + 0.72E_X^{B88} + 0.81E_C^{LYP} + 0.19E_C^{LSDA} \quad (2.5)$$

The PBE0[231-232] functional is given by

$$E_{XC}^{PBE0} = 0.25E_X^{exact} + 0.75E_X^{PBE} + E_C^{PBE} \quad (2.6)$$

Where E_X^{PBE} and E_C^{PBE} are the Perdew-Burke-Ernzerhof exchange and correlation functionals, respectively.

M06-2X,[233] is a hybrid meta-GGA functional, written as

$$E_{XC}^{M06-2X} = 0.54E_X^{exact} + 0.46E_X^{M05} + E_C^{M06} \quad (2.7)$$

The exchange (E_X^{M05}) and correlation (E_C^{M06}) functionals are the same as for M05 and M06, respectively.

2.1.4. CAM-B3LYP Functional

Although DFT functionals are successful for several applications, these are still unsuccessful in many important applications, such as the polarizability of long chains, excitations using TDDFT for Rydberg states, and most crucial charge transfer (CT) excitations.[234-235] This problem is overcome to a large extent by the long-range (LR) scheme,[234] where the electron repulsion operator $1/r_{12}$ splits into short-range and long-range parts by using the error function (erf). In consequence, the correct asymptotic $r_{12} \rightarrow \infty$ behaviour is retained, where the Coulomb and exchange potentials cancel each other. The equation is

$$\frac{1}{r_{12}} = \frac{1-\mathrm{er}f(\mu r_{12})}{r_{12}} + \frac{\mathrm{er}f(\mu r_{12})}{r_{12}} \quad (2.8)$$

Where μ is a range separating parameter, while the first term of this equation accounts for the short-range, the second term accounts for the long-range part. For the exchange energy term, the short-range and long-range parts are treated by the DFT and exact HF exchange, respectively. However, the electron correlation term is the same as the DFT functional.

Yanai et al.[235] have modified equation 2.8 by introducing two additional parameters (α and β) in the equation as,

$$\frac{1}{r_{12}} = \frac{1-[\alpha+\beta \mathrm{er}f(\mu r_{12})]}{r_{12}} + \frac{\alpha+\beta\, \mathrm{er}f(\mu r_{12})}{r_{12}} \quad (2.9)$$

Where $0 \leq \alpha + \beta \leq 1$, $0 \leq \alpha \leq 1$, $0 \leq \beta \leq 1$. The terms α and α + β represent the HF-exchange in short- and long-range limits, respectively. This Coulomb-attenuating method (CAM) with three parameters is more flexible than the LR-method. In the case of CAM-B3LYP functional,[235] the standard α, β, and μ parameters are 0.19, 0.46, and 0.33, respectively.

2.1.5. DFT with London Dispersion Corrections

Conventional DFT functionals which do not contain the physics of dispersion interactions often fail in cases where the dispersion interaction plays a vital role, such as in the case of determination of the geometries and thermodynamic properties of systems.[236-237] Out of various methods developed to incorporate the dispersion interaction, Grimme's DFT-D methods are well established, and at present, the DFT-D3 method is the most successful one. The addition of a small dispersion correction term significantly improves the accuracy at the expense of a low computational cost. The wave function does not change with the addition of this correction term, and thus other molecular properties are unaffected. However, as the dispersion correction alters the force acting on the atoms, optimizations with DFT and DFT-D3 levels lead to different geometries. The dispersion corrected total energy is given by

$$E_{DFT-D3} = E_{DFT} + E_{disp} \tag{2.10}$$

Where E_{DFT} is the energy obtained by the original DFT functional, and E_{disp} is the dispersion energy.

2.1.6. Basis Set

A basis set in quantum chemistry is a set of mathematical functions which are combined in linear combinations to create molecular orbitals. These functions are typically atomic orbitals centered on atoms, and the calculations are usually performed using a finite set of basis functions. The approximation of molecular orbitals in linear combinations of basis functions is known as the linear combination of atomic orbitals (LCAO).

2.1.7. Solvent Model

Electronic absorption and emission spectra usually exhibit a marked solvent dependence. A common approach to incorporate these solvent effects in quantum chemical calculations is the use of self-consistent reaction-field (SCRF) continuum models where the explicit solvent structure is not considered. However, its main advantage is that the solute's electronic structure can be treated quantitatively, and polarization effects are evaluated. The use of DFT within the continuum models for solvation is an efficient way to consider solvent effects.

2.2. Time-Dependent Density Functional Theory

Hohenberg-Kohn density functional theory (DFT) is one of the most popular method and is strictly limited to ground states only, which excludes its usage in photochemistry. Several routes have been followed to extend the conventional DFT to excited states, among which time-dependent density functional theory is the most popular method to treat excited states.[238-240] Time-dependent DFT (TDDFT) is an extension of DFT. It is used to determine the properties and dynamics of many-body systems in the presence of time-dependent potential. The Time-Dependent Schrodinger Equation explain the time evolution of a many-body state $\Psi(t)$, starting from an initial state $\Psi(t_0)$ in the presence of an external time-dependent potential $V(r,t)$,

$$i\hbar\frac{\partial}{\partial t}\Psi(r_1,\ldots\ldots,r_N,t) = (T+V(t)+W)\Psi(r_1,\ldots\ldots,r_N,t) \tag{2.11}$$

Where T and W kinetic energy operator and electron-electron interaction, respectively.

$$T = \sum_{j=1}^{N} -\frac{\hbar^2\nabla_j^2}{2m} \tag{2.12}$$

$$V(t) = \sum_{j=1}^{N} V(r_j,t) \tag{2.13}$$

$$W = \frac{1}{2}\sum_{j,k,j\neq k}^{N} \frac{e^2}{|r_j - r_k|} \tag{2.14}$$

Runge-Gross theorem,[241] is the foundation of the TDDFT, and it conveys an important message which states that, for all many-body systems evolving from a fixed initial state, a one-to-one mapping exists between the external time-dependent potential $V(r,t)$, and the time-dependent density $\rho(r,t)$.

$$\rho(\mathrm{r},\mathrm{t}) \overset{\Psi_0}{\leftrightarrow} \mathrm{V}(\mathrm{r},\mathrm{t}) \tag{2.15}$$

For a given initial-state Ψ_0 the time-evolving one-body density $\rho(r,t)$ tells everything about the time-evolving interacting electronic system, exactly.

Like DFT, the time-dependent KS (TDKS) equation is also developed by replacing the interacting system with a fictitious non-interacting system.

Let us assume that at $t < t_0$, the time-dependent potential is zero and the system is in its ground-state density, $\rho_0(r)$. At t_0, a small time-dependent perturbation, $v_1(r,t)$, is turned on, which induces a change in the density, and it can be written as,

$$\rho(r,t) - \rho_0(r) = \rho_1(r,t) + \rho_2(r,t) + \rho_3(r,t) + \cdots \tag{2.16}$$

Here, $\rho_1(r,t)$ is the linear response, $\rho_2(r,t)$ is the second-order response, etc. For weak perturbation, only the linear term can be considered, while ignoring higher-order terms. The first-order term is given by

$$\rho_1(r,t) = \int dt' \int d^3\, r' \chi(r,t,r',t') v_1(r',t') \tag{2.17}$$

Where χ is the linear density-density response function of the system and v_1 is the small time-dependent perturbation. According to the TDKS framework, we can calculate the linear change in density using the fictitious non-interacting system by the following equation,

$$\rho_1(r,t) = \int dt' \int d^3\, r' \chi_s(r,t,r',t') v_{s1}(r',t') \tag{2.18}$$

Where χ_s is the density-density response function for the non-interacting KS electrons and the term $v_{s1}(r,t)$ is the linear change of the effective potential, $v_s(r,t)$, of the time-dependent KS system, and it can be explicitly written as,

$$v_{s1}[\rho](r,t) = v_1(r,t) + \int d^3 r' \frac{\rho_1(r',t)}{|r-r'|} + v_{XC1}(r,t) \tag{2.19}$$

Where $v_1(r, t)$ is the external perturbation, the next term is the linearized time-dependent Hartree potential. The last term is the linearized *XC* potential, and it can be expressed as,

$$v_{XC1}(r,t) = \int dt' \int d^3 r' \frac{\delta v_{XC}[\rho](r,t)}{\delta\rho(r',t')} \rho_1(r',t') \tag{2.20}$$

Methods used in the thesis

Chapter 3. We optimized the structures of C102, phenol, and 1:2 C102-(phenol)$_2$ complexes by DFT method using the B3LYP and CAM-B3LYP functionals,[230, 234] and 6-31G(d,p) basis set,[242] using GAUSSIAN 09 package.[243] Basis set 6-31G(d,p) is used as it is computationally inexpensive and produce moderately accurate result. The geometry optimization in specific excited states was performed by TD-DFT calculations employing two hybrid functionals B3LYP and CAM-B3LYP. During optimisation process, the energy gradient value of $3*10^{-4}$ is used to achieve convergence. We started from more than one initial structure to demonstrate that we arrive at the same convergence structures. The absence of imaginary vibration frequencies verified the stability and correctness of the optimized structures. Calculations were performed both in the vacuum and in the solvent (cyclohexane) phase. The polarizable continuum model using the integral equation formalism (IEFPCM) was used as solvent model.[244] All the calculations are performed at a temperature of 300 K.

Chapter 4. In the ground state, the geometry configurations were fully optimized based on DFT while we applied TD-DFT for excited state optimizations in Gaussian 09 program.[243] All optimizations, frequency calculations, and relaxed scan were performed by using Coulomb-attenuated functional CAM-B3LYP.[234-235] For comparison, we also used another hybrid exchange-correlation functional PBE0,[231] and the hybrid Minnesota functionals M06-2X.[24] Triple zeta basis set 6-311G++(d,p) was used for all the calculations.[242] Polarizable continuum model (PCM) using the integral equation formalism variant (IEFPCM).[244] The potential energy surfaces of the S_0 and S_1 states were calculated without any restriction on other coordinates. Electrostatic potential (ESP) charges for the ground state and excited state were calculated using Merz-Singh-Kollman (MK) method.[245] All the calculations are performed at a temperature of 300 K.

Chapter 5. Ground state geometry of all the compounds and their complex (either in H-bonded or π-π stacking configurations) were fully optimized without any constraints using density functional theory (DFT). We applied time-dependent density functional theory (TD-DFT) for excited state optimizations using the Gaussian 09 program.[243] All optimizations, frequency calculations, charge population analysis, absorption spectra, and relaxed scan were performed by using Coulomb-attenuated functional CAM-B3LYP.[234-235] For comparison, we also used another well-known hybrid Minnesota functionals M06-2X.[1] All the quantum chemical calculations were reported by using a triple zeta basis set 6-311G++(d,p).[242] We also used another triple zeta basis set TZVP in some cases to check the consistency.[246] Grimme's D3 dispersion correction was included in all the calculations.[247] Solute electron density (SMD) continuum solvent model was incorporated with solvent water to account for the solvent effect.[248] The potential energy surfaces of the S_0 and S_1 states were calculated without any restriction on the other coordinates.

Electrostatic potential (ESP) charges for the ground state, and excited-state were calculated using Merz-Singh-Kollman (MK) method.[245] All the calculations are performed at a temperature of 300 K.

2.3. Classical Molecular Dynamics Simulation

In this thesis, the classical MD simulation technique has been used. It has been widely used to investigate the structure and dynamics over a period of time of bio-molecular systems, such as proteins, nucleic acids, macromolecules, and small molecules like amino acids, sugars, and drugs. In MD simulation, the potential energy function (U) is described by all interactions between the atoms that are covalently bonded as well as non-bonded interactions between atoms and molecules in the condensed phase. The so-called force field parameterization governs the interactions between particles.[249]

The potential energy function is written as a sum of bonded and non-bonded interaction terms

$$U = U_{bond} + U_{angle} + U_{dihedral} + U_{vdw} + U_{coulomb} \tag{2.21}$$

The first three terms (U_{bond}, U_{angle}, $U_{dihedral}$) are the bonded terms, which describe the bond stretching, angle bending, and torsion rotation, and the last two terms are for the non-bonded potential. In bonded terms, the bond and angle contributions are described by harmonic potentials, and all of the interactions between directly bonded atoms (1-2 interactions), angles (1-3 interactions, where two atoms bonded to a common atom), and torsion (interactions between pairs of 1-4 atoms) are defined as:

$$U_{bond} = \sum_{bonds} K_b (b_{ac} - b_{eq})^2 \tag{2.22}$$

$$U_{angle} = \sum_{angles} K_\theta (\theta_{ac} - \theta_{eq})^2 \tag{2.23}$$

$$U_{dihedral} = \sum_{dihedrals} \frac{V_n}{2} (1 + \cos(n\phi - \delta)) \tag{2.24}$$

The letters b, θ, ϕ, and δ represents the bond length, bond angle, dihedral angle, and phase angle, respectively. The subscripts '*ac*' stands for actual, and '*eq*' stands for equilibrium. The parameters K_b, K_θ, and V_n are the force constants for the bond, bond angle, and dihedral angle, respectively.

The non-bonded potentials are calculated using two terms. The first one is the Lennard-Jones term (U_{vdw}),[250] describing the van der Waals interaction, and the second one is the Coulomb term ($U_{coulomb}$),[251] that deals with the electrostatic interactions between particles having partial charges on them. The non-bonding interaction terms are defined as:

$$U_{vdw} = \sum_i \sum_{i<j} 4\epsilon_{ij} \left[\left(\frac{\sigma_{ij}}{r_{ij}}\right)^{12} - \left(\frac{\sigma_{ij}}{r_{ij}}\right)^{6} \right] \tag{2.25}$$

$$U_{coulomb} = \sum_i \sum_{i<j} [\frac{q_i q_j}{4\pi\epsilon_0 r_{ij}}] \tag{2.26}$$

Where the overall sum is over all the atom pairs i and j. Lennard-Jones parameters σ and ϵ are the diameter of atomic sites and well depth energy, respectively. r_{ij} is the inter-atomic distance. q_i and q_j are the partial charges on interaction sites i and j and ϵ_0 is the electrical permittivity.

The MD simulation aims to observe the evolution of atomic coordinates in time. We consider an N-particle system characterized by the following Hamiltonian

$$H = \sum_{i=1}^{N} \frac{p_i^2}{2m} + U(r^N) \tag{2.27}$$

where m is the mass of each particle, p_i is the momentum of the i-th particle, and $U(r^N)$ is the total potential energy of the system, which includes all the particle-particle interactions. The coordinates of the particles are denoted by $r^N = \{r_1, r_2 \ldots\ldots, r_N\}$. The position and velocity of i-th particle are represented by r_i and v_i, respectively.

The method of molecular dynamics consists of solving the equations of motion,

$$a_i = \frac{\boldsymbol{F}_i}{m_i} \tag{2.28}$$

Where $i = 1, 2, \ldots N$, m_i is the mass of i-th particle and $\mathbf{F}_i$ is the force acting on particle i. This equation is easily obtained from the Lagrangian,

$$L = \frac{1}{2} \sum_{i=1}^{N} m_i \mathrm{v_i} \, . \, \mathrm{v_i} - \frac{1}{2} \sum_{i=1}^{N} \sum_{j \neq i}^{N} u(r_{ij}) \tag{2.29}$$

Where the potential U has been assumed to be the sum of pair potentials u_{ij}. The Lagrangian equation of motion is,

$$\frac{d}{dt}\left(\frac{\partial L}{\partial \dot{q}_i}\right) - \frac{\partial L}{\partial \dot{q}_i} = 0 \tag{2.30}$$

It is clear from Eq. 2.30 that the dynamics of particles is described by the 3N number of second-order differential equations.

It is also possible to write down the Hamiltonian (H) for the system and solve the Hamiltonian equation,

$$\dot{q}_\kappa = \frac{\partial H}{\partial p_\kappa} \tag{2.31}$$

$$\dot{p}_\kappa = -\frac{\partial H}{\partial q_\kappa} \tag{2.32}$$

Where $\dot{q}_\kappa$ and $\dot{p}_\kappa$ represent generalized coordinates and momenta. For a system with pairwise interaction potential, the Hamiltonian is

$$H = \frac{1}{2}\sum_{i=1}^{N} m_i \mathrm{v_i} \,.\, \mathrm{v_i} + \frac{1}{2}\sum_{i=1}^{N}\sum_{j\neq i}^{N} u(r_{ij}) \tag{2.33}$$

And Eqs. 2.31 And 2.32 yield,

$$\frac{dr_i}{dt} = \frac{\mathrm{p_i}}{m_i} \tag{2.34}$$

$$-\dot{\mathrm{p}}_i = -\nabla \mathrm{u} = \mathrm{F_i} \tag{2.35}$$

Where i=1, 2.... N. There are now 6N first-order differential equations to be solved.

The equation of motion is solved numerically to yield particle velocities and positions as a function of time. It is usually integrated by using a finite difference approach. The Verlet algorithm is one of the most commonly used algorithm for this purpose.[252] Although it has the disadvantage of moderate precision during the calculation. As an improvement to the Verlet algorithm, the leap-frog algorithm has been developed.[253] But, it also has a disadvantage that the positions and velocities are not synchronized. As an alternative of Verlet or the leapfrog algorithm, the Velocity Verlet algorithm,[254] has been developed, and the following relations are used to calculate new position and velocity at the same time,

$$r(t+dt) = r(t) + v(t)dt + \frac{1}{2}a(t)dt^2 \tag{2.36}$$

$$v(t+dt) = v(t) + \frac{1}{2}[a(t) + a(t+dt)]dt \tag{2.37}$$

Methods used in the thesis

Chapter 3. To obtain the initial structures of the molecules, the electronically ground-state structures of C102, phenol, and cyclohexane were optimized using B3LYP/6-31G(d,p) level of theory in Gaussian 03W.[255] The partial charges on these structures were determined from population analysis of Merz–Singh–Kollman,[245] using HF/6-31G level followed by restrained electrostatic potential (RESP) charge fitting.[256] In a cubic box of dimension 40 Å × 40 Å × 40 Å, the initial structures were prepared by placing one coumarin (C102) molecule at the center while packing other solvent molecules (phenol and cyclohexane) randomly using the Packmol package.[257] The minimum tolerance between two units was set to be >2 Å. The simulation was performed in the AMBER12 program suit,[258] using generalized amber force field (GAFF),[259] parameters for C102, phenol, and cyclohexane. The GAFF force field has been proven satisfactory to reproduce the physical properties of common organic molecules, including phenol and cyclohexane.[260] To avoid bad Van der Waals contacts on the initial structures or unexpected coordinate collisions, energy minimization was performed for 5000 steps with the first 2000 steps in the steepest-descent manner followed by 3000 steps in the conjugate gradient method. Subsequently, each system was heated slowly up to 300 K within a period of 24 ps using the canonical (NVT) ensemble and keeping weak restraints (force constant= 1.0 kcal mol^{-1} $Å^{-2}$) overall atoms. A Langevin thermostat with a collision frequency of 2 ps^{-1} was used for temperature regulation. The systems were subsequently equilibrated in an isothermal-isobaric (NPT) ensemble without any restraint for 1 ns at atmospheric pressure. Finally, 15 ns production run was carried out in NPT ensemble at 1 atm pressure. To maintain the pressure, Berendsen barostat,[261] was used with a pressure relaxation time of 2 ps. The SHAKE algorithm was used to constrain bonds and angles involving hydrogen atoms.[262] A cut-off distance of 10 Å was applied for all non-bonding interactions and the long-range electrostatic interactions were treated using the particle mesh Ewald (PME),[263] summation method with periodic boundary conditions. Snapshots were saved after every 1 ps. The post-analysis of the simulation trajectories was carried out in the ptraj and cpptraj module of AMBER12, considering 15000 frames. The energy and density of the system remained consistent over the entire production run, ensuring the stability of the system (see *Appendix*, **Figure A.3.1, and A.3.2)**. The compositions of the mixtures used for simulation are given in **Table 2.1**.

Table 2.1. The composition of simulation boxes at different mole fractions of phenol (X_{phenol}).

X_{phenol}	N_{phenol}	$N_{cyclohexane}$	N_{C102}	**Total**
0.005	2	398	1	401
0.01	4	396	1	401
0.02	8	392	1	401
0.05	20	380	1	401
0.1	40	360	1	401
0.2	80	320	1	401
0.3	120	280	1	401
0.4	160	240	1	401

Chapter 6. MD simulations were performed using the AMBER12 software package.[258] The initial structure of β-CD was collected from CCDC (ref no: 1107195).[264] The structures of 2OH, 6SO_3-2OH, and 6CN-2OH were optimized in their electronic ground states using the HF/6-31G(d,p) in the Gaussian 03W.[255] The partial charge on these structures was calculated from the population analysis of the Merz-Singh-Kollman method,[245] using the HF/6-31G(d,p) followed by restrained electrostatic potential charge fitting (RESP).[256] The inclusion complexes were prepared by placing the photoacids near the center of the β-CD cavity. However, two different configurations may arise for each of the host-guest complexes– “up” and “down" (see *chapter 6*, **Figure 6.4**). In the “up” and “down” configurations, —OH group of the photoacids points towards the wide (containing secondary hydroxyl groups) and narrow rims (containing primary hydroxyl groups) of β-CD, respectively (see *chapter 6*, **Scheme 6.1**). The detailed composition of all the computed systems is given in **Table 2.2**. The carbohydrate force field GLYCAM06h was used for β-CD.[265] The force field parameters of the photoacids were generated using the General Amber Force Field (GAFF),[259] within the ANTECHAMBER,[266] module of AMBER12. A water cube of 13 Å thicknesses with TIP3P (three-point transferable intermolecular potential),[267] water model was included to solvate the system. For non-bonded interaction, the cutoff radius was set to 10 Å. The particle mesh Ewald (PME),[263] summation method with periodic boundary conditions (PBC) was used for long-range electrostatic interactions. SHAKE algorithm,[262] was

applied for constraining the covalent bonds involving hydrogen atoms. We performed three different types of energy minimization processes. In the 1st minimization process (5000 steps), we put a restraint on both the host and guest. Then, for the second minimization (5000 steps), restrain on the guest molecule was relieved. The final minimization was performed for 5000 steps, with the first 2000 steps in a steepest-descent manner without any restraint. Next, the system was slowly allowed to heat up to 300 K in 12 ps duration using the NVT ensemble with keeping a restraint of 10 kcal mol^{-1} Å^{-2} for both the host and guest molecule. The system was subsequently equilibrated with NPT ensemble (P = 1 atm) for 4 ns without any restraint. Finally, we carried out a 20 ns production run with the same NPT ensemble. Langevin thermostat,[268] and Berendsen barostat,[261] were applied to control the temperature and pressure, respectively. Snapshots were saved after every 1 ps. For better comparison, we also performed separate MD simulations of the β-CD and the photoacids individually in only water using a similar protocol. Post-analysis of the simulation trajectories was carried out in the ptraj and cpptraj modules of AMBER 12. Visual molecular dynamics (VMD) software[269] was used for visualization of the trajectories and also occasionally used for some analysis. The energy and density of the computed system remained consistent over the entire production run, ensuring the stability of the system.

Table 2.2. The number of different species taken for MD simulation of the photoacid:β-cyclodextrin complexes.

Complex	**Type**	**β-CD**	**Photoacid**	**Counter ions**	**Water molecule**	**Box volume (nm^3)**
2OH:β-CD	up	1	1	0	2212	68.18
	down	1	1	0	2212	68.18
6SO$_3$-2OH:β-CD	up	1	1	1	2215	68.56
	down	1	1	1	2215	68.36
6CN-2OH:β-CD	up	1	1	0	2211	68.51
	down	1	1	0	2212	68.51

Chapter 7. The AMBER12 software package was used to perform MD simulations.[258] The initial structure of α-CD was taken from CCDC (ref no: 125105).[270] The structure of 6CN-2OH was optimized in their electronic ground state using the HF/6-31G(d,p) in the Gaussian 03 program.[255] The partial charge on this structure was calculated from the population analysis of the Merz-Singh-Kollman method,[245] using the HF/6-31G(d,p) followed by restrained electrostatic potential charge fitting (RESP).[256] A capsule-like initial structure of the 1:2 inclusion complex was prepared by taking one 6CN-2OH molecule and two α-CD moieties at two ends. However, due to the asymmetric shape of the CD cavity, containing a narrow and a wide rim, three distinct combinations (defined as Type 1-3) are possible (see *appendix*, **Figure A.7.5**). In the 'Type 1' configuration (W-N), wider rime (containing secondary hydroxyl groups) of one α-CD faces the narrower rim (containing primary hydroxyl groups) of the other α-CD. For 'Type 2' configuration (N-N), narrower rims of both the α-CDs face each other. For 'Type 3' configuration (W-W), two wider rims of α-CD remain face to face each other. The carbohydrate force field GLYCAM06h was used for α-CD.[265] The force field parameters of the organic photoacid (6CN-2OH) were generated using the General Amber Force Field (GAFF)[259] with the ANTECHAMBER[266] module of AMBER12. A water cube of 14 Å thicknesses with TIP3P (three point transferable intermolecular potential),[267] water model was included to solvate the system. The detailed composition of all the computed systems is given in **Table 2.3**. For non-bonded interaction, the cutoff radius was set to 10 Å. The particle mesh Ewald (PME)[263] summation method with periodic boundary conditions (PBC) was used for long-range electrostatic interactions. SHAKE algorithm,[262] was applied for constraining the covalent bonds involving hydrogen atoms. Consecutive energy minimization processes were followed. At first minimization (5000 steps) restraints were imposed on both the host and guest Then, for the second minimization, restraint on guest molecule was relieved, and final minimization was performed without any kind of restraint for 5000 steps, of which the first 2000 steps were in a steepest-descent manner. Next, the system was slowly allowed to heat up to 300 K at a duration of 12 ps using NVT ensemble and keeping a restraint of 10 kcal mol^{-1} Å^{-2} over both the host and guest. The system was subsequently equilibrated with NPT ensemble (P = 1 atm) for 4 ns without any restraint. Finally, we carried out an 80 ns production run with the same NPT ensemble. Langevin thermostat,[268] and Berendsen barostat,[261] were applied to control the temperature and pressure, respectively. Snapshots were saved after every 1 ps. For better comparison, we also performed the MD simulation of the photoacid in water using a similar protocol. Post-analysis of the simulation trajectories was carried out in the ptraj and cpptraj modules of AMBER 12, considering the last 20000 frames (20 ns). Visual molecular dynamics (VMD) software[269] was used for visualization of the trajectories and also occasionally used for some analysis. The energy and density of the computed system remained consistent over the entire production run, ensuring the stability of the system.

Table 2.3. The number of different species taken for simulation of the 6CN-2OH:(α-CD)$_2$ complexes.

System	Host (α-CD)	Guest (6CN-2OH)	Water molecule	Box volume (nm^3)
Type 1	2	1	2540	79.26
Type 2	2	1	2562	79.92
Type 3	2	1	2549	79.61

Experimental Methods

2.4. Steady-State Measurements

Absorption spectroscopy refers the technique, which measures the absorption of radiation as a function of frequency (cm^{-1}) or wavelength (nm), resulted from the interaction between incident light with the sample.[271] When a sample is subjected to light irradiation of appropriate energy, it causes the rotational and vibrational transition followed by an electronic transition in the molecule. It is the most useful spectroscopic tool that provides valuable information about the wavelength of a transition and the corresponding molar extinction coefficient (ε) of a chromophore under investigation. Throughout the studies, the UV-Vis spectra of all the samples were recorded in Perkin-Elmer Lamda-750 spectrophotometers. Lamda-750 spectrophotometer consists of deuterium, tungsten, and halogen light source, double holographic grating monochromator, high sensitivity R928 photomultiplier tube (PMT). Samples in absorption spectrometer are filled in cell which is a rectangular quartz cuvette (usually 1 cm path length). A reference cell is an identical quartz cuvette filled with blank solvent. A reference cell is used to correct the blank absorption of cell and solvent if any. All the absorption measurements were carried out at room temperature (300 K).

Steady-state fluorescence spectrophotometer is an instrument that can measure both excitation and emission spectra. The emission spectrum is the "wavelength distribution of emission measured at a single excitation wavelength." In contrast, an excitation spectrum is the "dependence of emission intensity, measured at a single emission wavelength, upon scanning the excitation wavelength".[26, 272] Steady-state emission spectra of all the samples were recorded on Jobin Yvon Fluoromax4 spectrofluorometer. For all the steady-state measurements, we have used a quartz cuvette of path length 1 cm. The most commonly used light source for spectrofluorometer is a high-pressure 150 Watt xenon (ozone free) arc lamp. Fluorescence is recorded at right angles with respect to the incident beam while the emitted light is detected through a monochromator by a R928P photomultiplier tube (PMT). PMT is the detection device.

2.5. Time-Resolved Fluorescence Measurements

In the entire work, time-resolved fluorescence studies were performed in the time-correlated single photon counting (TCSPC) Horiba Scientific instruments. TCSPC is a very standard method to measure fluorescence decay from a few tens of picoseconds to millisecond/microsecond time scale.[26, 272-273] The actual time resolution and time window depend on the nature of the light source and electronic components of the spectrometer. In this technique, the sample is excited with a short light pulse from a light source with sufficient delay between pulses. In my case, the light source was a picosecond pulsed laser DeltaDiode-290 nm. The full width at half-maximum (FWHM) of this setup was typically ~800 ps measured using a liquid scatter (milk powder). The principle of TCSPC is the detection of single photons and measurement of their arrival times with respect to a reference signal from the light source. The TCSPC method needs a high repetitive light source to accumulate a sufficient number of photons since this is a statistical method and requires many numbers of statistical data precision. The resulting histogram of counts versus the time channels on the X-axis represents the curve of fluorescence decay profiles. Time-resolved data were analyzed with a deconvolution method based on a discrete components analysis model using the DAS6 software provided by the Horiba Scientific Instruments.

(a) Deconvolution Method and Lifetime Decay. An observed decay, N(t) is a convolution of the actual intensity decay, I(t) with a prompt instrumental response, L(t). To extract the fluorescence lifetime, it is essential to de-convolute the data and the convolution integral may be expressed as,[272]

$$N(t) = \int_0^{t'} L(t)I(t'-t)dt \tag{2.38}$$

Where *t* defines the variable time delays (in practice, channel numbers) of the infinitesimally small widths dt (i.e., channel widths) of which *L*(t) is composed.

The deconvolution is based on an iterative least square method. An excitation pulse profile is first recorded, and then the deconvolution starts with the mixing of the excitation pulse and a projected decay to form a new convoluted set. This data is compared with the experimentally obtained data, and the difference is summed, generating the χ^2 function for the fit. The equation of chi^2 is $\chi^2 = \sum_{i=1}^{N}\left[\frac{R(t_i)-R_c(t_i)}{\sigma(i)}\right]^2$, where $R(t_i)$ is experimental response and $R_c(t_i)$ is calculated response, N is the total number of data points and σ(i) is the standard deviation of the i-th data point. The deconvolution proceeds through a series of such iterations until an insignificant change in χ^2 occurs between two successive iterations. The quality of fit is usually assessed by inspection of the reduced χ^2, the plot of the weighted residuals, and the autocorrelation function of the residuals. The χ^2 value ~1 implies good fit, where a small deviation from 1 sometimes is considered to be acceptable for complicated heterogeneous systems.

$$I(t) = \sum_i a_i e^{-t/\tau_i} \tag{2.39}$$

All the lifetime decays were measured at the magic angle (55°) with respect to the analyzer and polarizer to avoid the contribution of rotational diffusion and anisotropy on the intensity decays. The picosecond decays are de-convoluted using DAS6 software.

(b) Anisotropy Decay. Fluorescence anisotropy decay provides information about the local environment around the probe. To measure fluorescence anisotropy decays, the analyzer was rotated at regular intervals to obtain parallel ($I_{||}$) and perpendicular ($I_{\perp}$) decay components of a fluorescence decay separately. The anisotropy function, r (t) was constructed using the expression

$$r(t) = \frac{I_{||}(t) - GI_{\perp}(t)}{I_{||}(t) + 2GI_{\perp}(t)} \tag{2.40}$$

G is the instrumental correction factor introduced for the polarization sensitivity of the detection system and monochromator. Since the fluorescence intensity of 6CN-2OH at

350 nm is very low in bulk water and hence, the anisotropy decay was measured at 470 nm, and was found to be 0.66.

For a simple isotropic rotor, r(t) decays with a single rotational correlation time (τ_r) represented by the following equation;[26, 272]

$$r(t) = r_0 \sum \beta_i \, exp^{-\frac{t}{\tau_{ri}}} \tag{2.41}$$

Where β and τ_{ri} are the fractional contribution of total depolarization and rotational correlation times of the i^th component, respectively. r_0 represents fundamental anisotropy. In terms of Stokes-Einstein theory, τ_r is related to the medium viscosity by;

$$\tau_r = \frac{\eta V}{kT} \tag{2.42}$$

Where η is the viscosity coefficient of the medium, V is the molecular volume, k is the Boltzmann's constant, T is the absolute temperature.

2.6. Isothermal Titration Calorimetry (ITC)

ITC is used to measure bio macromolecule-ligand interactions in the solution phase without the need of any immobilization or modification.[274] The association constant (K_a), the number of binding sites (n), and the thermodynamic parameters, including changes in enthalpy (ΔH), entropy (ΔS), and Gibbs free energy (ΔG) can be determined directly via the measurement of reaction heat. The most significant advantage in the ITC measurement is all the measurements are direct, excluding any indirect calculative measurements like Scatchard,[275] or Benesi-Hildebrand plot,[276] generation from fluorescence data. However, sometimes heterogeneous solvent medium in cell and syringe generates high dilution enthalpy, which interferes with the binding enthalpy of the association process. Hence, a similar solvent with the same pH in cell and syringe is required in the case of ITC. ITC instrument has two cells; one is the sample cell, and another one is the reference cell. The reference cell is filled with water (or base solvent). The sample cell contains the macromolecule/host solution, which is titrated stepwise with its binding partner through a computer-controlled injector or syringe. The syringe contains a concentrated solution (usually ten times or higher in concentration than cell solution) small molecule. During the experiment, the sample cell temperature is kept the same as that of the reference cell. During the experiment, a small fixed amount of aliquots of the titrant are injected into the sample cell at defined time intervals, and the reaction heat is recorded. The reaction heat is proportional to the bound fraction of the injected molecules. During such titration in ITC instrument the liberated heat is measured by the following equation;

$$Q = \frac{V_0 \Delta H_b [M]_t K_a [L]}{(1 + K_a [L])} \tag{2.43}$$

where V_0 is the cell volume, ΔH_b is the enthalpy change corresponding to the binding of one mole of ligand, $[M]_t$ is the total macromolecule concentration in the cell, K_a is the association constant, and [L] is the free ligand concentration. In the case of multiple binding sites, the equation is summed up for all binding sites. The accurate determination of concentration is highly crucial in ITC. After subtracting the baseline (solvent to solvent dilution enthalpy), the areas under the observed peaks give the enthalpy changes that belong to the reactions occurring upon injection steps.

2.7. Materials Used

α-Cyclodextrin (α-CD, Sigma, ≥98%) and β-Cyclodextrin (β-CD, Sigma, ≥97%), 2-naphthol (2OH, Sigma, 99%), 6-sulfonate 2-naphthol ($6SO_3$-2OH Sigma, 97%), and 6-cyano 2-naphthol (6CN-2OH, Sigma, 97%) were purchased from Sigma-Aldrich. We used Millipore water (resistivity, 18.2 MΩ cm, and pH = 5.8) throughout the experiment.

2.8. Preparation of Samples

Chapter 6. We first prepared ~10 μM solutions of each photoacid in water and a stock solution of 12 mM β-CD in water. From the 12 mM stock solution, we prepared 0.05 mM, 1 mM, 2 mM, 4 mM, 6 mM, 8 mM, 10 mM β-CD solution in water. These solutions were used throughout all absorption, steady-state, and time-resolved fluorescence measurements. Furthermore, for ITC measurement we injected 10 mM of β-CD solution in 0.15 mM 2OH solution, 15 mM of β-CD solution in 0.5 mM $6SO_3$-2OH solution and 15 mM of β-CD solution in 0.075 mM 6CN-2OH solution, respectively. All solutions were prepared in fresh Millipore water.

Chapter 7. Similarly, we first prepared ~10 μM solutions of photoacid 6CN-2OH in water and a stock solution of 130 mM α-CD in water. Here we performed the titration process for absorption and steady-state fluorescence measurement up to 20 mM. We gradually added the required amount of α-CD solution (130 mM) to the 6CN-2OH solution. The remaining used concentrations were discrete solutions that were prepared from 130 mM α-CD stock solution. For ITC measurement, we injected 50 mM of the α-CD solution to 0.1 mM of 6CN-2OH solution.

2.9. pK_a and pK_a^* Measurements

2.9.1. Determination of pK_a of Free and Complexed Photoacids

We first prepared ~10 μM solutions of each photoacid in water, and in 12 mM β-CD. We also prepared a standard solution of 0.01 M NaOH solution through standardization with an oxalic acid solution. The pH of the solutions was changed by adding different amounts of 0.005 M or 0.01 M NaOH solutions to the aqueous or cyclodextrin solutions. The pH of the solutions was measured using a Eutech pH 700 pH-meter having an accuracy of ±0.05 pH. We observed significant changes in the absorption spectrum with the increase of pH of the solution (see *Appendix*, **Figure A.6.1**). We also found a clear isosbestic point indicating the conversion of the photoacids from protonated to deprotonated form. In the ground state proton dissociation equilibrium is

$$HA \rightleftharpoons A^- + H^+$$

can be obtained from the Henderson-Hasselbalch equation as,[277-279]

$$pH = pK_a + log\frac{[A^-]}{[HA]} = pK_a + log\frac{[A^-]}{[HA]_0 - [A^-]} \tag{2.44}$$

The total concentration of photoacid ($[HA]_0$) is constant during the pH titrations. If we choose the absorbance of deprotonated form at a particular wavelength where there is no contribution from the protonated form, the absorbance (A) should vary with pH as follows.

$$Abs_{A^-} = \frac{\epsilon l[HA]_0}{1 + e^{2.303(pK_a - pH)}} \tag{2.45}$$

Where ε is the molar extinction coefficient of the deprotonated form at that wavelength, *l* is the optical path-length of the cuvette. At very high pH when almost all the photoacid is present is deprotonated form, then the Absorbance of A the numerator will be

$$\epsilon l[A^-]_{max} = Abs_{A^-}^{max} \tag{2.46}$$

Thus, the equation will be

$$Abs_{A^-} = \frac{Abs_{A^-}^{max}}{1 + e^{2.303(pK_a - pH)}} \tag{2.47}$$

Thus, pK_a of a photoacid can be determined from the absorbance of the deprotonated form against pH using equation (4) (see *Appendix*, **Figure A.6.2**).

2.9.2. Determination of pK_a^* of the Free and Complexed Photoacids

pK_a^* of the photoacids were obtained using the Förster cycle.[102, 280-281] Fluorescence spectra were recorded at a high pH and a low pH to achieve the emission spectrum of the deprotonated and protonated forms, respectively. From the intersection point of the absorption and fluorescence spectra normalized at the lowest energy band, the 0-0 energy (ν_{00}) of both protonated and deprotonated forms were obtained (see *Appendix*, **Figure A.6.3**). The pK_a^* can be obtained from the following equation (5),

$$\mathrm{p}K_a^* = \mathrm{p}K_a - \frac{\mathrm{N_A} hc(\nu_{\mathrm{ArOH}} - \nu_{\mathrm{ArO-}})}{2.303\mathrm{RT}} \tag{2.48}$$

Where c is the speed of light; ν is the transition frequencies of ArOH and $\mathrm{ArO^-}$ in wavenumbers ($\mathrm{cm^{-1}}$); *h* is the Planck's constant; $\mathrm{N_A}$ is Avogadro's constant; R is the ideal gas constant, and T is the temperature. The calculated values are given in **Table 6.1** of ***chapter 6***.

Similarly, in the case of 6CN-2OH:α-CD inclusion complex, we exactly followed the same procedure as described above using 10 μM solution of 6CN-2OH in water and 130 mM α-CD. The calculated values are given in **Table 7.1** of **chapter 7**.

Chapter-3

H-Bonding around C102 in a Phenol–Cyclohexane Mixture for Implications in H-Bond-Guided Photoinduced Electron Transfer[#]

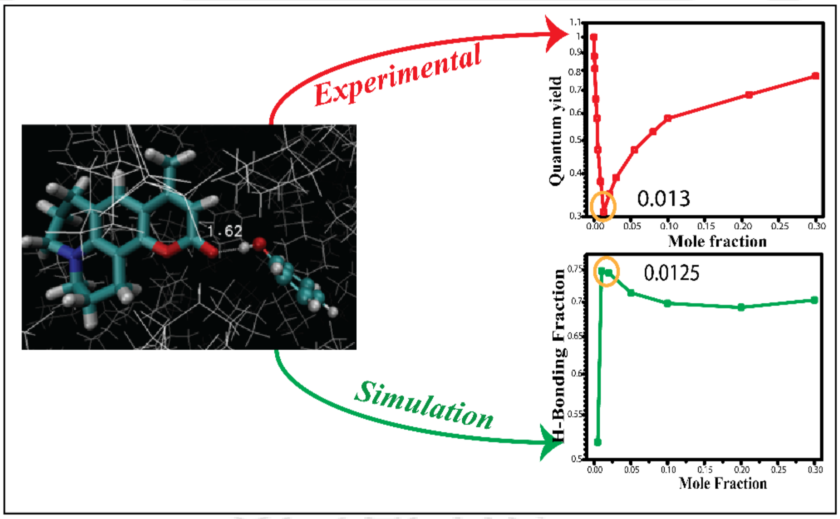

[#]This work has been published in *J. Phys. Chem. A* **2017,** *121* (3), 616-622.

Chapter 3: H-Bonding around C102 in a Phenol−Cyclohexane Mixture for Implications in H-Bond-Guided Photoinduced Electron Transfer

3.1. INTRODUCTION

The H-bonded complex of coumarin 102 (C102) and phenol has accomplished a special spotlight from the viewpoint of both the excited state H-bond dynamics and H-bond controlled photo-induced electron transfer (PET). Using ultrafast spectroscopy, Nibbering and co-workers suggested that H-bond breaks within ~200 fs of photo-excitation of the C102-phenol complex.[11, 68] Recently, Fang and co-workers also invoked H-bond breaking of C102 in ethanol medium using femtosecond stimulated Raman spectroscopy.[282] However, using time-dependent density functional (TD-DFT) calculation, Han and co-workers reinterpreted the hydrogen-bond dynamics of the C102-phenol complex. They suggested that the C102-phenol H-bond becomes significantly strengthen in the excited state rather than being cleaved.[20] Recent TD-DFT studies reported excited state H-bond strengthening for C102 in ethanolic,[283] and aqueous media.[284] Liu et al. adopted the H-bond strengthening formalism to investigate the H-bonding interaction of C102 with aniline in the excited state.[25]

Recently, our group revisited the C102-phenol complex.[65] It was observed that the fluorescence intensity of C102 was quenched drastically in the presence of phenol in non-interacting solvent cyclohexane (cyclohexane cannot participate in either electron transfer or H-bonding).[65] The quenching is very strong for *p*-Cl-phenol, which is a better H-bond donor than phenol. On the other hand, no quenching was observed for anisole, which cannot donate H-bond.[65] Furthermore, they found that fluorescence quenching modulates unusually with the mole fraction of phenol in inert solvent cyclohexane.[80] The quenching was found to be more pronounced at lower mole fraction (up to $X_{PH} = 0.013$) of phenol rather than at the higher mole fraction.[80] They proposed that at low mole fraction 1:1 C102-phenol complex is formed, but at higher mole fraction, higher-order C102–(phenol)$_n$ ($n \geq 2$) complex may be present. Moreover, the unusual modulation of fluorescence quenching was also repeatedly observed for both C102 and C153 in the aniline-cyclohexane mixtures.[81-82]

Molecular dynamics (MD) simulation is a valuable method to gain insight about physical properties that arise from local molecular rearrangement or H-bonding possibilities and has successfully applied to various systems, for example, in neat liquids,[285-287] host-guest complexes,[288-290] and so on. Following our previous successful MD simulation study,[82] in this chapter, we applied MD simulation to elucidate the exact H-bonding environment around the acceptor C102 at different mole fractions of phenol-cyclohexane to get further insight into the unusual modulation of the fluorescence intensity. Previously studied AN-cyclohexane mixture was somewhat restricted due to the immiscibility of aniline in cyclohexane over the mole fraction range 0.14-0.73.[82] Hence, we could not find the exact mole fraction, which corresponds to the highest quenching. The C102 dissolved in the phenol-cyclohexane binary mixture is a better system since there is no solubility restriction; the phenol-cyclohexane binary mixture is miscible in all proportions. This allows us to perform MD simulation at any mole fraction without solubility restriction.

3.2. RESULTS AND DISCUSSION

3.2.1. MD Simulations Results:

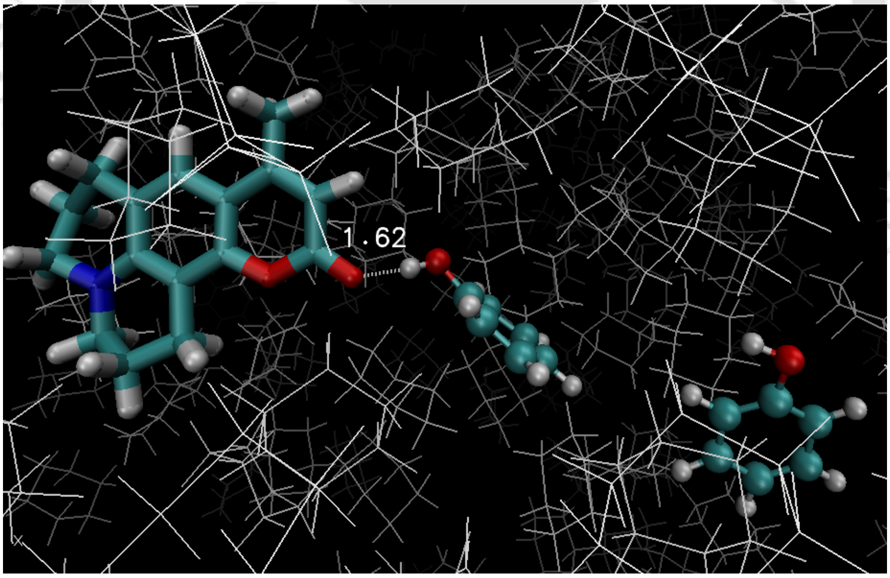

Figure 3.1. A representative MD simulation snapshot (taken after 15 ns) is showing C102-phenol H-bonding in the phenol-cyclohexane mixture at a phenol mole fraction of 0.005. C102, phenol, and cyclohexane molecules are denoted by LICORICE, CPK, and lines, respectively.

It is observed that in the mixture containing even the lowest (X_{PH} = 0.005) concentration, phenol is found to be populated around the C=O site of C102 in many snapshots, and are depleted from other parts of the acceptor (**Figure 3.1**). This is consistent with the fact that the C=O group of C102 is the primary site for the formation of H-bond. It is also noticed that in many snapshots, phenol makes 1:1 H-bonding complex with C102 (**Figure 3.1**).

3.2.1.1. Radial Distribution Function:

To get a more clear understanding of the distribution of phenol around the acceptor, radial distribution function (RDF) may be appropriate. The RDF of O1 (oxygen atom of carbonyl group) of C102 with H6 atom (hydrogen atom of hydroxyl group) of phenol, g(rO1…H6) would be most informative because it may indicate specific interaction due to hydrogen bonding. The atoms used for RDF calculation are labelled and shown below (**Figure 3.2**).

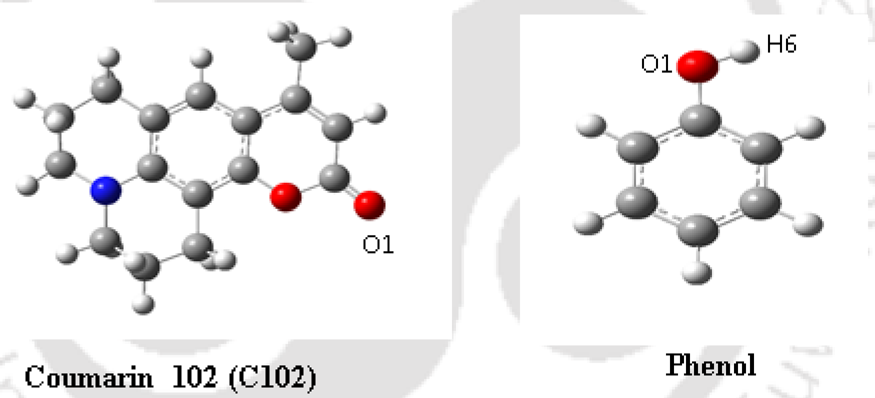

Coumarin 102 (C102)

Phenol

Figure 3.2. Structures of Coumarin 102 (C102) and phenol with the main atom labels used in the RDF calculations.

The O1(C102)-H6(phenol) RDF displays a very strong peak at ~1.8 Å at all mole fractions along with a weaker secondary broad peak at ~ 4 Å and a very faint peak at ~ 6 Å (**Figure 3.3**). Note that at higher mole fractions, the RDF persists over significantly long-distance range indicating the possibility of higher-order C102-(phenol)$_n$ clusters (n≥2). The peak strength of RDF denotes the difference in the local density compared to the average density and depends strongly on the phenol concentration (X_{PH}). Since the first maximum of RDF appears at ~1.8 Å and this is close to the ground state H-bond distance of the 1:1 C102-phenol complex,[20, 65] it further emphasizes the possibility of H-bond formation. It was found that with increasing of the phenol concentration, the 1st peak strength diminishes drastically. This suggests that the difference between the local density and the average density reduces with the increase of X_{PH}. It is important to note that a change in the mole fraction of phenol alters both the local density of the species around the acceptor and also its average number density. The enrichment of the polar component (phenol) in the vicinity of polar solute (C102) is commonly known as preferential solvation,[291-292] and mainly arises due to dipole-dipole interaction or H-bonding interaction. Since the interaction is found to be site-specific (accumulation of phenol only around the carbonyl site of C102), H-bonding interaction may be predominant in this case.

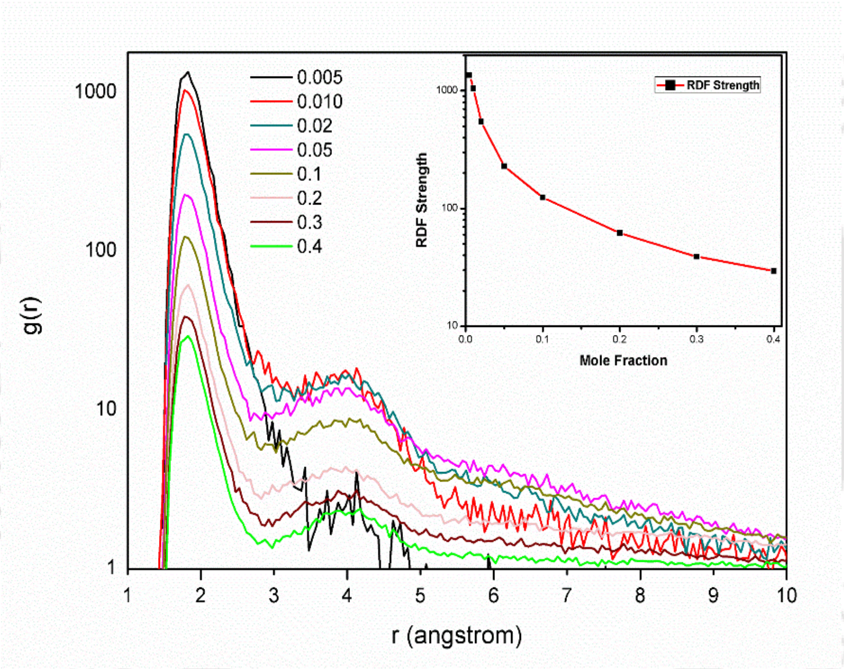

Figure 3.3. The radial distribution function, g(r) of the distance between the carbonyl oxygen (O1) of C102 and the hydroxyl hydrogen (H6) of phenol. The inset shows the 1st RDF peak strength against the mole fraction of phenol.

The integrated number density (also known as running coordination number) $n_i(r')$ of a particular solvent (i) present within a specified distance r′ from a defined site (α) of the acceptor may be defined as

$$n_i(r') = 4\pi\rho_i \int_0^{r'} g_{\alpha i}(r) r^2 \mathrm{dr} \tag{3.1}$$

Where ρ_i is the average number density of the solvent *i* in the system. We are mainly interested in the average number of phenol molecules present within a short distance (<2 Å) from the acceptor. These phenol molecules may involve in H-bonding and thus contribute to the fluorescence quenching process.

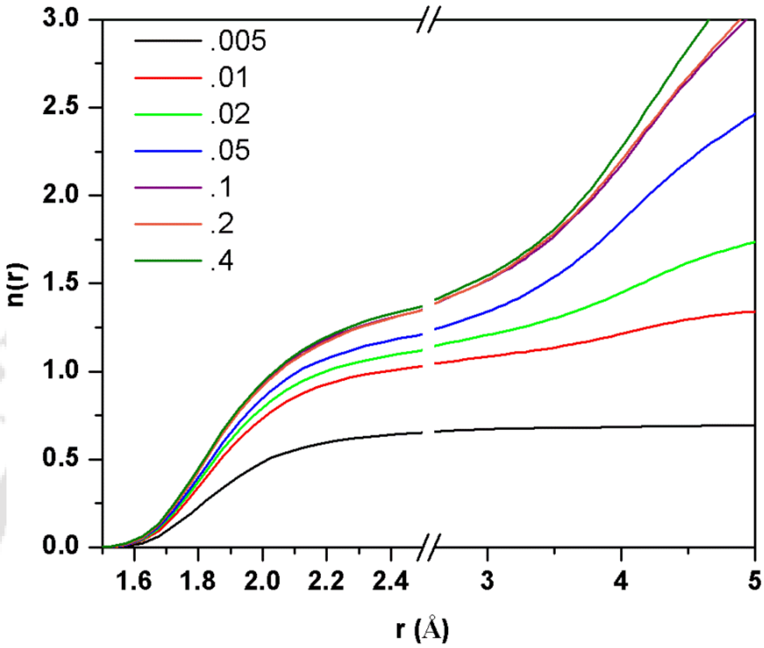

Figure 3.4. Integrated number n(r) is shown for above each mole fractions against distance.

From **Figure 3.4**, it is evident that the number of phenol molecules within 2 Å does not vary much upon variation of the phenol mole fraction. At the lowest (0.005) mole fraction, n(r) = 0.51 for r = 2 Å. This implies that in about one out of two frames, one phenol is found to be within 2 Å of C102. The value of n(r=2 Å) are 0.77, 0.83, 0.89 respectively at mole fractions 0.01, 0.02, 0.05. Thus, the variation is not very prominent, and at higher mole fractions (0.1-0.4) all have the same n(r) of 0.98 at r=2 Å. If these closest lying phenols are H-bonded to C102, we may say that H-bonding also regularly varies with the mole fraction of phenol and after certain mole fraction, probability of H-bonding levels off. However, we need to check whether all of the neighbouring phenols are involved in H-bonding or not.

3.2.1.2. Hydrogen Bonding Analysis:

We rigorously examined the number and type of hydrogen bonds possible between the carbonyl oxygen of C102 and the -OH group of phenol moiety in the mixtures. For this purpose, a distance cut off of 3 Å (1st minimum of RDF) and angle cut off of 135° was selected, where, the distance and the angle respectively denote the O…O distance and ∠OHO angle for the complex (phenol)O-H….O=C(C102). **Table 3.1** summarises the fraction of different types of H-bonding present at different mole fractions. We found that in some frames, no H-bonding is present; in some frames, C102 is H-bonded to one phenol (single HB), and in some cases, the carbonyl group of C102 is simultaneously H-bonded to two phenols (double HB). Very rarely, C102 is forming H-bond with three phenols (triple HB). From **Table 3.1**, it is clear that single HB is present in all mole fractions, but double HB is only significant at higher mole fractions. The triple HB complex is very rare and may not be needed to consider any further.

Table 3.1. Hydrogen bonding analysis of C102 in the cyclohexane-phenol mixtures at different mole fractions.

X_{PH}	No HB	single HB	Double HB	Triple HB	Total HB[§]
0.005	0.476	0.519	0.002	0.000	0.523
0.01	0.223	0.748	0.030	0.000	0.807
0.02	0.186	0.745	0.069	0.000	0.882
0.05	0.175	0.714	0.111	0.000	0.936
0.1	0.146	0.698	0.155	0.001	1.010
0.2	0.144	0.692	0.163	0.001	1.021
0.3	0.136	0.703	0.160	0.000	1.025
0.4	0.145	0.694	0.160	0.001	1.016

[§] **Total HB = 1 × single HB + 2 × double HB + 3 × triple HB**

Note that if all types of H-bonding are included, then the total fraction of H-bond increases gradually with the mole fraction of phenol. However, the fraction of singly H-bonded complex reaches a maximum within mole fraction 0.01 to 0.02 and after that decreases. Note that experimentally the fluorescence quenching was most prominent at a critical phenol mole fraction of 0.013 in the cyclohexane-phenol mixture.[80] Thus, we may expect that the singly H-bonded complex may contribute more dominantly towards PET than the doubly H-bonded complex. Thus, the main important point is that the agreement between the experiment and theory can only be achieved if we ignore contribution from the double or triple HB complex. Thus, the double HB or 1:2 hydrogen bonding (**Figure 3.5a**) may have little influence on fluorescence quenching. Note that a single HB complex may be of two types- pure 1:1 complex, where one C102 makes H-bond with one phenol (**Figure 3.1**) or 1:1:1 where one phenol makes H-bond with one C102 and another phenol (**Figure 3.5b**). Thus, different types of the hydrogen-bonded complex may have different influence over the PET process. In the next section, DFT and TD-DFT calculations are used to optimize these hydrogen-bonded complexes and determine their contribution towards PET.

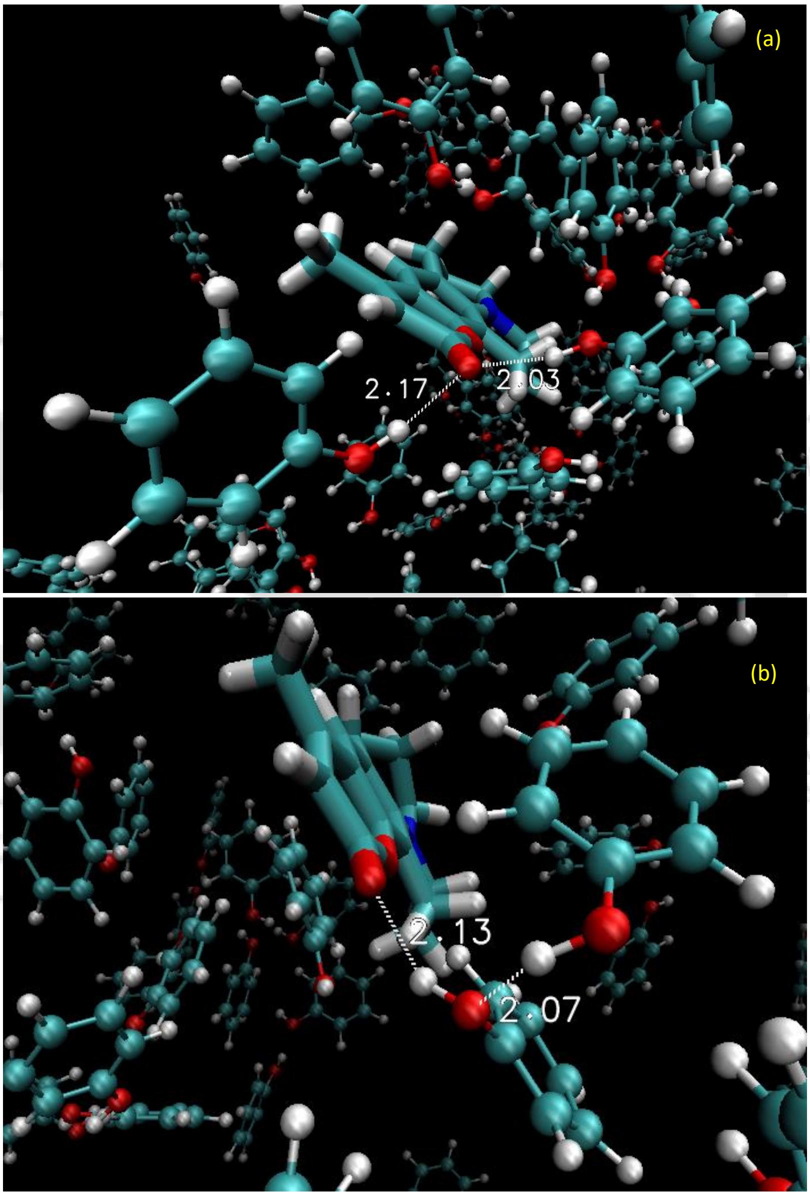

Figure 3.5. MD snapshots of mixtures forming 1:1:1 and 1:2 hydrogen bonds of phenol molecules with C102 at mole fraction of solvent phenol molecules (X_{ph}) - 0.3, where figure (a) shows MD snapshot for (1:2) complex and (b) shows MD snapshot for (1:1:1) complex. Cyclohexane molecules are omitted for clarity.

Note that our MD simulation is based on the classical approach, and hence, we cannot explicitly comment about the H-bond dynamics (breaking or strengthening). Besides, ground state charge densities on C102 are used in the MD calculation, and hence we are merely calculating the equilibrium probability of H-bonded complex formation between C102 and phenol. Despite that, our results show a very good prediction of the critical mole fraction (0.01-0.02) that was experimentally observed in the fluorescence experiment before.[80] Hence, for fluorescence dynamics, the equilibrium fraction of H-bonded complexes may be important, but the H-bond dynamics which occurs in very fast time scales compared to fluorescence lifetime may have only a very little influence on the fluoresce quenching. If we consider the view of Zhao and Han that H-bond strengthens in the excited state, we may expect an increased fraction of H-bonded species in the excited state than in the ground state.[20] On the other hand, the H-bond dynamics proposed by Nibbering and co-workers suggest that excited state favours free C102. Here, it was found that 1:1 H-bonding in the ground state is sufficient enough to reproduce the experimental behaviour. Thus, although the equilibrium constant between the free C102 and H-bonded complex may be lower or higher in the excited state but the contribution of the H-bonded complex towards the fluorescence quenching remains undoubtedly important.

3.2.2. DFT and TD-DFT Calculations:

From MD simulations, we get an overview of the H-bonding environment around C102 at different phenol mole fractions. At low concentration, only 1:1 C102-phenol complex exist along with free C102. But at higher phenol concentration, additionally two different types of the hydrogen-bonded C102-(phenol)$_2$ complexes were found (**Figure 3.5**). In the presence of both gas phase and solvent medium, DFT and TD-DFT calculations were applied on these complexes to understand the excited state H-bonding behaviours in addition to the ground state and their ability to undergo fluorescence quenching.

Although two different functionals have been used, the geometry of the complexes does not depend much on the functional or on the inclusion of the solvent model. The optimised H-bonded geometry obtained in presence of PCM solvent (cyclohexane as solvent) is almost similar with respect to H-bond length and angle to the optimised H-bond geometry obtained in the gas phase. The optimised geometry of complexes are same for different functionals and in the presence of solvent model. It was found that both the isolated C102 and phenol molecules have the planar conformations. However, the phenol molecule resides out of the plane of C102 molecule in both types (linear 1:1:1 and branched 1:2) of C102-(phenol)$_2$ complexes. In both the conformations, the hydrogen bond C=O---H-O remains in the plane of the C102 molecule. The gas phase optimised structures using the B3LYP functional are shown in **Figure 3.6 (a) and (b)**.

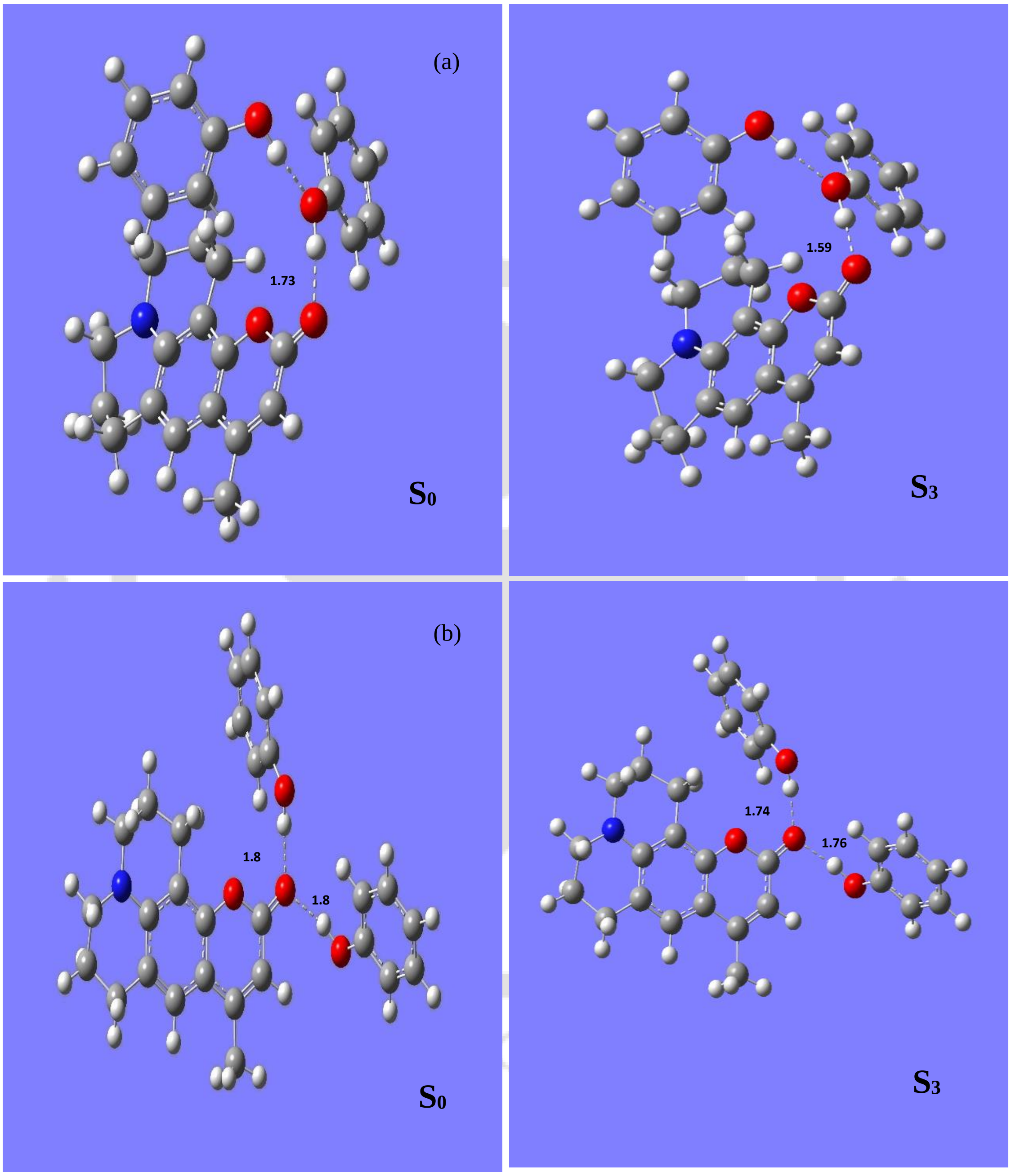

Figure 3.6. Optimized ground state (S_0) and excited state (S_3) structures of the hydrogen-bonded cumarin102-(phenol)$_2$ complexes are gas phase - (a) linear type structure (1:1:1) cumarin102-phenol-phenol complex, (b) bifurcated H-bonding of two phenols with one C102. It is evident that H-bond in (a) is shorter than in (b) complex in both states, and H-bond shortens in the excited state than in the ground state.

It was observed that the H-bond distance between C102 and phenol in the linear type (1:1:1) complex is found to be 1.728 Å (**Figure 3.6 (a)**). The distances of the two hydrogen bonds are 1.819 Å and 1.830 Å for the bifurcated hydrogen-bonded C102-(phenol)$_2$ complex (**Figure 3.6 (b)**). It indicates stronger C102-phenol H-bonding interaction between phenol and C102 in the linear 1:1:1 complex than in the 1:2 complex. Upon photo-excitation ($S_0 \rightarrow S_3$), the two H-bonds of 1:2 complex is shortened from 1.819 Å to 1.745 Å and 1.830 Å to 1.763 Å, respectively. Similarly, for 1:1:1 complex the H bond between carbonyl group (C102) and hydroxyl group (phenol) is drastically shortened to 1.597 Å from 1.728 Å. The shortening of these bond lengths should be attributed the significant strengthening of the intermolecular hydrogen bond C=O••••H-O in the photo-excited state. In addition, the relative strengths of these hydrogen bonds were also calculated. The hydrogen bond binding energies of C=O---H-O are calculated to be 50.5 kJ/mol for 1:1:1 complex, whereas in the case of 1:2 complex, it is 34.4 kJ/mol considering both H-bonds are of equal strengths by using BSSE corrections. Comparing this binding energy values, we can predict that the H-bond strength is higher for 1:1:1 than 1:2 complex in the ground state. These results agree with the more frequent occurrence of 1:1:1 complex compared to 1:2 complex in the MD snapshots.

Table 3.2. Calculated H-bond lengths (Å) for the H bonded 1:1 complex in the electronic ground state and the excited state using different hybrid functionals.

C102-Phenol (1:1)	B3LYP/ 6-31G(d,p)	CAM-B3LYP/ 6-31G(d,p)	BP-86/TZVP§
Ground state (gas)	1.789	1.770	1.786
Ground state (cyclohexane)	1.760	1.742	
Excited state (gas)	1.718	1.717	1.691
Excited state (cyclohexane)	1.678	1.678	

§From ref 20

H-bonding in 1:1 C102-phenol complex was thoroughly investigated earlier by Zhao and Han.[20] They applied GGA functional BP-86 and TZVP basis set in the gas phase. In this work, B3LYP and CAM-B3LYP hybrid functional was applied with 6-31G(d,p) level of theory, which is computationally inexpensive and hence could be extended to the lager 1:2 complexes. In addition, the solvent model (IEFPCM, cyclohexane) was included in some calculations. Both in the ground and the excited state, the H-bonding distances in the 1:1 complex are very consistent with that reported by Zhao and Han, and significant shortening of the H-bond is noticed in the excited state compared to the ground state. All the H-bond distances are given in **Table 3.2**. The H-bond distances obtained from B3LYP and CAM-B3LYP functionals are very similar. Note that upon application of the solvent model, H-bond distances are slightly shorter than the gas phase. Vertical transition energies and corresponding oscillator strengths were also calculated for first three electronic transitions from the optimized ground-state structures. Our B3LYP/6-31G(d,p) results qualitatively agree with that of Zhao and Han for the gas phase. In the 1:1 complex, the $S_0 \rightarrow S_2$ transition is found to be the strongest transition, and the S_1 state is found to be CT character (**Table 3.3 (a)**). Zhao and Han concluded that although free C102 is excited to the S_1 state but the 1:1 complex may be excited to the S_2 state. The internal conversion from LE (S_2) to CT (S_1) was proposed as a possibility for fluorescence quenching. However, when the solvent model (IEFPCM, cyclohexane), was included in the same calculation, the energy of the LE (S_1) state was found to be lower than the energy of the CT (S_2) state (**Table 3.3 (b)**). Thus, internal conversion from the LE to the CT state may not be feasible in this case as CT is now higher in energy than the LE state. For the CAM-B3LYP calculations, the CT state was found to be higher in energy than the LE state even in the gas phase (**Table 3.3 (a)**). It is important to note that if the energy gap between two states are close enough, then we can still get transition during short times.

Table 3.3. (a) Electronic excitation energies (in nm) and corresponding oscillator strengths (in the Parenthesis) of the low-lying electronically excited states calculated from the optimized ground state of hydrogen-bonded C102-phenol (1:1) complexes in gas phase.

C102-Phenol (1:1)	**TDDFT/B3LYP/6-31G(d,p)**	**TDDFT/CAM-B3LYP/ 6-31G(d,p)**
S_1	392.33 (0.001)	309.59 (0.514)
S_2	352.57 (0.400)	268.87 (0.013)
S_3	299.18 (0.000)	266.95 (0.001)

(b) Electronic excitation energies (in nm) and corresponding oscillator strengths (in the Parenthesis) of the low-lying electronically excited states calculated from the optimized ground state of hydrogen-bonded C102-phenol (1:1) complexes in cyclohexane solvent (using IEFPCM model).

C102-Phenol (1:1)	**TDDFT/B3LYP/ 6-31G(d,p)/IEFPCM**	**TDDFT/CAM-B3LYP/ 6-31G(d,p)/IEFPCM**
S_1	367.54 (0.491)	330.32 (0.657)
S_2	363.63 (0.006)	272.90 (0.011)
S_3	298.11 (0.022)	254.63 (0.001)

Furthermore, the vertical transitions from the optimized excited-state structure representing fluorescence transitions were calculated (**Table 3.4**). Both B3LYP and CAM-B3LYP showed significantly strong fluorescence transition from the S_1 states when the solvent model was included in the calculation. Thus, the simple LE to CT conversion formalism may only valid for some particular calculations, and the relative energies of LE to CT found to vary abruptly for the two functionals B3LYP and CAM-B3LYP.

Table 3.4. Electronic excitation energies (in nm) and corresponding oscillator strengths (in the Parenthesis) of the low-lying electronically excited states calculated from the optimized excited state of hydrogen-bonded C102-phenol (1:1) complexes in cyclohexane solvent (using IEFPCM model).

C102-Phenol (1:1)	**TDDFT/B3LYP/6-31G(d,p)**	**TDDFT/CAM-B3LYP/ 6-31G(d,p)**
S_1	401.34 (0.395)	354.13 (0.677)
S_2	408.54 (0.003)	279.83 (0.001)
S_3	321.25 (0.091)	273.89 (0.001)

Although the energies of the excited state differ significantly, we noticed a significant strengthening of the H-bond compared to the ground state for all complexes irrespective of the level of calculations. The excited H-bond lengths were similar for the 1:1 and 1:1:1 complex and are much shorter compared to their ground state values (**Table 3.5**). For the 1:2 complex also the H-bond becomes shorter compared to its ground state but significantly longer than the 1:1 and 1:1:1 complex.

Table 3.5. Calculated H-bond lengths (Å) for the H-bonded 1:1:1 & 1:2 complexes in the ground state and excited states by using CAM-B3LYP hybrid functional in cyclohexane solvent (using IEFPCM model).

Electronic state	**C102-(Phenol)$_2$ (1:1:1)** **CAM-B3LYP/** **6-31G(d,p)**	**C102-(Phenol)$_2$ (1:2)** **CAM-B3LYP/** **6-31G(d,p)**
Ground state (cyclohexane)	1.681	1.774 1.766
Excited state (cyclohexane)	1.63	1.720 1.719

Thus, the possible reason for the fluorescence quenching could be facile internal conversion from S_1 to S_0 state rather than internal conversion from S_2 to S_1 state. Excited-state strengthening may play a crucial role in the process. However, a more detail investigation with a higher-level theory is required to reveal the exact mechanism.

3.3. SUMMARY AND CONCLUSION

In this chapter, we provided an overview of the H-bonding environment around the fluorophore C102 at various phenol mole fractions in the phenol-cyclohexane mixture from our MD simulation study. The overall fraction of C102-phenol hydrogen bonding continuously increases with the increase of the phenol mole fraction and saturates at a significantly higher mole fraction than that corresponds to maximum fluorescence quenching. However, it was found that at higher mole fraction, a C102 molecule may simultaneously form H-bonding with more than one phenol molecules. If we only consider the subset of H-bonding complexes where H-bonding occurs between one C102 with one phenol, then we obtained an excellent correlation with the experimentally observed critical mole fraction. Thus, it was found that the single C102-phenol H-bonding is very important to inducing fluorescence quenching. TD-DFT calculations indicate that the H-bonding in the ground state becomes shorter in the excited state. Moreover, in the excited state C102-phenol H-bonding in the 1:1 and 1:1:1 complex is shorter than the 1:2 complex. It may be proposed that H-bonding may induce faster internal conversion from the $S_1 \rightarrow S_0$ state. Furthermore, isotopic substitution effect may add more valuable information in this issue.

Chapter-4

Proton Coupled Electron Transfer as a potential Fluorescence Quenching Mechanism in H-bonded C102-Phenol Complex[#]

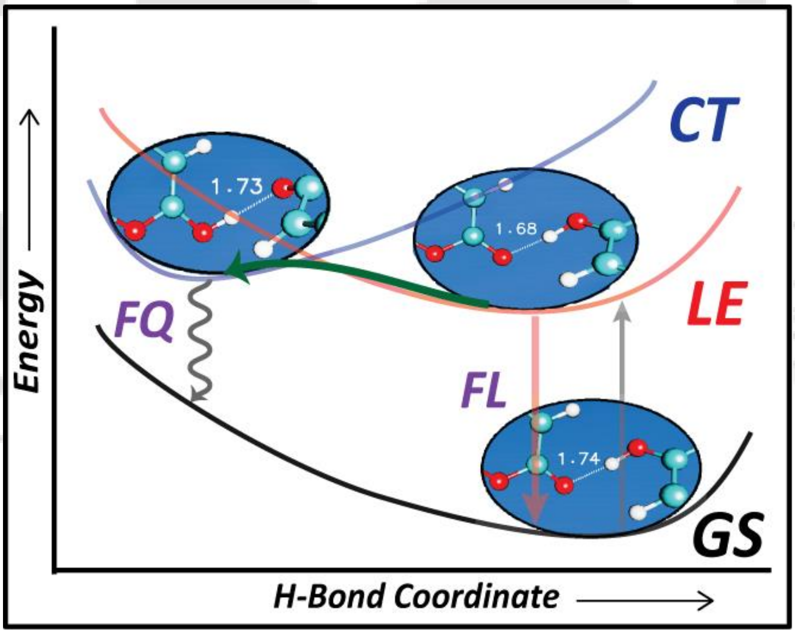

[#] This work has been published in *J. Phys. Chem. A* **2018,** *122* (9), 2394-2400.

Chapter 4: Proton Coupled Electron Transfer as a potential Fluorescence Quenching Mechanism in H-bonded C102-Phenol Complex

4.1. INTRODUCTION

Excited-state H-bond strengthening may trigger photoinduced electron transfer between an H-bonded donor and an acceptor molecule, which has been reviewed in *chapter 1* (see *section 1.1.4*).[293-295] The H-bonded coumarin 102 (C102)-phenol complex is an attractive system to understand the influence of H-bonding on photophysical processes. The C=O group of C102 forms an H-bond with the –OH group of phenol. Using time-dependent density functional (TD-DFT) methods Zhao and Han, for the first time, proposed that a strong H-bond strengthening occurs in the excited state and also proposed the possibility of fluorescence quenching in the complex. They obtained a charge transfer (CT, S_1) state lying below the locally excited (LE, S_2) state in the gas phase calculations which propelled them to the proposal of a facile internal conversion (IC) from LE to CT.[20] Later, the methodology was adopted in numerous H-bonded complexes.[25, 283-284] Recently, our group have experimentally confirmed fluorescence quenching in the H-bonded C102-phenol complex.[65] The fluorescence intensity of C102 is drastically quenched upon addition of phenol in a non-interacting solvent cyclohexane (nonpolar and aprotic). However, in our previous *chapter 3*, when we applied TD-DFT calculations, it was found that the energy ordering of the LE and CT states depends critically on the choice of the functional and solvent model.[296] The popular B3LYP function undermines the CT energy and the LE state was found to be higher in energy than the CT state. However, the use of long-range corrected CAM-B3LYP hybrid functional, which are usually recommended for excited states with charge transfer characteristics, leads to a dramatic switching of LE and CT energy ordering.[297] Now, the LE state has lower energy than the CT state, and thus, the suggested internal conversion pathway (LE to CT) may not be feasible here. Previously, Tian and his group performed TD-DFT calculation on C102-ethanol complex using B3LYP/6-311++G(d,p) with CPCM solvent model.[283] They also found that S_1 state is a locally excited state for the C102-ethanol complex.

Therefore, these studies influenced us to further investigate the C102-phenol system. In this chapter, we revisited the C102-phenol system to find an alternative mechanism of fluorescence quenching and to offer new insights on H-bond guided photophysics. We investigated whether proton-coupled electron transfer (PCET) can occur in this H-bonded complex which could be a probable fluorescence quenching pathway. A lot of studies are mentioned about the PCET in *chapter 1* (see *section 1.3.9*). Experimentally, it was found that the fluorescence quenching behaviour of the C102-phenol system is indeed dynamic in nature.[65] Thus, an excited state mechanism must be considered for the fluorescence quenching event.

4.2. RESULTS AND DISCUSSION

4.2.1. Potential Energy Surface of the H-bonded Complex:

The optimized ground state structure of the C102-phenol complex computed using CAM-B3LYP/6-311++G** including cyclohexane (IEFPCM) solvent was presented in the **Figure 4.1**. To describe the H-bonding parameters, a labelling scheme was shown in the **Figure 4.1**. The optimized H-bond distance is 1.744 Å in the electronic ground state of the C102-phenol complex.

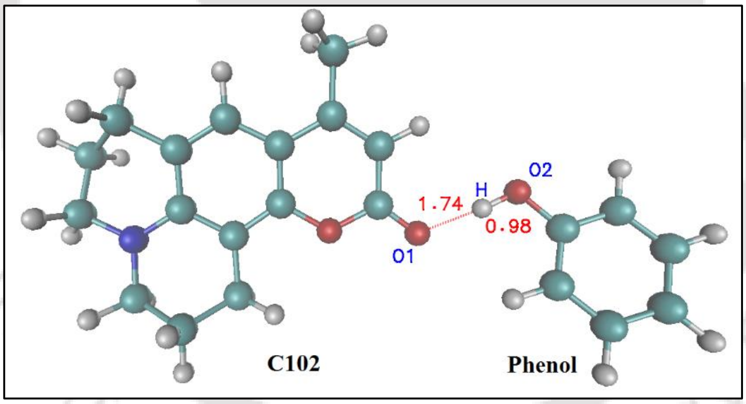

Figure 4.1. The energy minimized ground state structure of the C102-phenol complex computed using CAM-B3LYP/6-311++G** and IEFPCM solvent (cyclohexane) model. The atoms involved in the H-bonding are labelled for representing the potential energy surface along the H-bond coordinate.

In pursuit of new low energy structures, the potential energy surfaces (PES) of the electronic states were calculated along the H-bond coordinate. The complete H-bond coordinate ((C102)O^1•••HO^2(phenol)), which involves the transfer of H atom from the phenol –OH group to the O atom (O^1) of C102, was scanned. The distance between the H and O^1 was varied from 1.894 Å to 0.894 Å with an interval of 0.05 Å in both the S_0 and

S_1 states. During the scan, only the O^1•••H distance was fixed at different preset values, while all other coordinates of the complex were optimized (**Figure 4.2**). In this relaxed scan, the solvent model (cyclohexane, IEFPCM) was also included. Previously it was found that inclusion of the solvent model makes the S_1 state bright (contrary to the S_2 state in the gas phase), and this could be accessed by direct excitation.[296] Hence, our attention is only on the S_1 and S_0 states for consideration of H-bond dynamics. Zhao and Han had already applied a relaxed scan for the H-bonded C102-phenol complex using GGA functional BP86, but was restricted to a shorter range and also in the gas phase. In fact, we checked that such functional fails to calculate structures properly beyond a certain scan range.

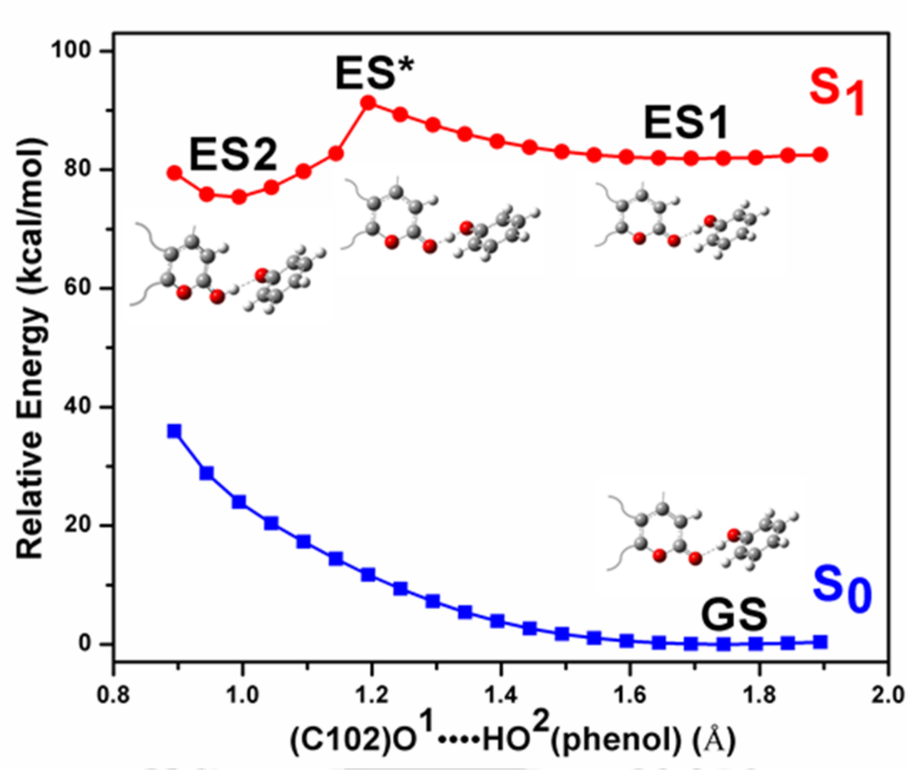

Figure 4.2. Potential energy surfaces of the C102-phenol complex in cyclohexane solution as a function of the H-atom transfer coordinate ((C102)O^1•••HO^2(phenol)) using CAM-B3LYP/6-311++G**(IEFPCM, cyclohexane). GS, ES1, ES2 and ES* respectively denote ground state minimum, two minima and barrier maximum in the first excited state.

In the relaxed potential energy surface (PES) for ground state (S_0), the energy of the complex continuously increases upon both shortening and lengthening of the distance between the H (initially belongs to phenol) and the O^1 (of C102) atoms. Note that a very close O^1•••H approach actually corresponds to the abstraction of H atom from phenol to C102 moiety but is energetically disfavoured in the ground state (**Figure 4.2**).

Interestingly, a very unique behaviour of the S_1 state PES was observed. Two different excited state structures were found corresponding to two minima- one at higher energy (local minimum, ES1) and other at lower energy (global minimum, ES2). The ES1 structure is very similar to that of the GS complex, but with a significantly shorter H-bond distance (1.694 Å) supporting the excited state H-bond strengthening phenomena of Zhao and Han.[20] However, in the ES2, H atom is bonded to C102 rather than to phenol and thus, corresponds to complete H atom transfer. The two minima are separated by a potential energy barrier. For the CAM-B3LYP computed PES, an intermediate structure (ES*) was found at 1.194 Å with corresponds to a maximum in the PES. Moreover, the electronic excitation of the H-bonded complex to S_1 state may progressively modify the bond and angle parameters of the complex (**Table 4.1**). The C102 protonated form ES2 of the C102-phenol complex lays 6.48 kcal mol^{-1} below the energy of the normal ES1 form. The potential energy barrier between ES1 and ES* is 9.38 kcal mol^{-1}. This amount of energy barrier may be accessible by the excited complex. However, for PBE0 functional this potential energy barrier for S_1 state reduces to a very lower value of 0.48 kcal mol$^{-1,}$ and for M06-2X functional, the energy barrier between ES1 and ES* is found to 8.16 kcal mol^{-1} (**Figure 4.3**).

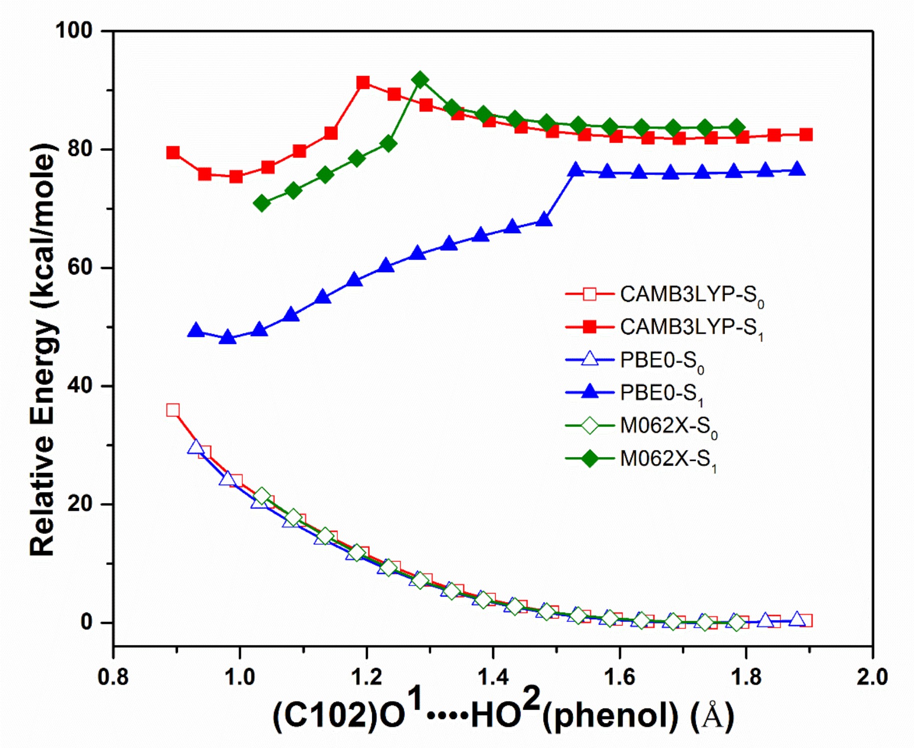

Figure 4.3. Potential energy surfaces of the C102-phenol complex in cyclohexane solution as a function of the H-atom transfer coordinate ((C102)O^1•••HO^2(phenol)) using CAM-

B3LYP/6-311++G(d,p), PBE0/6-311++G(d,p) and M06-2X/6-31G(d,p) including cyclohexane solvent (IEFPCM) in the ground state as well as excited state.

Table 4.1. Variation of the distance and angle parameters of the excited state complex during the scan along the O^1•••H distance (CAM-B3LYP functional is used with basis set 6-311G ++ (d,p) in cyclohexane).

O^1H (Å)	O^2H (Å)	O^1O^2 (Å)	C-O^1 (Å)	C-O^2 (Å)	∠O^1HO^2 (°)
1.844	0.977	2.821	1.221	1.353	178.65
1.794	0.979	2.774	1.233	1.352	179.57
1.744	0.983	2.726	1.233	1.351	179.28
1.694	0.986	2.680	1.235	1.350	178.59
1.644	0.990	2.635	1.236	1.348	178.16
1.594	0.996	2.590	1.237	1.347	177.84
1.544	1.003	2.547	1.238	1.345	177.57
1.494	1.011	2.505	1.240	1.344	177.31
1.444	1.021	2.465	1.242	1.342	177.08
1.394	1.035	2.428	1.244	1.339	176.82
1.344	1.052	2.395	1.246	1.336	176.39
1.294	1.073	2.366	1.249	1.333	176.21
1.244	1.101	2.344	1.253	1.330	175.89
1.194	1.137	2.330	1.258	1.326	175.70
1.144	1.393	2.532	1.319	1.261	172.72
1.094	1.504	2.591	1.326	1.257	170.89
1.044	1.621	2.652	1.332	1.255	168.27
0.994	1.732	2.702	1.336	1.253	164.25
0.944	1.841	2.745	1.339	1.252	159.34
0.894	1.924	2.768	1.341	1.251	156.75

To further check the correctness of the observation, the structures corresponding to each minimum in the excited state were fully optimized. All the bonds (even the HO^1) were allowed to be optimized. The minimization was confirmed by the absence of imaginary frequency. All the optimized structures are shown in **Figure 4.4**.

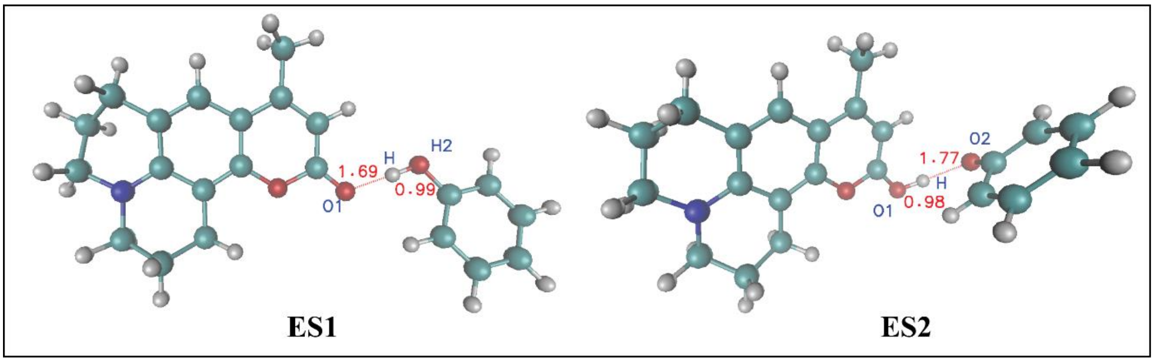

Figure 4.4. Optimized structures of two excited state minima (ES1 and ES2) calculated using CAM-B3LYP functional with 6-311++G(d,p) basis set.

4.2.2. Calculations of Electronic Charges and Dipole Moment Across Potential Energy Surface:

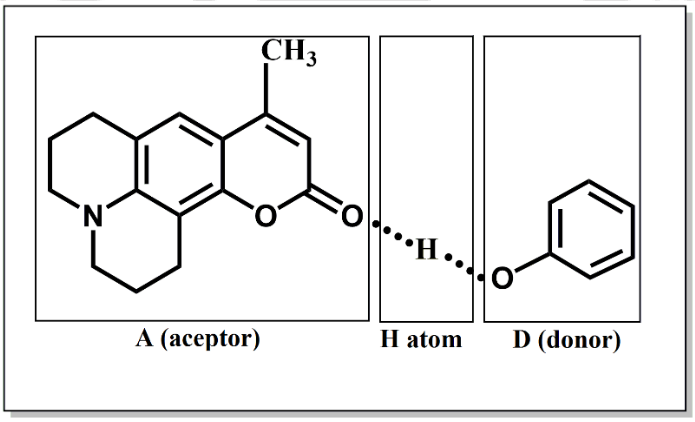

Scheme 4.1. Schematic representation of the grouping of the C102-phenol complex into different parts (A, H and D).

What is the actual nature of the H-atom transfer process in the excited state? Is it a proton transfer (PT) or a proton-coupled electron transfer (PCET)? Kaila and co-workers utilized electrostatic potential (ESP) charge calculation to explain excited state PCET process in a nice way for H-bonded p-nitrophenyl-phenol/t-butylamine complex.[213] Similarly, Lee and co-workers also showed a variation of Mulliken charges of the donor phenol along the H-bond coordinate in the ground state as well as in the excited state.[298] Therefore, the ESP charges over individual atoms on all the structures across the potential energy surface were calculated. For convenience, the charges were grouped over three units A-H-D representing the complex as A(O^1)....H....(O^2)D (**scheme 4.1**).

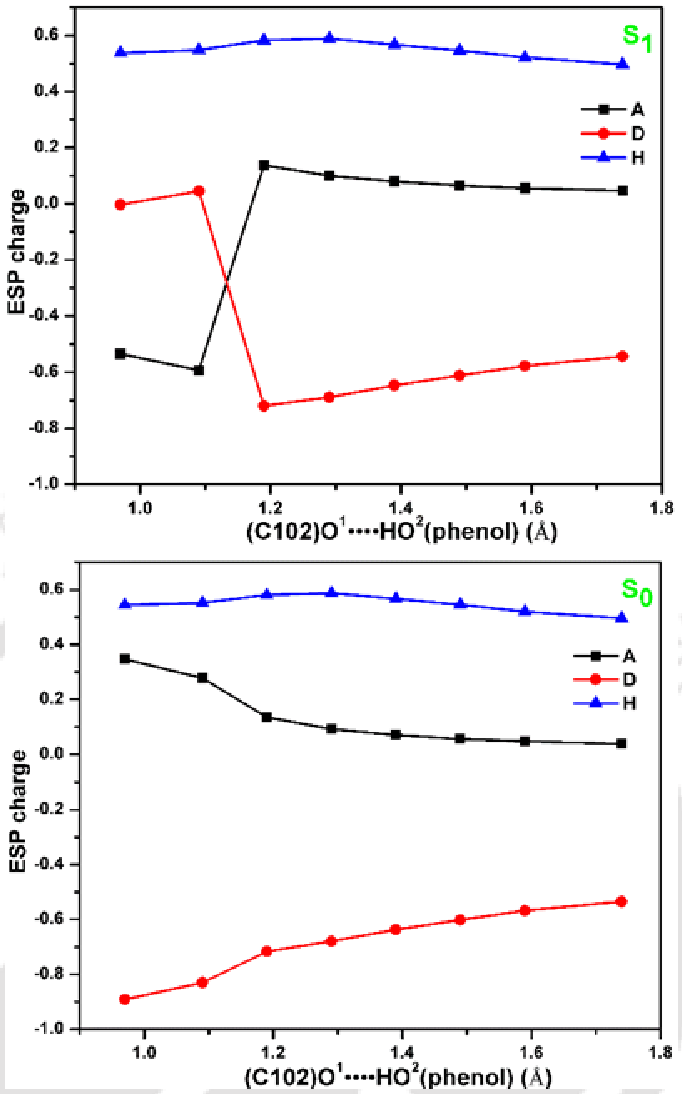

Figure 4.5. The ESP charge variation during the potential energy scan obtained by CAM-B3LYP/6-311++G(d,p). The charges are grouped into three segments A-H-D.

The positive charge of the H atom varies moderately over the PES; first grows up from + 0.496 to + 0.589 as the O^1•••H distance decreases from 1.74 Å to 1.29 Å but upon further shortening of the distance the magnitude of the charge diminishes (**Figure 4.5**). The ESP charges of the H at the two minima (ES1 and ES2) are very similar. Upon scanning the O^1•••H distance, we found very different variation of the charges of D (phenol unit without H) and A (C102) units in the ground and in the excited state. In both the ground and in the excited state, the overall charge of the D becomes progressively negative as the O^1•••H distance decreases (up to 1.19 Å) with concomitant accumulation of positive charge over the A. In the ground state, the charges continue to grow upon further shortening of O^1•••H distance (**Figure 4.5**). This implies that at the very short O^1•••H distance, C102 becomes protonated (charge ~ +1), and the phenol becomes deprotonated

(~ -1). Thus, in the ground state the process should be perceived as proton transfer, but this is energetically highly unfavourable. However, in the excited state, strong exchange of electronic charge between the D and A units occurs at O^1•••H distance of 1.19Å. Thus, the proton transfer is definitely associated with electron transfer, rendering the overall process as proton-coupled electron transfer or PCET.

Furthermore, the variation of the dipole moment of the C102-phenol complex in the S_0 and S_1 PES were also calculated (**Figure 4.6**). The dipole moment of the ground state increases steadily as the H atom is moved towards the acceptor oxygen (O^1) of C102. The continuous increase of the dipole-moment may be due to the charge separation as the proton is being transferred from the phenol to coumarin.

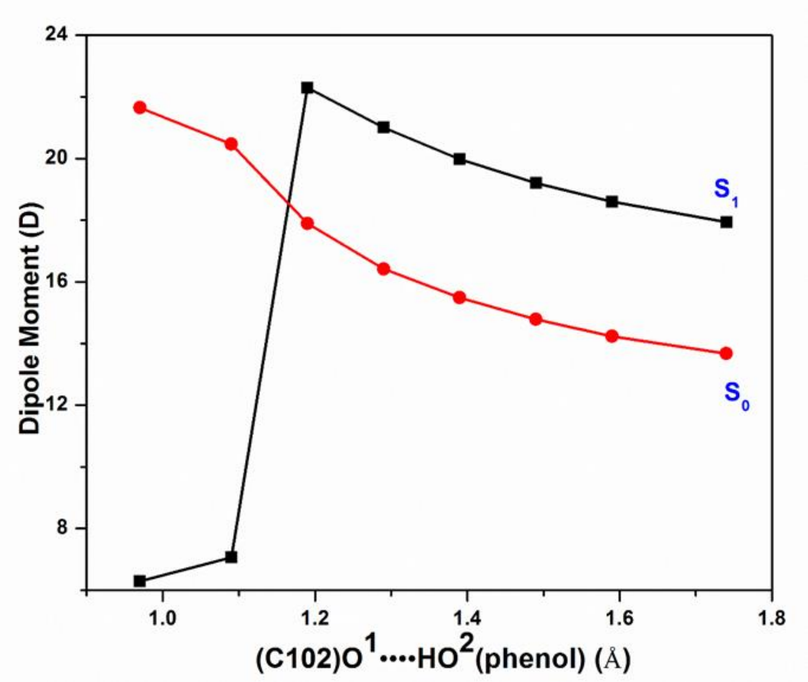

Figure 4.6. The variation of dipole moment of the C102-phenol complex during the potential energy scan obtained using CAM-B3LYP/6-311++G(d,p) in a dielectric continuum that mimics cyclohexane.

However, for S_1 state, the picture is totally different. The dipole moment first increases from 17.94 D (proton attached to phenol), then reaches a maximum value of 22.30 D (ES*) and thereafter decreases to 6.29 D at protonated C102-phenol complex (ES2). Earlier, we showed that at the transition state (ES*), where the proton is transferring from phenol to coumarin molecule, an electronic charge is also transferred between them. This charge transfer neutralizes the positively charged protonated C102 and negatively charged deprotonated phenol units in the excited state. The neutral character of the complex may be reflected as low dipole-moment at the ES2 configuration. This supports our conclusion that ES2 is a PCET state in the excited state.

4.2.3. PCET Rate Constant:

Once we established PCET as the possible mechanism for the C102-phenol system in the excited state, the PCET rate can be estimated using the obtained transition energy barrier for the process and applying transition state theory. To estimate the theoretical lifetime of the ESPT process of the C102-phenol complex in cyclohexane solution, the rate constant (k) is calculated using the transition state theory.

$$k = \frac{k_B T}{h} \exp\left(\frac{-\Delta E}{RT}\right) \tag{4.1}$$

Where, k_B is the Boltzmann constant, h is the Planck constant, R is the universal gas constant, ΔE is the activation free-energy and T is the temperature. All the experiments are performed at a temperature of 300 K. For calculations also we use a temperature of 300 K. We assume the energy difference between the energy of transition state ES* and the energy of local minima ES1 as ΔE. The calculated rate constant (k) are presented below (**Table 4.2**).

Table 4.2. Calculated values of the potential energy barrier, rate constant using different functionals.

Calculation level	**ΔE (kcal mol^{-1})**	**Rate constant (S^{-1})**
CAM-B3LYP/6-311++G(d,p)	9.38	8.33×10^{5}
M06-2X/6-31G(d,p)	8.16	6.51×10^{6}
PBE0/6-311++G(d,p)	0.48	2.73×10^{12}

It was observed that the barriers heights are quite different at different level of calculations, and consequently a significant variation is noticed on the predicted rate constant. Experimentally we observed a 400-600 ps component in the fluorescence transient for the quenching process.[65] Thus, the calculations either underestimate (CAM-B3LYP and M06-2X) or overestimate (PBE0 functional) the decay rates. Thus, more accurate excited state calculation may be needed for better agreement with the experimental results.

4.2.4. Electronic Relaxation and Fluorescence Quenching in the Excited Complex:

Figure 4.2 shows the minimum energy pathway for the excited state proton transfer from the phenol -OH group to the O atom of the carbonyl group of the coumarin. For a detailed discussion of the electronic excitation and relaxation, the transition nature of the excited states (LE, CT) are presented along the H-bond coordinate in **Figure 4.7**.

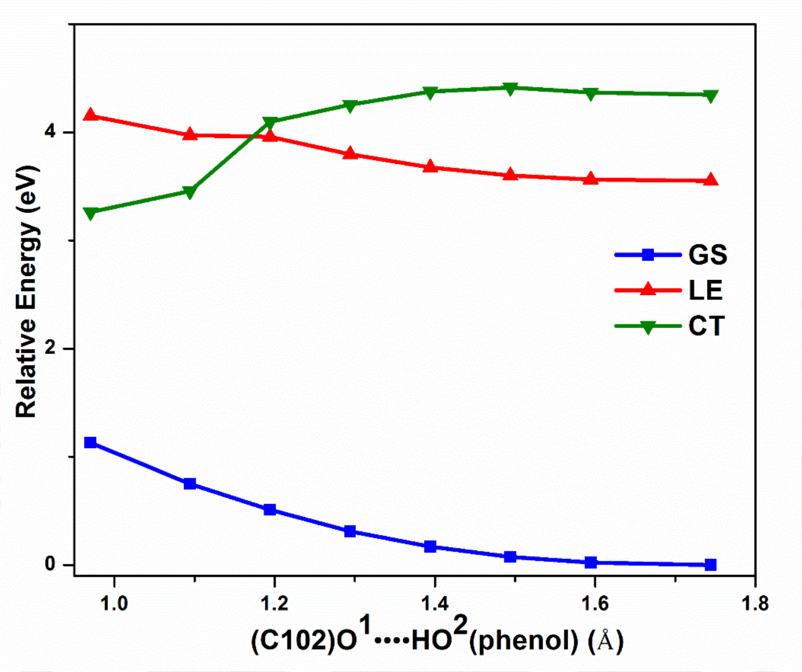

Figure 4.7. Potential energy states (GS, LE, CT) as a function of the H-bonding coordinate (C=O^1•••H–O^2, in Å) of C102-Phenol complex. CAM-B3LYP functional is used with basis set 6-311G++(d,p) in a dielectric continuum that mimics cyclohexane.

It is interesting to note that the PES of LE and CT states approaches each other, and there is a switching of the energy order at a certain O^1•••H distance (1.194Å). This point also corresponds to the maximum in the S_1 PES, and this point is defined as a transition state (ES*) for the electronic relaxation. For better understanding, the nature of the states and its effect on fluorescence quenching, oscillator strengths (*f*) of the LE and CT states with respect to H-bond coordinate of the C102-phenol complex are listed out (**Table 4.3**). Electronic excitation energies of the low-lying excited states are calculated from the optimized excited state H-bonded complex and presented in the *appendix* **Table A.4.1.**

LE and CT states denote mainly the bright (high oscillator strength) and dark (very low oscillator strength) states, respectively. Later the LE and CT nature of these states were confirm by orbital analysis. If we excited the H-bonded complex from its optimized ground state, it can directly excite the complex to the S_1 state. At this point, the S_1 is a locally excited (LE, *f* = 0.697) state, whereas S_2 is a charge transfer (CT, *f* = 0.002) state. After excitation, the complex may move to shorter O^1•••H distance to reach the ES1 state. At this point also LE state (*f* = 0.698) is lower in energy than CT (*f* = 0.002). As the proton is transferred towards the C102 moiety, the oscillator strength gradually decreases up to the TS (ES*). When the proton crossed the transition state (ES*) barrier then the oscillator strength goes down and tends to a very low value. Subsequently, a very low value of '*f*' (0.0037) was observed for the lowest energy excited state (S_1) at a O^1•••H distance of 1.094 Å. However, for the next higher energy excited state (S_2), *f* is quite high value (0.5775) at the same O^1•••H distance. This abrupt interchange of the oscillator strength strongly indicates the switching of energies of the LE and CT states at the transition state (ES*). That means that the CT state becomes lower in energy than LE state at ES2.

Table 4.3. Excited state oscillator strength (*f*) values with respect to distance throughout the S_1 potential energy surface curve. We applied CAM-B3LYP functional with basis set 6-311G++(d,p) in cyclohexane (IEFPCM) solvent.

Distance (Å)	**Oscillator strength (at S_1 state)**	**Oscillator strength (at S_2 state)**
1.74	0.697	0.002
1.59	0.698	0.002
1.49	0.698	0.003
1.39	0.697	0.001
1.29	0.693	0.001
1.19	0.680	0.003
1.09	0.004	0.578
0.97	0.001	0.082

4.2.5. Molecular Orbital Analysis of the Excited State Complex:

Frontier molecular orbital analysis was also performed on both ES1 and ES2 configurations. From **Figure 4.8**, it is evident that at the ES1 structure, the lowest energy HOMO→LUMO transition is LE type where electron density is mostly localized over the π orbitals of C102 only. However, in the ES2 minima, the HOMO→LUMO transition involves charge transfer (CT) from deprotonated phenol to protonated C102 moiety. All the involved molecular orbitals (LUMO, HOMO, HOMO-1 and HOMO-2) of the ES1 and ES2 are presented in the **Figure 4.8**.

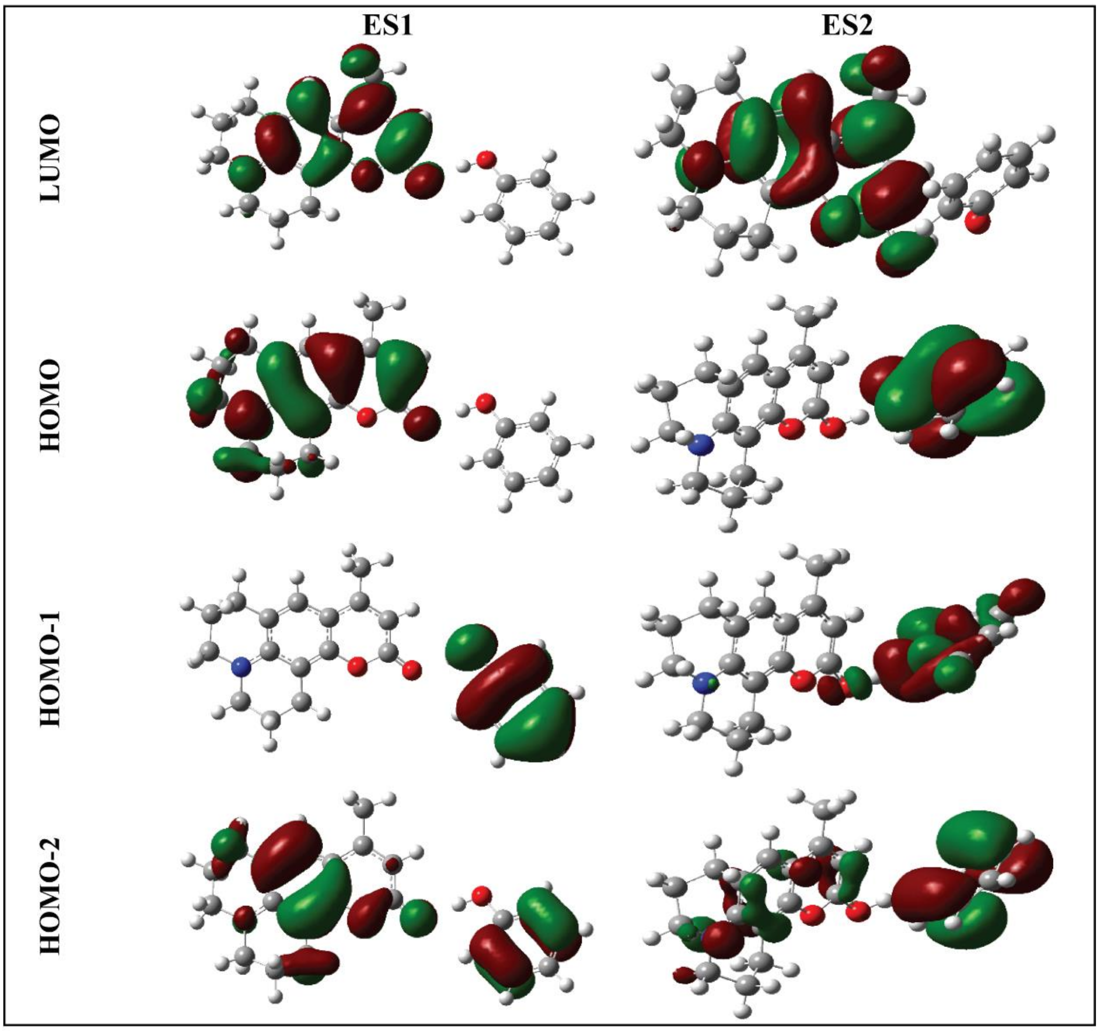

Figure 4.8. Frontier molecular orbitals of C102-phenol complex of the ES1 and ES2 configurations in the excited state (S_1). CAM-B3LYP functional was used in combination with the basis set 6-311G++(d,p) in a dielectric continuum that mimics cyclohexane.

4.3. SUMMARY AND CONCLUSION

In this chapter, we have found a new H-bond assisted fluorescence quenching pathway for the C102-phenol H-bonded complex via PCET. From a relaxed potential energy scan, it was found that in the excited state not only the H-bonded strengthened stable minimum (ES1) is favoured, but the further shortening of the O^1•••H distance may result in another stable minimum (ES2) where the H atom is completely transferred from phenol to coumarin. Through ESP charge and dipole moment calculations, we established that at a certain O^1•••H distance, both a proton and an electron were transferred together from phenol to coumarin in the excited state. At this point, the lowest excited state also changes its character from LE to CT-type after passing a potential energy barrier. Thus, the ground state complex is first excited to the LE state and thereafter, H-bond strengthening occurs to reach the first minima and finally, the complex reaches to the second minima. Once the complex crosses the maximum, the nature of the lowest excited state alters to a CT state, and hence fluorescence can be quenched.

Chapter-5

Proton-Coupled Electron Transfer Vs. Photoinduced Electron Transfer in Methylbipyridine/Phenol Complexes[#]

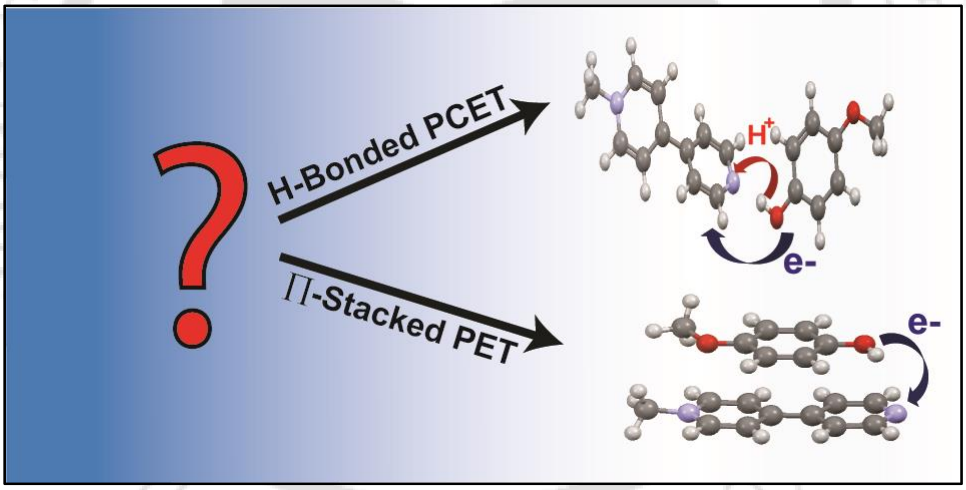

[#]This work has been published in *J. Phys. Chem. A* **2019,** *123* (38), 8122-8129.

Chapter 5: Proton-Coupled Electron Transfer Vs. Photoinduced Electron Transfer in Methylbipyridine/Phenol Complexes

5.1. INTRODUCTION

The importance of proton-coupled electron transfer (PCET) is substantially realized in many biophysical and catalytic processes.[183, 219, 299-301] In the past few years, a lot of PCET systems investigated experimentally and theoretically as discussed in *chapter 1* (see *section 1.3*). Concerted electron and proton transfer are essential to avoid high energy intermediates.[200, 217, 302-306] However, the signatures of the PCET process are not too different from the conventional charge transfer (CT) or electron transfer (ET).[205] The similarity of features between PCET and ET often creates confusion to track down the actual nature of the process. One such system is the complex between *N*-methyl-4, 4′-bipyridinium cation (MQ^+) and phenol.[201, 203] Gagliardi et al. performed steady-state and ultrafast transient absorption measurements on the complex of *N*-methyl-4, 4′-bipyridinium cation (MQ^+) with different phenols- tyrosine, 4-methyl phenol, and 4-methoxy phenol.[201] They used equimolar *N*-methyl-4,4 -bipyridinium and 4-methyl phenol in the concentration range of 5 to 50 mM, in 50 mM tris buffer at pH 8.5. They observed a weak red-shifted absorption band at 375 nm, which was attributed to the H-bonded complex between MQ^+ and phenol. Upon excitation at this new band, they observed transient absorption bands at 360 nm, 440 nm, and 560 nm. The transient bands were designated to the absorption of radical ions, which were proposed to occur via hydrogen bond (H-bond) aided PCET. MQ^+ accepts both proton and an electron from the phenol moiety (**Scheme 1.15a**).[201] However, performing a similar set of experiments at two different pHs (2 and 8.5), Tyburski et al. attributed the process as conventional charge transfer between the MQ^+/methoxyphenol system in the excited state rather than PCET. They also suggested that the charge transfer may be mediated by donor-acceptor interaction.[203]

In the previous *chapter 4*, we have demonstrated the hydrogen-bond guided fluorescence quenching mechanism of the C102-phenol complex via PCET. Here, in this chapter, density functional theory (DFT) and time-dependent density functional theory (TD-DFT) were implemented on the MQ^+/phenol system to reveal the nature of the excited state process, PCET or PET, and also to elucidate the nature of donor-acceptor interaction. Both protonated (HMQ^{2+}) and deprotonated (MQ^+) forms of MQ^+ were considered. The nature of interaction and excited-state properties of their complexes with 4-methoxyphenol were compared.

5.2. RESULTS AND DISCUSSION

5.2.1. Design Principles and Geometric Configurations:

Hammarstrom and co-workers investigated MQ^+/methoxyphenol complex at two different pH in a water medium.[203] Since the pK_a of HMQ^{2+} is 3.5 (**Scheme 1.15b**), they chose pH at 2 and 8.5, respectively, to deliberately select the protonated (HMQ^{2+}) and deprotonated (MQ^+) forms. At higher pH (8.5), N-atom of the pyridyl group will remain deprotonated, and there is a definite scope for the phenolic proton of 4-methoxyphenol to form H-bond with it. However, at pH = 2, the N atom of the pyridyl group of the MQ^+ will be protonated to form HMQ^{2+}. Therefore, the chance to form H-bond between N atom of the HMQ^{2+} and –OH of methoxyphenol is restricted. However, there is a possibility of H-bonding between O atom of the phenolic hydroxyl and the H atom of HMQ^{2+}.

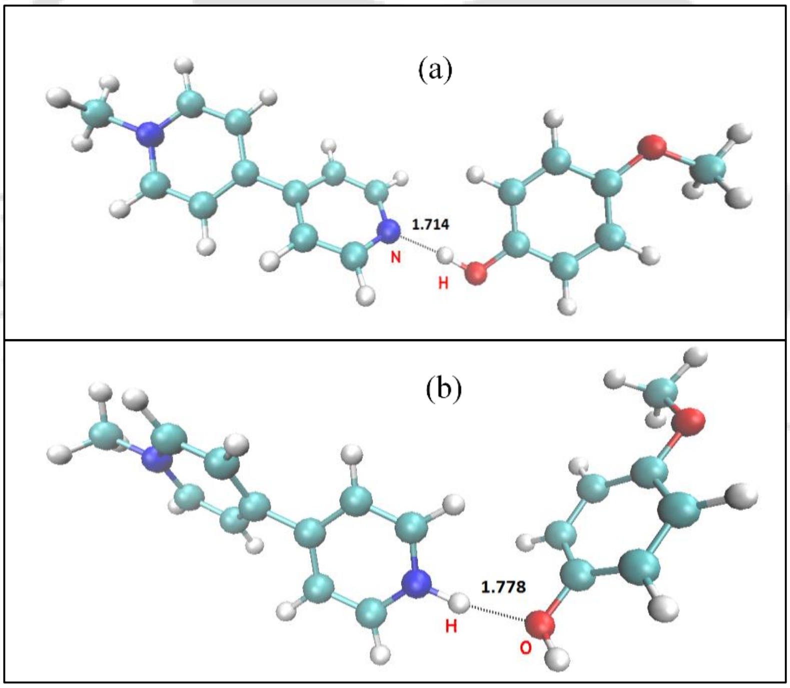

Figure 5.1. The optimized ground-state structures of the H-bonded (a) MQ^+/methoxyphenol and (b) HMQ^{2+}/methoxyphenol complexes computed using CAM-B3LYP-D3/6-311++G**/SMD (a dielectric continuum that mimics water).

In the present study, both forms of MQ^+ - deprotonated (MQ^+) and protonated (HMQ^{2+}) were considered as a representative at two different pH values. Recently, Pino and coworkers observed that H-bonded and π-stacked isomers are almost isoenergic for p-aminophenol - p-cresol complex in the ground state.[307] Similarly, both hydrogen bonding and π-stacking interaction between MQ^+ and 4-methoxyphenol were considered. The optimized ground state structure of the H-bonded complexes of MQ^+/methoxyphenol and HMQ^{2+}/methoxyphenol are presented in **Figure 5.1**. CAM-B3LYP-D3/6-311++G** including water (SMD) solvent were used for the computation. The optimized H-bond distance (N…H) is 1.714 Å, and the angle (∠N…H—O) between the participating atoms is 173.2° in the electronic ground state of the MQ^+/methoxyphenol complex (**Figure 5.1a**). In the case of HMQ^{2+}/methoxyphenol complex (**Figure 5.1b**), the N-atom of HMQ^{2+} is already protonated. Hence, there is no chance to form an H-bond between phenolic proton and N-atom of HMQ^{2+} in the ground state. However, an H-bonding of interaction (O…H-N^+) is present between the proton attached to the pyridine N of HMQ^{2+} and the oxygen of the hydroxyl group of 4-methoxyphenol. The optimized H-bond distance (O…H) is 1.778 Å, and the angle (∠N—H…O) between the participating atoms is 169.3° in the electronic ground state of the HMQ^{2+}/methoxyphenol complex (**Figure 5.1b**).

5.2.2. Possibility of PCET in the H-bonded MQ^+-Methoxyphenol Complex:

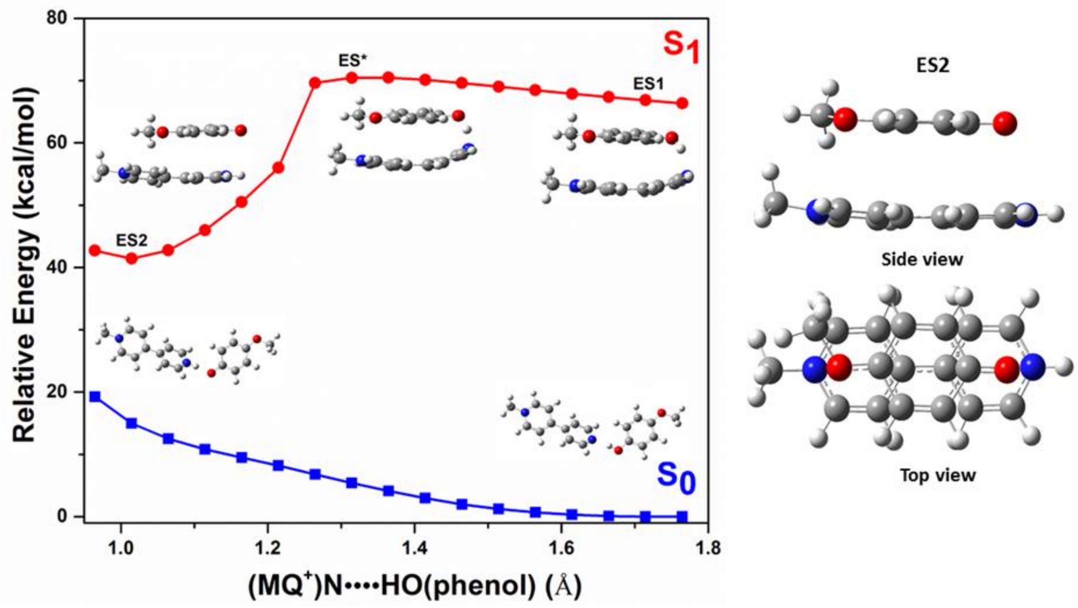

Figure 5.2. Potential energy surfaces of the MQ^+/methoxyphenol complex in a dielectric continuum that mimics water as a function of the H-atom transfer coordinate ((MQ^+)N…HO(phenol)) using CAM-B3LYP-D3/6-311++G** (water, SMD) in the ground state and the excited state, respectively. The optimized structure of the excited state minima (ES2) of MQ^+/methoxyphenol complex has been shown ("side" and "top" views) on the right side.

Taking the optimized H-bonded complex between MQ^+ and methoxyphenol (**Figure 5.1a**) as initial structure, a relaxed potential energy scan was performed by varying the distance between the N at 4-position of MQ^+ and the H of the hydroxyl group of 4-methoxyphenol. In the optimized ground state structure, this distance was 1.714 Å (**Figure 5.1a**). The complete H-bond coordinate ((MQ^+)N…HO(phenol)), which involves a transfer of H-atom from the —OH group of methoxyphenol to the N atom of MQ^+, was scanned (**Figure 5.2**). The distance between the H and N was varied from 1.764 Å to 0.964 Å with an interval of 0.05 Å in both the S_0 and S_1 states. The N…H distance was only fixed at different preset values during the scan leaving all other parameters free.

In the ground state, the energy of the MQ^+/methoxyphenol complex continuously increases upon shortening the distance between the H (initially belongs to phenol) and the N (of MQ^+) atoms. Thus, in the potential energy surface (PES), a very high energy structure is generated when the H atom is fully transferred to the N atom (of MQ^+) in comparison to the starting structure (where the H atom belongs to 4-methoxyphenol). This implies an unfavorable proton transfer in the ground state. Interestingly, a unique behavior of the PES was observed in the excited state (S_1); an unusual stacking between the aromatic rings of the methoxyphenol and MQ^+ was observed in addition to the H-bonding interaction. Thus, the starting structure of the excited complex (ES1) was very different in appearance compared to the ground state starting structure (**Figure 5.2**). In the PES scan, the energy of the S_1 complex first increases upon the shortening of the H-bond coordinate up to a particular N…H distance. The intermediate excited state structure (ES*), which corresponds to a maximum on the PES of the S_1 state has a N…H separation of 1.364 Å. In this structure, the H atom is almost equally shared between the N of MQ^+ and O of 4-methoxyphenol (N...H distance is 1.364 Å whereas O…H distance is 1.15 Å). The potential energy barrier between the ES* structure and the initially excited state structure (ES1) is 4.11 kcal mol^{-1}. With further lowering of the N…H distance, energy of the complex decreases, and PES reaches to a lower energy minimum structure (ES2), which corresponds to a complete proton transfer from 4-methoxyphenol to the N atom of MQ^+. The ES2 structure is energetically more stable compared to the ES1 structure by 24.93 kcal mol^{-1}. This result indicates a moderately favorable exothermic H atom or proton transfer in the excited state (S_1) from methoxyphenol to MQ^+ with a small potential energy barrier. We also calculated and compared the relaxed PES, especially for S_1 state by using another functional M06-2X (**Figure 5.3**). Quite similar PES was observed for this M06-2X functional and nearly identical energy barrier of 4.43 kcal mol^{-1} between ES1 and ES*. Furthermore, some critical structural parameters of the complex (H-bond length and bond angle of the involved atoms), which vary during the scan, were listed out in **Table 5.1**.

Table 5.1. Variation of distance and angle parameters in the excited state complex during the scan along the N…H distance (CAM-B3LYP-D3 functional is used with basis set 6-311G ++ (d,p) in SMD (a dielectric continuum that mimics water) solvent model.

N…H (Å)	**O-H (Å)**	**N…O (Å)**	**C-O (Å)**	**∠N…H-O (°)**
1.764	1.003	2.653	1.323	145.47
1.714	1.010	2.623	1.323	147.53
1.664	1.018	2.594	1.322	149.48
1.614	1.028	2.564	1.322	151.19
1.564	1.041	2.535	1.321	152.72
1.514	1.057	2.508	1.319	154.02
1.464	1.079	2.483	1.316	154.83
1.414	1.108	2.464	1.313	155.14
1.364	1.149	2.454	1.309	154.83
1.314	1.217	2.463	1.302	153.33
1.264	1.357	2.524	1.292	148.68
1.214	3.341	3.565	1.259	90.55
1.164	3.337	3.570	1.259	91.88
1.114	3.334	3.574	1.259	93.23
1.064	3.340	3.578	1.259	94.15
1.014	3.348	3.585	1.259	95.15
0.964	3.359	3.595	1.259	96.29

To further check the correctness of the excited state H-atom transfer, the minimum energy structure (ES2) was optimized without any restriction using TD-DFT methods at the same level of calculation. The absence of imaginary frequency confirms the correctness of the minimization process. The excited state optimized ES2 structure of MQ^{+}/methoxyphenol is shown in **Figure 5.2**. The two molecular units are top of each other and also maintain a parallel arrangement.

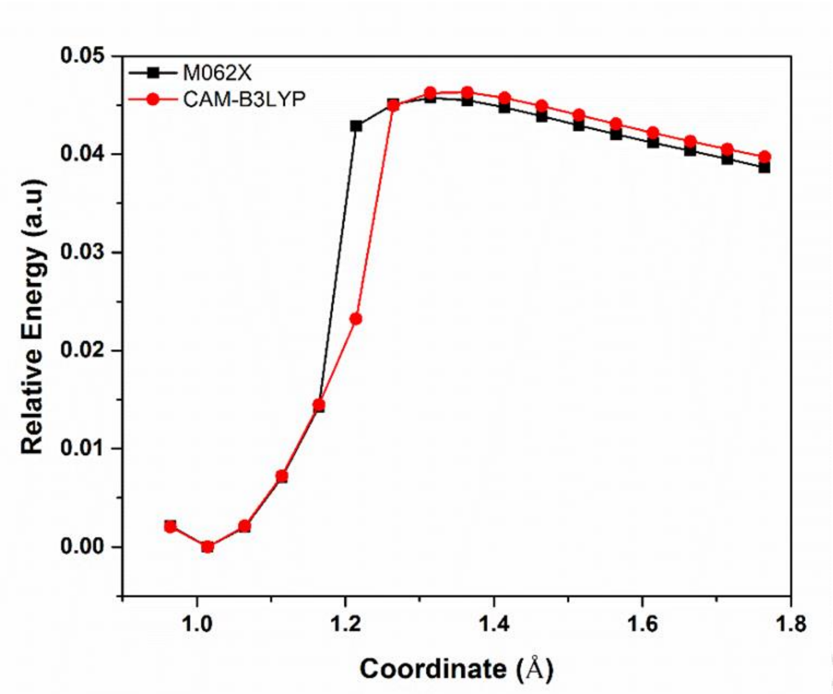

Figure 5.3. Computed relaxed PES as a function of the H-atom transfer coordinate (N…H-O, in Å) on non-adiabatic excited state (S_1) by using CAM-B3LYP-D3 and M06-2X functional with standard 6-31G(d,p) basis set in a dielectric continuum that mimics water (SMD model).

Does the H-atom transfer associate with simultaneous electron transfer? To answer this question, the variation of atomic charges during the transfer process were determined. ESP charge of each atom of the MQ^+/methoxyphenol complex was calculated across the potential energy surface for both the ground state and the excited state. For convenient representation, the calculated ESP charges were grouped into three units - donor (D), acceptor (A), and H-atom representing the complex as A(N)…H…D(O) (**Scheme 5.1**).

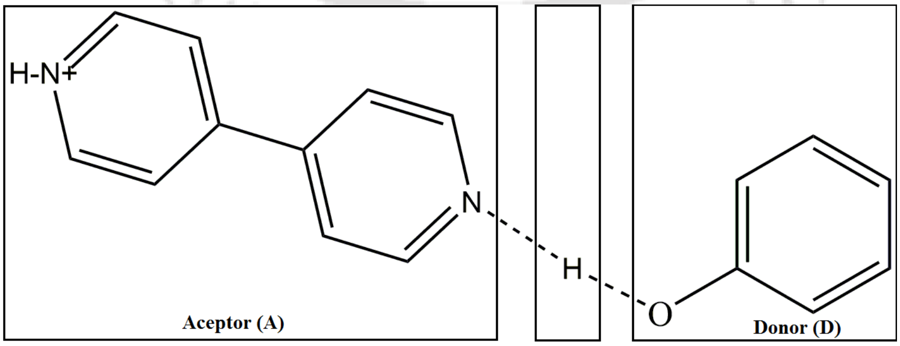

Scheme 5.1. Schematic representation of the grouping of the MQ^+/methoxyphenol Complex into Different Parts (A, H and D).

The ESP charge on the H-atom remains close to zero in the ground state as well as in the excited state in the PES scan. Upon scanning the N…H distance, a different type of variation of the ESP charges of D (phenol without H) and A (MQ^+) units were noticed in the ground and the excited state. In the ground state, the charges of the D and A fragments continue to grow upon shortening of the N…H distance (**Figure 5.4**). The results indicate that at the very short N…H distance, MQ^+ becomes protonated (i.e., the charge of HMQ^{2+} ~ +2) and methoxyphenol becomes deprotonated (charge ~ −1). Thus, in the ground state, the process should be considered as proton transfer, but obviously, it is energetically highly unfavorable. However, in the excited state, the scenario is quite different; an active exchange of electronic charge between the D and A units occurs at the N…H distance of 1.286 Å. Furthermore, it was observed that the amount of charge transfer from methoxyphenol to MQ^+ is 0.98e in the ES2 complex. Thus, the proton transfer is associated with electron transfer, and the overall process can be defined as proton-coupled electron transfer or PCET.

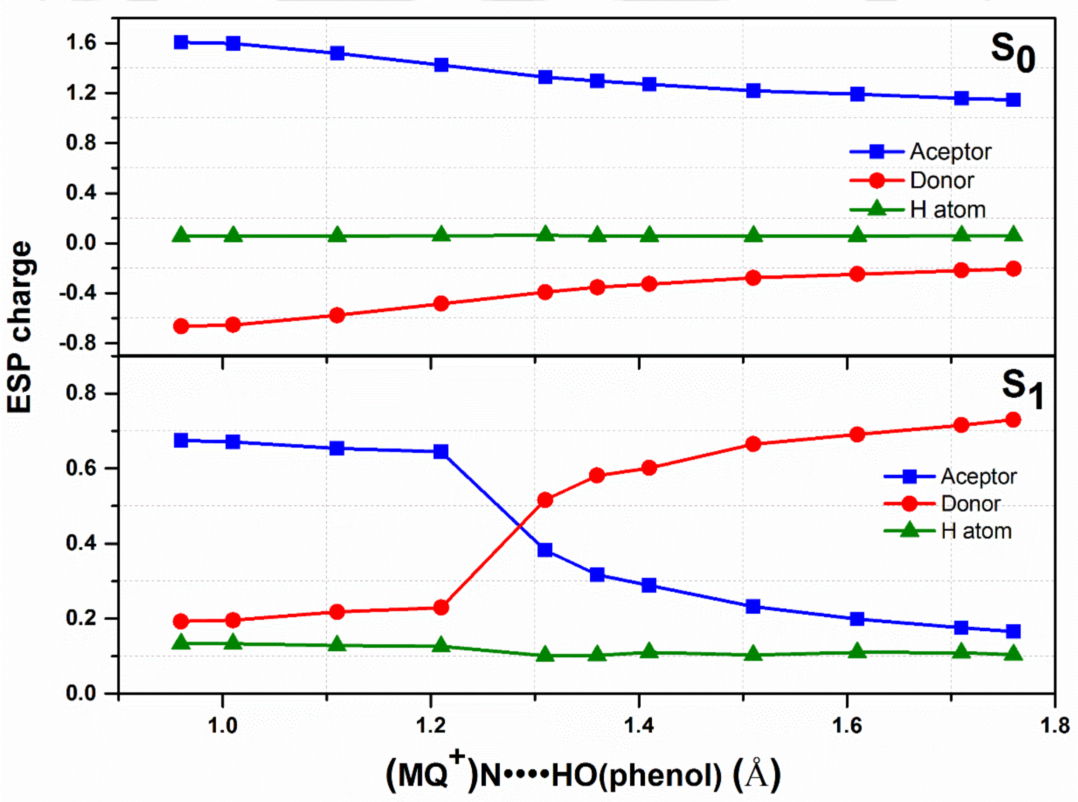

Figure 5.4. The ESP charge variation during the potential energy scan for the ground state (top panel) and excited state (bottom panel) was obtained by CAM-B3LYP-D3/6-311++G(d,p) in a dielectric continuum that mimics water (SMD). The charges are grouped into three segments A-H-D.

5.2.3. Photoinduced Electron Transfer in π-stacked HMQ^{2+}/Methoxyphenol Complex:

As the N atom of HMQ^{2+} is already protonated in the ground state, it can no longer accept a further proton from methoxyphenol and thus, there is no question of excited-state PCET process. To investigate the excited-state behavior of the complex, the structure of HMQ^{2+}/methoxyphenol has been fully optimized in the S_1 electronic state using the TD-DFT method. Interestingly, it was observed that the H-bonded configuration altered to a π-stacked configuration in the excited state for the HMQ^{2+}/methoxyphenol complex (**Figure 5.5**). This complex is similar in appearance to the π-stacked excited-state of MQ^{+}/methoxyphenol complex (ES2) observed as a result of PCET (**Figure 5.2**).

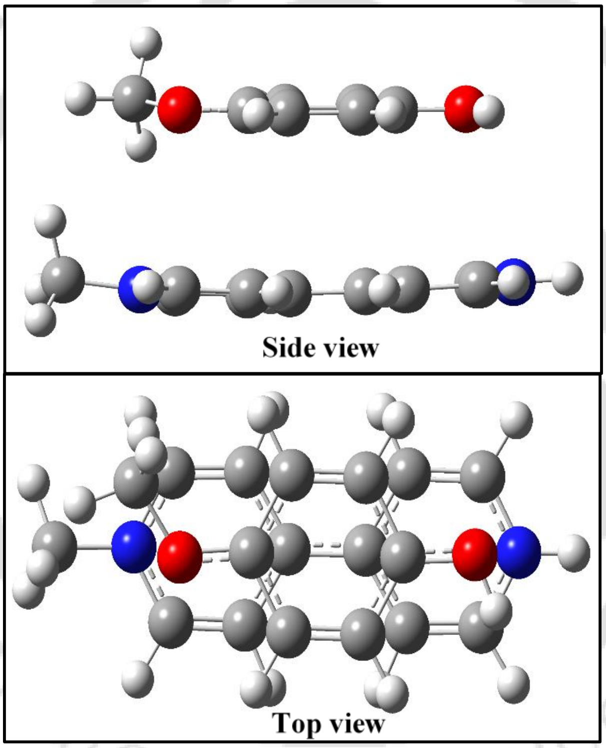

Figure 5.5. The excited state optimized structure of HMQ^{2+}/methoxyphenol complex has been shown in the side and top views by using CAM-B3LYP-D3 functional with 6-311++G(d,p) basis set in a dielectric continuum that mimics water (SMD solvent model).

To check the possibility of photoinduced electron transfer (PET) in the HMQ^{2+}/methoxyphenol complex, the ESP charges over individual atoms of the complex were determined in the H-bonded ground state and the π-stacked excited state, respectively. The amount of charge transfer from donor methoxyphenol to acceptor HMQ^{2+} were calculated in the ground state and the excited state, respectively. It was observed that the conventional charge transfer (PET) from methoxyphenol to HMQ^{2+} is only present in the excited state. The amount of charge transferred is 0.95e from methoxyphenol to HMQ^{2+} in the electronically excited state. However, only a negligible amount (0.06e) of electron transfer was noticed in the ground state. Hence, we can conclude that PET is the primary photophysical process for the HMQ^{2+}/methoxyphenol complex in the excited state.

5.2.4. π-stacking Parameter of the Complex:

Now **Figure 5.2** and **5.5** show that MQ^{+}/methoxyphenol (ES2) and HMQ^{2+}/methoxyphenol complexes form π-stacked dimer configuration in the excited state. Both MQ^{+} and HMQ^{2+} form perfectly face-to-face π-π stacking dimer with methoxyphenol complex in the electronically excited state (S_1). To describe the structure of the π-stacked complex, we calculated two important structural parameters – (i) inter-planar stacking distance, and (ii) the inter-planar angle between two π-stacked MQ^{+}/HMQ^{2+} and methoxyphenol molecules (**Table 5.2**). Two pyridine rings of MQ^{+} (or HMQ^{2+}) were labelled as 'A' and 'B' respectively; the ring which is attached to the methyl group is assumed as 'A' and the other one is 'B'. Similarly, the aromatic ring of methoxyphenol is mentioned as the 'C' ring (**Figure 5.6**).

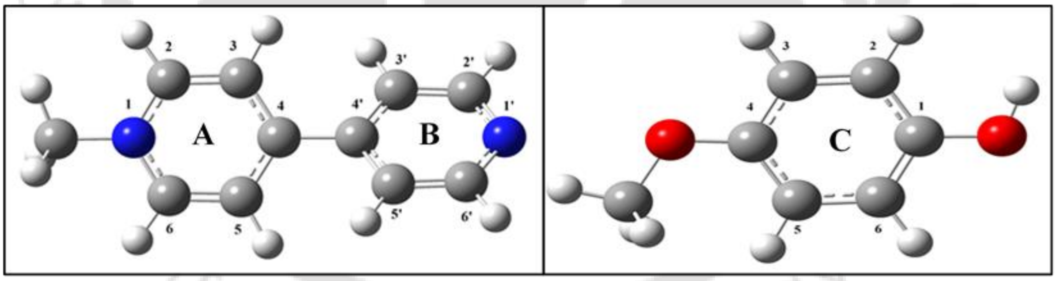

Figure 5.6. Assignment of rings for MQ^{+} and 4-methoxyphenol.

The inter-planar distance is calculated by considering the distance between the centroid of 'A+B' rings of MQ^{+}/HMQ^{2+} and centroid of 'C' ring (benzene ring) of methoxyphenol molecules (**Figure 5.7**). The calculated inter-planar distances are 3.16 Å and 3.13 Å, respectively for MQ^{+}/methoxyphenol and HMQ^{2+}/methoxyphenol complexes in the excited state. Similarly, the inter-planar angle is measured by considering the angle formed between the plane of 'A+B' rings of MQ^{+}/HMQ^{2+} and the plane of 'C' ring of methoxyphenol molecules (**Figure 5.7**). Since the π-stacked molecules are aligned nearly parallel to each other, the inter-planar angle is close to zero degrees. The measured inter-planar angles in the excited state are 2.3° and 2.8° for MQ^+/methoxyphenol and HMQ^{2+}/methoxyphenol complexes, respectively. Moreover, it was found that the angle between two pyridine rings ‘A’ and ‘B’ of MQ^+ and HMQ^{2+} molecule is reduced from ~35° of the H-bonded ground state to ~5° to 6° in the π-stacked excited state. Thus, in the π-stacked configuration of the complexes, both the pyridine rings of MQ^+/HMQ^{2+} almost reside in a common plane.

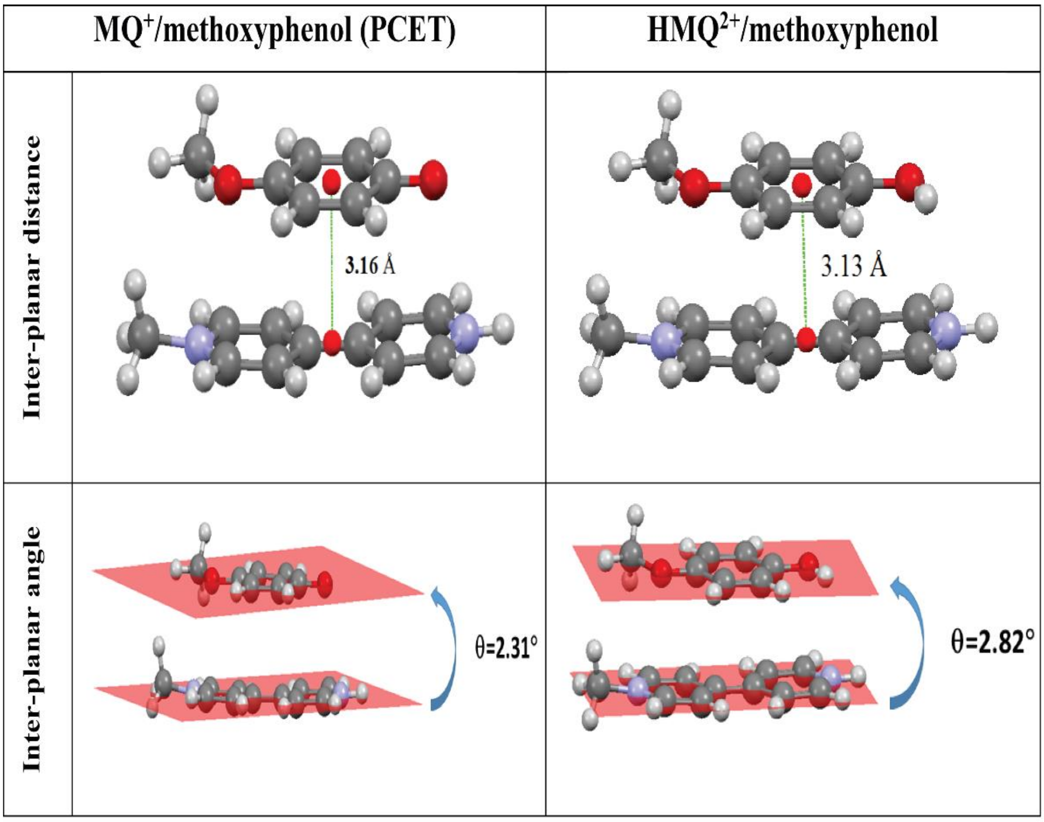

Figure 5.7. Representation of the inter-planar distance and angle of the excited state π-stacked structure of the MQ^+/methoxyphenol (ES2) and HMQ^{2+}/methoxyphenol complexes, respectively.

Furthermore, to confirm the π-stacking interaction between MQ^+/HMQ^{2+} and methoxyphenol in the S_1 state, the distribution of critical points (CP) were investigated using Atoms in Molecules (AIM) analysis by using the Multiwfn 3.6 program.[308] The wave functions used for the AIM analysis was calculated at the CAM-B3LYP/6-311++G(d,p)/water (SDM) level. The red, yellow, and green spheres represent positions of the bond critical points (BCPs), ring critical points (RCPs) and cage critical points (CCPs), respectively (**Figure 5.8**).

Table 5.2. Excited state optimized structural parameters (inter-planar angle and distance) of the π-stacked MQ^+/methoxyphenol (ES2) and HMQ^{2+}/methoxyphenol complexes. Calculations are done by using CAM-B3LYP-D3/6-311++G** with SMD (water) model.

Structural parameter	**MQ^+- 4-methoxyphenol**	**HMQ^{2+}- 4-methoxyphenol**
Distance between two centroids of two rings (A+B) and C (Å)	3.16	3.12
Angle between two planes of rings (A+B) and C (°)	2.31	2.82
Angle between two rings A and B of MQ^+ (°)	6.03	5.02

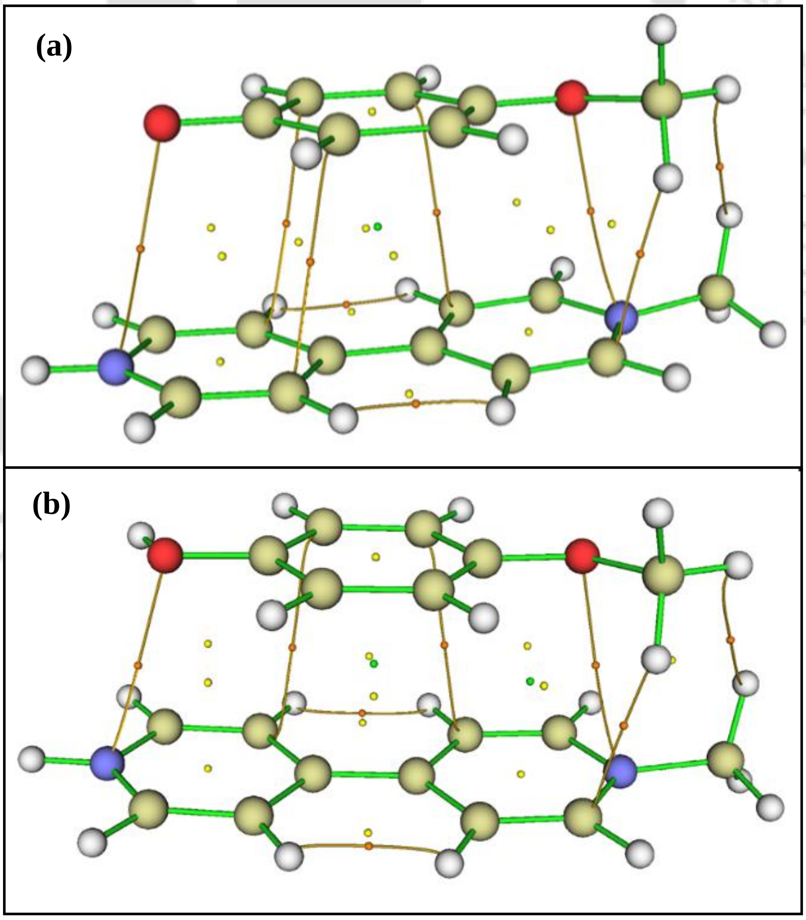

Figure 5.8. Distribution of bond, ring, and cage critical points (red, yellow and green spheres respectively) and bond paths for the excited state complexes of MQ^+/methoxyphenol (ES2) (a) and excited state HMQ^{2+}/methoxyphenol (b) complexes.

Seven and six intermolecular bond CPs (red spheres) and bond paths were observed for MQ^+/methoxyphenol and HMQ^{2+}/methoxyphenol complexes, respectively. Furthermore, π-stacking interaction was confirmed by the presence of several ring CPs (yellow spheres) and cage CPs (green spheres) in the complexes as it is common for π-stacking interaction. One and two cage critical points (CCP) were observed between the rings for MQ^+/methoxyphenol and HMQ^{2+}/methoxyphenol complexes, respectively. Interestingly, one C-H…π interaction has been characterized by one bond critical point and bond path along with the π…π interactions. The C-H…π interaction is present between the H-atom of the –OMe group of the methoxyphenol and one carbon atom of the aromatic pyridine ring 'A' of MQ^+/HMQ^{2+}. This C-H…π interaction is observed for both complexes.

5.2.5. Possibility of Formation of non-H-bonded π-stacked Complex in the Ground State:

Since π-stacked structure was already found for the excited state HMQ^{2+}/methoxyphenol complex, and also in the excited state of MQ^+/methoxyphenol complex after PCET, we are curious to know if a non-H-bonded ground state π-stacked is possible for MQ^+/methoxyphenol and HMQ^{2+}/methoxyphenol complexes. For this, a reasonable π-stacked type input structure was prepared for both the complexes and optimized them in the ground state at the same calculation level. Interestingly, stable π-stacked structures were found for both the complexes in the ground state (**Figure 5.9**). Thus, apart from H-bonding complexes, the π-stacked configuration may also be possible. Complexation energies were calculated for both the H-bonded and π-stacked configuration of MQ^+/methoxyphenol and HMQ^{2+}/methoxyphenol complexes in the ground state (**Table 5.3**). Surprisingly, it was observed that the magnitude of complexation energy of the π-stacked structures is higher than H-bonded structures for both the MQ^+/methoxyphenol and HMQ^{2+}/methoxyphenol complexes. In the case of the ground-state of H-bonded MQ^+/methoxyphenol complex, complexation energy is –3.75 kcal/mol, whereas for ground state π-stacked complex it is –14.81 kcal/mol. Similarly, the π-stacked complex is energetically more stable than H-bonded by 4.04 kcal/mol for the HMQ^{2+}/methoxyphenol complex in the ground state. Thus, we can conclude that π-stacked is more favorable for both MQ^+/methoxyphenol and HMQ^{2+}/methoxyphenol complexes in the ground state.

Note that when computing the complexation energy of a complex, an appropriate solvent model is critical.[309-310] In this case, water is both polar and H-bonding solvent. In literature, several studies tested the performance of continuum, discrete, and a mixture of both continuum and discrete models. The use of a continuum model is a minimum requirement to account for the polar and H-bonding effect but a mixed discrete-continuum model can further improve the accuracy.[309] Here, we applied the polarizable continuum model (PCM) which is an implicit solvent model. In implicit solvents or continuum solvents, no solvent molecules or no solvent coordinates are present. In continuum solvent, only a small number of parameters mainly the dielectric constant (ε) are used to represent the solvent. In this work, we used the widely applicable solvation model based on density (SMD) to mimics the dielectric continuum of water.

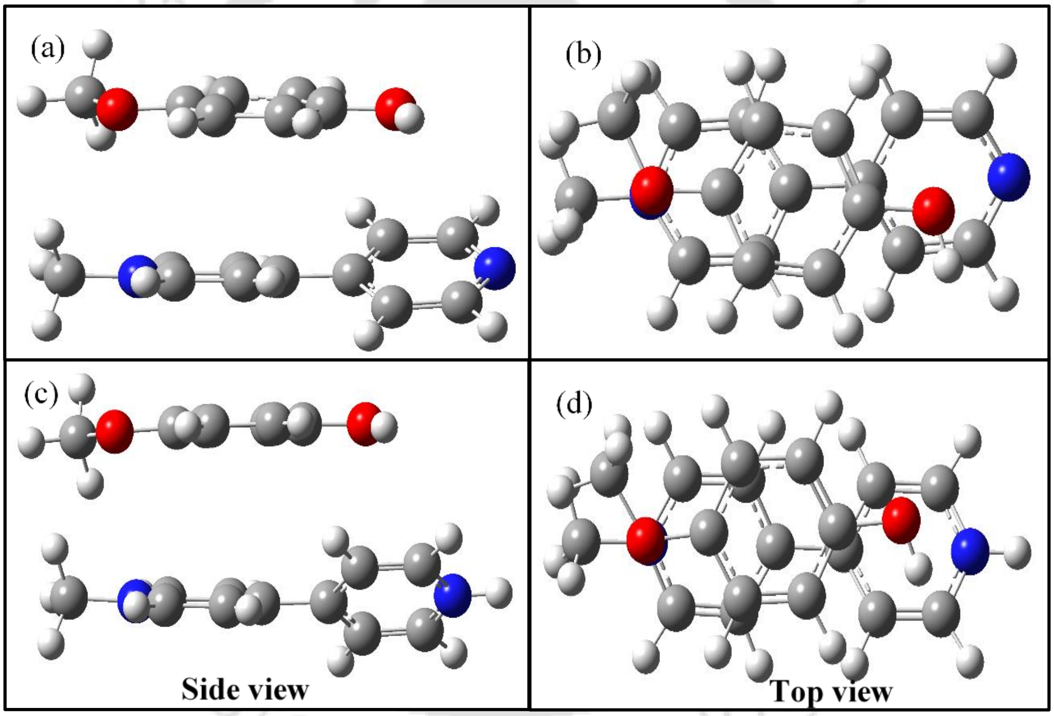

Figure 5.9. The ground state energy minimized π-stacked structures of the MQ^+/methoxyphenol (a and b) and HMQ^{2+}/methoxyphenol (c and d) complexes have been shown in the side and top views using CAM-B3LYP-D3/6-311++G** with SMD solvent (water) model.

Table 5.3. Ground state complexation energies of the MQ^+/methoxyphenol and HMQ^{2+}/methoxyphenol complexes. Calculations are obtained using CAM-B3LYP-D3/6-311++G** including SMD solvent (Water) model.

Complex Type	**Complexation Energy (kcal/mol)**	
	MQ^+- 4-methoxyphenol	**HMQ^{2+}- 4-methoxyphenol**
H-bonded	-3.75	-11.80
π-stacked	-14.81	-15.84

Furthermore, a close inspection of the ground state and excited state structures of the π-stacked configuration reveals that the aromatic ring of the methoxyphenol is displaced from a perfect face-to-face aligned structure with MQ^+ observed of the excited state (**Figure 5.9**). Also, due to such displacement, the inter-planar distance is increased from 3.16 Å in the S_1 state to 3.61 Å in the S_0 state. Hence, in the ground state, the shortest inter-planar distance is now considered as the distance between centroids of 'C' ring and C4 atom of the 'A' pyridine ring (**Figure 5.10**). The measured inter-planar distances are 3.48 Å and 3.50 Å for both the MQ^+/methoxyphenol and HMQ^{2+}/methoxyphenol complexes, respectively. Similarly, the inter-planar angle is measured by considering the angle formed between the plane of 'A' ring of MQ^+/HMQ^{2+} and the plane of 'C' ring of methoxyphenol molecules (**Figure 5.10**). The measured inter-planar angles are 4.90° and 3.87° for MQ^+/methoxyphenol and HMQ^{2+}/methoxyphenol complexes, respectively. The angle between two pyridine rings 'A' and 'B' of MQ^+ and HMQ^{2+} were also calculated for both the complexes and these are 29.4° and 34.3° for MQ^+ and HMQ^{2+}, respectively.

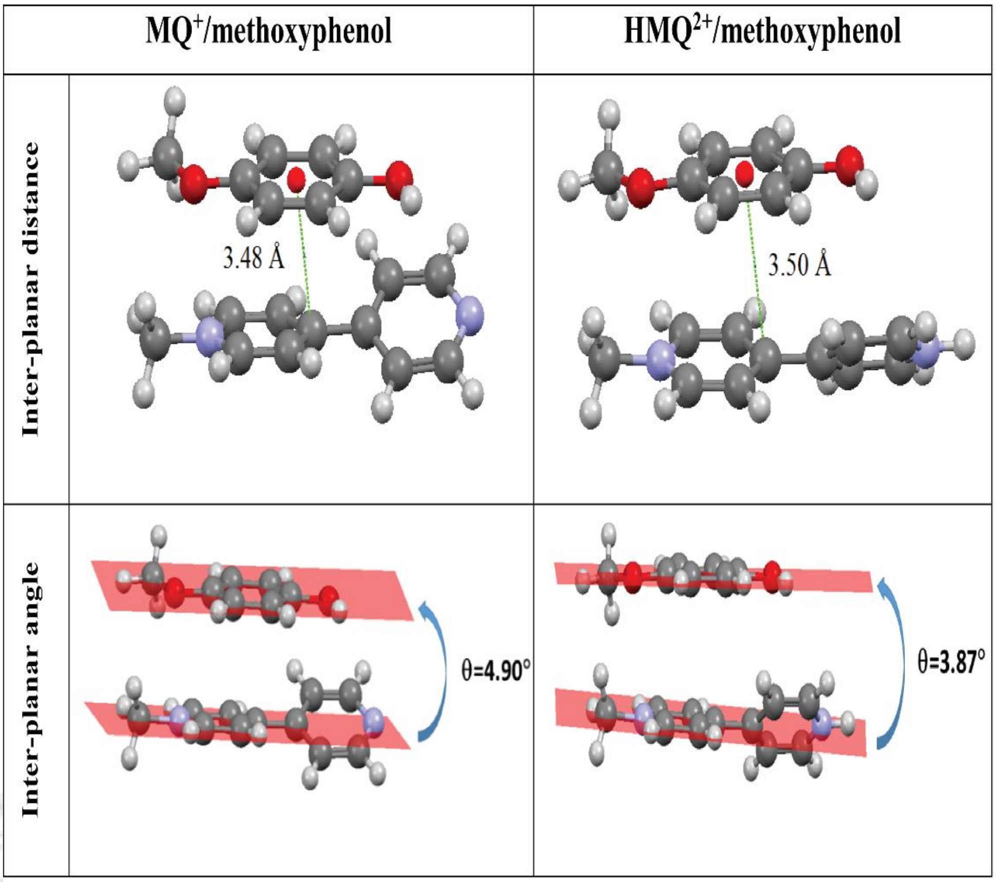

Figure 5.10. Representation of the inter-planar distance and angle of the ground state π-stacked structure of the MQ^+/methoxyphenol and HMQ^{2+}/methoxyphenol complexes, respectively.

5.2.6. Computation of Absorption Spectra of the Complexes, H-bonded vs. π-stacked:

To get more information about the photophysical properties of the MQ^+/methoxyphenol and HMQ^{2+}/methoxyphenol complexes, the absorption spectra of these complexes were computed for both π-stacked and H-bonded structures (**Figure 5.11**). The computed and experimental absorption maxima for the first electronic transition ($S_0 \rightarrow S_1$) are listed in **Table 5.4**. It was found that the absorption maxima calculated by two functionals (CAM-B3LYP and M06-2X) agree well with each other (see *Appendix*, **Figure A.5.1.**).

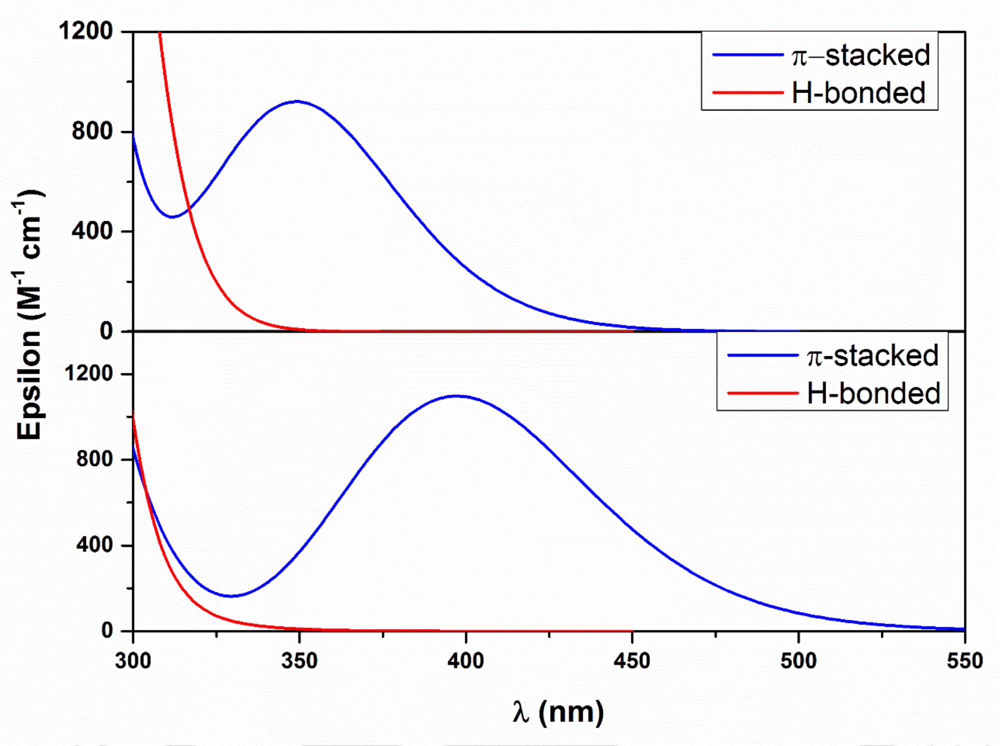

Figure 5.11. Calculated absorption spectra of MQ^{+}/methoxyphenol complex (top panel) and (b) HMQ^{2+}/methoxyphenol complex (bottom panel) are presented. All the spectra were calculated using TD-DFT method using CAM-B3LYP-D3/6-311++G** and SMD solvent (water) model on the ground state optimized structures.

Gagliardi et al. reported the UV-visible absorption spectrum of MQ^{+} and p-methoxyphenol complex in aqueous solutions containing equimolar concentrations of each species. They observed a low-energy shoulder at ~375 nm, which they assumed to occur due to the H-bonded complex.[201] On the other hand, Tyburski et al. reinvestigated the same system at two different pH values (pH 2 and 8.5) and observed nearly identical spectrum at both pHs.[203] They suggested that the low energy absorption band may be attributed to charge transfer.[203] Our computed UV-visible spectra for the π-stacked MQ^{+}/methoxyphenol complex shows a low energy shoulder peak at 349 nm while the H-bonded complex shows much more blue-shifted absorption band at 284 nm. Since, the absorption band of the π-stacked complex matches with the experimental absorption spectra, we may conclude that π-stacked complex is the main species in the ground state and the absorption band is due to charge transfer occurring in this complex. Likewise, Tyburski et al. observed an absorption band around 400 nm at pH 8.5 for the HMQ^{2+}/methoxyphenol complex.[203] Our computed absorption spectrum of the π-stacked HMQ^{2+}/methoxyphenol complex shows a lower energy band centered at 397 nm, which is almost identical to the experimental one. However, there is no absorption band near 400 nm for the H-bonded HMQ^{2+}/methoxyphenol complex. Thus, we may conclude that the absorption band at around 400 nm is solely due to π-stacked configuration rather than the H-bonded complex.

Table 5.4. Calculated vertical excited energies (nm), corresponding oscillator strengths (in the parenthesis) and major contribution for the complexes of MQ^+, HMQ^{2+} with 4-methoxyphenol in water medium using TD-DFT/CAM-B3LYP-D3/6-311G++(d,p) level.

System	configuration	S_1	Experimental value (nm)
MQ^+- 4-methoxyphenol	H-bonded	284.0 (0.001) H → L (96%)	375
	π-stacked	349.0 (0.022) H → L (99%)	
HMQ^{2+}- 4-methoxyphenol	H-bonded	308.2 (0.001) H → L (94%)	400
	π-stacked	397.3 (0.027) H → L (98%)	

5.2.7. Excited State Behavior of the π-stacked MQ^+/Methoxyphenol Complex:

Excited state geometry optimization of HMQ^{2+}/methoxyphenol complex leads to the exactly same π-stacked structure (**Figure 5.5**) irrespective of the ground state starting structure, H-bonded (**Figure 5.1b**) or π-stacked (**Figure 5.9b**). It indicates that π-stacked structure is overwhelmingly favored in the excited state. To investigate the behavior of the π-stacked MQ^+/methoxyphenol complex after optical excitation, the ground state π-stacked complex has been fully optimized in the electronically excited state using TD-DFT method at the same level of calculation.

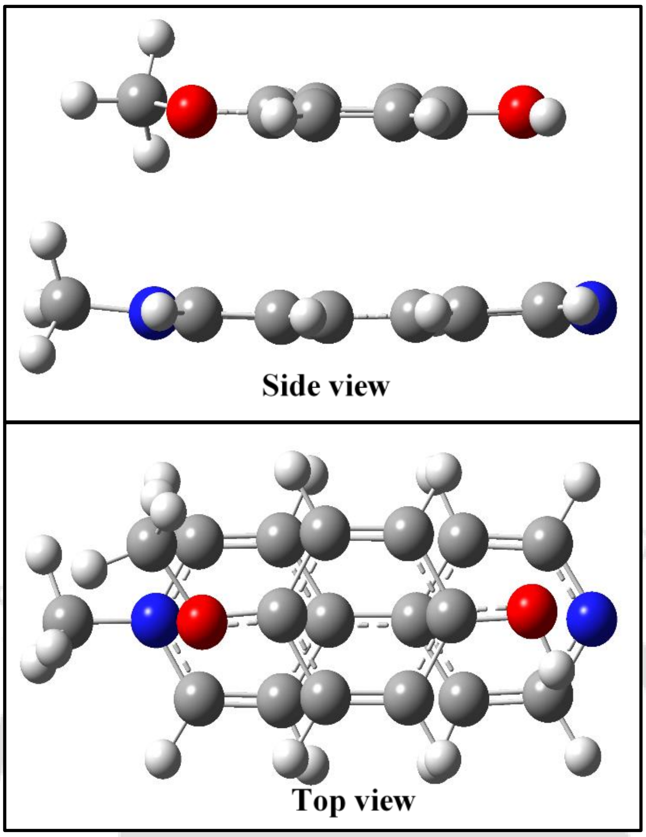

Figure 5.12. Excited state optimized structure of MQ^+/methoxyphenol complex obtained after optimization of the ground state π-stacked structure using CAM-B3LYP-D3 functional with 6-311++G(d,p) basis set including SMD (water) solvent model, respectively. Both the side and top view of the structure are given for clarity.

Surprisingly, in the case of MQ^+/methoxyphenol, different types of excited state π-stacked structure were found depending upon run on the initial ground state structure type, the H-bonded, and π-stacked. From ground state H-bonded complex, a π-stacked structure was found in the excited state where simultaneous proton and electron transfer occur from methoxyphenol to MQ^+ (ES2, **Figure 5.2**). However, when excited state optimization was initiated from the π-stacked structure, we did not found any transfer of H-atom from methoxyphenol to MQ^+ (**Figure 5.12**). This observation agrees well with the prediction of Tyburski's that no PCET occurs in such complexes.[203] Furthermore, it was found that the non-PCET π-stacked complex is more stable than the PCET complex by 4.4 kcal/mol in the S_1 state. Structural parameters, including the inter-planar distance and angle, were calculated for this π-stacked MQ^+/methoxyphenol complex (**Table 5.5**). The calculated inter-planar distance is 3.12 Å, and the measured inter-planar angle is 2.94° for

MQ$^+$/methoxyphenol complex. Furthermore, the AIM analysis also confirms π-stacking interaction present in the complex (**Figure 5.13**).

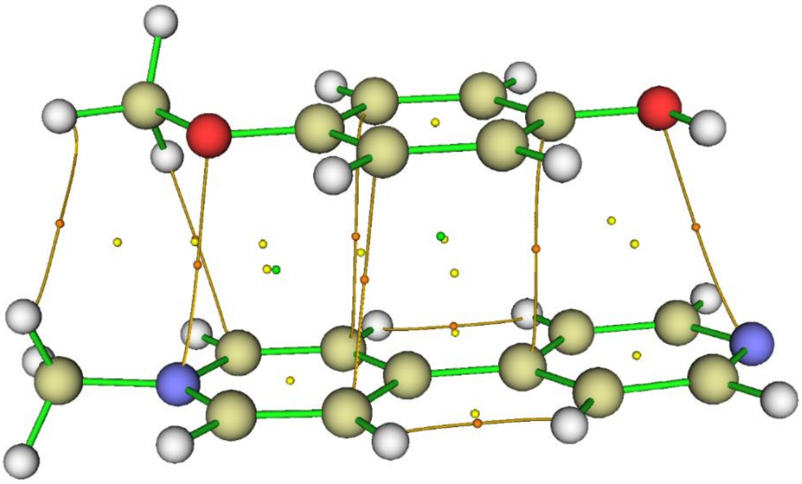

Figure 5.13. Distribution of bond, ring and cage critical points (red, yellow and green spheres respectively) and bond paths in the excited state MQ$^+$/methoxyphenol complex, which undergoes PET.

Table 5.5. Excited state optimized structural parameters (inter-planar angle and distance) of the π-stacked MQ$^+$/methoxyphenol (no PCET) complex**.** Calculations are obtained by using CAM-B3LYP-D3/6-311++G** with SMD solvent (water) model.

Structural parameter	**MQ$^+$- 4-methoxyphenol**
Distance between two centroids of two rings (A+B) and C (Å)	3.12
Angle between two planes of rings (A+B) and C (°)	2.94

5.2.8. Charge Transfer Analysis of the π-stacked MQ$^+$/Methoxyphenol Complex:

To understand the charge transfer process (CT), ESP charges over individual atom of the complex were calculated on the ground state and excited state optimized π-stacked structure of MQ$^+$/methoxyphenol complex. The exact amount of charge transfer from donor methoxyphenol to acceptor MQ$^+$ was determined for the ground state and excited state (**Figure 5.14**). In the ground state, almost no charge transfer (0.004e) was found from donor methoxyphenol to acceptor MQ^+ molecule. On the other hand, the observation is quite different in the S_1 state. An obvious charge transfer was found from the aromatic ring of the methoxyphenol to electron-deficient MQ^+ moiety. Amount of charge transfer is close to one (0.914e), which implies one electron gets transferred from the aromatic rings of the methoxyphenol to electron-deficient MQ^+ moiety (**Figure 5.14**).

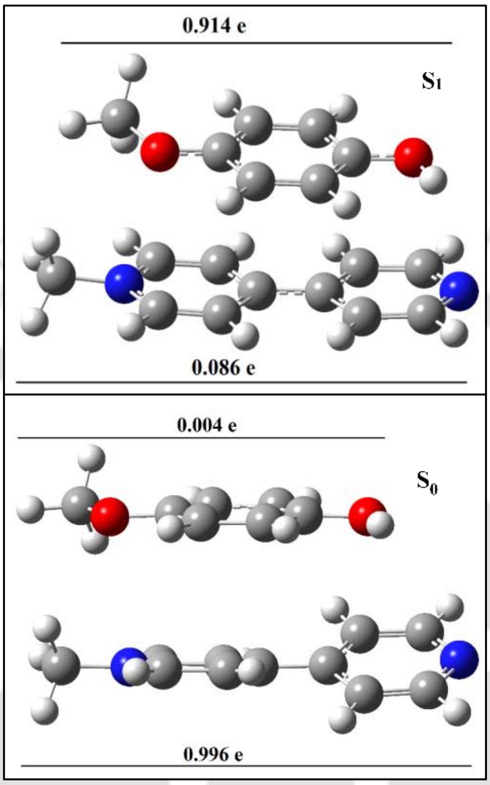

Figure 5.14. Calculated ESP charge on the S_0 state (bottom panel) and S_1 state (top panel) optimized structures of MQ^+/methoxyphenol by using CAM-B3LYP-D3/6-311G++(d,p) with SMD (water) solvent model.

5.2.9. Molecular Orbital Analysis of the Excited State π-stacked Complexes:

Furthermore, to confirm the charge transfer process, frontier molecular orbital analysis of the S_1 state of the complexes was performed by TD-DFT methods. From **Table 5.4**, we found that HOMO to LUMO charge transfer is solely responsible for $S_0 \rightarrow S_1$ transition. From **Figure 5.15**, it is evident that HOMO → LUMO transition involves charge (electron density) transfer from electron-rich methoxyphenol (donor) to electron-deficient MQ^+ molecule (acceptor). This observation also supports our ESP charge calculation results.

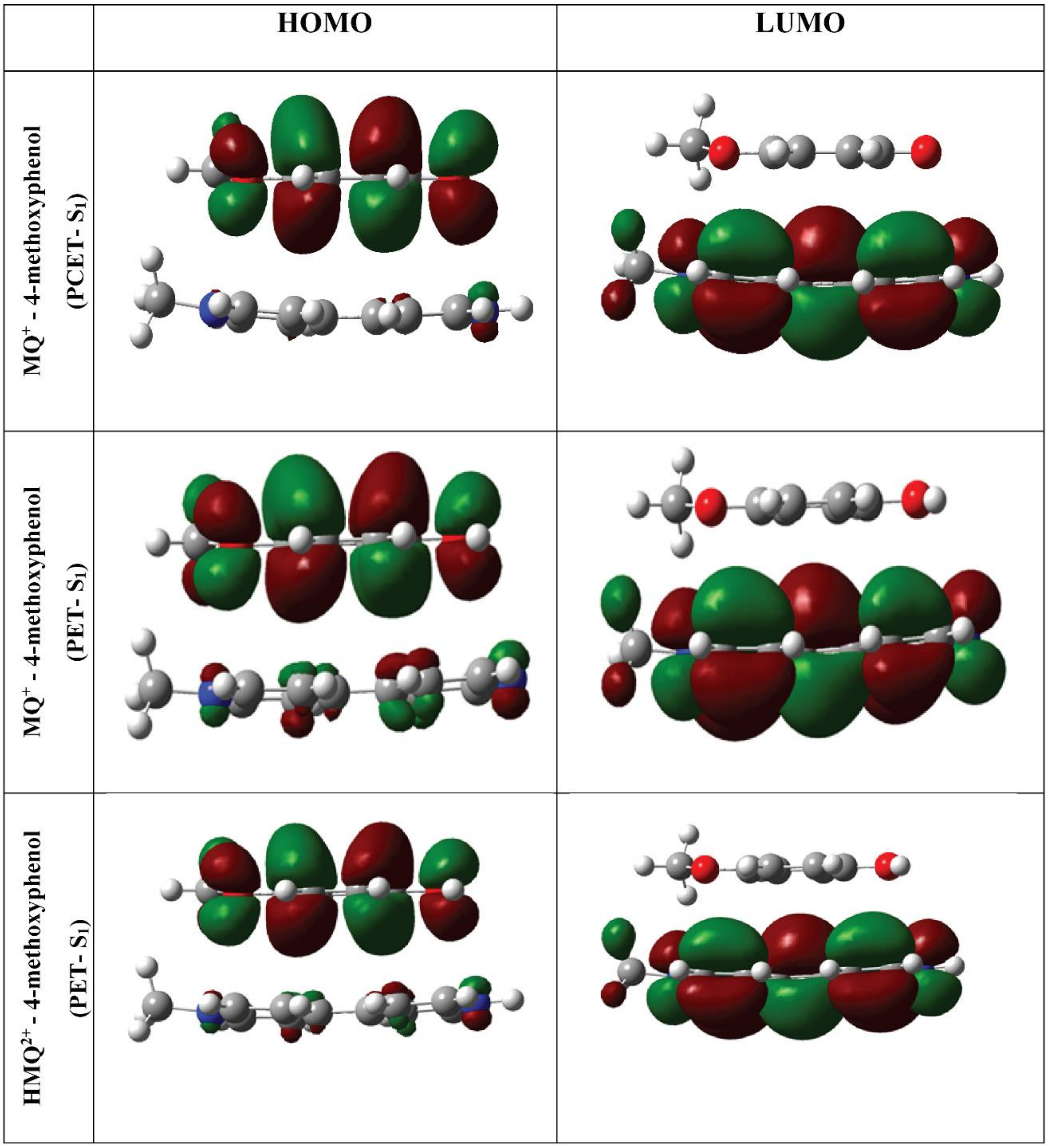

Figure 5.15. Frontier molecular orbitals of MQ^+/methoxyphenol and HMQ^{2+}/methoxyphenol complexes in the ground state and the excited state (S_1). CAM-B3LYP-D3 functional was used in combination with the basis set 6-311G++(d,p) in a dielectric continuum that mimics water (SMD).

5.3. SUMMARY AND CONCLUSION

In this chapter, we presented a thorough investigation of the excited-state processes of the MQ^+/methoxyphenol and HMQ^{2+}/methoxyphenol complexes. Our results show that two types of configuration are possible for both the complexes- H-bonded and π-stacked. PCET may take place only in the H-bonded MQ^+/methoxyphenol complex. We found clear evidence of charge transfer within π-stacked complexes in the excited state. In the ground state, the π-stacked complexes are energetically more favorable than the H-bonded complex. Thus, standard charge transfer within the π-stacked complex is much more favorable than the PCET process in the MQ^+/methoxyphenol. Since the energy difference between the H-bonded and π-stacked MQ^+/methoxyphenol complex is very high (~11.0 kcal/mol), the possibility of both processes occurring together can be ignored at room temperature.

Chapter-6

Effect of Photoacid Strength on Fluorescence Modulation of 2-Naphthol Derivatives inside β-Cyclodextrin[#]

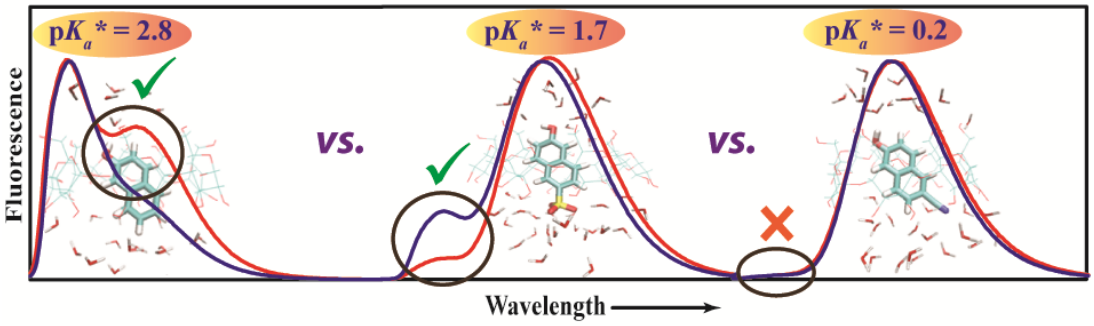

[#] This work has been published in *J. Phys. Chem. B* **2019,** *123* (44), 9291-9301.

Chapter 6: Effect of Photoacid Strength on Fluorescence Modulation of 2-Naphthol Derivatives inside β-Cyclodextrin

6.1. INTRODUCTION

Proton transfer (PT) is an elementary process occurring in diverse chemical and biological processes.[311-313] Excited-state proton transfer (ESPT) is a variant of PT triggered by photo-excitation of an aromatic fluorophore.[314-317] These molecules often termed as photoacids, are generally weak acids in the ground state but become strong acid in the excited electronic state and donate a proton to solvent medium (usually water). The ESPT process depends critically on the availability and the hydrogen bonding nature of water molecules around the photoacid.[318-321]

When a photoacid is encapsulated within a macrocyclic host, it may show a very different fluorescence response from that in water. The modified response, in turn, offers valuable insights about the microenvironment. A lot of studies are discussed in *chapter 1* (see *section 1.2.5*). Various photoacids, e.g., 1-naphthol and 2-naphthol derivatives, amino- and hydroxypyrene derivatives, etc., have been implemented to study ESPT inside CD cavity.[148, 152, 231, 322] However, the applicability of strong photoacids to report the characteristics of microenvironment inside organized assemblies, remain mostly unexplored. Moreover, different photoacids may report a different degree of fluorescence modulation upon inclusion. For example, Hansen et al. showed that ESPT rate increases for 1-aminopyrene but decreases for 1-naphthol inside β-CD.[148] Herein, we intended to study the link between fluorescence modulation and the strength of a photoacid inside a confined medium.

In this work, we deliberately chose 2-naphthol (2OH) and its two derivatives: 6-sulfonate-2-naphthol ($6SO_3$-2OH) and 6-cyano-2-naphthol (6CN-2OH) and investigated their fluorescence modulation upon complexation with β-CD (**Scheme 6.1**). The photoacid derivatives differ by the substitution at the 6-position and have very different pK_a^* values (**Table 6.1**). We measured the pK_a and pK_a^* value of the photoacids, which are close to the literature values (see *Chapter 2* and *Appendix* **Figure A.6.1, A.6.2, and A.6.3**). 2-Naphthol is a well-investigated photoacid and reportedly forms 1:1 inclusion complex with β-CD.[145-146, 323] Abdel-Shafi investigated the inclusion of $6SO_3$–2OH within the β-CD cavity by steady-state fluorescence and NMR spectroscopy and reported significant modulation of fluorescence spectrum inside the nanocavity.[324] However, ESPT of 6CN–2OH has never investigated within β-CD.

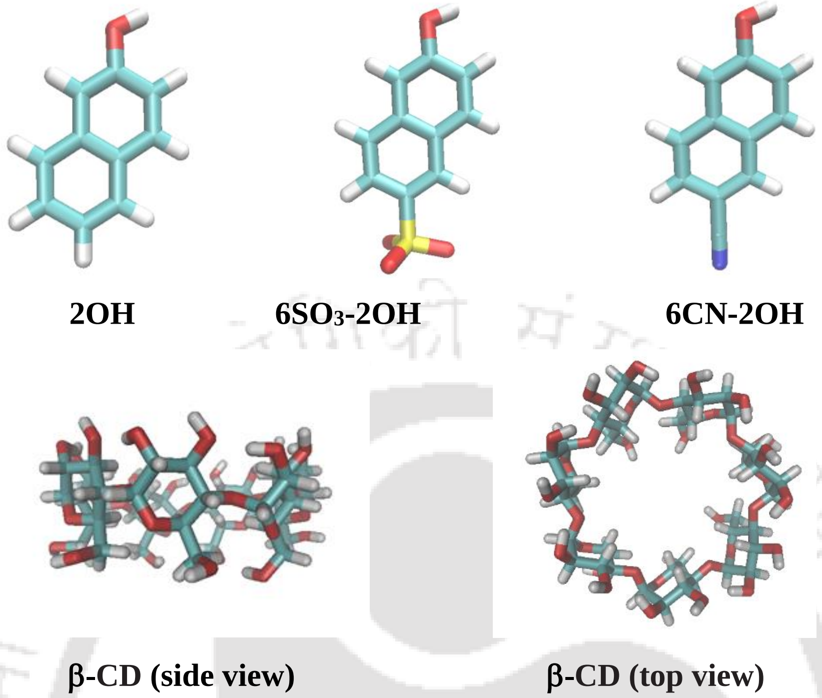

Scheme 6.1. Molecular structure of the photoacids: 2-napththol (2OH), 6-sulfonate-2-napththol ($6SO_3$-2OH), 6-cyano-2-naphthol (6CN-2OH) and β-CD host (side and top views).

Table 6.1. pK_a and pK_a^* of the free (in water) and complexed (with β-CD) photoacids.

Photoacid	**Free**		**Complexed**	
	pK_a	**pK_a^***	**pK_a**	**pK_a^***
2OH	9.61 ± 0.03 (9.45[a], 9.52[b], 9.5[c])	3.32 (2.8[a], 3.05[b])	10.00 ± 0.01 (10.0[b])	3.89 (3.60[b])
$6SO_3$-2OH	9.52 ± 0.03 (9.16[d], 9.4[e])	3.06 (1.7[d], 3.3[e])	9.65 ±0.10	3.03
6CN-2OH	8.55 ± 0.02 (8.4[a])	0.63 (0.2[a], -0.4[c])	8.42 ± 0.02	0.18

[a]taken from ref.[111] ;[b]taken from ref.[145] ;[c] taken from ref.[314] ;[d] taken from ref.[324] ; [e] taken from ref.[325]

6.2. RESULTS

6.2.1. Steady-State Emission Measurements:

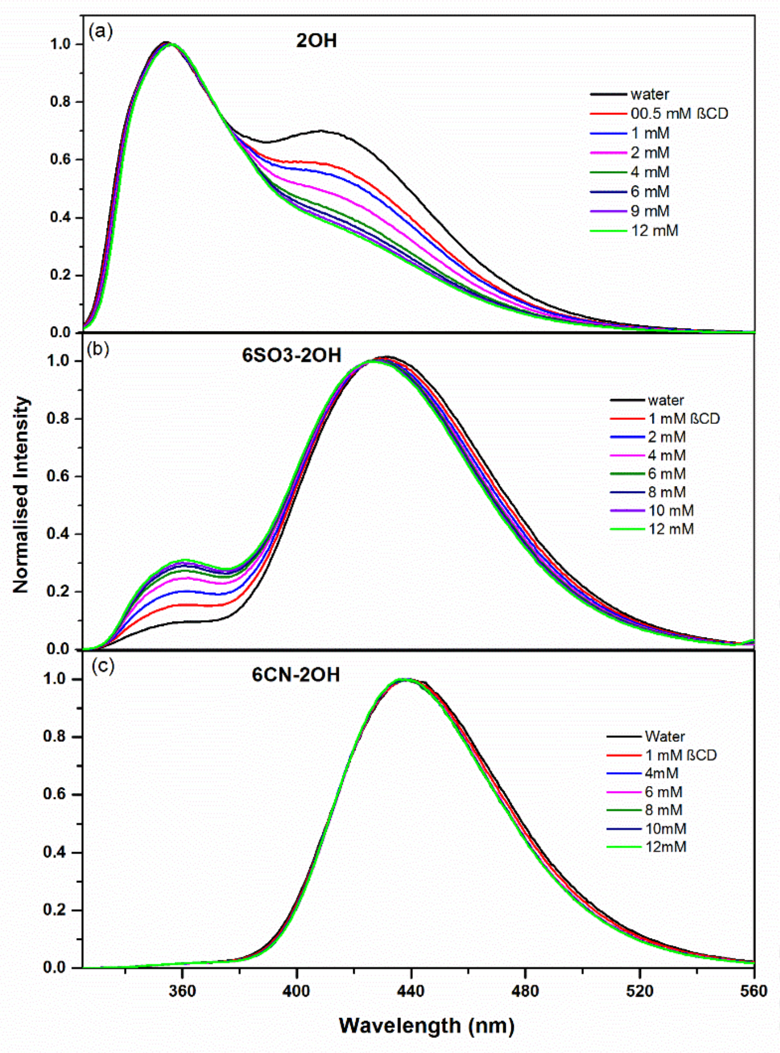

Figure 6.1. Emission spectra of (a) 2-OH, (b) $6SO_3$-2OH, and (c) 6CN-2OH in water and in the presence of various concentrations of β-CD (λ_{ex} = 310 nm). Emission spectra were normalized at the strongest band.

In water, all the photoacids exhibit two emission bands representing emission from the protonated and deprotonated species. In aqueous medium, emission maxima of the protonated band were at 354 nm, 358 nm, and 360 nm, respectively, and emission maxima of the deprotonated band were at 410 nm, 430 nm, and 440 nm, respectively for 2OH, $6SO_3$-2OH, and 6CN-2OH. For 2OH, the intensity of the protonated band is much stronger than the deprotonated band; the deprotonated band appears to be a shoulder to the protonated emission band. However, for both $6SO_3$-2OH and 6CN-2OH, the protonated emission band is much weaker than the deprotonated one. For 6CN-2OH, the protonated emission band is so weak that the emission spectrum appears to be a single band constituting only of the deprotonated emission. The relative intensity of the emission bands depends on the timescale of ESPT relative to the lifetime of the photoacid. In the case of very fast ESPT, initially excited protonated form converts almost instantaneously into the deprotonated form, which leads to a negligible emission from the protonated form. Thus, the very weak protonated band for 6CN-2OH indicates that ESPT may occur in ultrafast timescales.

In the presence of β-CD, the emission spectra alter substantially for both 2OH and $6SO_3$-2OH.[145, 324] The emission contribution of the deprotonated form suppresses significantly compared to the protonated form (**Figure 6.1a**). In other words, the emission contribution of the protonated form enhances significantly compared to the deprotonated form (**Figure 6.1b**). In contrast, the emission spectrum almost remains unchanged for 6CN-2OH in the absence and presence of β-CD (**Figure 6.1c**). To visualize the changes that occurred on the emission spectrum due to inclusion, we normalized the emission spectra at the stronger band. Area-normalized emission spectra are also added in the *Appendix* (see **Figure A.6.4**), which automatically corrects the error due to a slight difference in the concentration of fluorophores in different sets. All the emission spectra display clear isoemissive point, which indicates that the protonated and deprotonated bands are originating as the expense of each other.

The fluorescence quantum yield of 2-naphthol in aqueous solution is 0.2 (±0.01) and in presence β-CD quantum yield increases to 0.24 (±0.01). The fluorescence quantum yield of 6-sulfonate-2-naphthol in aqueous solution ($pH \leq 7$) is 0.31 (±0.03).

6.2.2. Time-Resolved Fluorescence Measurements:

Fluorescence decays of the photoacids were measured in water and in the presence of 12 mM β-CD to evaluate the effect of confinement on the ESPT dynamics of the photoacids. Two characteristic wavelengths,340 nm (or 350 nm) and 440 nm (or 470 nm), were selected for the protonated and deprotonated forms, respectively. It is important to emphasize that IRF of our set up (~700 ps) limits quantitative estimation of the ESPT dynamics.

In water, fluorescence decay of the protonated form (λ_{em} = 340 nm) of 2OH is exponential with a time constant of 4.8 ns (**Figure 6.2a**). The exponential nature of the decay was attributed to the irreversible ESPT (i.e., no re-protonation occurs in the excited state)[145]; the observed time constant (τ_o) can be related to the intrinsic lifetime (τ_n) and deprotonation time constant (τ_d) by the equation,[145]

$$\frac{1}{\tau_o}=\frac{1}{\tau_n}+\frac{1}{\tau_d} \qquad (6.1)$$

τ_n can be obtained from the decay time of the photoacids in highly acidic conditions (e.g., in 1-2M HCl) where ESPT is practically impossible. However, this may be complicated under additional quenching by the anions of the acids, and the quenching effect should be considered carefully (see *Appendix* **Figure A.6.5** and **A.6.6**).[145]

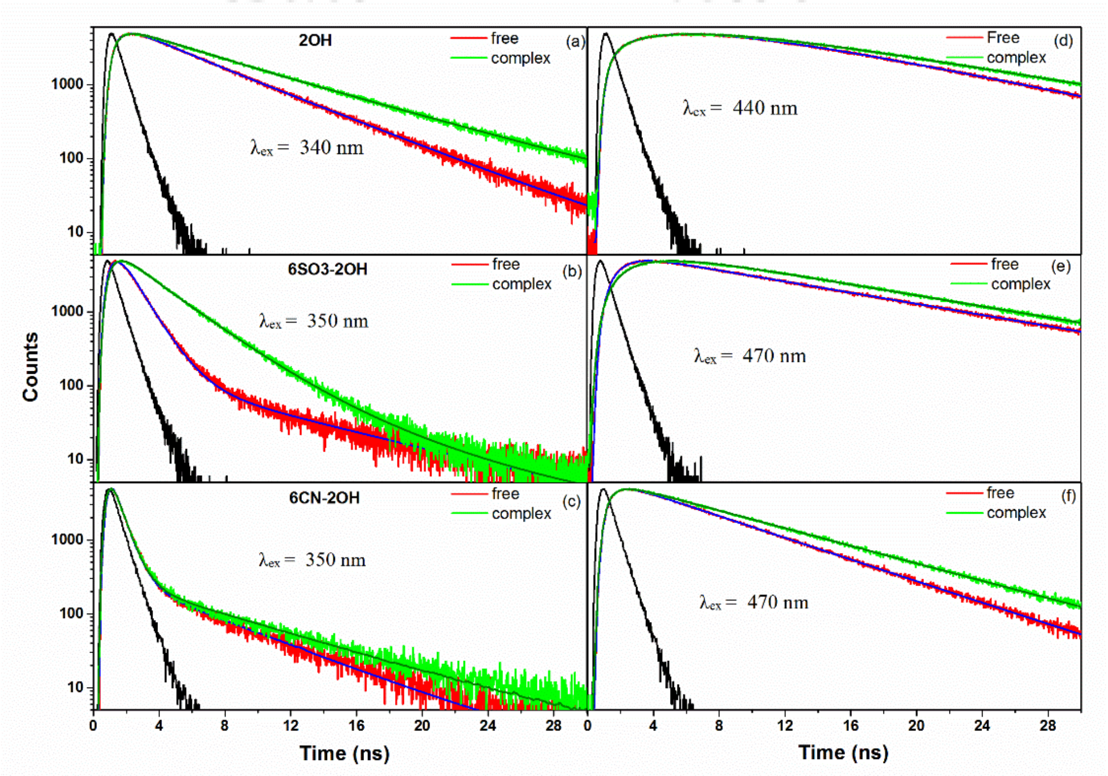

Figure 6.2. Fluorescence decays of the protonated (a-c) and deprotonated (d-f) forms of 2OH, 6SO$_3$-2OH and 6CN-2OH in water (free) and their complexes with β-CD ([β-CD] = 12 mM), upon excitation λ_{ex} = 292 nm.

The decays of the protonated form (λ_{em} = 350 nm) of both 6SO$_3$-2OH and 6CN-2OH were not entirely exponential; a major fast component is followed by a minor slow component (**Figure 6.2b** and **6.2c**). The minor component, although negligible, is necessary to get a reasonable fit. This small component may be a signature of geminate recombination, which is usually observed for strong photoacid.[326-327] Taking the major component as the observed lifetime, we can calculate the deprotonation time constants in water using equation (6.1). The deprotonation time is very long in the case of 2OH, moderate for $6SO_3$-2OH; however, very short for 6CN-2OH (**Table 6.2**). The vast differences in the deprotonation times are expected from substantial differences in the pK_a^* values.

Table 6.2. Fluorescence decay parameters of protonated and deprotonated forms of photoacids and their complexes with β-CD (12 mM). τ_1 and τ_2 represent the decay components and a_1 and a_2 respectively denote their relative contributions. τ_n and τ_d are intrinsic lifetime of the protonated form and the deprotonation time of the photoacids, respectively.

System	**λ_{em} (nm)**	**a_1**	**a_2**	**τ_1 (ns)**	**τ_2 (ns)**	**χ^2**	**τ_n (ns)**	**τ_d (ns)**
2OH	340	1.0	-	4.8	-	1.04	7.2	14.4
	440	-0.44	0.56	4.50	9.4	0.99	-	
2OH:βCD	340	0.26	0.74	3.90	7.2	1.03	9.2§	33.1
	440	-0.44	0.56	4.40	11.5	1.04	-	
$6SO_3$-2OH	350	0.98	0.02	1.10	7.7	1.04	6.7	1.3
	470	-0.44	0.56	0.80	11.5	1.04	-	
$6SO_3$-2OH:βCD	350	0.96	0.04	2.60	6.1	1.08	7.0	4.1
	470	-0.47	0.53	2.20	11.6	1.09	-	
6CN-2OH	350	0.99	0.01	0.16	5.20	1.02	4.8	0.17
	470	-0.30	0.70	0.17	5.88	1.01	-	
6CN-2OH:βCD	350	0.99	0.01	0.18	6.54	1.12	6.4	0.19
	470	-0.23	0.77	0.25	7.20	1.14	-	

§ taken from ref.[145]

In the presence of β-CD, the decay of 2OH becomes significantly slower and bi-exponential with components of 3.9 ns and 7.2 ns. The former component may be due to free 2OH, which may be slightly quenched in the presence of β-CD. The slower component was attributed to the decay of complexed 2OH.[145] A clear rise indicative of ESPT is observed in the emission transient (λ_{em} = 440 nm or 470 nm) of the deprotonated form, both in water and in the presence of β-CD (**Figure 6.2d**). However, no difference was observed in the rise times of the deprotonated transients in the presence (τ_1 = 4.4 ns) and absence (τ_1 = 4.5 ns) of β-CD, although a clear difference was noticed at the long-time tails (**Table 6.2**). A similar magnitude of the rise components, in the presence and absence of β-CD, implies that the rise component may only occur due to deprotonation of free 2OH. Deprotonation time of the complexed 2OH is beyond the lifetime of 2OH and hence, may not contribute in the measured decay.[145]

For $6SO_3$-2OH, the fluorescence decay at 350 nm is significantly slower in the presence of β-CD compared to that in water. The rise component of the deprotonated form (λ_{em} = 470 nm) of $6SO_3$-2OH is also significantly slower in the presence of β-CD, indicating a marked slowing down of ESPT (**Figure 6.2e**). The decay time of protonated transient is quite similar to the rise time of the deprotonated form. However, for 6CN-2OH, hardly any change was observed for the emission transients recorded in the presence and absence of β-CD. Likewise, we did not observe any significant difference in the rise component of the deprotonated form (λ_{em} = 470 nm) before and after the addition of β-CD (**Figure 6.2f**).

Thus, steady-state and time-resolved fluorescence measurements illustrate that fluorescence modulation is significant for 2OH and $6SO_3$-2OH, but almost none for 6CN-2OH upon inclusion inside β-CD. Now, we are interested to understand the origin of the differential modulation within the family of 2-naphthol photoacids. The possibilities could be as follows: (1) The binding pattern (i.e., binding constant or binding mode) of the photoacids with β-CD may be different, and hence, each photoacid may experience a different degree of confinement. (2) Perturbation of the hydrogen-bonding network of water molecules around the proton donation site (hydroxyl group) of the photoacid may be different for different photoacids. (3) The ESPT modulation may be intrinsically linked to the acidities of the excited state. In the following sections, we will dissect each of these possibilities.

6.2.3. Isothermal Titration Calorimetry (ITC) Measurements:

ITC measurement was performed to acquire thermodynamic binding parameters of the photoacid:β-CD complexes. **Figure 6.3** depicts the heat burst curves obtained from titration of aqueous solutions of different photoacids with β-CD. The thermodynamic parameters— enthalpy (ΔH), entropy (ΔS) and association constants (K_a) obtained from the ITC measurements are given in **Table 6.3**.

A single site model implying a 1:1 binding stoichiometry for all the host-guest systems can fit the raw ITC data satisfactorily. For all the complexes, a favorable exothermic enthalpic (negative ΔH) contribution is coupled with an unfavorable entropic contribution. However, the net free energy change is negative ($\Delta G < 0$), which is characteristic of the spontaneous inclusion process (**Table 6.3**). Two types of hydrophobic interactions— classical and non-classical are generally considered for host-guest complexations.[328-329] An entropy-driven process ($T\Delta S > 0$) is known as classical hydrophobic interaction, whereas an enthalpy-driven process ($\Delta H < 0$) is considered as non-classical hydrophobic interaction. Thus, the inclusion process for the photoacids here is driven primarily by non-classical hydrophobic interaction. It is important to note that the binding nature and the binding constants are comparable for all three photoacids (**Table 6.3**). Thus, the drastic variation in the fluorescence modulation, observed for different photoacids upon inclusion within β-CD, cannot be explained from their binding thermodynamics.

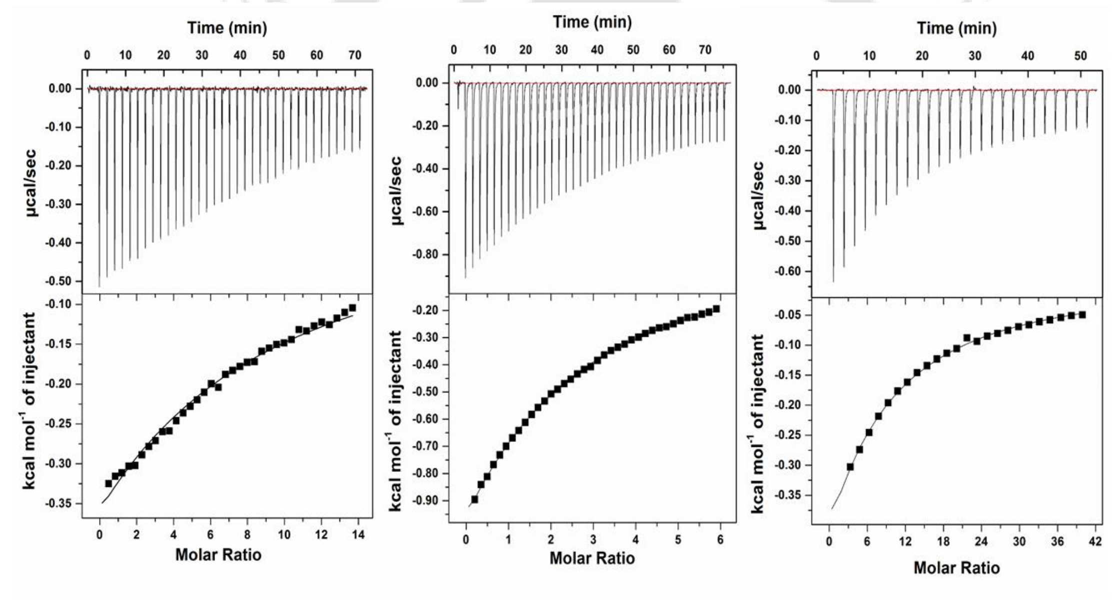

Figure 6.3. ITC profiles for the titration of three photoacids (2OH, $6SO_3$-2OH and 6CN-2OH) *vs.* β-CD in terms of molar ratio ([photoacid] / [β-CD]) at 298 K. Upper part of the ITC diagram is primary heat burst curves after correction of heat of dilution, and bottom part is ITC enthalpograms. The solid lines passing through the points are the best fit lines of the one-site binding model to the raw data.

Table 6.3. Thermodynamic binding parameters of different photoacids with β-CD obtained from ITC measurements.

photoacid	**K_a (10^2 M^{-1})**	**ΔH (kcal mol^{-1})**	**$T\Delta S$ (kcal mol^{-1})**	**ΔG (kcal mol^{-1})**
2OH	2.83 ± 0.08	-8.63± 0.18	-5.29	-3.33
$6SO_3$-2OH	4.18 ± 0.28	-5.39± 0.02	-1.81	-3.58
6CN-2OH	5.81 ± 0.08	-9.07± 0.07	-5.29	-3.78

6.2.4. Molecular Dynamics (MD) Simulation:

Although ITC provides binding affinities of the photoacids towards β-CD, molecular insights of the binding mode is essential to ascertain if there are any discernible changes in the binding pattern. MD simulation is generally used to reveal insight into the host-guest geometry.[290, 330-331]

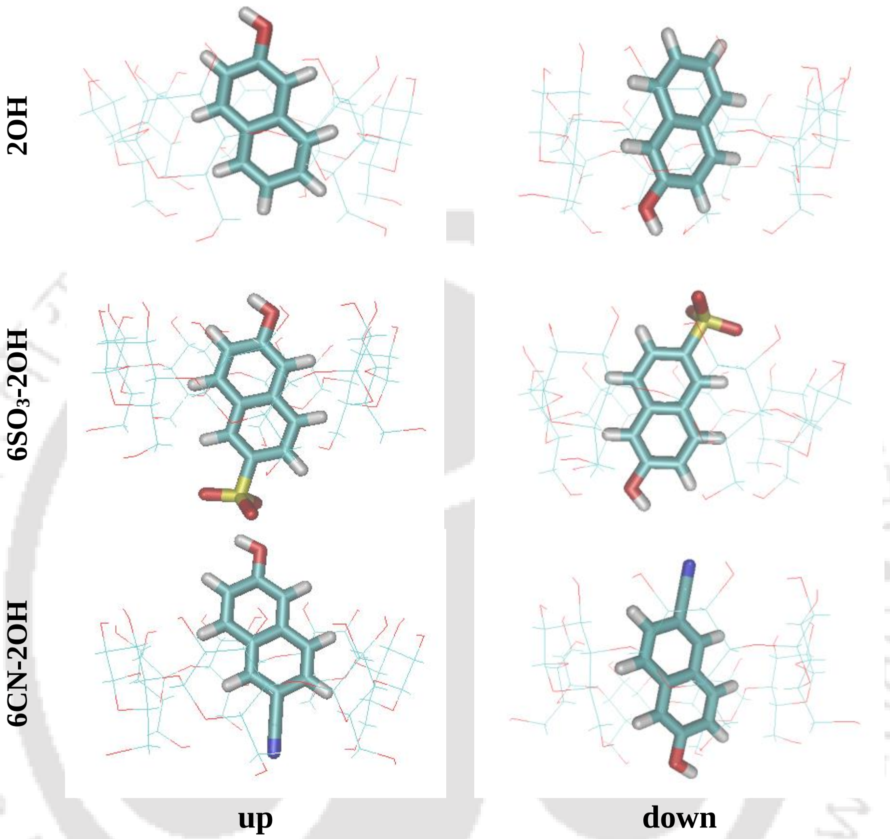

Figure 6.4. Initial configuration (t = 0 ns) of the Photoacid:β-CD “up” and “down” complexes are shown, respectively. Water molecules are omitted for clarity.

First, it was checked if there was any preferred "up" or "down" configuration for the photoacid:β-CD inclusion complex. The initial configurations of both “up” and “down” complexes are presented in **Figure 6.4**. It was found that the “down” complex is very stable for all the photoacid:β-CD complexes; the photoacids remain inside the cavity throughout the MD trajectories. However, the “up” complex was found to be unstable for both 2OH and 6CN-2OH. In this configuration, 2OH came out of the cavity after an interval and subsequently remained outside. 6CN-2OH also escapes; however, it enters into the cavity again in the reversed configuration. Thus, MD simulations indicate “down” configuration as a preferred mode for the inclusion of 2OH and 6CN-2OH. However, no mode preference was observed for $6SO_3$-2OH. A possible reason is that the host-guest exchange time for this complex may be beyond our simulation period. Using NMR spectroscopy, Abdel-Shafi et al. predicted that the binding mode of 6SO$_3$-2OH as "down configure".[324] Since all the photoacids are stable in the down configuration, henceforth, only the down complex are discussed.

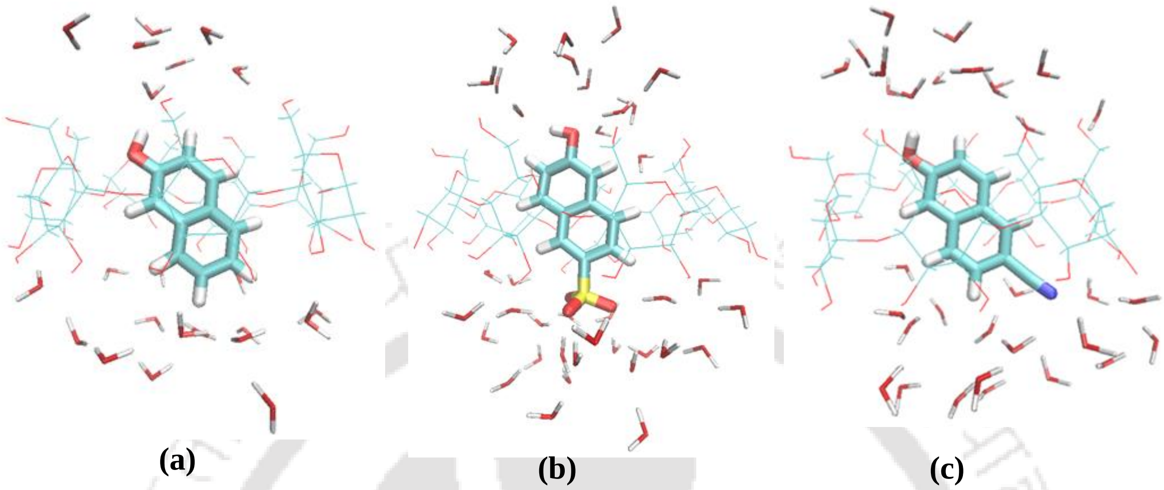

Figure 6.5. Representative MD simulation snapshot of the β-CD inclusion complexes of (a) 2OH, (b) 6SO$_3$-2OH, and (c) 6CN-2OH after 20 ns simulation. Water molecules present within 5 Å around the photoacid are displayed.

Visual inspection of the snapshots of photoacid:β-CD confers almost complete insertion of the photoacids inside the β-CD cavity (**Figure 6.5**). The naphthalene ring of the photoacids remains inside the hydrophobic cavity of β-CD throughout the simulation period (20 ns). Entropy effect arising from the removal of water molecules from β-CD cavity may dominate the inclusion of naphthyl guest into the β-CD cavity. The hydrophilic hydroxyl group (-OH) of the photoacids tends to protrude from the cavity through the narrower ring. The other functional groups (-SO$_3^-$ and -CN) also extrude out from the wide rim.

6.2.4.1. Distance between Center of Mass (COM) of β-CD and the Center of the Central C-C Bond of the Naphthalene Ring:

To check the depth of the inclusion of each photoacid, the distance between COM of β-CD and the center of the C-C bond present at the center of the naphthalene ring were plotted against number of frames in the **Figure 6.6**. This separation may be a better descriptor of the inclusion depth than the usual COM(host)-COM(guest) separation, because the COM of the photoacids may present at different locations due to different substitutions. The **Figure 6.6** shows the stability of the photoacids inside the cavity of the cyclodextrin throughout the simulation period. Furthermore, quite short distances were found for all the three photoacid:β-CD complexes during simulation times (**Table 6.4**), which values imply complete insertion of photoacids into the cavity of host β-CD.

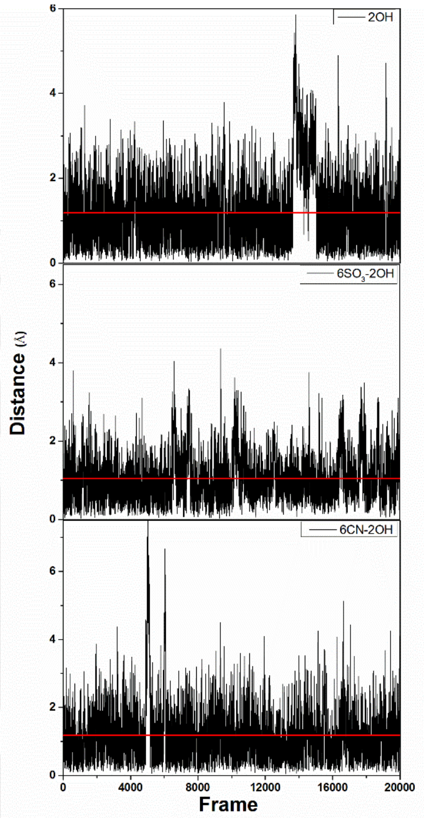

Figure 6.6. Distance between center of mass (COM) of β-CD and the center of the central C-C bond (C3-C4) of the naphthalene ring of the photoacids versus frame.

Table 6.4. Distance (in Å) between center of mass (COM) of β-CD and the center of central C-C bond of the naphthalene ring of the photoacids.

2OH:βCD	$6SO_3$-2OH:βCD	6CN-2OH:βCD
1.186±0.005	1.042±0.004	1.174±0.005

6.2.4.2. Radial Distribution of Water Molecules Around the Hydroxyl Group of Photoacids:

To get a clear idea of the distribution of water molecules around the hydroxyl group (-OH) of the photoacids both in the presence and absence of β-CD, the radial distribution function (RDF) was determined. RDF involving oxygen(O) of the hydroxyl group of photoacid and oxygen(O_w) of water may be useful (**Figure 6.7**).

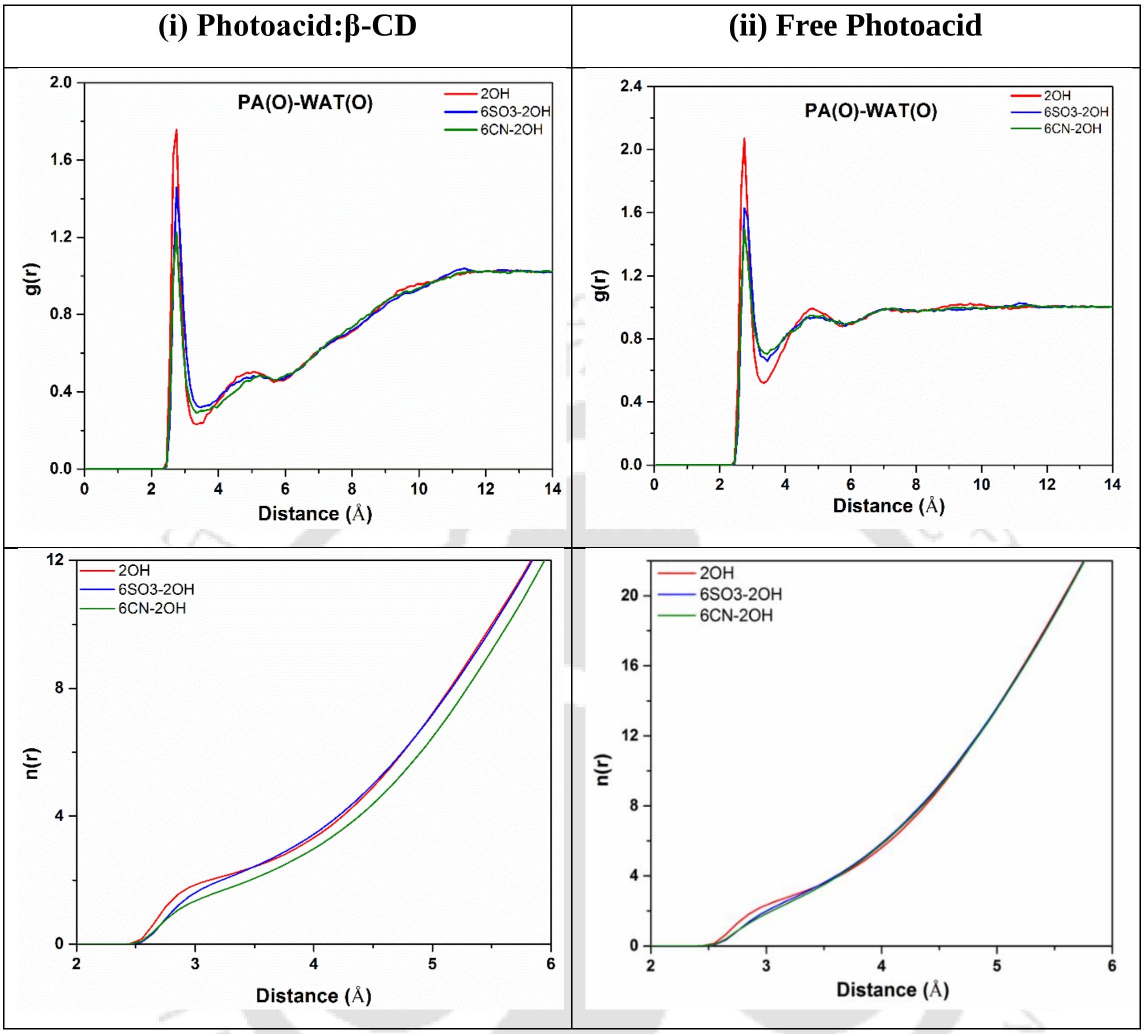

Figure 6.7. Radial distribution function (upper panel) and running coordination number (lower panel) involving oxygen atom (photoacid)-oxygen atom (O_w) of water situations in the (i) presence and (ii) absence of β-CD.

There is remarkable similarity among the RDFs of different photoacids both in water and inside β-CD, but the RDF of a photoacid within the β-CD complex is remarkably different from that in bulk water. The O-O_w RDF shows a distinct maximum at ~2.75 Å for all three photoacids both in the presence and absence of β-CD (**Figure 6.7i, and 6.7ii**). The height of the 1st peak, which is proportional to the number of water molecules present in the first hydration shell, follows a moderate variation in the order 2OH> $6SO_3$-2OH> 6CN-2OH. However, this variation in the order is common in the absence and presence of β-CD. This confirms that this variation is not due to CD cavity. The height of the first peak decreases in the presence of β-CD compared to that in water. This implies that the hydroxyl group is less hydrated upon inclusion inside the cavity. It is also clear from the RDF that the availability of water molecules around the photoacid inside β-CD is much less compared to that in neat water. The distribution of water molecules become severely perturbed at least up to three solvation layers around the hydroxyl group of the photoacid.

To find out the exact number of water molecules closely distributed around the hydroxyl group of the photoacids, the running coordination number (RCN) was calculated around the O atom of the hydroxyl group of different photoacids in the first and second coordination shells (**Table 6.5**). The running coordination number $n_i(r')$ of a particular solvent (i) present within a specified distance r′ from a defined site (α) of the acceptor may be defined as

$$n_i(r') = 4\pi\rho_i \int_0^{r'} g_{\alpha i}(r) r^2 \mathrm{d}r \tag{6.2}$$

Where ρ_i is the average number density of the solvent i in the system. We took the cut off distance for 1st and 2nd water shells as 3.35 Å and 5.75 Å, respectively which correspond to the 1st and 2nd minima in the RDF.

Table 6.5. The average number of water molecules in the first and second water shells for three photoacid:β-CD systems (in the parenthesis presented the number of water molecules in the absence of β-CD for the same).

Guest molecule	1st water shell	2nd water shell
2OH	2.242 (3.172)	11.474 (21.986)
$6SO_3$-2OH	2.192 (3.102)	11.401(21.934)
6CN-2OH	1.836 (2.970)	10.696 (21.781)

In the present study, we are mainly interested in the water molecules residing in the 1st solvation shell molecules as these may form H-bond with the photoacids and could directly participate in ESPT. Average numbers of water molecules within the first solvation shell around 2OH, $6SO_3$-2OH, and 6CN-2OH are 2.24, 2.19, and 1.84, respectively, inside the cavity, which is significantly lower compared to that in bulk water (**Table 6.5**). The total number of water molecules present up to the second solvation shell around the photoacid is reduced by a factor of two inside the β-CD cavity from that in water.

6.2.4.3. Water Density Contour Plot:

Figure 6.8 depicts the density of water within 3.4 Å of the O-atom of the hydroxyl group of the photoacids both in the presence and absence of β-CD. The water density plots suggest that the hydroxyl group of the guest molecules are protruding out of the cavity and are easily accessible by water molecules. The water densities around the hydroxyl group of photoacids are quite similar. However, the water density around the photoacids markedly decreases upon inclusion into the cavity for all the photoacids.

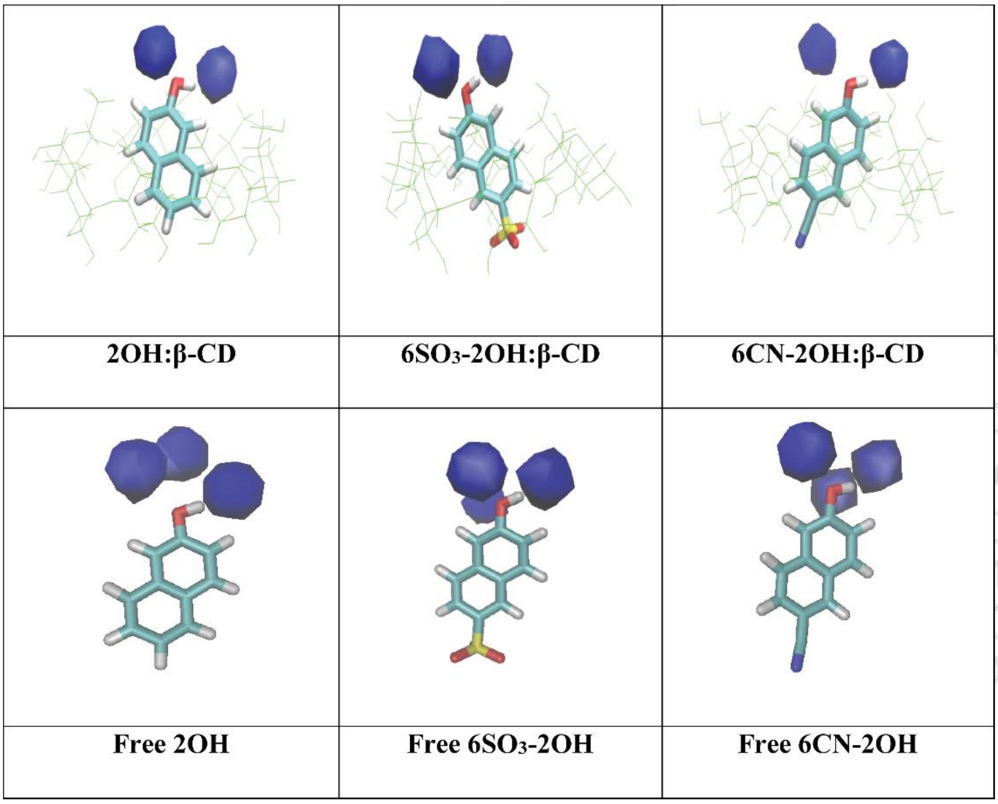

2OH:β-CD **6SO$_3$-2OH:β-CD** **6CN-2OH:β-CD**

Free 2OH **Free 6SO$_3$-2OH** **Free 6CN-2OH**

Figure 6.8. Contour plots of water density within 3.4 Å around the oxygen atom of the hydroxyl groups of the photoacids - photoacid in the presence of β-CD, i.e., photoacid: "down" complex (1:1) (top), photoacid in the absence of β-CD (bottom). For clear visualization, the remaining water molecules are left off.

6.2.4.4. Hydrogen Bonding Analysis:

Hydrogen-bond analysis was performed to understand the probability and nature of the H-bonding. The hydroxyl group of the photoacids can act as both donor and acceptor sites for H-bonding. Moreover, there can be two different types of H-bonds: photoacid-water and photoacid-β-CD (hydroxyl group of β-CD) H-bonds. However, we are interested primarily in the H-bonding between photoacid and water, since we are concerned with the

ESPT dynamics of photoacids. The criteria of H-bond formation were set such that the maximum oxygen–oxygen interatomic distance $r_{DA} \leq 3.4$ Å (1st RDF g(r) minima between oxygen atom (photoacid)-oxygen atom of water) and the angle ∠D–H–A ≥ 135°. The average number of photoacid-water H-bonds are given in **Table 6.6**. It was found that the average number of hydrogen bonds formed by each photoacid in the presence of β-CD is reduced drastically compared to bulk water.[332]

Table 6.6. The average number of photoacid−water hydrogen bonds (data of neat water in the parenthesis).

Avg. Number H-bond	**2OH:βCD**	**$6SO_3$-2OH:βCD**	**6CN-2OH:βCD**
Photoacid(O1)-Water(O)	1.950 (2.487)	1.760 (2.191)	1.419 (1.942)

From MD simulation analyses including calculation of the extent of inclusion of photoacids into CD cavity, radial distribution function (RDF), running coordination number (RCN) and H-bonding, we can conclude that the difference in the fluorescence modulation upon inclusion with β-CD cannot be attributed to the difference in the binding process.

6.3. DISCUSSION

Fluorescence measurements, together with ITC experiments and MD simulations were carried out to investigate and rationalize the fluorescence modulation behavior of three 2-naphthol derived photoacids inside the β-CD cavity. From steady-state and time-resolved fluorescence measurements, we observed significant modulation of the emission spectra for both 2OH and $6SO_3$-2OH upon the addition of β-CD. In contrast, no modulation was observed for 6CN-2OH upon complexation with β-CD. From these observations, one may argue that the photoacids may bind differently to β-CD; 2OH and $6SO_3$-2OH may bind favorably, while 6CN-2OH may not bind at all. However, the ITC investigation confirms that all the photoacids form 1:1 complex with comparable binding constants. Moreover, ITC measurement also confirms that the host-guest complexation is governed by enthalpy-driven non-classical hydrophobic interaction.

MD simulation revealed that a down configuration is stable for all the photoacids. The extent of inclusion is quite similar for all the complexes. The aromatic ring remains inside the cavity; the center of the naphthol ring remains close to the center of the β-CD cavity. Calculation of RDFs further presents the distribution of the water molecules around the oxygen atom of the hydroxyl group of the photoacid in the β-CD complexes. The nature of the RDFs (peak position and peak strength order) is quite alike for all the photoacids. However, the RDFs are remarkably different inside the β-CD compared to water. The height of the peaks, especially second and third, decrease dramatically in the presence of β-CD compared to that in bulk water, implying that the hydroxyl group is less hydrated upon inclusion inside the cavity. RDF plot shows a sharp peak at ~ 2.75 Å for all three complexes in β-CD solution and in bulk water indicating the possibility of H-bond formation between the oxygen atom of the photoacid (PA(O1)) with the oxygen atom of water molecules (O_w). Furthermore, the number of water molecules present in the first hydration shell follows a moderate variation in the order 2OH> $6SO_3$-2OH> 6CN-2OH, and this variation in the order is common in the absence and presence of β-CD. A similar trend suggests that variation is intrinsic in nature. To get an exact quantitative estimation of the number of water molecules present around the O-atom of the photoacids for the 1st and 2nd solvation shell running coordination number (RCN) was accounted. This finding is also in accordance with the RDF results. It is found for all three photoacids that the number of water molecules around the O-atom of the photoacids for the 1st and 2nd solvation shell decreases in the presence of β-CD compared to that in water. This finding is further visualized from water density map, which also reveals less water density in the 1st solvation shell around O-atom of the photoacids inside β-CD compared to that in water. Moreover, the water densities around the hydroxyl group of all three photoacids are quite similar. Hydrogen bond analysis was performed to get an exact idea of hydrogen bonding nature of the O-atom of the photoacids with water molecules, it was observed that the average number of hydrogen bonds formed by each photoacid with water molecules is reduced drastically in the presence of β-CD compared to bulk water.

Thus various analyses of MD simulation, including the extent of inclusion, radial distribution function (RDF), running coordination number (RCN) and H-bonding, confirm that nothing special in the binding pattern of 6CN-2OH to β-CD with respect to other two photoacids 2OH and $6SO_3$-2OH. The limitation of classical MD simulation is that it can only predict the distribution of water molecules around the photoacid in the ground state.

One may use excited state charges of the photoacids to add further insight into the arrangement of water around the excited photoacid.[333] However, classical MD simulation still cannot predict whether ESPT occurs or not. Ab initio simulations can be more appropriate but may not be possible to perform for such large systems.[334]

Our results may be compared with the results of Hansen et al.[148] They investigated two photoacids with very different natures- 1-aminopyrene, a very strong cationic photoacid and 1-naphthol, a moderately strong neutral photoacid. For the neutral photoacid 1- naphthol, pK_a and pK_a^* shift to higher values upon complexation compared to water, while the ESPT rate becomes retarded. On the other hand, the pK_a and pK_a^* of the cationic photoacid move to lower values upon complexation and the rate of ESPT increases relative to bulk water. Thus, the electronic structure of the photoacid may depict the effect of complexation within the non-polar cavity of β-cyclodextrin.[148]

In our case, 2OH is a neutral weak photoacid and complexation increases both the pK_a and pK_a^* due to the destabilization of the conjugate photobase anion in the cavity (**Table 6.1**). The $6SO_3$-2OH is a negatively charged photoacid and hence, complexation may be affected by the destabilization of the doubly charged photobase anion and enhanced charge transfer to the naphthalene ring induced by the negatively charged SO_3^- group. However, we found that the pK_a^* shifts to a little lower value inside the β-CD cavity compared to water. This unexpected result may be due to the presence of the negative charges at two opposite ends, which may be staying outside the cavity and may be solvated effectively in the complexed form. For 6CN-2OH, we found that pK_a and pK_a^* do not follow the same trend as that of 2OH, despite both are neutral photoacids. The pK_a and pK_a^* values shit to lower values compared to water. The electronegative –CN group may drag charges from the deprotonated hydroxyl group, and the charge transfer state may be more stabilized inside the β-CD compared to that in water. However, detailed studies are needed to fully comprehend the behavior at the molecular level.

Finally, we try to rationalize the observed variation in the ESPT rate from the generalized free energy correlation between pK_a^* and logarithm of ESPT rate (**Figure 6.9**).[120, 124, 335] It was found that 2OH, in both free and complexed form, correlates nicely to the correlation plot reported by Spies et al. using various photoacids.[124] The complexation makes 2OH significantly weaker photoacid, and hence, it may deprotonate at a slower rate compared to that in water. The free energy correlation is also valid for 6CN-2OH:β-CD complex; although it follows an opposite behaviour to that of 2OH. The complexation makes 6CN-2OH somewhat stronger photoacid and hence, deprotonates at a faster rate compared to that in water. Although we do not have sufficient time resolution to discriminate the rate constants of the free and complex forms quantitatively, the free energy correlation supports our observation that the deprotonation is faster in the complexed form. The anionic photoacid $6SO_3$-2OH seems to violate the free energy correlation, since pK_a^* decreases upon complexation while the ESPT rate is suppressed. However, if we incorporate the extra energy required for charge separation in the case of the charged photoacids in the free energy correlation, the results may be justified. The energy of separation of charges is given by $\frac{R_D}{2.3a}$ where, R_D is the Debye radius (= $\frac{|z_1 z_2| e^2}{\epsilon k_B T}$, where z_1 and z_2 are charges for proton and the conjugate base; e charge of electron, ε is static dielectric constant) and *a* is the contact radius. The contact radius can be very different for the free and complexed form. If we assume *a* to be 5.5 Å and 8Å, respectively in the free and the complexed form and R_D to be 14.2 Å,[124] then it can be shown that the effect pK_a^* is higher in the complexed form and hence, slower deprotonation is justified from the free energy correlation (see appendix **Figure A.6.7**).

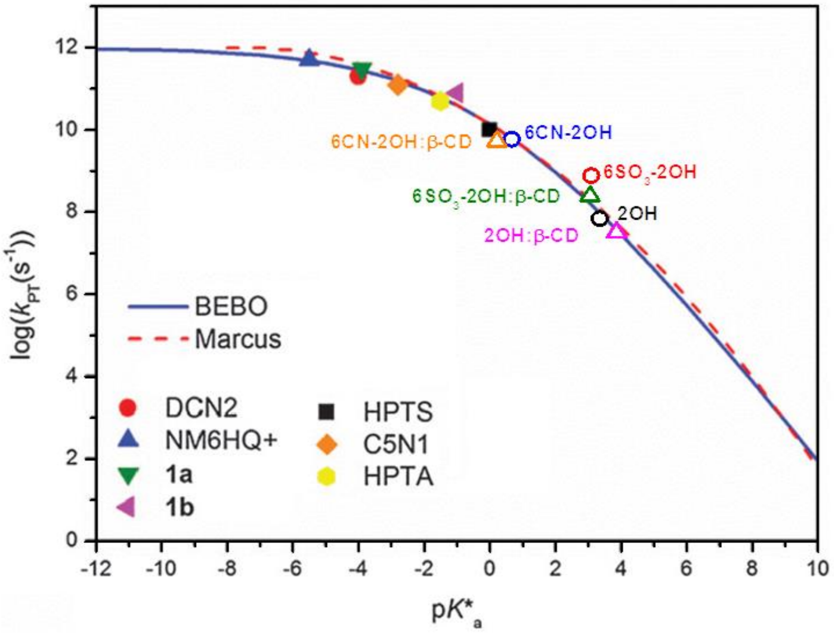

Figure 6.9. The proton dissociation rate constant of the photoacids (2OH, $6SO_3$-2OH and 6CN-2OH) in water and in the presence of β-CD are included to the free-energy correlation reported by Spies et al.[124] The solid symbols denote their data (1a, 1b, DCN2, NM6HQ+, HPTS, HPTA and 5C1N in water) while the open symbols denote our data.

6.4. SUMMARY AND CONCLUSION

In this chapter, we have shown that fluorescence modulation of the photoacids is not due to very different modulation of the hydration environment around the deprotonation site (hydroxyl group) but rather, is related to the intrinsic chemical nature ($\mathrm{p}K_\mathrm{a}^*$) of the photoacids. Thus, an optimum choice of photoacid is necessary to effectively sense the change in the local arrangement of water around the photoacid and consequently, to obtain the best fluorescence modulation. Too strong photoacid does not require any favourable arrangement of water and thus may be insensitive towards the slight alteration of water arrangement upon confinement. For too weak photoacid, ESPT is quite unfavourable even in bulk water or deprotonation is very slow compared to its lifetime, and hence, such a photoacid cannot sense minute changes occurred in water rearrangement. Thus, in conclusion, a moderate strength photoacid may be more useful; however, the strength may depend on the type of confinement under study.

Chapter-7

Contrasting pK_a Shift and Fluorescence Modulation of 6-Cyano-2-Naphthol inside α- and β-Cyclodextrins[#]

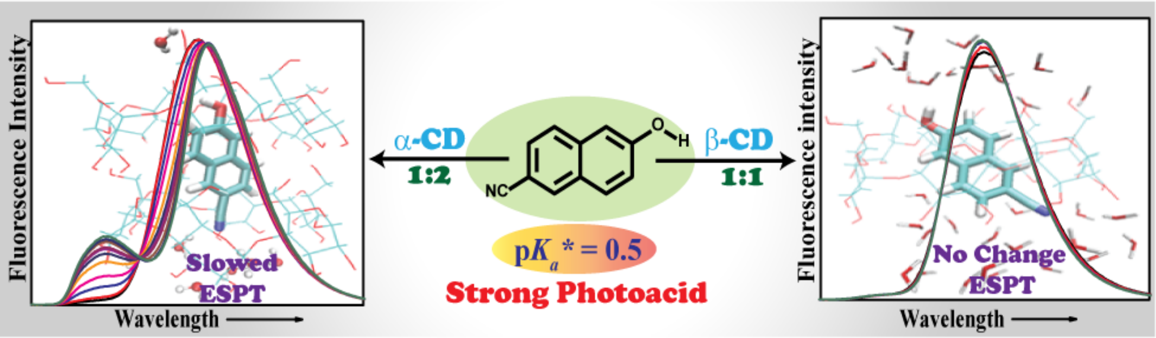

[#] This work has been communicated.

Chapter 7: Contrasting pK_a Shift and Fluorescence Modulation of 6-Cyano-2-Naphthol inside α- and β-Cyclodextrins

7.1. INTRODUCTION

Macrocyclic host-guest complexes have gained research attention due to their widespread applications across various fields, e.g., drug delivery, the pharmaceutical and food industries, sensing, catalysis, etc.[336-338] Most importantly, inclusion complex formation can dramatically alter the acid-base nature of a guest molecule. The modulation of the acid-base properties, as indicated by a pK_a shift, may have an enormous impact on the bioavailability of a guest drug molecule. Thus, it is very important to develop a clear understanding of the structure-function relationship, which causes the pK_a shift.

Several intriguing observations on the inclusion-induced pK_a shift have already inferred some valuable insights.[148, 339-340] The pK_a shift depends mainly on the electrostatic nature of the guest molecule at different protonation states and the type of the host macrocycle. For example, Hansen et al. showed that complexation with β-cyclodextrin (β-CD) lowers the pK_a of the guest 1-aminopyrene, whereas raises the pK_a of 1-naphthol.[148] As a result, the ESPT rate increases for 1-aminopyrene but decreases for 1-naphthol inside β-CD.[148] Shaikh et al. shows that complexation with cucurbit[7]uril (CB7, pK_a = 12.7) and β-CD (pK_a = 9.1) induces opposite pK_a shifts for acridine orange (AO), which may exist either as a cationic or neutral form with pK_a of 9.8 in water.[339] The guest becomes less acidic in CB7, because it preferentially stabilizes the protonated form by ion-dipole interaction, whereas, β-CD makes the guest more acidic by favorably stabilizing the neutral form over the cationic form.

Inclusion complex formation may also have a pronounced effect on the photophysics of aromatic guest fluorophores (photoacid), whose acidity increases markedly after photoexcitation. These photoacids eject a proton to the surrounding water molecules and this process is known as the excited-state proton transfer (ESPT). ESPT dynamics depends on the availability and the H-bonding nature of the water molecules. Inclusion complex formation can modulate the hydration environment around the photoacid and hence, can modulate the ESPT process. Generally, CD inclusion complex formation leads to suppression of ESPT rates compared to water for many photoacids, e.g., for 1- and 2-naphthol,[322-323] or naphthylamines,[341] hydroxypyrene derivatives.[152, 231, 342] However, enhancement of the deprotonation rate of the photoacid inside CD cavities is also reported as for carbazole,[343] or aminopyrene.[148]

In the previous *chapter 6*, we showed that 2-naphthol derivatives show a different amount of pK_a shifts inside β-CD.[344] The opposite pK_a shift basically results from the choice of the guest or the host that can stabilize either the neutral or the charged form of the guest and hence, a significant dissimilarity should be present between the chosen guests or hosts. Following our previous work, in this chapter, we have compared the pK_a shift of 6-cyano-2-naphthol (6CN-2OH) in two chemically similar cyclodextrins (α-CD vs. β-CD). α-CD has six glucopyranoside units, while β-CD has seven glucopyranoside units and interconnected by glycosidic α(1→ 4) linkages.[338, 345] α-CD is smaller in size than β-CD. The internal cavity diameter of α-CD is 5.3 Å. In contrast, for β-CD, it is 7.5 Å.[346] It would be interesting to see the nature of fluorescence modulation of the 6-cyano-2-naphthol with two cyclodextrins α-CD and β-CD, which may form different types of inclusion complexes.

7.2. RESULTS AND DISCUSSION

7.2.1. Absorption Spectra and pK_a Measurements:

The spectral features of 6CN-2OH in the presence of α-CD are distinctly different from that of β-CD. The absorption spectra of 6CN-2OH in water (pH = 5.8) exhibits an absorption maximum at 300 nm, which is the characteristic peak of the protonated form of 6CN-2OH. The absorption spectra undergo distinct changes upon change of pH. It was observed that the contribution of the lowest energy absorption band centered at ~300 nm decreases while a new band at ~326 nm gradually emerges with an increase in pH. (see *appendix* **Figure A.7.1**). The isosbestic point at ~306 nm indicates a transformation between protonated and deprotonated forms. The plot of the absorbance at a longer wavelength (360 nm), exclusively representing the deprotonated form against pH conveniently provides the pK_a (**Figure 7.1**). In the water, the ground-state pK_a value of 6CN-2OH was found to be 8.55 (**Table 7.1**), which is almost close to the earlier reported value (in the parentheses).[111] The variation of the absorption spectrum of the photoacid in the presence of α-CD was quite similar to that in water, but the transition from the protonated to deprotonated form occurs at a much higher pH (**Figure 7.1**). Thus, the pK_a becomes higher by more than two units from 8.55 to 10.76 after forming the inclusion complex with α-CD, in contrast to our earlier observation with β-CD whether inclusion lowers the pK_a compared to that in water (**Table 7.1**).[344] Hence, the enhancement of pK_a value in the presence of α-CD indicates that neutral form (protonated) of 6CN-2OH binds favourably with α-CD, whereas reduction of pK_a value in the presence of β-CD implies anionic form (deprotonated) is more stable inside the cavity.

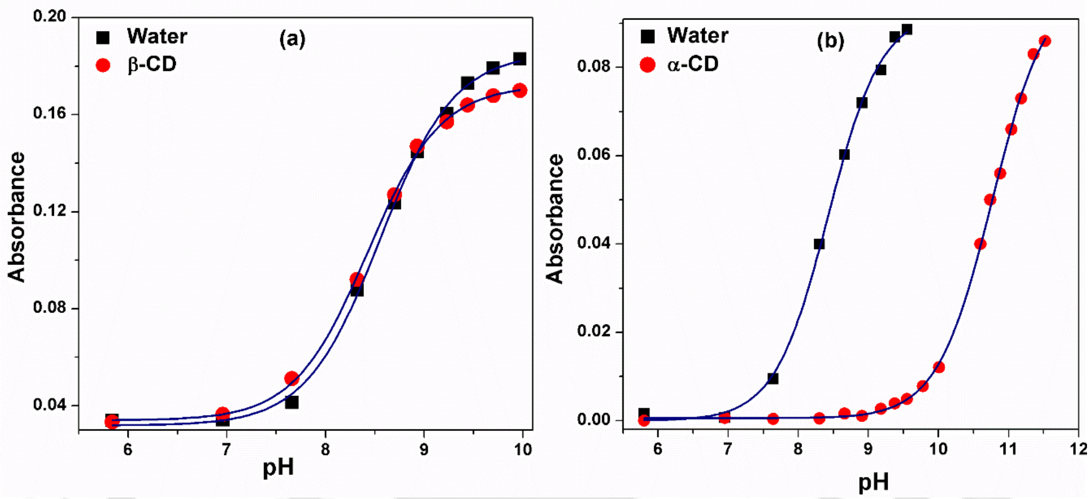

Figure 7.1. The plot of absorbance of the deprotonated (or base) form against pH of the solutions for 6CN-2OH, (a) 6CN-2OH:β-CD, and (b) 6CN-2OH:α-CD (absorbance at 360 nm).

Table 7.1. pK_a and pK_a^* of the free photoacid (in water) and complexed (with β-CD and α-CD).

Water		**β-CD complex**		**α-CD complex**	
pK_a	**pK_a^***	**pK_a**	**pK_a^***	**pK_a**	**pK_a^***
8.55 ± 0.03 (8.4[a])	0.63 (0.2[a])	8.42 ± 0.02	0.18	10.76 ± 0.02	3.77

[a]Taken from ref 106.

7.2.2. Steady-State Fluorescence Emission Measurements:

To get a clear insight into the complexation process, emission profiles of the photoacid 6CN-2OH were recorded in the presence of α-CD and β-CD having different cavity sizes (**Figure 7.2a and 7.2b**).

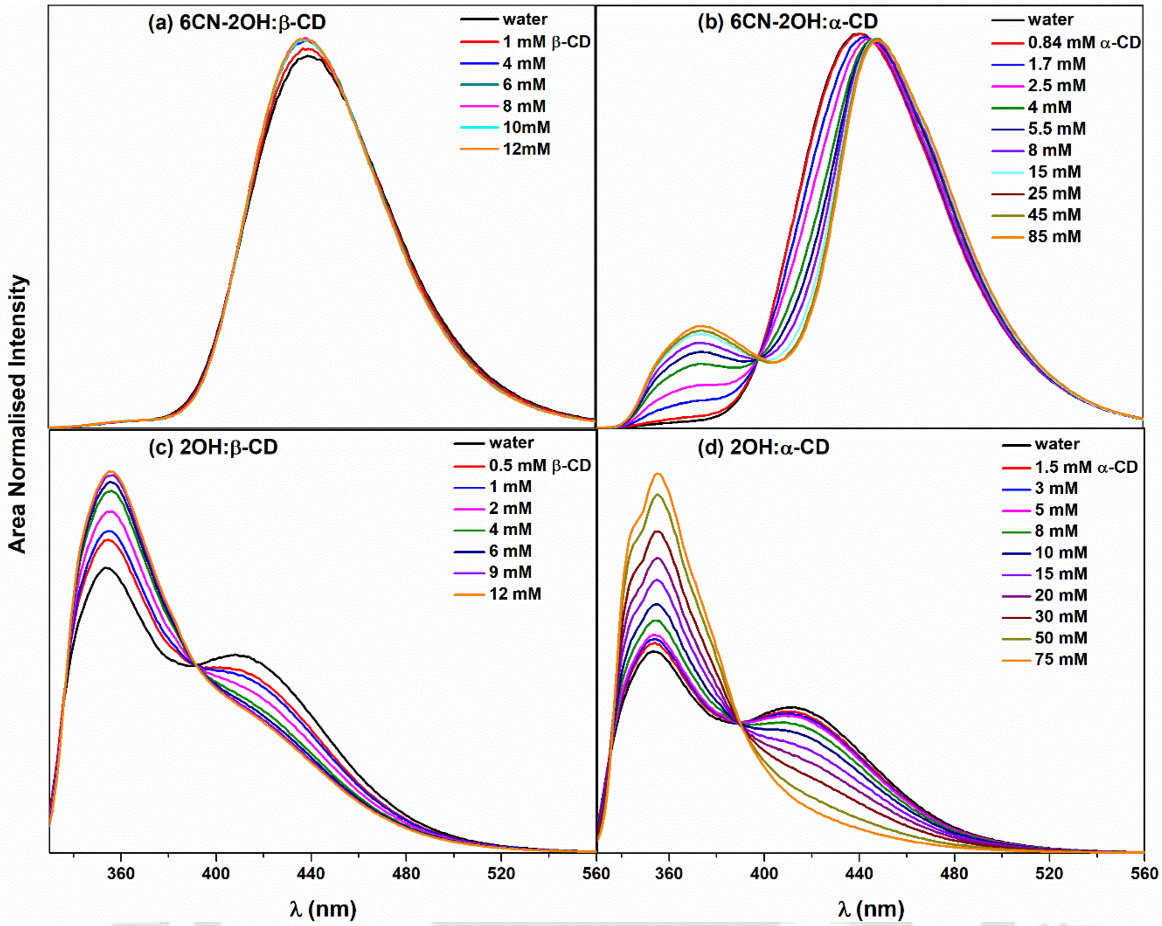

Figure 7.2. In the presence of various concentrations of β-CD and α-CD steady-state emission spectra of 6-cyano-2-naphthol (6CN-2OH) (a and b); and 2-naphthol (2OH) (c and d), respectively (λ_{ex} = 310 nm).

A protonated photoacid undergoes deprotonation in the excited state and usually shows two distinct bands representing emission from both the protonated and deprotonated form. However, the protonated emission band is so weak compared to the deprotonated band that the emission spectrum of 6CN-2OH in water almost appears to be a single band emission (**Figure 7.2**). The emission maximum of the deprotonated band of 6CN-2OH exhibits a peak at 440 nm in water. We noticed different modulation of the fluorescence spectrum of 6CN-2OH in the presence of α-CD and β-CD. We observed almost no change in the emission spectrum of 6CN-2OH in the presence of β-CD (**Figure 7.2a**).[344] However, the modulation of the emission spectrum in the presence of α-CD is quite significant; the protonated emission peak at ~ 370 nm becomes prominent and the deprotonated emission peak becomes narrower and shifted to higher wavelength upon gradual addition of α-CD. A clear isoemissive point at 398 nm confirms the presence of the coexistence of both protonated and deprotonated forms in the excited state. It is important to note that the distinct differential fluorescence modulation of the parent 2-naphthol (2OH) was not found for the α-CD and β-CD inclusion complexes.[145] The ESPT process of 2OH was suppressed for both CDs complexes; however the extent of suppression is more for 1:2 2OH:(α-CD)$_2$ complexes than 1:1 2OH:β-CD.

In order to check whether the excited state acidity (pK_a^*) of 6CN-2OH is affected or not in the presence of α-CD and β-CD, the excited-state pK_a^* value of 6CN-2OH was calculated using the Förster cycle.[102] The pK_a^* is found to be 0.63 in water. In the presence of α- vs. β-CD, the pK_a^* shows a different shift similar to the ground-state pK_a shift. The pK_a^* increases to 3.77 inside α-CD, whereas it decreases to 0.18 inside β-CD compared to water (see **Table 7.1** and *appendix* **Figure A.7.2**). Thus, we observed a different modulation of photoacidity of 6CN-2OH in the presence of α-and β-CD.

7.2.3. Time-Resolved Fluorescence Decay Measurements:

Modulation in radiative properties of 6CN-2OH upon interaction with α- and β-CD is illustrated by time-resolved fluorescence lifetime measurements. 6-cyano-2-naphthol (6CN-2OH) is a strong photoacid and undergoes ultrafast ESPT in water. We know that ultrafast fluorescence decay measurement could reveal the detailed scenario of the ESPT dynamics and should be measured in a femtosecond up-conversion set up. But unfortunately, we do not have a femtosecond up-conversion setup in our lab and at this excitation wavelength (third harmonic of Ti-Saphire laser), it may available in few places. Since we are interested more about the comparison rather than the absolute dynamics, regular TCSPC measured fluorescence decays can serve the purpose satisfactorily. Fluorescence decays of 6CN-2OH were measured at two wavelengths of 350 nm and 470 nm for the protonated and deprotonated forms, respectively. All fluorescence decays can be fitted to a bi-exponential function (**Table 7.2**).

In water, the decay of the protonated form (λ_{em} = 350 nm) of 6CN-2OH shows a major fast component of 0.16 ns (99%), and a minor component of 5.20 ns (1%) (**Figure 7.3** upper panel and **Table 7.2**). The minor component may be due to geminate recombination, which is usually reported for strong photoacids in water.[326-327] The deprotonation time constant of 6CN-2OH in water was found to be is 0.17 ns.[344] In the presence of β-CD, the fluorescence decay (λ_{em} = 350 nm) did not show any change, but a significant slowing down was observed in the presence of α-CD. The fast lifetime component (major) increases from 0.16 ns in water to 1.72 ns at maximum α-CD concentration. Increased lifetime of 6CN-2OH in the presence of α-CD indicates retardation of the ESPT process inside the nanocavity of α-CD.

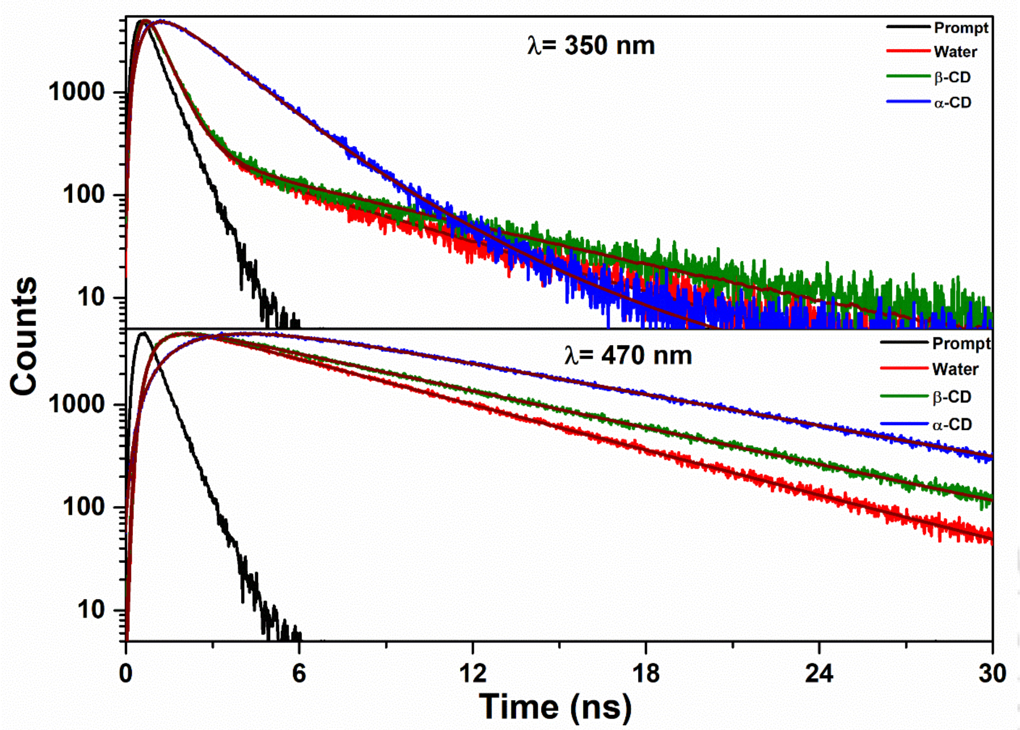

Figure 7.3. Fluorescence decays of 6CN-2OH of the protonated (upper panel, emission at 350 nm) and deprotonated (bottom panel, emission at 470 nm) forms in water, the presence of β-CD ([β-CD] = 12 mM) and α-CD ([α-CD] = 85 mM), respectively, upon excitation λ_{ex} = 292 nm.

No significant difference is observed in the rise component of the deprotonated form (λ_{em} = 470 nm) in the absence and presence of β-CD. However, the rise time of the deprotonated form (λ_{em} = 470 nm) of 6CN-2OH increases to 1.82 ns in the case of α-CD, indicating a marked slowing down of ESPT (**Figure 7.3** bottom pannel and **Table 7.2**). Furthermore, we found that the deprotonation time of 6CN-2OH increases from 0.17 ns in water to 2.4 ns in the presence of the α-CD but almost none for β-CD (see *appendix* **Figure A.7.3** and **A.7.4**). As an outcome of the fluorescence lifetime measurements, 6CN-2OH exhibits more vivid changes in lifetime profiles (deprotonation time) in the presence of α-CD compared to β-CD.

Table 7.2. Fit parameters of fluorescence decays of 6CN-2OH in water and in the presence of β-CD (12 mM) and α-CD (85 mM) at emission wavelengths of 350 nm and 470 nm.

System	**λ_{em} (nm)**	**a_1**	**a_2**	**τ_1 (ns)**	**τ_2 (ns)**	**χ^2**	**τ_n (ns)**	**τ_d (ns)**
water	350	0.99	0.01	0.16	5.20	1.02	4.8	0.17
	470	-0.30	0.70	0.17	5.88	1.01		
βCD	350	0.99	0.01	0.18	6.54	1.12	6.4	0.19
	470	-0.23	0.77	0.25	7.20	1.14	-	-
α-CD	350	0.94	0.06	1.72	7.80	1.06	6.06	2.4
	470	-0.47	0.53	1.82	8.38	1.03		

7.2.4. Time-Resolved Fluorescence Anisotropy Decay Measurements:

Time-resolved fluorescence anisotropy decay of 6CN-2OH was measured to understand how CD inclusion affects the rotational motions of the 6CN-2OH. Anisotropy decay profiles of 6CN-2OH in water and in the presence of α- and β-CD host molecules are shown in **Figure 7.4** and **Table 7.3**. Since the fluorescence intensity of 6CN-2OH at 350 nm is very low in the water, hence the anisotropy decay was measured at 470 nm. 6CN-2OH exhibits mono exponential anisotropy decay in water with a rotational relaxation time of ~ 330 ps. However, it is important to mention that the measured rotational relaxation time in water may not be measured accurately by using our TCSPC setup due to the low time resolution of our set up. The rotational relaxation becomes significantly slower in the presence of both the CDs. The rotational relaxation times are 650 ps and 1100 ps in the presence of β-CD (12 mM) and α-CD (130 mM), respectively. In the presence of CD host molecules, the rotational relaxation time of 6CN-2OH increases because of increased rigidity due to the formation of an inclusion complex with the host. Furthermore, higher rotational relaxation time in the presence of α-CD implies that 6CN-2OH is more restricted inside the α-CD cavity compared to β-CD, due to the smaller cavity size of the former host. The hydrodynamic diameter of the overall system is much higher when the photoacid 6CN-2OH confines itself inside the CD cavity. To estimate the size of these CD complexes, we calculated the hydrodynamic radius (r_h) using the rotational relaxation time constant. The rotational relaxation time constant of anisotropy decay (τ_R) is related to the hydrodynamic radius (r_h) by the stokes–Einstein equation,[347]

$$\tau_R = \frac{4\pi\eta r_h^3}{3kT} \tag{7.1}$$

where r_h is the hydrodynamic radius of the CD complexes, η is the viscosity of the medium (1.336 and 1.026 mPa S at 298 K for α-CD and β-CD, respectively),[348] and k the Boltzmann constant and T is the experimental temperature which is 298 K.

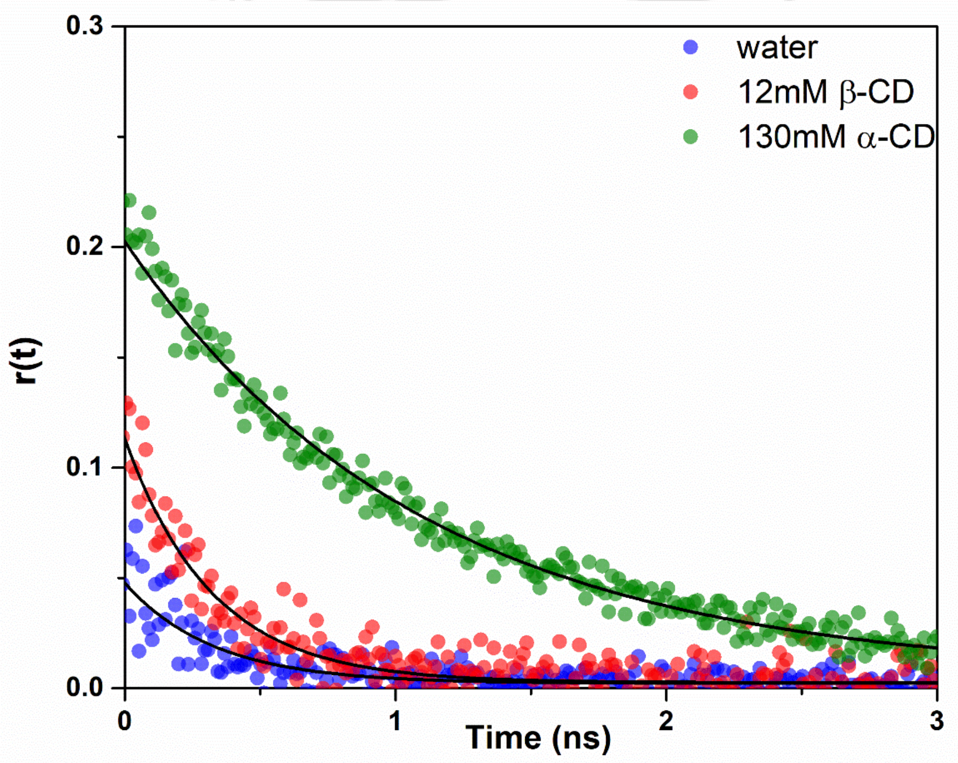

Figure 7.4. Fluorescence anisotropy decay of 6CN-2OH (λ_{em} = 470 nm and λ_{ex} = 292 nm) in water (blue) and in the presence of β-CD (12 mM, red) and α-CD (130 mM, green), respectively.

In the case of the 6CN-2OH:α-CD complex, the estimated hydrodynamic radius (r_h) is 9.3 Å. Thus, the estimated diameter of the 6CN-2OH:α-CD complex is ~ 18.6 Å. Since the reported height of the cyclodextrins are 7.9 Å,[346] hence the diameter of the complex (~18.6 Å) is roughly equal or greater than the sum of the height of two α-CD molecules. Therefore, we can conclude that 1:2 complex is formed between 6CN-2OH and α-CD, i.e., 6CN-2OH:(α-CD)$_2$. The estimated hydrodynamic radius (r_h) is ~ 8.5 Å for 6CN-2OH:β-CD complex. This corresponds the calculated diameter ($2r_h$) to be 17 Å. Previously, we confirmed 6CN-2OH forms 1:1 complex with β-CD from our ITC and fluorescence measurement.[344] Therefore, this high value of diameter implies that a large portion of the probe is projected out of the cavity of β-CD.

Table 7.3. Parameters of fluorescence anisotropy decay of 6CN-2OH in water, 12 mM β-CD, and 130 mM α-CD.

System	r_0	τ_r (ps)	χ^2
Water	0.05	330	1.05
β-CD (12 mM)	0.12	650	1.05
α-CD (130 mM)	0.20	1100	1.10

7.2.5. Isothermal Titration Calorimetric Measurements:

To compare the binding affinity of the 6CN-2OH between α-CD and β-CD, we performed isothermal titration calorimetry (ITC) measurement. ITC measurement confirmed that 6CN-2OH forms 1:1 inclusion complex with β-CD with a moderate binding constant of 580 M^{-1}. The binding process is enthalpy-driven ($\Delta H = -9.07$ kcal mol^{-1}) process with a negative entropy change ($\Delta S = -5.29$ kcal mol^{-1}), and the overall process is a spontaneous one ($\Delta G = -3.78$ kcal mol^{-1}) (**Figure 7.5a** and **Table 7.4**).[344] In contrast, the obtained ITC data of the interaction between 6CN-2OH and α-CD can be fitted by a two-site sequential binding model (**Figure 7.5b**). Therefore, the complexation between the photoacid 6CN-2OH and α-CD may be of 1:2 type.

Upon gradual addition of α-CD, at first, a 1:1 complex (K_1) is formed, and then the 1:2 complex (K_2) is formed. For the first 1:1 complexation (6CN-2OH:α-CD), the binding constant (K_1) value is 0.51×10^2 M^{-1}. It was observed that a favorable exothermic enthalpic ($\Delta H < 0$) contribution is coupled with an unfavorable entropic (negative ΔS) contribution for 6CN-2OH:α-CD complex (**Table 7.4**) as earlier observed for 6CN-2OH:β-CD complex. The Gibb's free energy of formation of 6CN-2OH:α-CD complex is –2.26 kcal mol^{-1}. In the literature, two types of hydrophobic interactions are reported for the host-guest system- classical hydrophobic interaction (entropy-driven process (T$\Delta S > 0$)), and non-classical hydrophobic interaction (enthalpy driven process ($\Delta H < 0$)).[328, 349] Therefore, we found a non-classical hydrophobic interaction for the 1st 1:1 binding of 6CN-2OH:α-CD. Dominant enthalpic contribution ($\Delta H < 0$) over entropic contribution can be rationalized by the displacement of the cavity water molecules. These water molecules are extremely disordered owing to their inability to form a hydrogen-bonding network inside the α-CD cavity. Due to complexation, these trapped water molecules are released from the cavity and form new hydrogen bonds with bulk water. This leads to a decrease in the disorder. As a result, the entropy of the system decreases.[350-351]

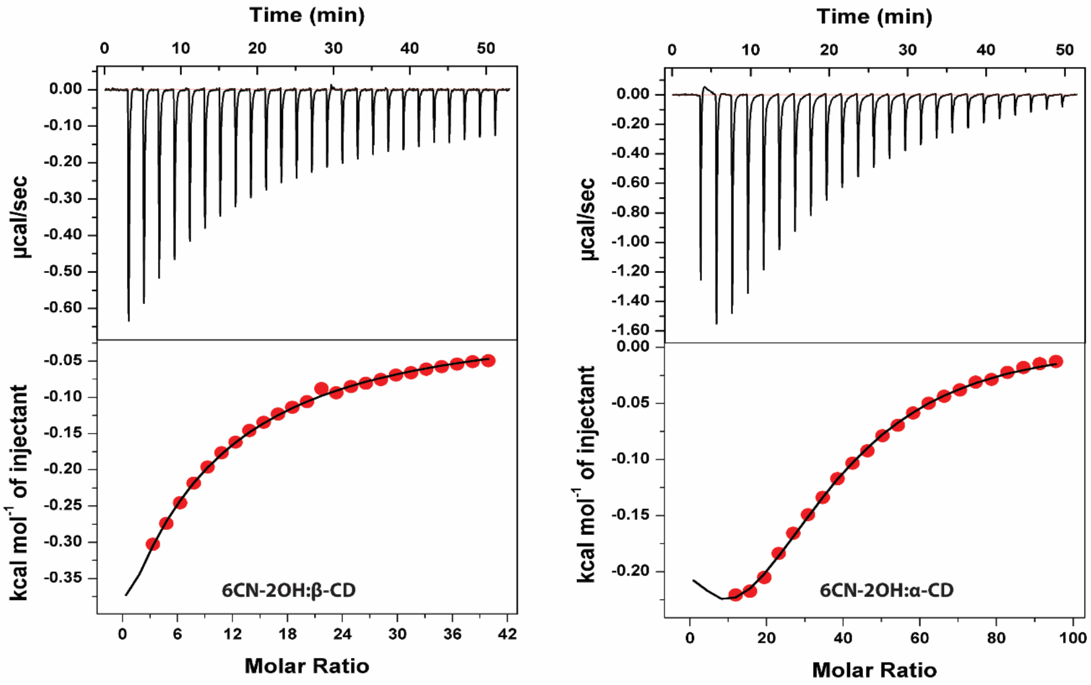

Figure 7.5. ITC profiles for the titration of 6CN-2OH *vs.* CD in terms of molar ratio ([6CN-2OH] / [CD]) at 298 K (a) β-CD and (b) α-CD. The upper part of the ITC diagram is the primary heat burst curves after correction of the heat of dilution, and the bottom part is ITC enthalpograms. The solid lines passing through the points are the best fit lines for one-site and two-site sequential binding model to the raw data of (a) β-CD and (b) α-CD, respectively.

For the 2nd sequential step (6CN-2OH:(α-CD)$_2$), the binding constant (K_2) is 9.82×10^2 M^{-1}. Interestingly, we found that the 2nd binding step is entropy-driven ($|T\Delta S|>|\Delta H|$) with spontaneous Gibb's free energy change (ΔG= -2.97 kcal mol^{-1}). In literature, these entropy-driven interactions are known as classical hydrophobic interaction. In the 2nd step, the positive entropy change can be explained by the dehydration of the ordered water molecules. The structured water molecules surrounding the 6CN-2OH and α-CD collapse due to complete insertion into the cavities and attain a more random conformation.[352] Therefore, the entropy of the system increases ($\Delta S > 0$). Thus, the overall interaction of 6CN-2OH with α-CD is an entropy-driven, thermodynamically favourable process. Furthermore, the overall binding constant value ($K = K_1 \times K_2$) obtained from ITC measurement is 50082 M^{-2}.

Table 7.4. Thermodynamic binding parameters of photoacid 6CN-2OH with β-CD and α-CD obtained from ITC measurements.

System	**K_1 (M^{-1})**	**ΔH_1 (kcal mol^{-1})**	**$T\Delta S_1$ (kcal mol^{-1})**	**ΔG_1 (kcal mol^{-1})**	**K_2 (M^{-1})**	**ΔH_2 (kcal mol^{-1})**	**$T\Delta S_2$ (kcal mol^{-1})**	**ΔG_2 (kcal mol^{-1})**
β-CD	5.81 (±0.08) × 10^2	−9.07 (±0.07)	−5.29	−3.78	-	-	-	-
α-CD	0.51 (±0.03) × 10^2	−40.69 (±2.22)	−38.43	−2.26	9.8 (±0.5) × 10^2	32.76 (±2.34)	35.73	−2.97

7.2.6. Molecular Dynamics Simulation:

To get a molecular picture of the 1:2 complex as well as to gain insight into the stability inclusion complex, we performed molecular dynamics simulation. We prepared three different types of configurations depending upon α-CD orientation (see *appendix* **Figure A.7.5**). Out of these three possible types of the 1:2 6CN-2OH:$(\alpha\text{-CD})_2$ complexes, we found that the ‘Type 1’ and ‘Type 3’ configurations are stable throughout the 80 ns MD trajectories (**Figure 7.6**). However, in the case of ‘Type 2’ configuration, 1:2 complex releases one CD unit after ~ 20 ns, and after that remains as 1:1 complex (6CN-2OH:α-CD) for the rest of the simulation period. Thus, only two types (‘Type 1’ and ‘Type 3’) of 1:2 complexes may be possible, and hence, all the post-simulation analyses are performed taking the last 20 ns frames of these simulations. Details of the MD simulations of 6CN-2OH in water and inside different CDs have been discussed in *chapter 2* (see *section 2.3*).

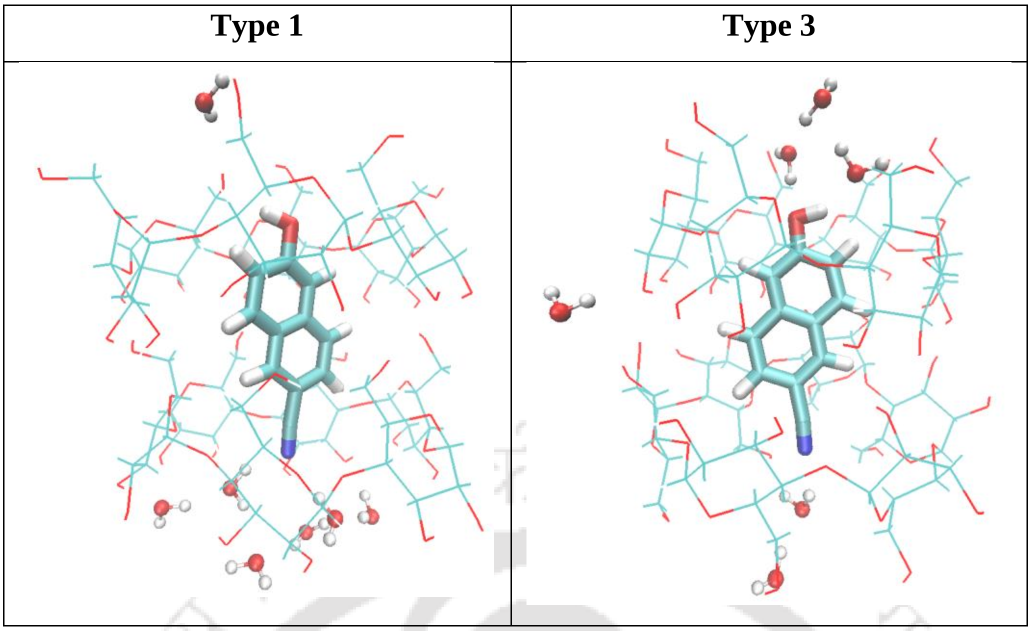

Figure 7.6. Representative MD simulation snapshot of ‘Type 1’ and ‘Type 3’configuration of the 1:2 inclusion complexes of 6CN-2OH after 80 ns simulation. Water molecules are presented as a CPK model within 5 Å around the photoacid.

The stability of the 1:2 inclusion complex during the simulation was further checked by calculating the separation distance between the center of masses (COM) of the two α-CD rings (see *appendix* **Figure A.7.6**). Nearly invariant COM-COM distance in all the frames suggests that the 1:2 complexation remains intact throughout the simulation period. Furthermore, average COM-COM distances are very similar for both ‘type 1’ (7.70 ± 0.001 Å) and ‘type 3’ (7.67 ± 0.002 Å) configurations.

7.2.6.1. Radial Distribution of Water Molecules Around the Hydroxyl Group of Photoacids:

The distribution of water molecules around the proton donating hydroxyl group may be most important in the ESPT process. Therefore, we calculated the radial distribution function (RDF) between the O-atom of the hydroxyl group of 6CN-2OH and O-atom of the water molecules, and compared the result with the RDF obtained in water and the 1:1 β-CD inclusion complex (**Figure 7.7 (a)**).

The O-O_w RDF of 6CN-2OH shows a strong peak at ~2.70 Å, and the first RDF minimum (limit of the first hydration shell) is observed at 3.35 Å in all cases

(**Figure 7.7a**). The sharp first RDF peak of $O{-}O_w$ of 6CN-2OH at ~2.70 Å indicates the possibility of hydrogen bond formation between the hydroxyl group of 6CN-2OH and water molecules ($O{-}H\cdots O_w$). The height of the 1st peak is proportional to the number of water molecules present in the first hydration shell of 6CN-2OH. The 1st peak height follows a moderate variation in the order - water > β-CD > α-CD Type 3 > α-CD Type 1. This order implies that the hydroxyl group of 6CN-2OH is less hydrated upon inclusion inside the CD cavity, and perturbation of the water density is more for α-CD compared to β-CD. Furthermore, among the two configurations of 'Type 1' and 'Type 3' of α-CD complex, we observed that the 1st RDF peak strength of 'Type 1' is very small compared to 'Type 3'. This is possibly due to the fact that the O-atom of the hydroxyl group of the 6CN-2OH of 'Type 1' configuration strongly forms a hydrogen bond with the O-atom of the secondary hydroxyl group of the α-CD (see *Appendix*, **Figure A.7.7,** and **A.7.8**). But such kind of interaction is absent in the 'Type 3' configuration. Since the hydroxyl group of the 6CN-2OH is already engaged with the secondary hydroxyl group of the α-CD, hence –OH group of the 6CN-2OH is less available towards water molecules for 'Type 1'. It is important to note that the distribution of water molecules becomes severely perturbed for 2nd and 3rd solvation shells around the hydroxyl group of the 6CN-2OH in the presence of the CD cavities compared to bulk water. Hence, 2nd and 3rd RDF peaks due to 2nd and 3rd solvation shells are less profound in the presence of CDs.

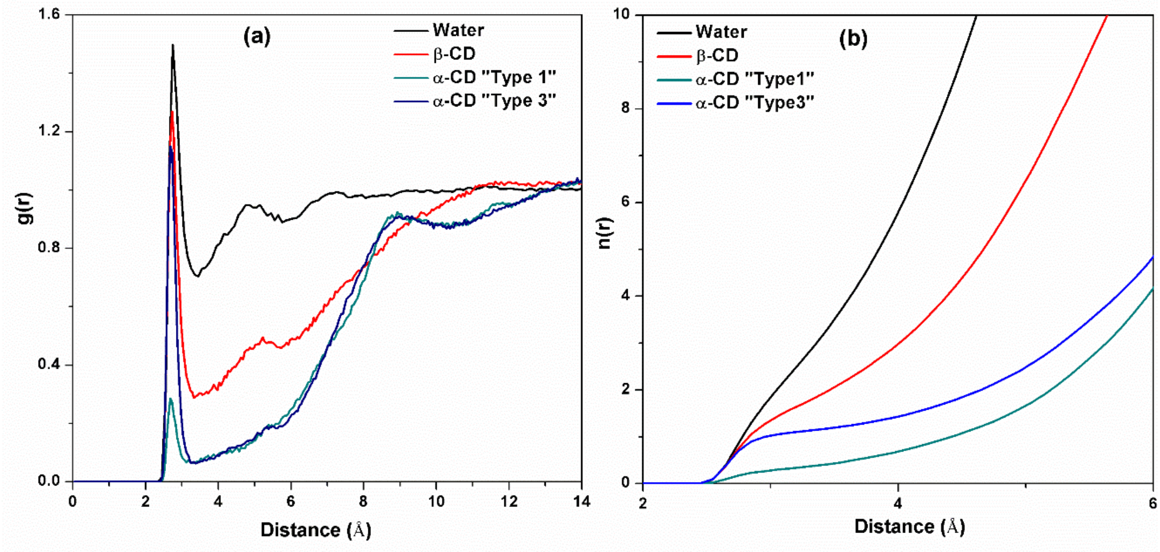

Figure 7.7. (a) Radial distribution function, and (b) running coordination number involving oxygen atom (of 6CN-2OH) - oxygen atom (O_w) of water situations in neat water, β-CD and α-CD.

7.2.6.2. Running Coordination Number:

To get more insights into the solvation of 6CN-2OH molecule by water molecules, the running coordination number (RCN) around the O atom of the hydroxyl group of the 6CN-2OH was determined for the 1st solvation shell. In **Figure 7.7b**, the change in the RCN value of the O-atom of 6CN-2OH was plotted as a function of the distance between O-Ow. The average number of water molecules present around hydroxyl oxygen atom of 6CN-2OH was determined using site-site distribution function, $g_{\alpha\beta}(r)$, by the following equation,

$$n_i(r') = 4\pi\rho_i \int_0^{r'} g_{\alpha i}(r) r^2 \mathrm{d}r \qquad (7.2)$$

Where ρ_i is the average number density of the solvent *i* in the system. We took the cut off distance for 1st water shells as 3.35 Å, which corresponds to the 1st minima in the RDF.

In the current study, we are focused on the 1st solvation shell water molecules as these water molecules may directly engage with the 6CN-2OH to form hydrogen bonds and participate in the ESPT process. The average number of water molecules within the first solvation shell of the 6CN-2OH in water is ~ 2.97. Previously, it was found that the average number of the first solvation shell molecule decreases to 1.84 in the 1:1 6CN-2OH:β-CD complex.[344] Here, in the presence of α-CD cavities, the average number of the first solvation shell water molecules are 0.38 and 1.15 for ‘Type 1’ and ‘Type 3’ configurations, respectively (**Table 7.5**). It is evident from the RCN value that the number of water molecules in the 1st solvation shell is markedly lesser for α-CD complexes (especially for Type 1) compared to β-CD complex and neat water.

Table 7.5. The average number of water molecules in the first water shell in neat water, 6CN-2OH:β-CD, and 6CN-2OH:$(\alpha\text{-CD})_2$ system for two different configurations.

Solvation shell	**Neat water**	**β-CD**	**α-CD Type 1**	**α-CD Type 3**
1st	2.97	1.84	0.38	1.15

7.2.6.3. Hydrogen Bonding Analysis:

To get more quantitative information about the hydrogen bonding interaction between 6CN-2OH and water molecules in neat water and the presence of CDs, we performed the hydrogen bond analysis between the hydroxyl group of 6CN-2OH and water molecules. It is important to note that the hydroxyl group of 6CN-2OH can act as both - hydrogen bond donor and acceptor. Moreover, in our present system, they can form hydrogen bonds at two different sites – (i) bulk water or (ii) the primary and secondary hydroxyl group of CD. Since our primary interest is to study the perturbation of ESPT dynamics of 6CN-2OH inside hydrophobic cavities of CD, hence we are mainly focused on the hydrogen bonding between 6CN-2OH and water. The applied geometric criteria for hydrogen bond formation is the maximum oxygen–oxygen interatomic distance is less than or equal to 3.35 Å (1st RDF minima between oxygen atom (6CN-2OH)-oxygen atom of water) and, simultaneously, the angle $O\text{-}H\cdots O_w$ is greater than or equal to 135°. The average number of 6CN-2OH-water hydrogen bonds for ‘Type 1’ and ‘Type 3’configurations of α-CD are 0.21 and 0.97, respectively (in **Table 7.6**). The hydrogen bonding analysis results are in accordance with RCN and RDF results. Moreover, we also observed that compared to bulk water and β-CD, the average number of hydrogen bonds formed by 6CN-2OH is reduced drastically in the presence of α-CD.

Table 7.6. The average number of photoacid−water hydrogen bonds.

H-bond (6CN:O1-Water:O)	Neat water	β-CD	α-CD Type 1	α-CD Type 3
Total fraction	1.94	1.42	0.21	0.97

Thus, MD simulations showed that the perturbation of the H-bonding network of water molecules around the hydroxyl group of 6CN-2OH is more significant in the presence of α-CD (especially for Type 1) than β-CD.

7.3. SUMMARY AND CONCLUSION

In this chapter, we have demonstrated contrasting pK_a shift and different fluorescence modulation of the strong photoacid 6CN-2OH inside the nanocavity of two cyclodextrins, α-CD, and β-CD. The pK_a and pK_a^* of the 6CN-2OH increases upon complexation with α-CD, while decreases upon complexation with β-CD compared to water. In bulk water, 6CN-2OH exhibits a single emission peak, which is originated from the deprotonated form (RO^-*). Interestingly, the emission intensity of the protonated form (ROH*) of 6CN-2OH increases with the gradual addition of α-CD but almost no change in the presence of β-CD. Fluorescence decays show that the ESPT dynamics is retarded inside the α-CD cavity. In contrast, we did not observe any change in the decay component in the presence of β-CD. ITC measurement confirms that α-CD forms 1:2 inclusion complex with 6CN-2OH, whereas β-CD forms 1:1 complex. Strikingly, the binding affinity for β-CD complexation is less compared to α-CD complexation. Time-resolved fluorescence anisotropy decay shows significantly lower the rotational motion of 6CN-2OH for the α-CD complex compared to the β-CD complex. This result indicates that 6CN-2OH is entirely trapped inside the hydrophobic cavity of the capsule formed by two α -CD molecules. Finally, the molecular picture of the 1:2 and 1:1 inclusion complex of 6CN-2OH with α-CD and β-CD are obtained by MD simulation. Moreover, MD simulation analysis showed that the distribution of water molecules around the proton-donating hydroxyl group of the 6CN-2OH decreases in the order – water> β-CD > α-CD. Based on all the above observations, we may propose that the retardation of EPST dynamics of 6CN-2OH inside the α-CD cavity compared to β-CD may be due to the complete encapsulation of 6CN-2OH by two α-CD cavities. As a consequence, the number of water molecules engaged in the ESPT of 6CN-2OH decreases, and the hydrogen-bonding network of water molecules with 6CN-2OH disrupt in the presence of α-CD. Thus, the significant essence of this study is that the fluorescence modulation of the 6CN-2OH is different in different confined environments.

Appendix

For Chapter 3.

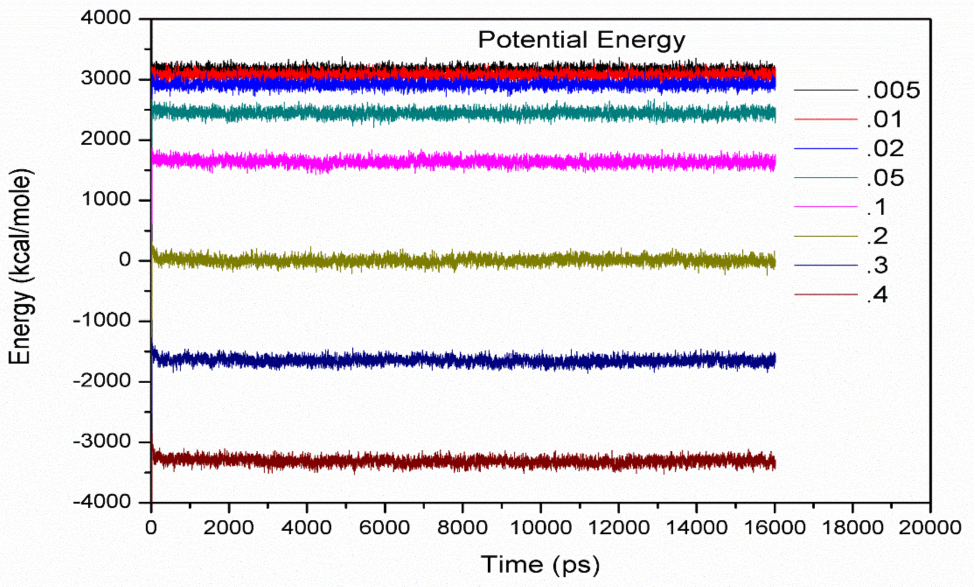

Figure A.3.1. Potential Energy of simulated systems at different mole fractions of phenol.

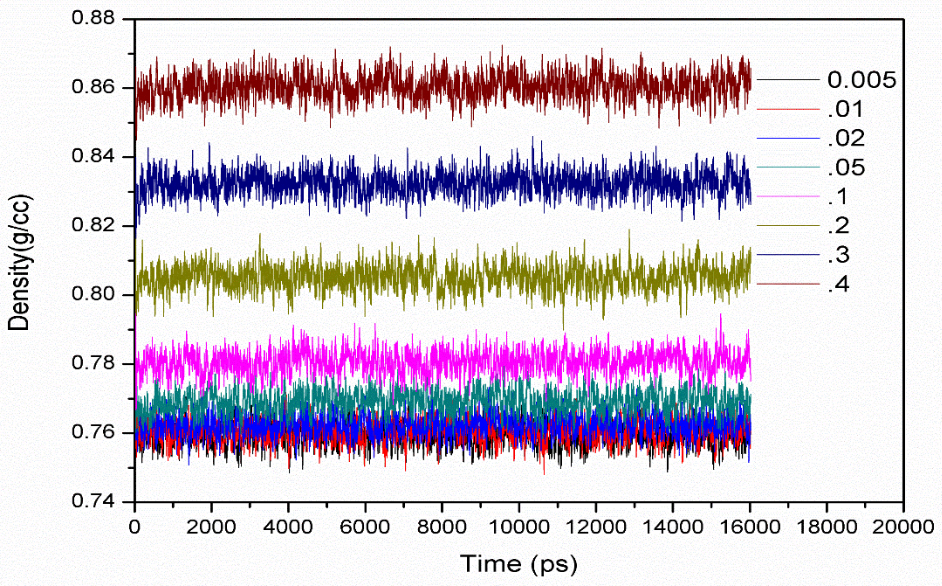

Figure A.3.2. The variation of density within the simulation period for different the systems at various mole fractions of phenol.

For Chapter 4.

Table A.4.1. Electronic Excitation Energies (in eV) and Corresponding Oscillator Strengths (in the Parenthesis) of the Low-Lying Electronically Excited States Calculated from the Optimized Excited State of Hydrogen-Bonded C102-phenol (1:1) Complexes in cyclohexane solvent (using CAM-B3LYP functional with basis set 6-311G++(d,p) in cyclohexane (IEFPCM) solvent)

Distance (Å)	**First Excited state (S_1) eV**	**Second Excited state (S_2) eV**	**Third Excited state (S_3) eV**
0.970	1.451 (0.001)	3.019 (0.082)	3.187 (0.434)
1.094	1.969 (0.004)	3.223 (0.576)	3.747 (0.003)
1.194	3.325 (0.680)	3.587 (0.003)	4.327 (0.008)
1.294	3.355 (0.693)	3.943 (0.001)	4.338 (0.005)
1.394	3.375 (0.697)	4.208 (0.001)	4.345 (0.003)
1.494	3.389 (0.698)	4.339 (0.003)	4.425 (0.000)
1.594	3.399 (0.698)	4.345 (0.002)	4.587 (0.000)
1.744	3.41 (0.697)	4.347 (0.002)	4.731 (0.000)

For Chapter 5.

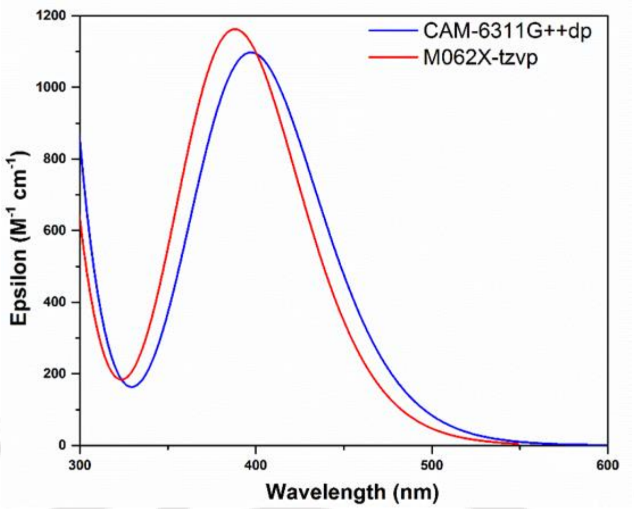

Figure A.5.1. Calculated absorption of HMQ^{2+} with 4-methoxyphenol is presented. All the spectra were calculated using TD-DFT method using CAM-B3LYP-D3/6-311++G** and M06-2X/TZVP with SMD (water) solvent model.

For Chapter 6.

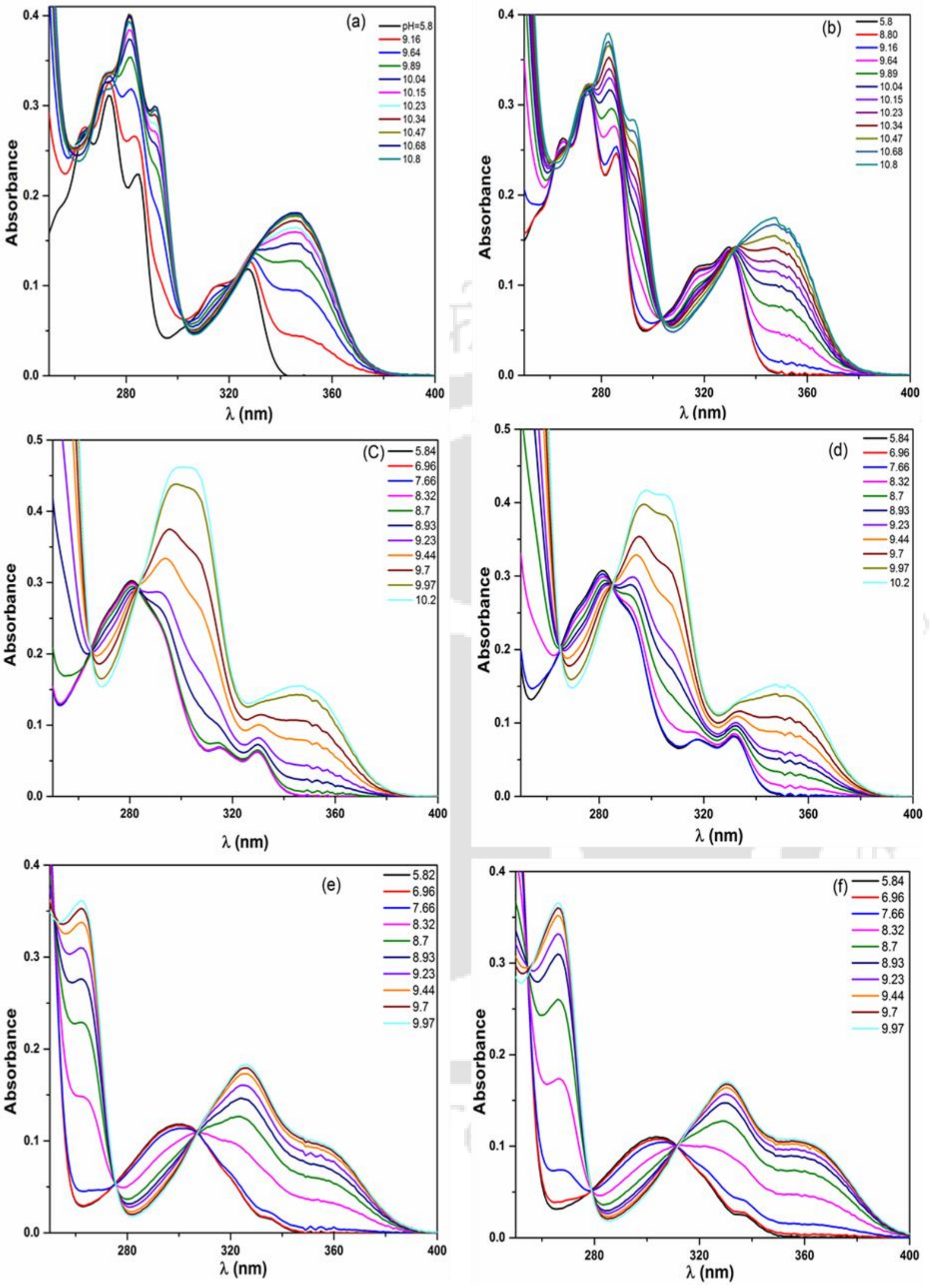

Figure A.6.1. Absorption spectra of different photoacids and their complexes with β-CD at different pH values – (a) 2OH, (b) 2OH:β-CD, (c) $6SO_3$-2OH, (d) $6SO_3$-2OH:β-CD, (e) 6CN-2OH, (f) 6CN-2OH:β-CD.

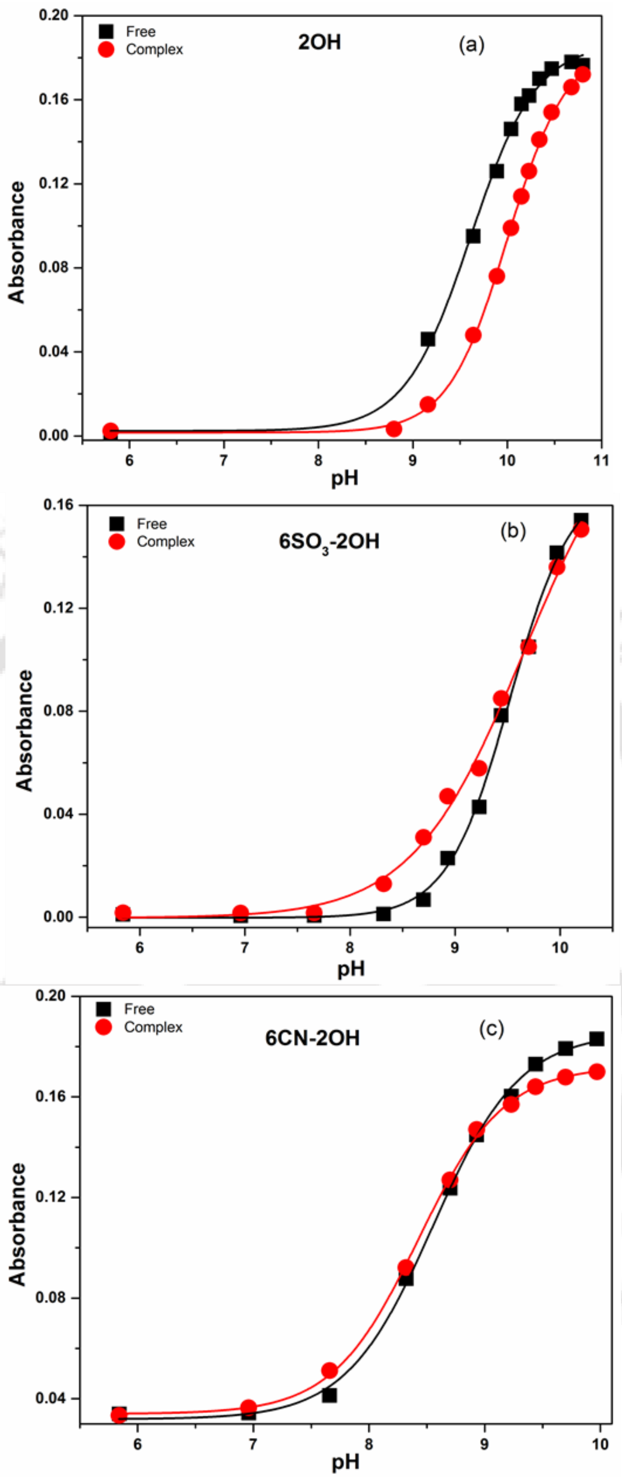

Figure A.6.2. The plot of absorbance of the deprotonated (or base) form against pH of the solutions for (a) 2OH and 2OH:β-CD (absorbance at 342 and 348 nm respectively), (b) 6SO$_3$-2OH and 6SO$_3$-2OH:β-CD (absorbance at 348 nm), (c) 6CN-2OH and 6CN-2OH:β-CD (absorbance at 326 and 330 nm respectively). The solid line represents a fit equation (4).

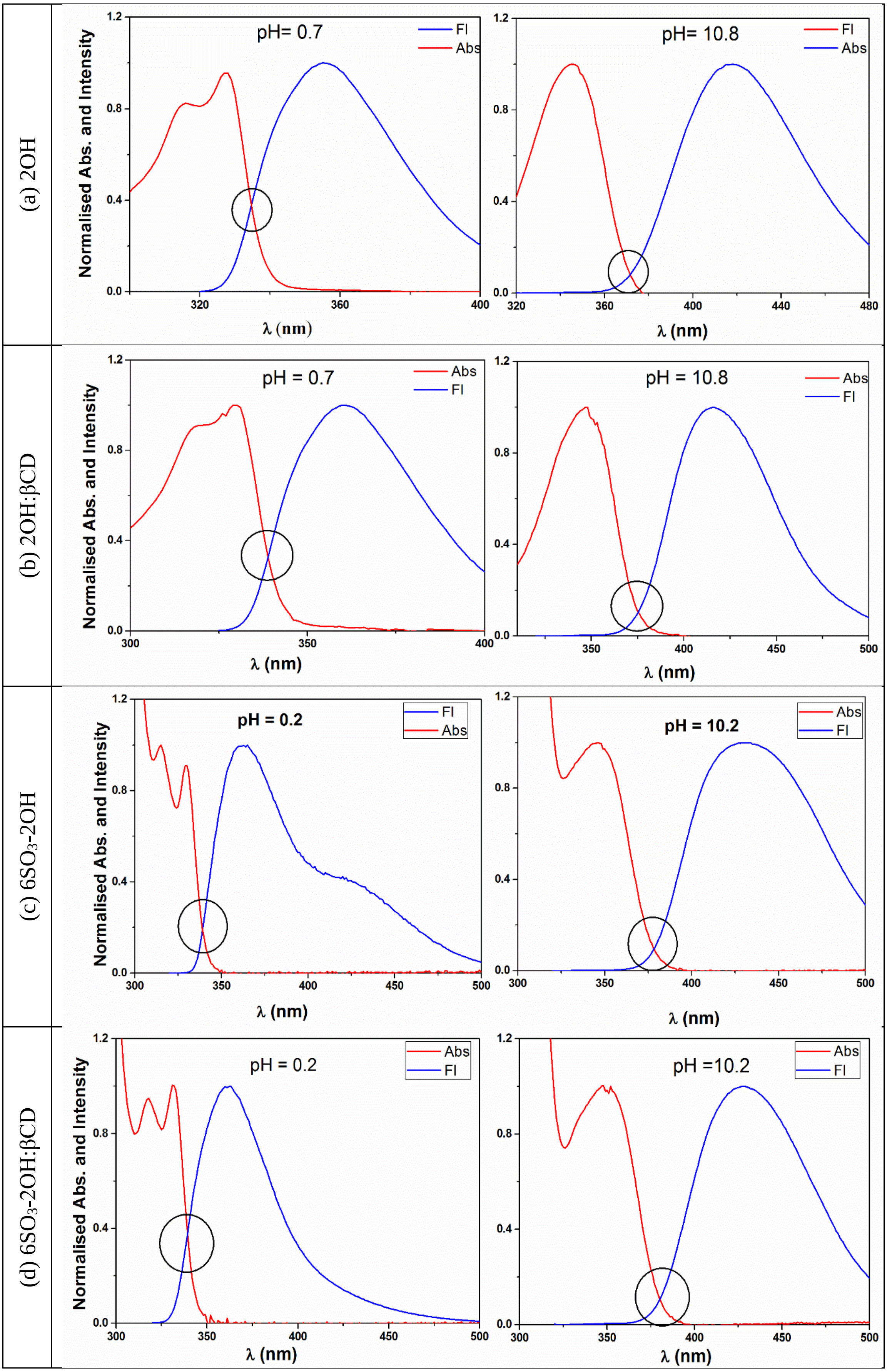
(a) 2OH
(b) 2OH:βCD
(c) 6SO$_3$-2OH
(d) 6SO$_3$-2OH:βCD
Normalised Abs. and Intensity
λ (nm)
pH= 0.7
pH= 10.8
pH = 0.7
pH = 10.8
pH = 0.2
pH = 10.2
pH = 0.2
pH =10.2
Fl
Abs
0.0
0.4
0.8
1.2
300
320
350
360
400
440
450
480
500

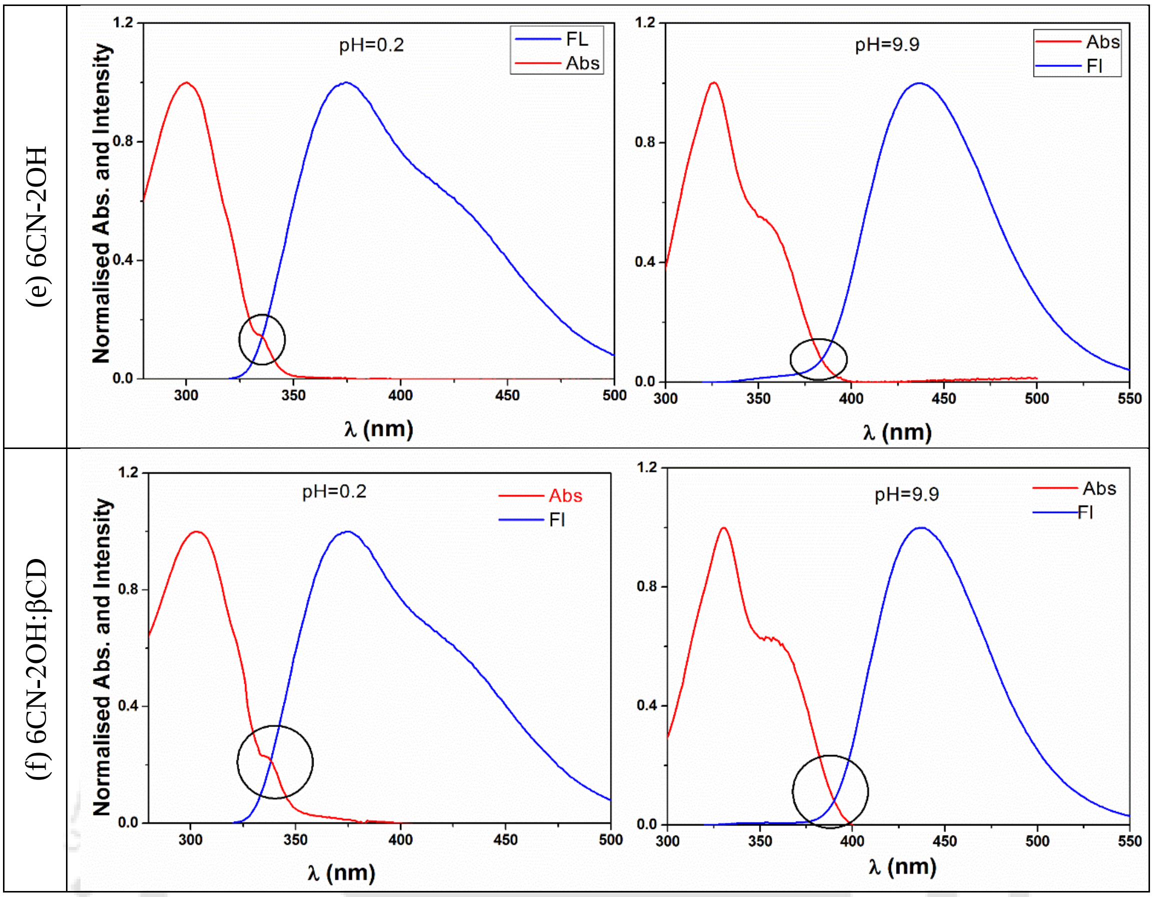

Figure A.6.3. Normalized absorption and emission spectra of the protonated (or acid) and deprotonated form of (a) free 2OH and (b) complexed 2OH with βCD (measured at pH 0.7 and pH 10.8 respectively), (c) free $6SO_3$-2OH and (d) complexed $6SO_3$-2OH with βCD (measured at pH 0.2 and pH 10.2 respectively), (e) free 6CN-2OH and (f) complexed 6CN-2OH with βCD (measured at pH 0.2 and pH 9.9 respectively). 0-0 energy was measured from the wavelength where two curves intersect.

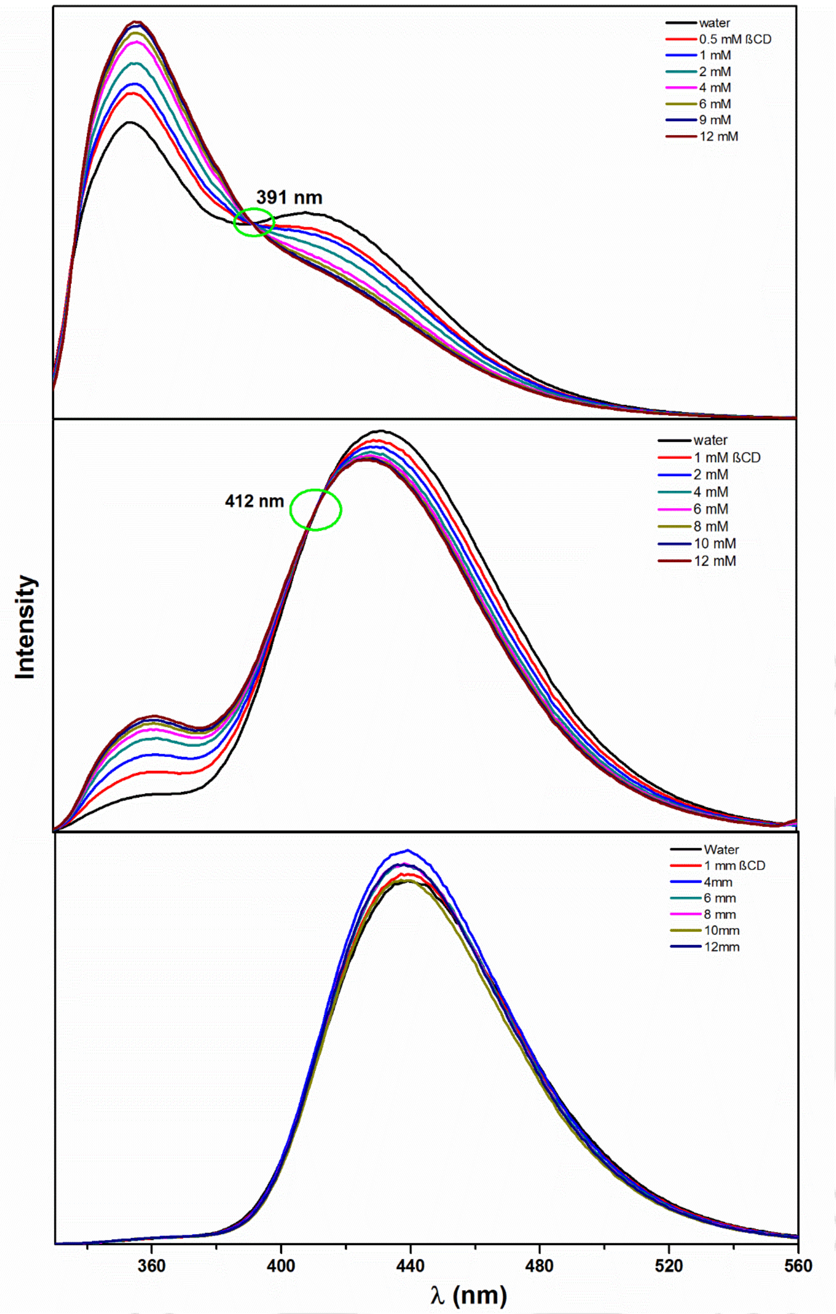

Figure A.6.4. Area-normalized emission spectra of (a) 2-OH, (b) $6SO_3$-2OH, and (c) 6CN-2OH in water and in the presence of various concentrations of β-CD (λ_{ex} = 310 nm).

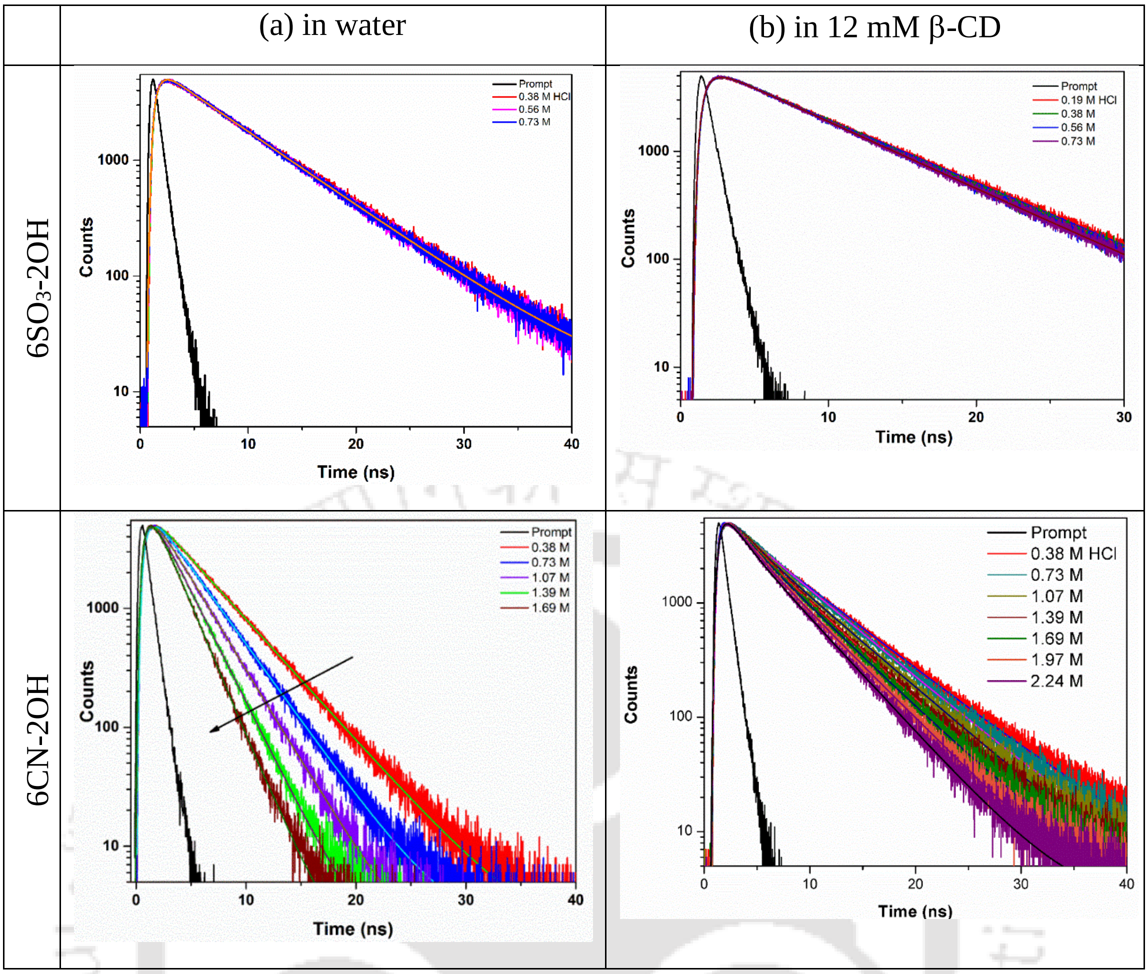

Figure A.6.5. Fluorescence decays of the protonated $6SO_3$-2OH (top) and protonated 6CN-2OH (bottom) in water (a) and 12 mM β-CD solution (b) by varying concentration of HCl at 350 nm.

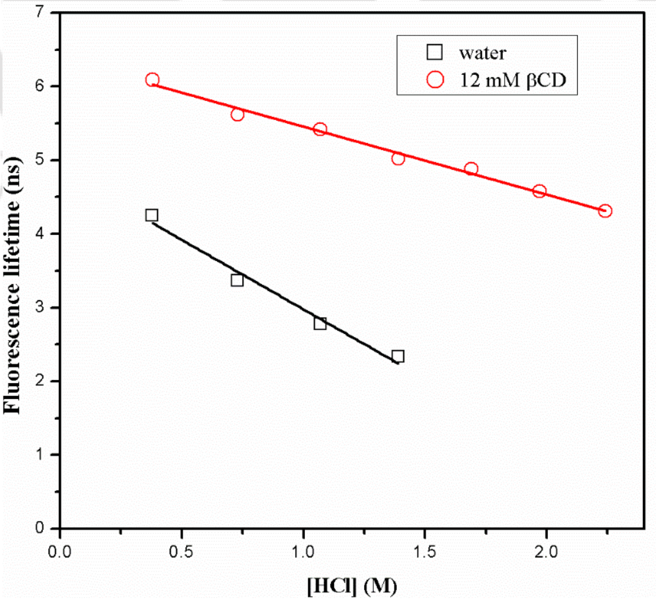

Figure A.6.6. Variation of a lifetime of 6CN-2OH with the concentration of HCl (M) in water and in the presence of 12 mM βCD. The data were fitted with a straight line and the intercept present the intrinsic (τ_n) lifetime used in table 6.2**.**

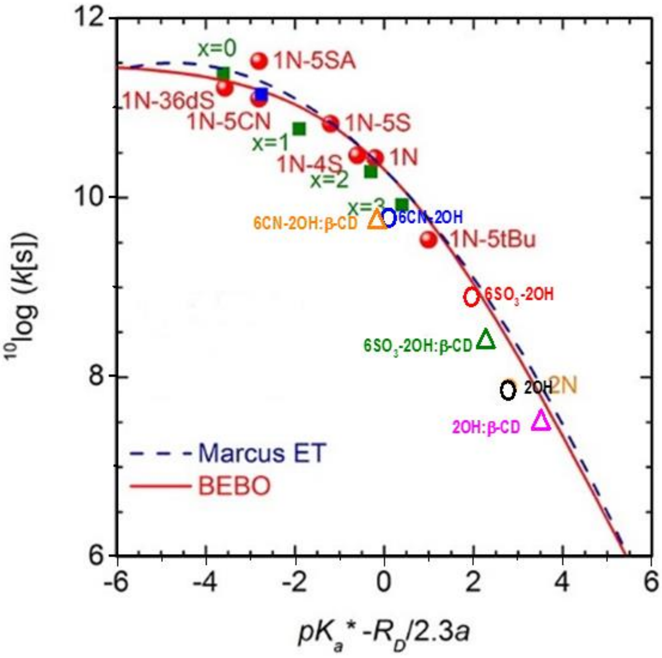

Figure A.6.7. The proton dissociation rate constant of the photoacids (2OH, 6SO$_3$-2OH and 6CN-2OH) in water and in the presence of β-CD are included to the free-energy correlation reported by Spies et al.[120, 124, 335] The solid symbols denote their data (1-naphthol derivatives, 5-sulfamide substituent of 1-naphthol (1N-5SA), 2-naphthol (2N)) while the open symbols denote our data.

In **Figure A.6.7**, R_D is the Debye radius $R_D = \frac{|z_1 z_2| e^2}{\epsilon k_B T}$ (where z_1 and z_2 are charges for conjugate base and the proton; e charge of electron, ε is static dielectric constant) and 'a' is the contact radius.

In case of 2OH and 6CN-2OH, $z_1 = -1$, $z_2 = 1$.

In case of 6SO$_3$-2OH, $z_1 = -2$, $z_2 = 1$.

For photoacids (2OH, 6SO$_3$-2OH and 6CN-2OH) in water, we have considered contact radius 'a' = 5.5 Å.

For photoacids (2OH, 6SO$_3$-2OH and 6CN-2OH) in the presence of β-CD, we have considered roughly contact radius 'a' = 8 Å.

For Chapter 7.

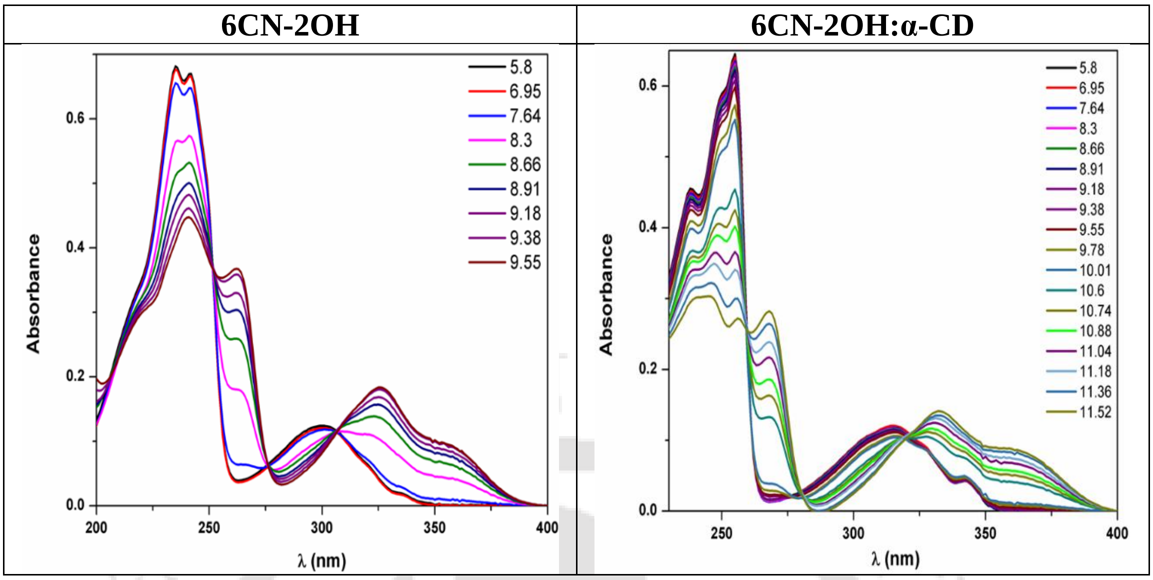

Figure A.7.1. Absorption spectra of 6CN-2OH photoacid and it's complex with α-CD at different pH values – (left side) 6CN-2OH and (right side) 6CN-2OH:α-CD.

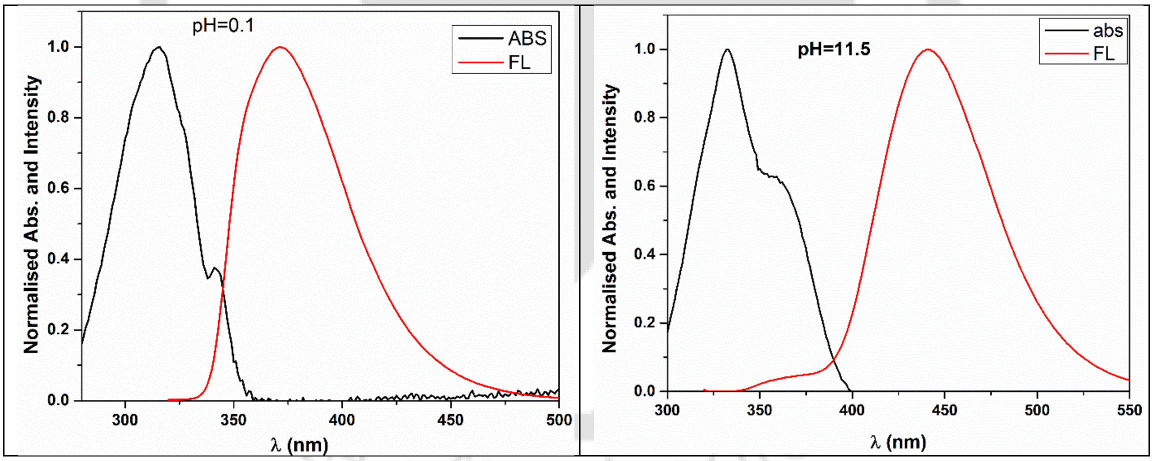

Figure A.7.2. Normalized absorption and emission spectra of the protonated (or acid) and deprotonated form of (left side) free 6CN-2OH and (right side) complexed 6CN-2OH with α-CD (measured at pH 0.1 and pH 11.5 respectively). 0-0 energy was measured from the wavelength where two curves intersect.

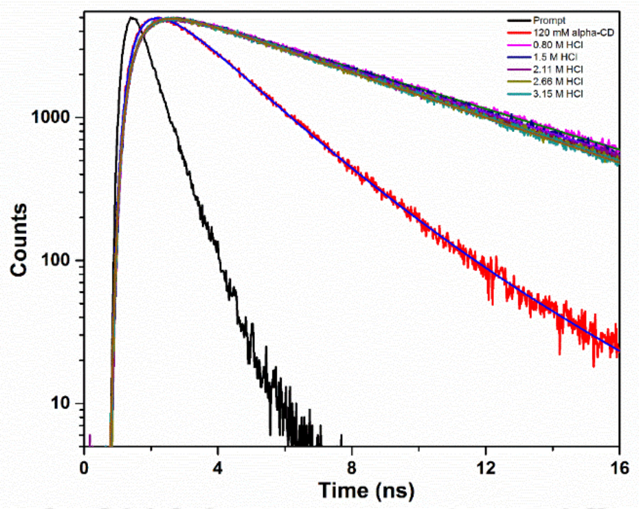

Figure A.7.3. Fluorescence decays of the protonated 6CN-2OH 120 mM α-CD solution by varying concentration of HCl at 350 nm.

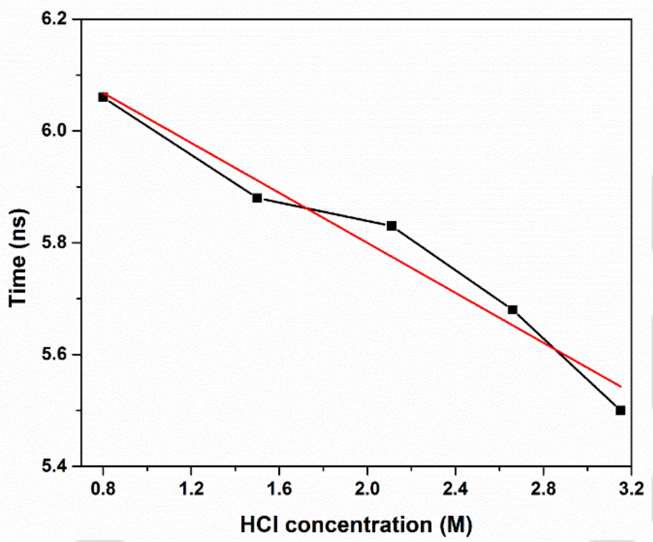

Figure A.7.4. Variation of lifetime of 6CN-2OH with concentration of HCl (M) in the presence of 120 mM α-CD. The data were fitted with a straight line and the intercept present the intrinsic (τ_n) lifetime used in Table 7.2**.**

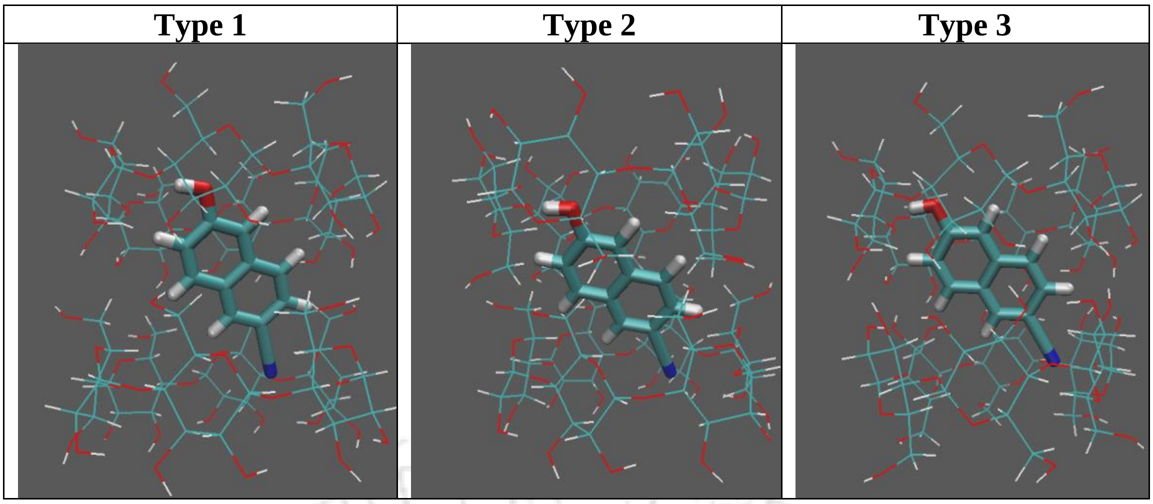

Figure A.7.5. Capsule-like initial structure of 'Type 1', 'Type 2', and 'Type 3'configuration of the 1:2 inclusion complexes of 6CN-2OH with α-CD for MD simulation.

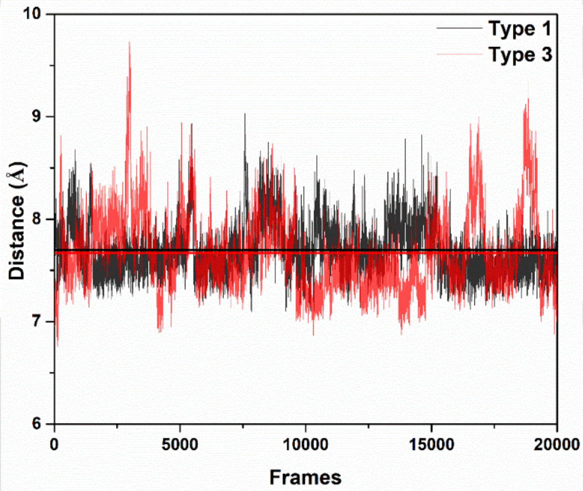

Figure A.7.6. Distance between center of masses (COM) of two α-CD rings versus frame.

Radial distribution of O-atom of the hydroxyl group of the 6CN-2OH and the different O-atoms (O4, O5, and O6) of the α –CD:

We calculated the radial distribution function g(r) between O-atom of the hydroxyl group of the 6CN-2OH and the different O-atoms (O4, O5, and O6) of the α –CD. From the RDF plot **Figure A.7.7**, we interestingly observed a strong sharp first peak appears at around 2.76 Å with a small board second peak at ~5.5 Å for O6 atom (O-atom of the secondary hydroxyl group of α-CD) of the 'Type 1' configuration. In the case of O4 and O5 atoms no strong sharp peak was found within 3 Å, and a board peaks at ~ 4.1 to 4.6 Å for O4 and O5 atoms was observed of the 'Type 1' configuration. In the case of 'Type 3' configuration, we found similar board peaks within ~ 4.3 to 4.7 Å for all three O-atoms

(O4, O5, and O6) of the, and no sharp peak was noticed within 3 Å region. In the case of ‘Type 1’ configuration, the sharp first peak at 2.76 Å indicates a possibility of strong hydrogen bond present between O-atom of the hydroxyl group of the 6CN-2OH and the O-atom of the secondary hydroxyl group of the α-CD. Furthermore, from H-bond analysis between O-atom of the 6CN-2OH and the O6-atom of the α-CD, the average number of hydrogen bonds was observed between O-O6 is 0.76 for the ‘Type 1’ configuration. This observation confirms that a hydrogen bonding interaction is present between O-atom of the 6CN-2OH and O6 atom (O-atom of secondary hydroxyl group) of the α-CD. Moreover, distance *vs.* simulation frames plot between H-atom of the hydroxyl group of 6CN-2OH and O6 atom of α-CD also depicts that the number of frames show close contact (between 2 to 3 Å) between them (**Figure A.7.8**). Therefore, we can predict that since the hydroxyl group of the 6CN-2OH engages with the hydroxyl group of the α-CD through H-bonding, –OH group of the 6CN-2OH is less available towards water molecules for solvation.

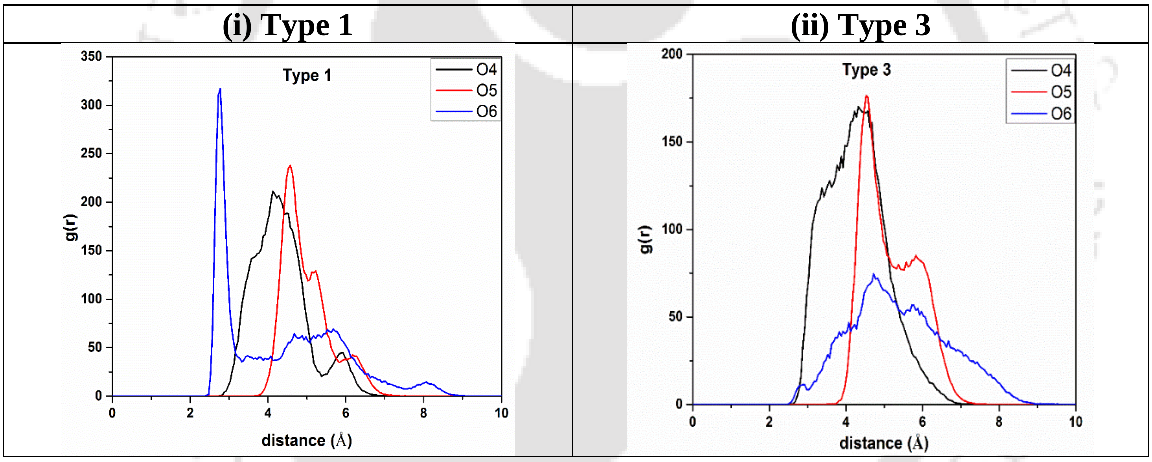
(i) Type 1 **(ii) Type 3**

Figure A.7.7. Radial distribution function involving oxygen atom (of 6CN-2OH) - oxygen atoms (O4, O5, and O6) of the α –CD - (i) ‘Type 1’ and (ii) ‘Type 3’ configurations.

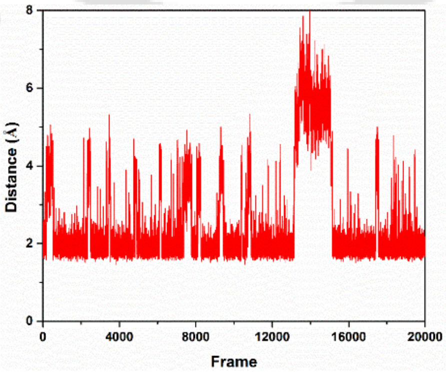

Figure A.7.8. Distance between H-atom of the hydroxyl group of 6CN-2OH and O6 atom of α-CD versus frame.

References

1. Wu, Y.-D.; Han, W.; Wang, D.-P.; Gao, Y.; Zhao, Y.-L., Theoretical Analysis of Secondary Structures of β-Peptides. *Acc. Chem. Res.* **2008,** *41* (10), 1418-1427.
2. Alexander, A. J.; Zare, R. N., Molecular TennisFlat Smashes and Wicked Cuts. *Acc. Chem. Res.* **2000,** *33* (4), 199-205.
3. Wu, Y. D.; Houk, K. N.; Valentine, J. S.; Nam, W., Is intramolecular hydrogen-bonding important for bleomycin reactivity? A molecular mechanics study. *Inorg. Chem.* **1992,** *31* (5), 718-720.
4. Wagner, B. D., Hydrogen bonding of excited states in supramolecular host-guest inclusion complexes. *Phys. Chem. Chem. Phys.* **2012,** *14* (25), 8825-8835.
5. Zilberg, S.; Kahan, A.; Haas, Y., The photo-dissociation of the pyrrole-ammonia complex-the role of hydrogen bonding in Rydberg states photochemistry. *Phys. Chem. Chem. Phys.* **2012,** *14* (25), 8836-8841.
6. Hardman, S. J. O.; Thompson, K. C., Influence of Base Stacking and Hydrogen Bonding on the Fluorescence of 2-Aminopurine and Pyrrolocytosine in Nucleic Acids. *Biochemistry* **2006,** *45* (30), 9145-9155.
7. Perun, S.; Sobolewski, A. L.; Domcke, W., Role of Electron-Driven Proton-Transfer Processes in the Excited-State Deactivation of the Adenine−Thymine Base Pair. *J. Phys. Chem. A* **2006,** *110* (29), 9031-9038.
8. Catalán, J.; Kasha, M., Photophysics of 7-Azaindole, Its Doubly-H-Bonded Base-Pair, and Corresponding Proton-Transfer-Tautomer Dimeric Species, via Defining Experimental and Theoretical Results. *J. Phys. Chem. A* **2000,** *104* (46), 10812-10820.
9. Elangannan, A.; Gautam, R. D.; Roger, A. K.; Joanna, S.; Steve, S.; Ibon, A.; David, C. C.; Robert, H. C.; Joseph, J. D.; Pavel, H.; Henrik, G. K.; Anthony, C. L.; Benedetta, M.; David, J. N., Definition of the hydrogen bond (IUPAC Recommendations 2011). *Pure Appl. Chem.* **2011,** *83* (8), 1637-1641.
10. Zhao, G.-J.; Han, K.-L., Hydrogen Bonding in the Electronic Excited State. *Acc. Chem. Res.* **2012,** *45* (3), 404-413.
11. Chudoba, C.; Nibbering, E. T. J.; Elsaesser, T., Ultrafast Structural Response of Hydrogen Bonded Complexes to Electronic Excitation in the Liquid Phase. *J. Phys. Chem. A* **1999,** *103* (29), 5625-5628.
12. Zhao, G.-J.; Han, K.-L., Effects of Hydrogen Bonding on Tuning Photochemistry: Concerted Hydrogen-Bond Strengthening and Weakening. *ChemPhysChem* **2008,** *9* (13), 1842-1846.
13. Nibbering, E. T. J.; Elsaesser, T., Ultrafast Vibrational Dynamics of Hydrogen Bonds in the Condensed Phase. *Chem. Rev.* **2004,** *104* (4), 1887-1914.
14. Cramer, C. J.; Truhlar, D. G., A Universal Approach to Solvation Modeling. *Acc. Chem. Res.* **2008,** *41* (6), 760-768.
15. Olsen, S.; Smith, S. C., Bond Selection in the Photoisomerization Reaction of Anionic Green Fluorescent Protein and Kindling Fluorescent Protein Chromophore Models. *J. Am. Chem. Soc.* **2008,** *130* (27), 8677-8689.
16. Schlücker, S.; Singh, R. K.; Asthana, B. P.; Popp, J.; Kiefer, W., Hydrogen-Bonded Pyridine−Water Complexes Studied by Density Functional Theory and Raman Spectroscopy. *J. Phys. Chem. A* **2001,** *105* (43), 9983-9989.
17. Neela, Y. I.; Mahadevi, A. S.; Sastry, G. N., Hydrogen Bonding in Water Clusters and Their Ionized Counterparts. *J. Phys. Chem. B* **2010,** *114* (51), 17162-17171.
18. Alabugin, I. V.; Manoharan, M.; Peabody, S.; Weinhold, F., Electronic Basis of Improper Hydrogen Bonding: A Subtle Balance of Hyperconjugation and Rehybridization. *J. Am. Chem. Soc.* **2003,** *125* (19), 5973-5987.
19. Stoner-Ma, D.; Jaye, A. A.; Matousek, P.; Towrie, M.; Meech, S. R.; Tonge, P. J., Observation of Excited-State Proton Transfer in Green Fluorescent Protein using Ultrafast Vibrational Spectroscopy. *J. Am. Chem. Soc.* **2005,** *127* (9), 2864-2865.

20. Zhao, G.-J.; Han, K.-L., Early Time Hydrogen-Bonding Dynamics of Photoexcited Coumarin 102 in Hydrogen-Donating Solvents: Theoretical Study. *J. Phys. Chem. A* **2007,** *111* (13), 2469-2474.

21. Zhao, G.-J.; Han, K.-L., Ultrafast Hydrogen Bond Strengthening of the Photoexcited Fluorenone in Alcohols for Facilitating the Fluorescence Quenching. *J. Phys. Chem. A* **2007,** *111* (38), 9218-9223.

22. Zhao, G.-J.; Han, K.-L., Role of Intramolecular and Intermolecular Hydrogen Bonding in Both Singlet and Triplet Excited States of Aminofluorenones on Internal Conversion, Intersystem Crossing, and Twisted Intramolecular Charge Transfer. *J. Phys. Chem. A* **2009,** *113* (52), 14329-14335.

23. Zhao, G.-J.; Liu, J.-Y.; Zhou, L.-C.; Han, K.-L., Site-Selective Photoinduced Electron Transfer from Alcoholic Solvents to the Chromophore Facilitated by Hydrogen Bonding: A New Fluorescence Quenching Mechanism. *J. Phys. Chem. B* **2007,** *111* (30), 8940-8945.

24. Zhao, G. J.; Han, K. L., Effects of Hydrogen Bonding on Tuning Photochemistry: Concerted Hydrogen-Bond Strengthening and Weakening. *ChemPhysChem* **2008,** *9* (13), 1842-1846.

25. Liu, Y.; Ding, J.; Shi, D.; Sun, J., Time-Dependent Density Functional Theory Study on Electronically Excited States of Coumarin 102 Chromophore in Aniline Solvent: Reconsideration of the Electronic Excited-State Hydrogen-Bonding Dynamics. *J. Phys. Chem. A* **2008,** *112* (28), 6244-6248.

26. Valeur, B., *Molecular fluorescence: principles and applications*. Wiley-VCH: 2002.

27. Nomrowski, J.; Wenger, O. S., Exploiting Potential Inversion for Photoinduced Multielectron Transfer and Accumulation of Redox Equivalents in a Molecular Heptad. *J. Am. Chem. Soc.* **2018,** *140* (16), 5343-5346.

28. V. May, O. K., Charge and Energy Transfer Dynamics in Molecular Systems. Wiely - VCH Verlag GmbH: 2000.

29. Suppan, P., In *Chemistry and Light,* The Royal Society of Chemistry: 1994; pp 27-86.

30. Giese, B.; Amaudrut, J.; Kohler, A.-K.; Spormann, M.; Wessely, S., Direct observation of hole transfer through DNA by hopping between adenine bases and by tunnelling. *Nature* **2001,** *412* (6844), 318-320.

31. de Rege, P.; Williams, S.; Therien, M., Direct evaluation of electronic coupling mediated by hydrogen bonds: implications for biological electron transfer. *Science* **1995,** *269* (5229), 1409-1413.

32. Barbara, P. F.; Meyer, T. J.; Ratner, M. A., Contemporary Issues in Electron Transfer Research. *J. Phys. Chem.* **1996,** *100* (31), 13148-13168.

33. Weaver, M. J.; McManis, G. E., Dynamical solvent effects on electron-transfer processes: recent progress and perspectives. *Acc. Chem. Res.* **1990,** *23* (9), 294-300.

34. Marcus, R. A., On the Theory of Oxidation-Reduction Reactions Involving Electron Transfer. I. *J. Chem. Phys.* **1956,** *24* (5), 966-978.

35. Rehm, D.; Weller, A., Kinetics of Fluorescence Quenching by Electron and H-Atom Transfer. *Isr. J. Chem.* **1970,** *8*, 259-271.

36. Fox, M. A., Introduction - Electron Transfer: A Critical Link between Subdisciplines in Chemistry. *Chem. Rev.* **1992,** *92* (3), 365-368.

37. Calef, D. F.; Wolynes, P. G., Classical solvent dynamics and electron transfer. 1. Continuum theory. *J. Phys. Chem.* **1983,** *87* (18), 3387-3400.

38. Hynes, J. T., Outer-sphere electron-transfer reactions and frequency-dependent friction. *J. Phys. Chem.* **1986,** *90* (16), 3701-3706.

39. Ikeda, N.; Miyasaka, H.; Okada, T.; Mataga, N., Picosecond laser photolysis studies of deactivation processes of excited hydrogen bonding complexes. 3. Detection of the nonfluorescent charge-transfer state in the excited 1-aminopyrene-pyridine hydrogen bonded pair and related systems. *J. Am. Chem. Soc.* **1983,** *105* (16), 5206-5211.

40. Roy, S.; Bagchi, B., Adiabatic and nonadiabatic outersphere electron transfer reactions in methanol: Effects of the ultrafast solvent polarization modes. *J. Chem. Phys.* **1995,** *102* (17), 6719-6726.

41. Nagasawa, Y.; Yartsev, A. P.; Tominaga, K.; Johnson, A. E.; Yoshihara, K., Substituent effects on intermolecular electron transfer: coumarins in electron-donating solvents. *J. Am. Chem. Soc.* **1993,** *115* (17), 7922-7923.
42. Nagasawa, Y.; Yartsev, A. P.; Tominaga, K.; Johnson, A. E.; Yoshihara, K., Temperature dependence of ultrafast intermolecular electron transfer faster than solvation process. *J. Chem. Phys.* **1994,** *101* (7), 5717-5726.
43. Nagasawa, Y.; Yartsev, A. P.; Tominaga, K.; Bisht, P. B.; Johnson, A. E.; Yoshihara, K., Dynamic Aspects of Ultrafast Intermolecular Electron Transfer Faster Than Solvation Process: Substituent Effects and Energy Gap Dependence. *J. Phys. Chem.* **1995,** *99* (2), 653-662.
44. Shirota, H.; Pal, H.; Tominaga, K.; Yoshihara, K., Substituent Effect and Deuterium Isotope Effect of Ultrafast Intermolecular Electron Transfer: Coumarin in Electron-Donating Solvent. *J. Phys. Chem. A* **1998,** *102* (18), 3089-3102.
45. Pal, H.; Shirota, H.; Tominaga, K.; Yoshihara, K., Ultrafast intermolecular electron transfer from orthomethoxyaniline to excited coumarin dyes. *J. Chem. Phys.* **1999,** *110* (23), 11454-11465.
46. Pal, H.; Nagasawa, Y.; Tominaga, K.; Yoshihara, K., Deuterium Isotope Effect on Ultrafast Intermolecular Electron Transfer. *J. Phys. Chem.* **1996,** *100* (29), 11964-11974.
47. Yoshihara, K., Ultrafast Intermolecular Electron Trasnfer in Solution. In *Adv. Chem. Phys.*, 1999; Vol. 107, p 37.
48. Kumar, K.; Tepper, R. J.; Zeng, Y.; Zimmt, M. B., Syntheses of Rigid and Semirigid Molecules for Investigations of Photoinduced Electron Transfer Reactions. *J. Org. Chem.* **1995,** *60* (13), 4051-4066.
49. Maruyama, K.; Otsuki, T.; Tai, S., Photoinduced electron-transfer-initiated aromatic cyclization. *J. Org. Chem.* **1985,** *50* (1), 52-60.
50. Wong, K.-T.; Ku, S.-Y.; Cheng, Y.-M.; Lin, X.-Y.; Hung, Y.-Y.; Pu, S.-C.; Chou, P.-T.; Lee, G.-H.; Peng, S.-M., Synthesis, Structures, and Photoinduced Electron Transfer Reaction in the 9,9‘-Spirobifluorene-Bridged Bipolar Systems. *J. Org. Chem.* **2005,** *71* (2), 456-465.
51. Marcus, R. A., Electrostatic Free Energy and Other Properties of States Having Nonequilibrium Polarization. I. *J. Chem. Phys.* **1956,** *24* (5), 979-989.
52. Marcus, Y., The effectivity of solvents as electron pair donors. *J. Solution Chem.* **1984,** *13* (9), 599-624.
53. Barman, N.; Singha, D.; Sahu, K., Faster photoinduced electron transfer in a diluted mixture than in a neat donor solvent: effect of excited-state H-bonding. *Phys. Chem. Chem. Phys.* **2014,** *16* (13), 6159-6166.
54. Marcus, R. A., Chemical and Electrochemical Electron-Transfer Theory. *Annu. Rev. Phys. Chem.* **1964,** *15* (1), 155-196.
55. Zhao, G.-J.; Liu, J.-Y.; Zhou, L.-C.; Han, K.-L., Site-Selective Photoinduced Electron Transfer from Alcoholic Solvents to the Chromophore Facilitated by Hydrogen Bonding: A New Fluorescence Quenching Mechanism. *J. Phys. Chem. B* **2007,** *111* (30), 8940-8945.
56. Yoshihara, K.; Tominaga, K.; Nagasawa, Y., Effects of the Solvent Dynamics and Vibrational Motions in Electron Transfer. *Bull. Chem. Soc. Jpn.* **1995,** *68* (3), 696-712.
57. Williamson, D. A.; Bowler, B. E., Electron Transfer through the Hydrogen-Bonded Interface of a β-Turn-Forming Depsipeptide. *J. Am. Chem. Soc.* **1998,** *120* (42), 10902-10911.
58. Mohammed, O. F.; Kwon, O.-H.; Othon, C. M.; Zewail, A. H., Charge Transfer Assisted by Collective Hydrogen-Bonding Dynamics. *Angew. Chem.* **2009,** *48* (34), 6251-6256.
59. Trifonov, A.; Buchvarov, I.; Wagenknecht, H.-A.; Fiebig, T., Real-time observation of hydrogen bond-assisted electron transfer to a DNA base. *Chem. Phys. Lett.* **2005,** *409* (4–6), 277-280.
60. Pereira, R. V.; Gehlen, M. H., H-bonding assisted intramolecular charge transfer in 1-aminopyrene derivatives. *Chem. Phys. Lett.* **2006,** *426* (4–6), 311-317.
61. Fonseca Guerra, C.; Bickelhaupt, F. M.; Snijders, J. G.; Baerends, E. J., The Nature of the Hydrogen Bond in DNA Base Pairs: The Role of Charge Transfer and Resonance Assistance. *Chem. Eur. J.* **1999,** *5* (12), 3581-3594.
62. Kirby, J. P.; Roberts, J. A.; Nocera, D. G., Significant Effect of Salt Bridges on Electron Transfer. *J. Am. Chem. Soc.* **1997,** *119* (39), 9230-9236.

63. Ghosh, H. N.; Verma, S.; Nibbering, E. T. J., Ultrafast Forward and Backward Electron Transfer Dynamics of Coumarin 337 in Hydrogen-Bonded Anilines As Studied with Femtosecond UV-Pump/IR-Probe Spectroscopy. *J. Phys. Chem. A* **2010,** *115* (5), 664-670.

64. Yang, D.; Liu, Y.; Shi, D.; Sun, J., Theoretical study on the excited-state photoinduced electron transfer facilitated by hydrogen bonding strengthening in the C337–AN/MAN complexes. *Comput. Theor. Chem.* **2012,** *984* (0), 76-84.

65. Barman, N.; Singha, D.; Sahu, K., Fluorescence Quenching of Hydrogen-Bonded Coumarin 102-Phenol Complex: Effect of Excited-State Hydrogen Bonding Strength. *J. Phys. Chem. A* **2013,** *117* (19), 3945-3953.

66. Palit, D. K.; Zhang, T.; Kumazaki, S.; Yoshihara, K., Hydrogen-Bond Dynamics in the Excited State of Coumarin 102−Aniline Hydrogen-Bonded Complex. *J. Phys. Chem. A* **2003,** *107* (49), 10798-10804.

67. Chudoba, C.; Nibbering, E. T. J.; Elsaesser, T., Site-Specific Excited-State Solute-Solvent Interactions Probed by Femtosecond Vibrational Spectroscopy. *Phys. Rev. Lett* **1998,** *81* (14), 3010-3013.

68. Nibbering, E. T. J.; Tschirschwitz, F.; Chudoba, C.; Elsaesser, T., Femtochemistry of Hydrogen Bonded Complexes after Electronic Excitation in the Liquid Phase: The Case of Coumarin 102. *J. Phys. Chem. A* **2000,** *104* (18), 4236-4246.

69. Nibbering, E. T. J.; Chudoba, C.; Elsaesser, T., Hydrogen-Bond Dynamics and Solvation of Electronically Excited States as Determined by Femtosecond Vibrational Spectroscopy. *Isr. J. Chem.* **1999,** *39* (3-4), 333-346.

70. Samant, V.; Singh, A. K.; Ramakrishna, G.; Ghosh, H. N.; Ghanty, T. K.; Palit, D. K., Ultrafast Intermolecular Hydrogen Bond Dynamics in the Excited State of Fluorenone. *J. Phys. Chem. A* **2005,** *109* (39), 8693-8704.

71. Engleitner, S.; Seel, M.; Zinth, W., Nonexponentialities in the Ultrafast Electron-Transfer Dynamics in the System Oxazine 1 in N,N-Dimethylaniline. *J. Phys. Chem. A* **1999,** *103* (16), 3013-3019.

72. Weaver, M. J.; Nettles, S. M., Solvent isotope effects upon the thermodynamics of some transition-metal redox couples in aqueous media. *Inorg. Chem.* **1980,** *19* (6), 1641-1646.

73. Siders, P.; Marcus, R. A., Quantum effects in electron-transfer reactions. *J. Am. Chem. Soc.* **1981,** *103* (4), 741-747.

74. Reid, P. J.; Silva, C.; Barbara, P. F.; Karki, L.; Hupp, J. T., Electronic Coherence, Vibrational Coherence, and Solvent Degrees of Freedom in the Femtosecond Spectroscopy of Mixed-Valence Metal Dimers in H2O and D2O. *J. Phys. Chem.* **1995,** *99* (9), 2609-2616.

75. Némethy, G.; Scheraga, H. A., Structure of Water and Hydrophobic Bonding in Proteins. IV. The Thermodynamic Properties of Liquid Deuterium Oxide. *J. Chem. Phys.* **1964,** *41* (3), 680-689.

76. Kliner, D. A. V.; Tominaga, K.; Walker, G. C.; Barbara, P. F., Comparison of experimental and theoretical absolute rates for intervalence electron transfer. *J. Am. Chem. Soc.* **1992,** *114* (21), 8323-8325.

77. Ghosh, H. N.; Adamczyk, K.; Verma, S.; Dreyer, J.; Nibbering, E. T. J., On the Role of Hydrogen Bonds in Photoinduced Electron-Transfer Dynamics between 9-Fluorenone and Amine Solvents. *Chem. Eur. J.* **2012,** *18* (16), 4930-4937.

78. Castner, E. W.; Kennedy, D.; Cave, R. J., Solvent as Electron Donor: Donor/Acceptor Electronic Coupling Is a Dynamical Variable. *J. Phys. Chem. A* **2000,** *104* (13), 2869-2885.

79. Pugžlys, A.; den Hartog, H. P.; Baltuška, A.; Pshenichnikov, M. S.; Umapathy, S.; Wiersma, D. A., Solvent-Controlled Acceleration of Electron Transfer in Binary Mixtures. *J. Phys. Chem. A* **2001,** *105* (51), 11407-11413.

80. Barman, N.; Sahu, K., Reduced fluorescence quenching of coumarin 102 at higher phenol mole fractions in cyclohexane–phenol and anisole–phenol solvent mixtures: role of competitive hydrogen bonding. *RSC Adv.* **2014,** *4* (102), 58299-58306.

81. Barman, N.; Sahu, K., Anomalous modulation of photoinduced electron transfer of coumarin 102 in aniline–dimethylaniline mixture: dominant role of hydrogen bonding. *Phys. Chem. Chem. Phys.* **2014,** *16* (48), 27096-27103.

82. Barman, N.; Hossen, T.; Mondal, K.; Sahu, K., Modulation of ultrafast photoinduced electron transfer in H-bonding environment: PET from aniline to coumarin 153 in the presence of an inert co-solvent cyclohexane. *Phys. Chem. Chem. Phys.* **2015,** *17* (48), 32556-32563.

83. Smitha, M. A.; Gopidas, K. R., Temperature dependence of photoinduced electron transfer in hydrogen-bonded donor–acceptor systems. *Chem. Phys. Lett.* **2001,** *350* (1), 86-92.

84. Shi, Z.; Peng, P.; Strohecker, D.; Liao, Y., Long-Lived Photoacid Based upon a Photochromic Reaction. *J. Am. Chem. Soc.* **2011,** *133* (37), 14699-14703.

85. Presiado, I.; Erez, Y.; Huppert, D., Excited-State Intermolecular Proton Transfer of Firefly Luciferin III. Proton Transfer to a Mild Base. *J. Phys. Chem. A* **2010,** *114* (51), 13337-13346.

86. Baranov, M. S.; Lukyanov, K. A.; Borissova, A. O.; Shamir, J.; Kosenkov, D.; Slipchenko, L. V.; Tolbert, L. M.; Yampolsky, I. V.; Solntsev, K. M., Conformationally Locked Chromophores as Models of Excited-State Proton Transfer in Fluorescent Proteins. *J. Am. Chem. Soc.* **2012,** *134* (13), 6025-6032.

87. Scheiner, S., Theoretical Studies of Excited State Proton Transfer in Small Model Systems. *J. Phys. Chem. A* **2000,** *104* (25), 5898-5909.

88. Pradhan, R.; Harshan, A. K.; Krishnavilasam Chandrika, G. S.; Srinivasan, A.; Lourderaj, U., Time-Dependent Density Functional Theoretical Investigation of Photoinduced Excited-State Intramolecular Dual Proton Transfer in Diformyl Dipyrromethanes. *J. Phys. Chem. A* **2016,** *120* (50), 9894-9906.

89. Coe, J. D.; Levine, B. G.; Martínez, T. J., Ab Initio Molecular Dynamics of Excited-State Intramolecular Proton Transfer Using Multireference Perturbation Theory. *J. Phys. Chem. A* **2007,** *111* (44), 11302-11310.

90. Clark, J. H.; Shapiro, S. L.; Campillo, A. J.; Winn, K. R., Picosecond studies of excited-state protonation and deprotonation kinetics. The laser pH jump. *J. Am. Chem. Soc.* **1979,** *101* (3), 746-748.

91. Politi, M. J.; Fendler, J. H., Laser pH-jump initiated proton transfer on charged micellar surfaces. *J. Am. Chem. Soc.* **1984,** *106* (2), 265-273.

92. Zhou, P.; Han, K., Unraveling the Detailed Mechanism of Excited-State Proton Transfer. *Acc. Chem. Res.* **2018,** *51* (7), 1681-1690.

93. Liu, Y.-H.; Chu, T.-S., Size effect of water cluster on the excited-state proton transfer in aqueous solvent. *Chem. Phys. Lett.* **2011,** *505* (4), 117-121.

94. Tang, Z.; Qi, Y.; Wang, Y.; Zhou, P.; Tian, J.; Fei, X., Excited-State Proton Transfer Mechanism of 2,6-Diazaindoles·(H2O)n (n = 2–4) Clusters. *J. Phys. Chem. B* **2018,** *122* (14), 3988-3995.

95. Li, G.-Y.; Zhao, G.-J.; Han, K.-L.; He, G.-Z., A TD-DFT study on the cyanide-chemosensing mechanism of 8-formyl-7-hydroxycoumarin. *J. Comput. Chem.* **2011,** *32* (4), 668-674.

96. Pines, E.; Huppert, D., Geminate recombination proton-transfer reactions. *Chem. Phys. Lett.* **1986,** *126* (1), 88-91.

97. Cotter, L. F.; Brown, P. J.; Nelson, R. C.; Takematsu, K., Divergent Hammett Plots of the Ground- and Excited-State Proton Transfer Reactions of 7-Substituted-2-Naphthol Compounds. *J. Phys. Chem. B* **2019,** *123* (19), 4301-4310.

98. Leiderman, P.; Genosar, L.; Huppert, D., Excited-State Proton Transfer: Indication of Three Steps in the Dissociation and Recombination Process. *J. Phys. Chem. A* **2005,** *109* (27), 5965-5977.

99. Leiderman, P.; Gepshtein, R.; Tsimberov, I.; Huppert, D., Effect of Temperature on Excited-State Proton Tunneling in wt-Green Fluorescent Protein. *J. Phys. Chem. B* **2008,** *112* (4), 1232-1239.

100. Simkovitch, R.; Shomer, S.; Gepshtein, R.; Shabat, D.; Huppert, D., Temperature Dependence of the Excited-State Proton-Transfer Reaction of Quinone-cyanine-7. *J. Phys. Chem. A* **2013,** *117* (19), 3925-3934.

101. Imadul Islam, S.; Das, A.; Mitra, R. K., Excited state proton transfer in reverse micelles: Effect of temperature and a possible interplay with solvation. *J. Photochem. Photobiol. A* **2021,** *404*, 112928.

102. T. Förster, *Z. Elektrochem.*, **1950,** *54*, 531.

103. Simkovitch, R.; Shomer, S.; Gepshtein, R.; Huppert, D., How Fast Can a Proton-Transfer Reaction Be beyond the Solvent-Control Limit? *J. Phys. Chem. B* **2015,** *119* (6), 2253-2262.

104. Agmon, N.; Huppert, D.; Masad, A.; Pines, E., Excited-state proton transfer to methanol-water mixtures. *J. Phys. Chem.* **1991,** *95* (25), 10407-10413.

105. Karton-Lifshin, N.; Albertazzi, L.; Bendikov, M.; Baran, P. S.; Shabat, D., "Donor–Two-Acceptor" Dye Design: A Distinct Gateway to NIR Fluorescence. *J. Am. Chem. Soc.* **2012,** *134* (50), 20412-20420.

106. Spry, D. B.; Fayer, M. D., Charge redistribution and photoacidity: Neutral versus cationic photoacids. *J. Chem. Phys.* **2008,** *128* (8), 084508.

107. Weller, A., Fast reactions of excited molecules. *Prog. React. Kinet. Mech.* **1961,** *1*, 187-192.

108. Huppert, D.; Kolodney, E., Picosecond proton transfer studies in water-alcohols solutions. *Chem. Phys.* **1981,** *63* (3), 401-410.

109. Schulman, S. G.; Kelly, R. N.; Gonzalez, N. J., Steady-state fluorimetric studies of proton-transfer kinetics of some photoexcited hydroxyaromatics in DMSO-water solutions. In *Pure Appl. Chem.*, 1987; Vol. 59, p 655.

110. Krishnan, R.; Fillingim, T.; Lee, J.; Robinson, G., Solvent structural effects on proton dissociation. *J. Am. Chem. Soc.* **1990,** *112* (4), 1353-1357.

111. Tolbert, L. M.; Haubrich, J. E., Enhanced photoacidities of cyanonaphthols. *J. Am. Chem. Soc.* **1990,** *112* (22), 8163-8165.

112. Klevens, H. B.; Platt, J. R., Spectral Resemblances of Cata-Condensed Hydrocarbons. *J. Chem. Phys.* **1949,** *17* (5), 470-481.

113. Tolbert, L. M.; Haubrich, J. E., Photoexcited Proton Transfer from Enhanced Photoacids. *J. Am. Chem. Soc.* **1994,** *116* (23), 10593-10600.

114. Agmon, N.; Rettig, W.; Groth, C., Electronic Determinants of Photoacidity in Cyanonaphthols. *J. Am. Chem. Soc.* **2002,** *124* (6), 1089-1096.

115. Baba, H.; Suzuki, S., Electronic Spectra and Hydrogen Bonding. I. Phenol and Naphthols. *J. Chem. Phys.* **1961,** *35* (3), 1118-1127.

116. Wu, C.-H.; Karas, L. J.; Ottosson, H.; Wu, J. I.-C., Excited-state proton transfer relieves antiaromaticity in molecules. *Proc. Natl. Acad. Sci. U.S.A.* **2019,** *116* (41), 20303-20308.

117. Karadakov, P. B., Ground- and Excited-State Aromaticity and Antiaromaticity in Benzene and Cyclobutadiene. *J. Phys. Chem. A* **2008,** *112* (31), 7303-7309.

118. Groves, M. S.; Nelson, K. J.; Nelson, R. C.; Takematsu, K., pH switch for OH-photoacidity in 5-amino-2-naphthol and 8-amino-2-naphthol. *Phys. Chem. Chem. Phys.* **2018,** *20* (33), 21325-21333.

119. Nelson, K. J.; Brown, P. J.; Rudel, H. E.; Takematsu, K., Divergent excited state proton transfer reactions of bifunctional photoacids 1-ammonium-2-naphthol and 3-ammonium-2-naphthol in water and methanol. *Phys. Chem. Chem. Phys.* **2019,** *21* (44), 24383-24392.

120. Ditkovich, J.; Mukra, T.; Pines, D.; Huppert, D.; Pines, E., Bifunctional Photoacids: Remote Protonation Affecting Chemical Reactivity. *J. Phys. Chem. B* **2015,** *119* (6), 2690-2701.

121. Marcus, R. A., Theoretical relations among rate constants, barriers, and Broensted slopes of chemical reactions. *J. Phys. Chem.* **1968,** *72* (3), 891-899.

122. Marcus, R. A., Unusual slopes of free energy plots in kinetics. *J. Am. Chem. Soc.* **1969,** *91* (26), 7224-7225.

123. Cohen, A. O.; Marcus, R. A., Slope of free energy plots in chemical kinetics. *J. Phys. Chem.* **1968,** *72* (12), 4249-4256.

124. Spies, C.; Shomer, S.; Finkler, B.; Pines, D.; Pines, E.; Jung, G.; Huppert, D., Solvent dependence of excited-state proton transfer from pyranine-derived photoacids. *Phys. Chem. Chem. Phys.* **2014,** *16* (19), 9104-9114.

125. Prémont-Schwarz, M.; Barak, T.; Pines, D.; Nibbering, E. T. J.; Pines, E., Ultrafast Excited-State Proton-Transfer Reaction of 1-Naphthol-3,6-Disulfonate and Several 5-Substituted 1-Naphthol Derivatives. *J. Phys. Chem. B* **2013,** *117* (16), 4594-4603.

126. Carmeli, I.; Huppert, D.; Tolbert, L. M.; Haubrich, J. E., Ultrafast excited-state proton transfer from dicyano-naphthol. *Chem. Phys. Lett.* **1996,** *260* (1), 109-114.

127. Gould, E.-A.; Popov, A. V.; Tolbert, L. M.; Presiado, I.; Erez, Y.; Huppert, D.; Solntsev, K. M., Excited-state proton transfer in N-methyl-6-hydroxyquinolinium salts: solvent and temperature effects. *Phys. Chem. Chem. Phys.* **2012,** *14* (25), 8964-8973.
128. Kim, T. G.; Topp, M. R., Ultrafast Excited-State Deprotonation and Electron Transfer in Hydroxyquinoline Derivatives. *J. Phys. Chem. A* **2004,** *108* (46), 10060-10065.
129. Sousa, F. B. D.; Denadai, Â. M. L.; Lula, I. S.; Nascimento Jr, C. S.; Neto, N. S. G. F.; Lima, A. C.; Almeida, W. B. D.; Sinisterra, R. D., Supramolecular Self-Assembly of Cyclodextrin and Higher Water Soluble Guest: Thermodynamics and Topological Studies. *J. Am. Chem. Soc.* **2008,** *130* (26), 8426-8436.
130. Shaikh, M.; Mohanty, J.; Sundararajan, M.; Bhasikuttan, A. C.; Pal, H., Supramolecular Host–Guest Interactions of Oxazine-1 Dye with β- and γ-Cyclodextrins: A Photophysical and Quantum Chemical Study. *J. Phys. Chem. B* **2012,** *116* (41), 12450-12459.
131. Inoue, Y.; Hakushi, T.; Liu, Y.; Tong, L.; Shen, B.; Jin, D., Thermodynamics of molecular recognition by cyclodextrins. 1. Calorimetric titration of inclusion complexation of naphthalenesulfonates with .alpha.-, .beta.-, and .gamma.-cyclodextrins: enthalpy-entropy compensation. *J. Am. Chem. Soc.* **1993,** *115* (2), 475-481.
132. Alsbaiee, A.; Smith, B. J.; Xiao, L.; Ling, Y.; Helbling, D. E.; Dichtel, W. R., Rapid removal of organic micropollutants from water by a porous β-cyclodextrin polymer. *Nature* **2016,** *529* (7585), 190-194.
133. Jana, B.; Mohapatra, S.; Mondal, P.; Barman, S.; Pradhan, K.; Saha, A.; Ghosh, S., α-Cyclodextrin Interacts Close to Vinblastine Site of Tubulin and Delivers Curcumin Preferentially to the Tubulin Surface of Cancer Cell. *ACS Appl. Mater. Interfaces* **2016,** *8* (22), 13793-13803.
134. Szejtli, J., Past, present and futute of cyclodextrin research. In *Pure Appl. Chem.*, 2004; Vol. 76, p 1825.
135. Sayed, M.; Pal, H., Supramolecularly assisted modulations in chromophoric properties and their possible applications: an overview. *J. Mater. Chem. C* **2016,** *4* (14), 2685-2706.
136. He, J.; Li, Y.; Wang, C.; Zhang, K.; Lin, D.; Kong, L.; Liu, J., Rapid adsorption of Pb, Cu and Cd from aqueous solutions by β-cyclodextrin polymers. *Appl. Surf. Sci.* **2017,** *426* (Supplement C), 29-39.
137. Douhal, A., Ultrafast Guest Dynamics in Cyclodextrin Nanocavities. *Chem. Rev.* **2004,** *104* (4), 1955-1976.
138. Szejtli, J., Dimethyl-β-cyclodextrin as parenteral drug carrier. *J. Incl. Phenom.* **1983,** *1* (2), 135-150.
139. Challa, R.; Ahuja, A.; Ali, J.; Khar, R. K., Cyclodextrins in drug delivery: An updated review. *AAPS PharmSciTech* **2005,** *6* (2), E329-E357.
140. Loftsson, T.; Jarho, P.; Másson, M.; Järvinen, T., Cyclodextrins in drug delivery. *Expert Opin. Drug Deliv.* **2005,** *2* (2), 335-351.
141. Uekama, K.; Hirayama, F.; Irie, T., Cyclodextrin Drug Carrier Systems. *Chem. Rev.* **1998,** *98* (5), 2045-2076.
142. Karnes, J. J.; Benjamin, I., SN2 Reaction Rate Enhancement by β-Cyclodextrin at the Liquid/Liquid Interface. *J. Phys. Chem. C* **2017,** *121* (35), 19209-19217.
143. Lee, J. W.; Samal, S.; Selvapalam, N.; Kim, H.-J.; Kim, K., Cucurbituril Homologues and Derivatives: New Opportunities in Supramolecular Chemistry. *Acc. Chem. Res.* **2003,** *36* (8), 621-630.
144. Lagona, J.; Mukhopadhyay, P.; Chakrabarti, S.; Isaacs, L., The Cucurbit[n]uril Family. *Angew. Chem.* **2005,** *44* (31), 4844-4870.
145. Park, H.-R.; Mayer, B.; Wolschann, P.; Koehler, G., Excited-State Proton Transfer of 2-Naphthol Inclusion Complexes with Cyclodextrins. *J. Phys. Chem.* **1994,** *98* (24), 6158-6166.
146. van Stam, J.; De Feyter, S.; De Schryver, F. C.; Evans, C. H., 2-Naphthol Complexation by β-Cyclodextrin: Influence of Added Short Linear Alcohols. *J. Phys. Chem.* **1996,** *100* (51), 19959-19966.
147. Basílio, N.; Laia, C. A. T.; Pina, F., Excited-State Proton Transfer in Confined Medium. 4-Methyl-7-hydroxyflavylium and β-Naphthol Incorporated in Cucurbit[7]uril. *J. Phys. Chem. B* **2015,** *119* (6), 2749-2757.

148. Hansen, J. E.; Pines, E.; Fleming, G. R., Excited-state proton transfer of protonated 1-aminopyrene complexes with .beta.-cyclodextrin. *J. Phys. Chem.* **1992,** *96* (17), 6904-6910.
149. Abdel-Shafi, A. A., Spectroscopic studies on the inclusion complex of 2-naphthol-6-sulfonate with β-cyclodextrin. *Spectrochim. Acta A* **2007,** *66* (3), 732-738.
150. Amer, A. S. I.; Alazaly, A. M. M.; Abdel-Shafi, A. A., Solvatochromism of 1-naphthol-4-sulfonate photoacid and its encapsulation in cyclodextrin derivatives. *J. Photochem. Photobiol. A* **2019,** *369*, 202-211.
151. Gepshtein, R.; Leiderman, P.; Huppert, D.; Project, E.; Nachliel, E.; Gutman, M., Proton Antenna Effect of the γ-Cyclodextrin Outer Surface, Measured by Excited State Proton Transfer. *J. Phys. Chem. B* **2006,** *110* (51), 26354-26364.
152. Mondal, S. K.; Sahu, K.; Sen, P.; Roy, D.; Ghosh, S.; Bhattacharyya, K., Excited state proton transfer of pyranine in a γ-cyclodextrin cavity. *Chem. Phys. Lett.* **2005,** *412* (1), 228-234.
153. Mondal, S. K.; Sahu, K.; Ghosh, S.; Sen, P.; Bhattacharyya, K., Excited-State Proton Transfer from Pyranine to Acetate in γ-Cyclodextrin and Hydroxypropyl γ-Cyclodextrin. *J. Phys. Chem. A* **2006,** *110* (51), 13646-13652.
154. Hammes-Schiffer, S.; Soudackov, A. V., Proton-Coupled Electron Transfer in Solution, Proteins, and Electrochemistry. *J. Phys. Chem. B* **2008,** *112* (45), 14108-14123.
155. Weinberg, D. R.; Gagliardi, C. J.; Hull, J. F.; Murphy, C. F.; Kent, C. A.; Westlake, B. C.; Paul, A.; Ess, D. H.; McCafferty, D. G.; Meyer, T. J., Proton-Coupled Electron Transfer. *Chem. Rev.* **2012,** *112* (7), 4016-4093.
156. Huynh, M. H. V.; Meyer, T. J., Proton-Coupled Electron Transfer. *Chem. Rev.* **2007,** *107* (11), 5004-5064.
157. Magnuson, A.; Anderlund, M.; Johansson, O.; Lindblad, P.; Lomoth, R.; Polivka, T.; Ott, S.; Stensjö, K.; Styring, S.; Sundström, V.; Hammarström, L., Biomimetic and Microbial Approaches to Solar Fuel Generation. *Acc. Chem. Res.* **2009,** *42* (12), 1899-1909.
158. Gust, D.; Moore, T. A.; Moore, A. L., Solar Fuels via Artificial Photosynthesis. *Acc. Chem. Res.* **2009,** *42* (12), 1890-1898.
159. Alstrum-Acevedo, J. H.; Brennaman, M. K.; Meyer, T. J., Chemical Approaches to Artificial Photosynthesis. 2. *Inorg. Chem.* **2005,** *44* (20), 6802-6827.
160. Ponseca, C. S.; Chábera, P.; Uhlig, J.; Persson, P.; Sundström, V., Ultrafast Electron Dynamics in Solar Energy Conversion. *Chem. Rev.* **2017,** *117* (16), 10940-11024.
161. Mora, S. J.; Odella, E.; Moore, G. F.; Gust, D.; Moore, T. A.; Moore, A. L., Proton-Coupled Electron Transfer in Artificial Photosynthetic Systems. *Acc. Chem. Res.* **2018,** *51* (2), 445-453.
162. Dempsey, J. L.; Brunschwig, B. S.; Winkler, J. R.; Gray, H. B., Hydrogen Evolution Catalyzed by Cobaloximes. *Acc. Chem. Res.* **2009,** *42* (12), 1995-2004.
163. DuBois, D. L.; Bullock, R. M., Molecular Electrocatalysts for the Oxidation of Hydrogen and the Production of Hydrogen – The Role of Pendant Amines as Proton Relays. *Eur. J. Inorg. Chem.* **2011,** *2011* (7), 1017-1027.
164. Gentry, E. C.; Knowles, R. R., Synthetic Applications of Proton-Coupled Electron Transfer. *Acc. Chem. Res.* **2016,** *49* (8), 1546-1556.
165. Stubbe, J.; Nocera, D. G.; Yee, C. S.; Chang, M. C. Y., Radical Initiation in the Class I Ribonucleotide Reductase: Long-Range Proton-Coupled Electron Transfer? *Chem. Rev.* **2003,** *103* (6), 2167-2202.
166. Klinman, J. P.; Offenbacher, A. R., Understanding Biological Hydrogen Transfer Through the Lens of Temperature Dependent Kinetic Isotope Effects. *Acc. Chem. Res.* **2018,** *51* (9), 1966-1974.
167. Mayer, J. M.; Hrovat, D. A.; Thomas, J. L.; Borden, W. T., Proton-Coupled Electron Transfer versus Hydrogen Atom Transfer in Benzyl/Toluene, Methoxyl/Methanol, and Phenoxyl/Phenol Self-Exchange Reactions. *J. Am. Chem. Soc.* **2002,** *124* (37), 11142-11147.
168. Darcy, J. W.; Koronkiewicz, B.; Parada, G. A.; Mayer, J. M., A Continuum of Proton-Coupled Electron Transfer Reactivity. *Acc. Chem. Res.* **2018,** *51* (10), 2391-2399.
169. Fecenko, C. J.; Meyer, T. J.; Thorp, H. H., Electrocatalytic Oxidation of Tyrosine by Parallel Rate-Limiting Proton Transfer and Multisite Electron−Proton Transfer. *J. Am. Chem. Soc.* **2006,** *128* (34), 11020-11021.

170. Fecenko, C. J.; Thorp, H. H.; Meyer, T. J., The Role of Free Energy Change in Coupled Electron−Proton Transfer. *J. Am. Chem. Soc.* **2007,** *129* (49), 15098-15099.

171. Soudackov, A.; Hammes-Schiffer, S., Multistate continuum theory for multiple charge transfer reactions in solution. *J. Chem. Phys.* **1999,** *111* (10), 4672-4687.

172. Hammes-Schiffer, S., Proton-Coupled Electron Transfer: Moving Together and Charging Forward. *J. Am. Chem. Soc.* **2015,** *137* (28), 8860-8871.

173. Hammes-Schiffer, S., Theoretical Perspectives on Proton-Coupled Electron Transfer Reactions. *Acc. Chem. Res.* **2001,** *34* (4), 273-281.

174. Borgis, D.; Hynes, J. T., Dynamical theory of proton tunneling transfer rates in solution: general formulation. *Chem. Phys.* **1993,** *170* (3), 315-346.

175. Soudackov, A.; Hammes-Schiffer, S., Derivation of rate expressions for nonadiabatic proton-coupled electron transfer reactions in solution. *J. Chem. Phys.* **2000,** *113* (6), 2385-2396.

176. Markle, T. F.; Rhile, I. J.; Mayer, J. M., Kinetic Effects of Increased Proton Transfer Distance on Proton-Coupled Oxidations of Phenol-Amines. *J. Am. Chem. Soc.* **2011,** *133* (43), 17341-17352.

177. Zhang, M.-T.; Irebo, T.; Johansson, O.; Hammarström, L., Proton-Coupled Electron Transfer from Tyrosine: A Strong Rate Dependence on Intramolecular Proton Transfer Distance. *J. Am. Chem. Soc.* **2011,** *133* (34), 13224-13227.

178. Blomberg, M. R. A.; Siegbahn, P. E. M., A Quantum Chemical Approach to the Study of Reaction Mechanisms of Redox-Active Metalloenzymes. *J. Phys. Chem. B* **2001,** *105* (39), 9375-9386.

179. Himo, F.; Siegbahn, P. E. M., Quantum Chemical Studies of Radical-Containing Enzymes. *Chem. Rev.* **2003,** *103* (6), 2421-2456.

180. Knapp, M. J.; Rickert, K.; Klinman, J. P., Temperature-Dependent Isotope Effects in Soybean Lipoxygenase-1: Correlating Hydrogen Tunneling with Protein Dynamics. *J. Am. Chem. Soc.* **2002,** *124* (15), 3865-3874.

181. Hatcher, E.; Soudackov, A. V.; Hammes-Schiffer, S., Proton-Coupled Electron Transfer in Soybean Lipoxygenase. *J. Am. Chem. Soc.* **2004,** *126* (18), 5763-5775.

182. Shimizu, M.; Katsuda, N.; Katsurada, T.; Mitani, M.; Yoshioka, Y., Mechanism on Two-Electron Oxidation of Ubiquinol at the Qp Site in Cytochrome bc1 Complex: B3LYP Study with Broken Symmetry. *J. Phys. Chem. B* **2008,** *112* (47), 15116-15126.

183. Saura, P.; Kaila, V. R. I., Energetics and Dynamics of Proton-Coupled Electron Transfer in the NADH/FMN Site of Respiratory Complex I. *J. Am. Chem. Soc.* **2019,** *141* (14), 5710-5719.

184. Luo, Y.; Liu, Y.-J., Theoretical Insight into a Nonadiabatic Proton-Coupled Electron Transfer Mechanism of Reduced Flavin Oxygenation. *J. Phys. Chem. A* **2019,** *123* (20), 4354-4359.

185. Litwinienko, G.; Ingold, K. U., Solvent Effects on the Rates and Mechanisms of Reaction of Phenols with Free Radicals. *Acc. Chem. Res.* **2007,** *40* (3), 222-230.

186. Musialik, M.; Kuzmicz, R.; Pawłowski, T. S.; Litwinienko, G., Acidity of Hydroxyl Groups: An Overlooked Influence on Antiradical Properties of Flavonoids. *J. Org. Chem.* **2009,** *74* (7), 2699-2709.

187. Warren, J. J.; Mayer, J. M., Surprisingly Long-Lived Ascorbyl Radicals in Acetonitrile: Concerted Proton−Electron Transfer Reactions and Thermochemistry. *J. Am. Chem. Soc.* **2008,** *130* (24), 7546-7547.

188. Chatgilialoglu, C.; D'Angelantonio, M.; Kaloudis, P.; Mulazzani, Q. G.; Guerra, M., One-Electron Reduction of 8-Bromoisoguanosine and 8-Bromoxanthosine in the Aqueous Phase: Sequential versus Concerted Proton-Coupled Electron Routes. *J. Phys. Chem. Lett.* **2010,** *1* (1), 174-177.

189. Costentin, C.; Robert, M.; Savéant, J.-M.; Teillout, A.-L., Concerted proton-coupled electron transfers in aquo/hydroxo/oxo metal complexes: Electrochemistry of [Os^{II}(bpy)₂py(OH₂)]²⁺ in water. *Proc. Natl. Acad. Sci. U.S.A.* **2009,** *106* (29), 11829-11836.

190. Costentin, C.; Robert, M.; Savéant, J.-M.; Teillout, A.-L., Concerted and Stepwise Proton-Coupled Electron Transfers in Aquo/Hydroxo Complex Couples in Water: Oxidative Electrochemistry of [OsII(bpy)2(py)(OH2)]2+. *ChemPhysChem* **2009,** *10* (1), 191-198.

191. Edwards, S. J.; Soudackov, A. V.; Hammes-Schiffer, S., Analysis of Kinetic Isotope Effects for Proton-Coupled Electron Transfer Reactions. *J. Phys. Chem. A* **2009,** *113* (10), 2117-2126.

192. DiLabio, G. A.; Johnson, E. R., Lone Pair−π and π−π Interactions Play an Important Role in Proton-Coupled Electron Transfer Reactions. *J. Am. Chem. Soc.* **2007,** *129* (19), 6199-6203.

193. Gagliardi, C. J.; Westlake, B. C.; Kent, C. A.; Paul, J. J.; Papanikolas, J. M.; Meyer, T. J., Integrating proton coupled electron transfer (PCET) and excited states. *Coord. Chem. Rev.* **2010,** *254* (21), 2459-2471.

194. Venkataraman, C.; Soudackov, A. V.; Hammes-Schiffer, S., Photoinduced homogeneous proton-coupled electron transfer: Model study of isotope effects on reaction dynamics. *J. Chem. Phys.* **2009,** *131* (15), 154502.

195. Tishchenko, O.; Truhlar, D. G.; Ceulemans, A.; Nguyen, M. T., A Unified Perspective on the Hydrogen Atom Transfer and Proton-Coupled Electron Transfer Mechanisms in Terms of Topographic Features of the Ground and Excited Potential Energy Surfaces As Exemplified by the Reaction between Phenol and Radicals. *J. Am. Chem. Soc.* **2008,** *130* (22), 7000-7010.

196. Irebo, T.; Reece, S. Y.; Sjödin, M.; Nocera, D. G.; Hammarström, L., Proton-Coupled Electron Transfer of Tyrosine Oxidation: Buffer Dependence and Parallel Mechanisms. *J. Am. Chem. Soc.* **2007,** *129* (50), 15462-15464.

197. Skone, J. H.; Soudackov, A. V.; Hammes-Schiffer, S., Calculation of Vibronic Couplings for Phenoxyl/Phenol and Benzyl/Toluene Self-Exchange Reactions: Implications for Proton-Coupled Electron Transfer Mechanisms. *J. Am. Chem. Soc.* **2006,** *128* (51), 16655-16663.

198. Mayer, J. M.; Rhile, I. J., Thermodynamics and kinetics of proton-coupled electron transfer: stepwise vs. concerted pathways. *Biochim. Biophys. Acta* **2004,** *1655*, 51-58.

199. Lennox, J. C.; Kurtz, D. A.; Huang, T.; Dempsey, J. L., Excited-State Proton-Coupled Electron Transfer: Different Avenues for Promoting Proton/Electron Movement with Solar Photons. *ACS Energy Lett.* **2017,** *2* (5), 1246-1256.

200. Westlake, B. C.; Brennaman, M. K.; Concepcion, J. J.; Paul, J. J.; Bettis, S. E.; Hampton, S. D.; Miller, S. A.; Lebedeva, N. V.; Forbes, M. D. E.; Moran, A. M.; Meyer, T. J.; Papanikolas, J. M., Concerted electron-proton transfer in the optical excitation of hydrogen-bonded dyes. *Proc. Natl. Acad. Sci. U.S.A.* **2011,** *108* (21), 8554-8558.

201. Gagliardi, C. J.; Wang, L.; Dongare, P.; Brennaman, M. K.; Papanikolas, J. M.; Meyer, T. J.; Thompson, D. W., Direct Observation of Light-Driven, Concerted Electron-ProtonTransfer. *Proc. Natl. Acad. Sci. U.S.A.* **2016,** *113* (40), 11106-11109.

202. Hossen, T.; Sahu, K., Photo-induced Electron Transfer or Proton-Coupled Electron Transfer in Methylbipyridine/Phenol Complexes: A Time-Dependent Density Functional Theory Investigation. *J. Phys. Chem. A* **2019,** *123* (38), 8122-8129.

203. Tyburski, R.; Fohlinger, J.; Hammarstrom, L., Light Driven Electron Transfer in Methylbipyridine/Phenol Complexes Is Not Proton Coupled. *J. Phys. Chem. A* **2018,** *122* (18), 4425-4429.

204. Eisenhart, T. T.; Dempsey, J. L., Photo-induced Proton-Coupled Electron Transfer Reactions of Acridine Orange: Comprehensive Spectral and Kinetics Analysis. *J. Am. Chem. Soc.* **2014,** *136* (35), 12221-12224.

205. Parada, G. A.; Goldsmith, Z. K.; Kolmar, S.; Pettersson Rimgard, B.; Mercado, B. Q.; Hammarström, L.; Hammes-Schiffer, S.; Mayer, J. M., Concerted proton-electron transfer reactions in the Marcus inverted region. *Science* **2019,** *364* (6439), 471-475.

206. Bowring, M. A.; Bradshaw, L. R.; Parada, G. A.; Pollock, T. P.; Fernández-Terán, R. J.; Kolmar, S. S.; Mercado, B. Q.; Schlenker, C. W.; Gamelin, D. R.; Mayer, J. M., Activationless Multiple-Site Concerted Proton–Electron Tunneling. *J. Am. Chem. Soc.* **2018,** *140* (24), 7449-7452.

207. Sayfutyarova, E. R.; Hammes-Schiffer, S., Substituent Effects on Photochemistry of Anthracene–Phenol–Pyridine Triads Revealed by Multireference Calculations. *J. Am. Chem. Soc.* **2020,** *142* (1), 487-494.

208. Rabe, E. J.; Corp, K. L.; Huang, X.; Ehrmaier, J.; Flores, R. G.; Estes, S. L.; Sobolewski, A. L.; Domcke, W.; Schlenker, C. W., Barrierless Heptazine-Driven Excited State Proton-Coupled

Electron Transfer: Implications for Controlling Photochemistry of Carbon Nitrides and Aza-Arenes. *J. Phys. Chem. C* **2019,** *123* (49), 29580-29588.

209. Rabe, E. J.; Corp, K. L.; Sobolewski, A. L.; Domcke, W.; Schlenker, C. W., Proton-Coupled Electron Transfer from Water to a Model Heptazine-Based Molecular Photocatalyst. *J. Phys. Chem. Lett.* **2018,** *9* (21), 6257-6261.

210. Ko, C.; Solis, B. H.; Soudackov, A. V.; Hammes-Schiffer, S., Photoinduced Proton-Coupled Electron Transfer of Hydrogen-Bonded p-Nitrophenylphenol–Methylamine Complex in Solution. *J. Phys. Chem. B* **2013,** *117* (1), 316-325.

211. Goyal, P.; Schwerdtfeger, C. A.; Soudackov, A. V.; Hammes-Schiffer, S., Proton Quantization and Vibrational Relaxation in Nonadiabatic Dynamics of Photoinduced Proton-Coupled Electron Transfer in a Solvated Phenol-Amine Complex. *J. Phys. Chem. B* **2016,** *120* (9), 2407-2417.

212. Goyal, P.; Hammes-Schiffer, S., Role of Solvent Dynamics in Photoinduced Proton-Coupled Electron Transfer in a Phenol–Amine Complex in Solution. *J. Phys. Chem. Lett.* **2015,** *6* (18), 3515-3520.

213. Gamiz-Hernandez, A. P.; Magomedov, A.; Hummer, G.; Kaila, V. R. I., Linear Energy Relationships in Ground State Proton Transfer and Excited State Proton-Coupled Electron Transfer. *J. Phys. Chem. B* **2015,** *119* (6), 2611-2619.

214. Ren, G.; Meng, Q.; Zhao, J.; Chu, T., Molecular Design for Electron-Driven Double-Proton Transfer: A New Scenario for Excited-State Proton-Coupled Electron Transfer. *J. Phys. Chem. A* **2018,** *122* (47), 9191-9198.

215. Wenger, O. S., Proton-Coupled Electron Transfer with Photoexcited Metal Complexes. *Acc. Chem. Res.* **2013,** *46* (7), 1517-1526.

216. Freys, J. C.; Bernardinelli, G.; Wenger, O. S., Proton-coupled electron transfer from a luminescent excited state. *ChemComm* **2008,** (36), 4267-4269.

217. Martinez, K.; Stash, J.; Benson, K. R.; Paul, J. J.; Schmehl, R. H., Direct Observation of Sequential Electron and Proton Transfer in Excited-State ET/PT Reactions. *J. Phys. Chem. C* **2019,** *123* (5), 2728-2735.

218. Khade, R. V.; Dutta Choudhury, S.; Pal, H.; Kumbhar, A. S., Excited State Interaction of Ruthenium (II) Imidazole Phenanthroline Complex [Ru(bpy)2ipH]2+ with 1,4-Benzoquinone: Simple Electron Transfer or Proton-Coupled Electron Transfer? *ChemPhysChem* **2018,** *19* (18), 2380-2388.

219. Concepcion, J. J.; Brennaman, M. K.; Deyton, J. R.; Lebedeva, N. V.; Forbes, M. D. E.; Papanikolas, J. M.; Meyer, T. J., Excited-State Quenching by Proton-Coupled Electron Transfer. *J. Am. Chem. Soc.* **2007,** *129* (22), 6968-6969.

220. Lebedeva, N. V.; Schmidt, R. D.; Concepcion, J. J.; Brennaman, M. K.; Stanton, I. N.; Therien, M. J.; Meyer, T. J.; Forbes, M. D. E., Structural and pH Dependence of Excited State PCET Reactions Involving Reductive Quenching of the MLCT Excited State of [RuII(bpy)2(bpz)]2+ by Hydroquinones. *J. Phys. Chem. A* **2011,** *115* (15), 3346-3356.

221. Dongare, P.; Bonn, A. G.; Maji, S.; Hammarström, L., Analysis of Hydrogen-Bonding Effects on Excited-State Proton-Coupled Electron Transfer from a Series of Phenols to a Re(I) Polypyridyl Complex. *J. Phys. Chem. C* **2017,** *121* (23), 12569-12576.

222. Goings, J. J.; Reinhardt, C. R.; Hammes-Schiffer, S., Propensity for Proton Relay and Electrostatic Impact of Protein Reorganization in Slr1694 BLUF Photoreceptor. *J. Am. Chem. Soc.* **2018,** *140* (45), 15241-15251.

223. Sayfutyarova, E. R.; Goings, J. J.; Hammes-Schiffer, S., Electron-Coupled Double Proton Transfer in the Slr1694 BLUF Photoreceptor: A Multireference Electronic Structure Study. *J. Phys. Chem. B* **2019,** *123* (2), 439-447.

224. Goings, J. J.; Hammes-Schiffer, S., Early Photocycle of Slr1694 Blue-Light Using Flavin Photoreceptor Unraveled through Adiabatic Excited-State Quantum Mechanical/Molecular Mechanical Dynamics. *J. Am. Chem. Soc.* **2019,** *141* (51), 20470-20479.

225. Lacombat, F.; Espagne, A.; Dozova, N.; Plaza, P.; Müller, P.; Brettel, K.; Franz-Badur, S.; Essen, L.-O., Ultrafast Oxidation of a Tyrosine by Proton-Coupled Electron Transfer Promotes Light Activation of an Animal-like Cryptochrome. *J. Am. Chem. Soc.* **2019,** *141* (34), 13394-13409.

226. Robert, G. P.; Yang, W., *Density-functional theory of atoms and molecules*. Oxford University Press: New York, 1994.

227. Lewars, E. G., *Computational Chemistry*. Springer: 2011.

228. Kohn, W.; Sham, L. J., Self-Consistent Equations Including Exchange and Correlation Effects. *Phys. Rev.* **1965,** *140* (4A), A1133-A1138.

229. Hohenberg, P.; Kohn, W., Inhomogeneous Electron Gas. *Phys. Rev.* **1964,** *136* (3B), B864-B871.

230. Stephens, P. J.; Devlin, F. J.; Chabalowski, C. F.; Frisch, M. J., Ab Initio Calculation of Vibrational Absorption and Circular Dichroism Spectra Using Density Functional Force Fields. *J. Phys. Chem.* **1994,** *98* (45), 11623-11627.

231. Adamo, C.; Barone, V., Toward reliable density functional methods without adjustable parameters: The PBE0 model. *J. Chem. Phys.* **1999,** *110* (13), 6158-6170.

232. Perdew, J. P.; Ernzerhof, M.; Burke, K., Rationale for mixing exact exchange with density functional approximations. *J. Chem. Phys.* **1996,** *105* (22), 9982-9985.

233. Zhao, Y.; Truhlar, D. G., The M06 suite of density functionals for main group thermochemistry, thermochemical kinetics, noncovalent interactions, excited states, and transition elements: two new functionals and systematic testing of four M06-class functionals and 12 other functionals. *Theor. Chem. Acc.* **2008,** *120* (1), 215-241.

234. Tawada, Y.; Tsuneda, T.; Yanagisawa, S.; Yanai, T.; Hirao, K., A long-range-corrected time-dependent density functional theory. *J. Chem. Phys.* **2004,** *120* (18), 8425-8433.

235. Yanai, T.; Tew, D. P.; Handy, N. C., A new hybrid exchange–correlation functional using the Coulomb-attenuating method (CAM-B3LYP). *Chem. Phys. Lett.* **2004,** *393* (1), 51-57.

236. Grimme, S., Density functional theory with London dispersion corrections. *Wiley Interdiscip. Rev. Comput. Mol. Sci.* **2011,** *1* (2), 211-228.

237. Chai, J.-D.; Head-Gordon, M., Long-range corrected hybrid density functionals with damped atom–atom dispersion corrections. *Phys. Chem. Chem. Phys.* **2008,** *10* (44), 6615-6620.

238. Gross, E. K. U. D., J. F.; Petersilka, M., Density Functional Theory II. Top. Curr. Chem.: 1996; Vol. 181, p 81.

239. Van Leeuwen, R., Key concepts in time-dependent density-functional theory. *Int. J. Mod. Phys. B* **2001,** *15* (14), 1969-2023.

240. Onida, G.; Reining, L.; Rubio, A., Electronic excitations: density-functional versus many-body Green's-function approaches. *Rev. Mod. Phys.* **2002,** *74* (2), 601.

241. Runge, E.; Gross, E. K. U., Density-Functional Theory for Time-Dependent Systems. *Phys. Rev. Lett* **1984,** *52* (12), 997-1000.

242. McLean, A. D.; Chandler, G. S., Contracted Gaussian Basis Sets for Molecular Calculations. I. Second Row Atoms, Z=11–18. *J. Chem. Phys.* **1980,** *72* (10), 5639-5648.

243. Frisch, M. J.; Trucks, G. W.; Schlegel, H. B.; Scuseria, G. E.; Robb, M. A.; Cheeseman, J. R.; Scalmani, G.; Barone, V.; Petersson, G. A.; Nakatsuji, H.; Li, X.; Caricato, M.; Marenich, A.; Bloino, J.; Janesko, B. G.; Gomperts, R.; Mennucci, B.; Hratchian, H. P.; Ortiz, J. V.; Izmaylov, A. F.; Sonnenberg, J. L.; Williams-Young, D.; Ding, F.; Lipparini, F.; Egidi, F.; Goings, J.; Peng, B.; Petrone, A.; Henderson, T.; Ranasinghe, D.; Zakrzewski, V. G.; Gao, J.; Rega, N.; Zheng, G.; Liang, W.; Hada, M.; Ehara, M.; Toyota, K.; Fukuda, R.; Hasegawa, J.; Ishida, M.; Nakajima, T.; Honda, Y.; Kitao, O.; Nakai, H.; Vreven, T.; Throssell, K.; Jr., J. A. M.; Peralta, J. E.; Ogliaro, F.; Bearpark, M.; Heyd, J. J.; Brothers, E.; Kudin, K. N.; Staroverov, V. N.; Keith, T.; Kobayashi, R.; Normand, J.; Raghavachari, K.; Rendell, A.; Burant, J. C.; Iyengar, S. S.; Tomasi, J.; Cossi, M.; Millam, J. M.; Klene, M.; Adamo, C.; Cammi, R.; Ochterski, J. W.; Martin, R. L.; Morokuma, K.; Farkas, O.; Foresman, J. B.; Fox, D. J., Gaussian 09, Revision A.02. *Gaussian, Inc., Wallingford CT* **2016**.

244. Mennucci, B.; Cancès, E.; Tomasi, J., Evaluation of Solvent Effects in Isotropic and Anisotropic Dielectrics and in Ionic Solutions with a Unified Integral Equation Method: Theoretical Bases, Computational Implementation, and Numerical Applications. *J. Phys. Chem. B* **1997,** *101* (49), 10506-10517.

245. Singh, U. C.; Kollman, P. A., An Approach to Computing Electrostatic Charges for Molecules. *J. Comput. Chem.* **1984,** *5* (2), 129-145.

246. Weigend, F.; Ahlrichs, R., Balanced Basis Sets of Split Valence, Triple Zeta Valence and Quadruple Zeta Valence Quality for H to Rn: Design and Assessment of Accuracy. *Phys. Chem. Chem. Phys.* **2005,** *7* (18), 3297-3305.
247. Grimme, S.; Antony, J.; Ehrlich, S.; Krieg, H., A Consistent and Accurate Ab initio Parametrization of Density Functional Dispersion Correction (DFT-D) for the 94 Elements H-Pu. *J. Chem. Phys.* **2010,** *132* (15), 154104.
248. Marenich, A. V.; Cramer, C. J.; Truhlar, D. G., Universal Solvation Model Based on Solute Electron Density and on a Continuum Model of the Solvent Defined by the Bulk Dielectric Constant and Atomic Surface Tensions. *J. Phys. Chem. B* **2009,** *113* (18), 6378-6396.
249. Ponder, J. W.; Case, D. A., Force Fields for Protein Simulations. In *Advances in Protein Chemistry*, Academic Press: 2003; Vol. 66, pp 27-85.
250. Jones, J. E.; Chapman, S., On the determination of molecular fields. —II. From the equation of state of a gas. *Proc. R. Soc. Lond.* **1924,** *106* (738), 463-477.
251. Coulomb, C. A., *Collection de ´memoires relatifs `a la physique Gauthier-Villars*. 1884; p 569-638.
252. Verlet, L., Computer "Experiments" on Classical Fluids. I. Thermodynamical Properties of Lennard-Jones Molecules. *Phys. Rev.* **1967,** *159* (1), 98-103.
253. Eastwood., R. W. H. a. J. W., *Computer simulations using particles*. Adam Hilger: Bristol, 1988.
254. Swope, W. C.; Andersen, H. C.; Berens, P. H.; Wilson, K. R., A computer simulation method for the calculation of equilibrium constants for the formation of physical clusters of molecules: Application to small water clusters. *J. Chem. Phys.* **1982,** *76* (1), 637-649.
255. Frisch, M. J. T., G. W.; Schlegel, H. B.; Scuseria, G. E.; Robb, M. A.; Cheeseman, J. R.; Montgomery, Jr., J. A.; Vreven, T.; Kudin, K. N.; Burant, J. C.; Millam, J. M.; Iyengar, S. S.; Tomasi, J.; Barone, V.; Mennucci, B.; Cossi, M.; Scalmani, G.; Rega, N.; Petersson, G. A.; Nakatsuji, H.; Hada, M.; Ehara, M.; Toyota, K.; Fukuda, R.; Hasegawa, J.; Ishida, M.; Nakajima, T.; Honda, Y.; Kitao, O.; Nakai, H.; Klene, M.; Li, X.; Knox, J. E.; Hratchian, H. P.; Cross, J. B.; Bakken, V.; Adamo, C.; Jaramillo, J.; Gomperts, R.; Stratmann, R. E.; Yazyev, O.; Austin, A. J.; Cammi, R.; Pomelli, C.; Ochterski, J. W.; Ayala, P. Y.; Morokuma, K.; Voth, G. A.; Salvador, P.; Dannenberg, J. J.; Zakrzewski, V. G.; Dapprich, S.; Daniels, A. D.; Strain, M. C.; Farkas, O.; Malick, D. K.; Rabuck, A. D.; Raghavachari, K.; Foresman, J. B.; Ortiz, J. V.; Cui, Q.; Baboul, A. G.; Clifford, S.; Cioslowski, J.; Stefanov, B. B.; Liu, G.; Liashenko, A.; Piskorz, P.; Komaromi, I.; Martin, R. L.; Fox, D. J.; Keith, T.; Al-Laham, M. A.; Peng, C. Y.; Nanayakkara, A.; Challacombe, M.; Gill, P. M. W.; Johnson, B.; Chen, W.; Wong, M. W.; Gonzalez, C.; and Pople, J. A., Gaussian 03, Revision C.02. *Gaussian, Inc., Wallingford CT.* **2004**.
256. Bayly, C. I.; Cieplak, P.; Cornell, W.; Kollman, P. A., A Well-Behaved Electrostatic Potential Based Method Using Charge Restraints for Deriving Atomic Charges: the RESP Model. *J. Phys. Chem.* **1993,** *97* (40), 10269-10280.
257. Martínez, L.; Andrade, R.; Birgin, E. G.; Martínez, J. M., PACKMOL: A package for building initial configurations for molecular dynamics simulations. *J. Comput. Chem.* **2009,** *30* (13), 2157-2164.
258. Case, D. A.; Darden, T. A.; Cheatham III, T. E.; Simmerling, C. L.; Wang, J.; Duke, R. E.; Luo, R.; Walker, R. C.; Zhang, W.; Merz, K. M.; Roberts, B.; Hayik, S.; Roitberg, A.; Seabra, G.; Swails, J.; Götz, A. W.; Kolossváry, I.; Wong, K. F.; Paesani, F.; Vanicek, J.; Wolf, R. M.; Liu, J.; Wu, X.; Brozell, S. R.; Steinbrecher, T.; Gohlke, H.; Cai, Q.; Ye, X.; Wang, J.; Hsieh, M.-J.; Cui, G.; Roe, D. R.; Mathews, D. H.; Seetin, M. G.; Salomon-Ferrer, R.; Sagui, C.; Babin, V.; Luchko, T.; Gusarov, S.; Kovalenko, A.; Kollman, P. A., *AMBER 12, University of California, San Francisco* **2012**.
259. Wang, J.; Wolf, R. M.; Caldwell, J. W.; Kollman, P. A.; Case, D. A., Development and Testing of a General Amber Force Field. *J. Comput. Chem.* **2004,** *25* (9), 1157-1174.
260. Wang, J.; Hou, T., Application of Molecular Dynamics Simulations in Molecular Property Prediction. 1. Density and Heat of Vaporization. *J. Chem. Theory Comput.* **2011,** *7* (7), 2151-2165.
261. Berendsen, H. J. C.; Postma, J. P. M.; van Gunsteren, W. F.; DiNola, A.; Haak, J. R., Molecular Dynamics with Coupling to an External Bath. *J. Chem. Phys.* **1984,** *81* (8), 3684-3690.

262. Ryckaert, J.-P.; Ciccotti, G.; Berendsen, H. J. C., Numerical Integration of the Cartesian Equations of Motion of a System with Constraints: Molecular Dynamics of n-Alkanes. *J. Comput. Phys.* **1977,** *23* (3), 327-341.
263. Essmann, U.; Perera, L.; Berkowitz, M. L.; Darden, T.; Lee, H.; Pedersen, L. G., A Smooth Particle Mesh Ewald Method. *J. Chem. Phys.* **1995,** *103* (19), 8577-8593.
264. Lindner, K.; Saenger, W., Crystal and molecular structure of cyclohepta-amylose dodecahydrate. *Carbohydr. Res.* **1982,** *99* (2), 103-115.
265. Kirschner, K. N.; Yongye, A. B.; Tschampel, S. M.; González-Outeiriño, J.; Daniels, C. R.; Foley, B. L.; Woods, R. J., GLYCAM06: A Generalizable Biomolecular Force Field. Carbohydrates. *J. Comput. Chem.* **2008,** *29* (4), 622-655.
266. Wang, J.; Wang, W.; Kollman, P. A.; Case, D. A., Automatic Atom Type and Bond Type Perception in Molecular Mechanical Calculations. *J. Mol. Graph. Model.* **2006,** *25* (2), 247-260.
267. Jorgensen, W. L.; Chandrasekhar, J.; Madura, J. D.; Impey, R. W.; Klein, M. L., Comparison of Simple Potential Functions for Simulating Liquid Water. *J. Chem. Phys.* **1983,** *79* (2), 926-935.
268. Hünenberger, P. H., Thermostat Algorithms for Molecular Dynamics Simulations. In *Advanced Computer Simulation: Approaches for Soft Matter Sciences I*, Dr. Holm, C.; Prof. Dr. Kremer, K., Eds. Springer Berlin Heidelberg: Berlin, Heidelberg, 2005; pp 105-149.
269. Humphrey, W.; Dalke, A.; Schulten, K., VMD: Visual Molecular Dynamics. *J. Mol. Graph.* **1996,** *14* (1), 33-38.
270. Puliti, R.; Mattia, C. A.; Paduano, L., Crystal structure of a new α-cyclodextrin hydrate form. Molecular geometry and packing features: disordered solvent contribution. *Carbohydr. Res.* **1998,** *310* (1), 1-8.
271. Bauman, R. P., *Absorption spectroscopy*. Wiley: 1962.
272. Lakowicz, J. R., *Principles of fluorescence spectroscopy*. Springer Verlay: 2007.
273. D. V. O'Conor & Philips, D., *Time correlated single photon counting*. Academic Press: New York, 1984.
274. Frederic P. Miller, A. F. V. J., M., *Isothermal titration calorimetry*. VDM Publishing: 2010.
275. Healy, E. F., Quantitative Determination of DNA–Ligand Binding Using Fluorescence Spectroscopy. *J. Chem. Educ.* **2007,** *84* (8), 1304.
276. Benesi, H. A.; Hildebrand, J. H., A Spectrophotometric Investigation of the Interaction of Iodine with Aromatic Hydrocarbons. *J. Am. Chem. Soc.* **1949,** *71* (8), 2703-2707.
277. Henderson, L. J., The Theory of Neutrality Regulation in the Animal Organism. *Am. J. Physiol.-Legacy Content* **1908,** *21* (4), 427-448.
278. Henderson, L. J., Concerning the Relationship Between the Strength of Acids and Their Capacity to Preserve Neutrality. *Am. J. Physiol.-Legacy Content* **1908,** *21* (2), 173-179.
279. Po, H. N.; Senozan, N. M., The Henderson-Hasselbalch Equation: Its History and Limitations. *J. Chem. Educ.* **2001,** *78* (11), 1499.
280. Venkatachalapathy, B.; Ramamurthy, P., Excited State Proton and Electron Transfer Reactions of Acridinedione Dyes with Amines. *Phys. Chem. Chem. Phys.* **1999,** *1* (9), 2223-2230.
281. Purkayastha, P.; Bera, S. C.; Chattopadhyay, N., Ground and Excited State Proton Transfer of Some Carbazole Derivatives : A linear Correlation Between the Acidity Constant and Charge Density on the Deprotonation Centre. *J. Mol. Liq.* **2000,** *88* (1), 33-42.
282. Han, F.; Liu, W.; Zhu, L.; Wang, Y.; Fang, C., Initial hydrogen-bonding dynamics of photoexcited coumarin in solution with femtosecond stimulated Raman spectroscopy. *J. Mater. Chem. C* **2016,** *4* (14), 2954-2963.
283. Su, J.; Tian, D., Strengthening of hydrogen bonded coumarin 102 in ethanol solvent upon photoexcitation. *New J. Chem.* **2014,** *38* (2), 568-573.
284. Miao, C.; Shi, Y., Reconsideration on hydrogen bond strengthening or cleavage of photoexcited coumarin 102 in aqueous solvent: A DFT/TDDFT study. *J. Comput. Chem.* **2011,** *32* (14), 3058-3061.
285. Marekha, B. A.; Koverga, V. A.; Chesneau, E.; Kalugin, O. N.; Takamuku, T.; Jedlovszky, P.; Idrissi, A., Local Structure in Terms of Nearest-Neighbor Approach in 1-Butyl-3-

methylimidazolium-Based Ionic Liquids: MD Simulations. *J. Phys. Chem. B* **2016,** *120* (22), 5029-5041.
286. Mesele, O. O.; Vartia, A. A.; Laage, D.; Thompson, W. H., Reorientation of Isomeric Butanols: The Multiple Effects of Steric Bulk Arrangement on Hydrogen-Bond Dynamics. *J. Phys. Chem. B* **2016,** *120* (8), 1546-1559.
287. Alcalde, R.; Atilhan, M.; Trenzado, J. L.; Aparicio, S., Physicochemical Insights on Alkylcarbonate–Alkanol Solutions. *J. Phys. Chem. B* **2016,** *120* (22), 5015-5028.
288. Hiratsuka, M.; Ohmura, R.; Sum, A. K.; Alavi, S.; Yasuoka, K., A molecular dynamics study of guest-host hydrogen bonding in alcohol clathrate hydrates. *Phys. Chem. Chem. Phys.* **2015,** *17* (19), 12639-12647.
289. Zhang, H.; Tan, T.; Feng, W.; van der Spoel, D., Molecular Recognition in Different Environments: β-Cyclodextrin Dimer Formation in Organic Solvents. *J. Phys. Chem. B* **2012,** *116* (42), 12684-12693.
290. Jana, M.; Bandyopadhyay, S., Molecular Dynamics Study of β-Cyclodextrin–Phenylalanine (1:1) Inclusion Complex in Aqueous Medium. *J. Phys. Chem. B* **2013,** *117* (31), 9280-9287.
291. Pallewela, G. N.; Smith, P. E., Preferential Solvation in Binary and Ternary Mixtures. *J. Phys. Chem. B* **2015,** *119* (51), 15706-15717.
292. Laha, A. K.; Das, P. K.; Bagchi, S., Study of Preferential Solvation in Mixed Binary Solvent as a Function of Solvent Composition and Temperature by UV−Vis Spectroscopic Method. *J. Phys. Chem. A* **2002,** *106* (13), 3230-3234.
293. Turro, C.; Chang, C. K.; Leroi, G. E.; Cukier, R. I.; Nocera, D. G., Photoinduced electron transfer mediated by a hydrogen-bonded interface. *J. Am. Chem. Soc.* **1992,** *114* (10), 4013-4015.
294. Hodgkiss, J. M.; Damrauer, N. H.; Pressé, S.; Rosenthal, J.; Nocera, D. G., Electron Transfer Driven by Proton Fluctuations in a Hydrogen-Bonded Donor−Acceptor Assembly. *J. Phys. Chem. B* **2006,** *110* (38), 18853-18858.
295. Dey, A.; Dana, J.; Aute, S.; Maity, P.; Das, A.; Ghosh, H. N., Proton-Coupled Electron-Transfer Processes in Ultrafast Time Domain: Evidence for Effects of Hydrogen-Bond Stabilization on Photoinduced Electron Transfer. *Chem. Eur. J.* **2017,** *23* (14), 3455-3465.
296. Hossen, T.; Sahu, K., Elucidating the H-Bonding Environment of Coumarin 102 in a Phenol–Cyclohexane Mixture by Molecular Dynamics Simulation: Implications for H-Bond-Guided Photoinduced Electron Transfer. *J. Phys. Chem. A* **2017,** *121* (3), 616-622.
297. Liu, Y.-H.; Lan, S.-C.; Zhu, C.; Lin, S.-H., Intersystem Crossing Pathway in Quinoline–Pyrazole Isomerism: A Time-Dependent Density Functional Theory Study on Excited-State Intramolecular Proton Transfer. *J. Phys. Chem. A* **2015,** *119* (24), 6269-6274.
298. Kang, B.; Shi, H.; Yan, S.; Lee, J. Y., Solvent Effect on Electron and Proton Transfer in the Excited State of a Hydrogen Bonded Phenol–Imidazole Complex. *RSC Adv.* **2014,** *4* (73), 38551-38557.
299. Warren, J. J.; Tronic, T. A.; Mayer, J. M., Thermochemistry of Proton-Coupled Electron Transfer Reagents and its Implications. *Chem. Rev.* **2010,** *110* (12), 6961-7001.
300. Hammes-Schiffer, S.; Stuchebrukhov, A. A., Theory of Coupled Electron and Proton Transfer Reactions. *Chem. Rev.* **2010,** *110* (12), 6939-6960.
301. Liu, T. F.; Guo, M. Y.; Orthaber, A.; Lomoth, R.; Lundberg, M.; Ott, S.; Hammarstrom, L., Accelerating Proton-Coupled Electron Transfer of Metal Hydrides in Catalyst Model Reactions. *Nat. Chem.* **2018,** *10* (8), 881-887.
302. Solis, B. H.; Hammes-Schiffer, S., Proton-Coupled Electron Transfer in Molecular Electrocatalysis: Theoretical Methods and Design Principles. *Inorg. Chem.* **2014,** *53* (13), 6427-6443.
303. Chen, J. Q.; Wu, K. F.; Rudshteyn, B.; Jia, Y. Y.; Ding, W. D.; Xie, Z. X.; Batista, V. S.; Lian, T. Q., Ultrafast Photoinduced Interfacial Proton Coupled Electron Transfer from CdSe Quantum Dots to 4,4 '-Bipyridine. *J. Am. Chem. Soc.* **2016,** *138* (3), 884-892.
304. Amin, M.; Vogt, L.; Vassiliev, S.; Rivalta, I.; Sultan, M. M.; Bruce, D.; Brudvig, G. W.; Batista, V. S.; Gunner, M. R., Electrostatic Effects on Proton Coupled Electron Transfer in Oxomanganese Complexes Inspired by the Oxygen-Evolving Complex of Photosystem II. *J. Phys. Chem. B* **2013,** *117* (20), 6217-6226.

305. Safko, T. M.; Jiang, S. L.; Zhang, L.; Zhang, Q.; Weiss, R. G., Proton-Coupled Charge-Transfer Reactions and Photoacidity of N, N-Dimethyl-3-arylpropan-1-ammonium chloride Salts. *Photochem. Photobiol. Sci.* **2017,** *16* (6), 972-984.

306. Safko, T. M.; Faleiros, M. M.; Atvars, T. D. Z.; Weiss, R. G., Intramolecular, Exciplex-Mediated, Proton-Coupled, Charge-Transfer Processes in N,N-Dimethyl-3-(1-pyrenyl)propan-1-ammonium Cations: Influence of Anion, Solvent Polarity, and Temperature. *J. Phys. Chem. A* **2016,** *120* (23), 3983-3991.

307. Capello, M. C.; Hernández, F. J.; Broquier, M.; Dedonder-Lardeux, C.; Jouvet, C.; Pino, G. A., Hydrogen Bonds vs. π-Stacking Interactions in the p-Aminophenol···p-Cresol Dimer: an Experimental and Theoretical Study. *Phys. Chem. Chem. Phys.* **2016,** *18* (45), 31260-31267.

308. Lu, T.; Chen, F. W., Multiwfn: A Multifunctional Wavefunction Analyzer. *J. Comput. Chem.* **2012,** *33* (5), 580-592.

309. Mennucci, B., Hydrogen Bond versus Polar Effects: An Ab Initio Analysis on n → π* Absorption Spectra and N Nuclear Shieldings of Diazines in Solution. *J. Am. Chem. Soc.* **2002,** *124* (7), 1506-1515.

310. Zhang, J.; Zhang, H.; Wu, T.; Wang, Q.; van der Spoel, D., Comparison of Implicit and Explicit Solvent Models for the Calculation of Solvation Free Energy in Organic Solvents. *J. Chem. Theory Comput.* **2017,** *13* (3), 1034-1043.

311. Fang, C.; Frontiera, R. R.; Tran, R.; Mathies, R. A., Mapping GFP Structure Evolution during Proton Transfer with Femtosecond Raman Spectroscopy. *Nature* **2009,** *462*, 200.

312. Masgrau, L.; Roujeinikova, A.; Johannissen, L. O.; Hothi, P.; Basran, J.; Ranaghan, K. E.; Mulholland, A. J.; Sutcliffe, M. J.; Scrutton, N. S.; Leys, D., Atomic Description of an Enzyme Reaction Dominated by Proton Tunneling. *Science* **2006,** *312*, 237.

313. Bhattacharyya, K., Solvation Dynamics and Proton Transfer in Supramolecular Assemblies. *Acc. Chem. Res.* **2002,** *36* (2), 95-101.

314. Agmon, N., Elementary Steps in Excited-State Proton Transfer. *J. Phys. Chem. A* **2005,** *109*, 13.

315. Kalyanasis, S.; Kumar, M. S.; Subhadip, G.; Kankan, B., Ultrafast Dynamics in Biological Systems and in Nano-Confined Environments. *Bull. Chem. Soc. Jpn.* **2007,** *80* (6), 1033-1043.

316. Chou, P.-T.; Solntsev, K. M., Photoinduced Proton Transfer in Chemistry and Biology. *J. Phys. Chem. B* **2015,** *119* (6), 2089-2089.

317. Tolbert, L. M.; Solntsev, K. M., Excited-State Proton Transfer: From Constrained Systems to “Super” Photoacids to Superfast Proton Transfer. *Acc. Chem. Res.* **2002,** *35* (1), 19-27.

318. Sedgwick, M.; Cole, R. L.; Rithner, C. D.; Crans, D. C.; Levinger, N. E., Correlating Proton Transfer Dynamics To Probe Location in Confined Environments. *J. Am. Chem. Soc.* **2012,** *134* (29), 11904-11907.

319. Phukon, A.; Barman, N.; Sahu, K., Wet Interface of Benzylhexadecyldimethylammonium Chloride Reverse Micelle Revealed by Excited State Proton Transfer of a Localized Probe. *Langmuir* **2015,** *31*, 12587.

320. Phukon, A.; Ray, S.; Sahu, K., How Does Interfacial Hydration Alter during Rod to Sphere Transition in DDAB/Water/Cyclohexane Reverse Micelles? Insights from Excited State Proton Transfer and Fluorescence Anisotropy. *Langmuir* **2016,** *32*, 6656.

321. Phukon, A.; Sahu, K., How Do the Interfacial Properties of Zwitterionic Sulfobetaine Micelles Differ from those of Cationic Alkyl Quaternary Ammonium Micelles? An Excited State Proton Transfer Study. *Phys. Chem. Chem. Phys.* **2017,** *19*, 31461.

322. Agbaria, R. A.; Uzan, B.; Gill, D., Fluorescence of 1,6-naphthalenediol with cyclodextrins. *J. Phys. Chem.* **1989,** *93* (9), 3855-3859.

323. Yorozu, T.; Hoshino, M.; Imamura, M.; Shizuka, H., Photoexcited Inclusion Complexes of .Beta.-Naphthol with .Alpha.-, .beta.-, and .Gamma.-Cyclodextrins in Aqueous Solutions. *J. Phys. Chem.* **1982,** *86* (22), 4422-4426.

324. Abdel-Shafi, A. A., Spectroscopic studies on the inclusion complex of 2-naphthol-6-sulfonate with β-cyclodextrin. *Spectrochim. Acta, Part A* **2007,** *66*, 732.

325. Alazaly, A. M. M.; Amer, A. S. I.; Fathi, A. M.; Abdel-Shafi, A. A., Photoacids as Singlet Oxygen Photosensitizers: Direct Determination of the Excited State Acidity by Time-Resolved Spectroscopy. *J. Photochem. Photobiol. A* **2018,** *364*, 819-825.

326. Pines, E.; Huppert, D., Observation of Geminate Recombination in Excited State Proton Transfer. *J. Chem. Phys.* **1986,** *84* (6), 3576-3577.
327. Simkovitch, R.; Pines, D.; Agmon, N.; Pines, E.; Huppert, D., Reversible Excited-State Proton Geminate Recombination: Revisited. *J. Phys. Chem. B* **2016,** *120* (49), 12615-12632.
328. Syme, N. R.; Dennis, C.; Phillips, S. E. V.; Homans, S. W., Origin of Heat Capacity Changes in a "Nonclassical" Hydrophobic Interaction. *ChemBioChem* **2007,** *8*, 1509.
329. Eskici, G.; Axelsen, P. H., The Size of AOT Reverse Micelles. *J. Phys. Chem. B* **2016,** *120* (44), 11337-11347.
330. Biswas, S.; Santra, S.; Yesylevskyy, S.; Maiti, J.; Jana, M.; Das, R., Picosecond Solvation Dynamics in Nanoconfinement: Role of Water and Host–Guest Complexation. *J. Phys. Chem. B* **2018,** *122* (14), 3996-4005.
331. Zheng, X.; Wang, D.; Shuai, Z.; Zhang, X., Molecular Dynamics Simulations of the Supramolecular Assembly between an Azobenzene-Containing Surfactant and α-Cyclodextrin: Role of Photoisomerization. *J. Phys. Chem. B* **2012,** *116* (2), 823-832.
332. Hajari, T.; Bandyopadhyay, S., Water Structure Around Hydrophobic Amino Acid Side Chain Analogs Using Different Water Models. *J. Chem. Phys.* **2017,** *146* (22), 225104.
333. Singh, M. K.; Shweta, H.; Khan, M. F.; Sen, S., New Insight into Probe-Location Dependent Polarity and Hydration at Lipid/Water Interfaces: Comparison between Gel- and Fluid-Phases of Lipid Bilayers. *Phys. Chem. Chem. Phys.* **2016,** *18* (35), 24185-24197.
334. Borah, S.; Padma Kumar, P., Ab Initio Molecular Dynamics Investigation of Structural, Dynamic and Spectroscopic Aspects of Se(vi) Species in the Aqueous Environment. *Phys. Chem. Chem. Phys.* **2016,** *18* (21), 14561-14568.
335. Munitz, N.; Avital, Y.; Pines, D.; Nibbering, E. T. J.; Pines, E., Cation-Enhanced Deprotonation of Water by a Strong Photobase. *Isr. J. Chem.* **2009,** *49* (2), 261-272.
336. Hedges, A. R., Industrial Applications of Cyclodextrins. *Chem. Rev.* **1998,** *98* (5), 2035-2044.
337. Tiwari, G.; Tiwari, R.; Rai, A., Cyclodextrins in delivery systems: Applications. *J. Pharm. Bioallied Sci.* **2010,** *2* (2), 72-79.
338. Crini, G., Review: A History of Cyclodextrins. *Chem. Rev.* **2014,** *114*, 10940.
339. Shaikh, M.; Mohanty, J.; Singh, P. K.; Nau, W. M.; Pal, H., Complexation of acridine orange by cucurbit[7]uril and β-cyclodextrin: photophysical effects and pKa shifts. *Photochem. Photobiol. Sci.* **2008,** *7* (4), 408-414.
340. Mohanty, J.; Bhasikuttan, A. C.; Nau, W. M.; Pal, H., Host−Guest Complexation of Neutral Red with Macrocyclic Host Molecules: Contrasting pKa Shifts and Binding Affinities for Cucurbit[7]uril and β-Cyclodextrin. *J. Phys. Chem. B* **2006,** *110* (10), 5132-5138.
341. Chattopadhyay, N., Effect of cyclodextrin complexation on excited state proton transfer reactions. *J. Photochem. Photobiol. A* **1991,** *58* (1), 31-36.
342. Mukhopadhyay, M.; Banerjee, D.; Mukherjee, S., Proton-Transfer Reaction of 4-Methyl 2,6-Diformyl Phenol in Cyclodextrin Nanocage. *J. Phys. Chem. A* **2006,** *110* (47), 12743-12751.
343. Chattopadhyay, N.; Chakraborty, T.; Nag, A.; Chowdhury, M., Effect of inclusion of cyclodextrin on excited state proton transfer: Carbazole—γ-cyclodextrin. *J. Photochem. Photobiol. A* **1990,** *52* (1), 199-204.
344. Hossen, T.; Sahu, K., Effect of Photoacid Strength on Fluorescence Modulation of 2-Naphthol Derivatives inside β-Cyclodextrin Cavity: Insights from Fluorescence, Isothermal Calorimetry, and Molecular Dynamics Simulations. *J. Phys. Chem. B* **2019,** *123* (44), 9291-9301.
345. Naidoo, K. J.; Gamieldien, M. R.; Chen, J. Y. J.; Widmalm, G.; Maliniak, A., Glucose Orientation and Dynamics in α-, β-, and γ-Cyclodextrins. *J. Phys. Chem. B* **2008,** *112*, 15151.
346. Saenger, W.; Jacob, J.; Gessler, K.; Steiner, T.; Hoffmann, D.; Sanbe, H.; Koizumi, K.; Smith, S. M.; Takaha, T., Structures of the Common Cyclodextrins and Their Larger AnaloguesBeyond the Doughnut. *Chem. Rev.* **1998,** *98* (5), 1787-1802.
347. Shi, Z.; Debenedetti, P. G.; Stillinger, F. H., Relaxation processes in liquids: Variations on a theme by Stokes and Einstein. *J. Chem. Phys.* **2013,** *138* (12), 12A526.
348. Paduano, L.; Sartorio, R.; Vitagliano, V.; Costantino, L., Diffusion properties of cyclodextrins in aqueous solution at 25°C. *J. Solution Chem.* **1990,** *19* (1), 31-39.

349. Paul, B. K.; Ghosh, N.; Mukherjee, S., Interaction of Bile Salts with β-Cyclodextrins Reveals Nonclassical Hydrophobic Effect and Enthalpy–Entropy Compensation. *J. Phys. Chem. B* **2016,** *120*, 3963.
350. Nilsson, M.; Valente, A. J. M.; Olofsson, G.; Söderman, O.; Bonini, M., Thermodynamic and Kinetic Characterization of Host−Guest Association between Bolaform Surfactants and α- and β-Cyclodextrins. *J. Phys. Chem. B* **2008,** *112* (36), 11310-11316.
351. Paul, B. K.; Ghosh, N.; Mondal, R.; Mukherjee, S., Contrasting Effects of Salt and Temperature on Niosome-Bound Norharmane: Direct Evidence for Positive Heat Capacity Change in the Niosome:β-Cyclodextrin Interaction. *J. Phys. Chem. B* **2016,** *120* (17), 4091-4101.
352. Mondal, R.; Ghosh, N.; Mukherjee, S., Enhanced Binding of Phenosafranin to Triblock Copolymer F127 Induced by Sodium Dodecyl Sulfate: A Mixed Micellar System as an Efficient Drug Delivery Vehicle. *J. Phys. Chem. B* **2016,** *120* (11), 2968-2976.